Université Catholique de Louvain

Faculté des Sciences

Institut de Recherche en Mathematique et Physique

Center for Cosmology, Particle Physics and Phenomenology

Beyond Standard Model Phenomenology at the LHC

Doctoral dissertation presented by

Priscila de Aquino

in partial fulfillment of the requirements for the degree of Doctor in Sciences

Jury de thèse:

Prof. Dr. Fabio Maltoni, *Promoteur*	UCL
Prof. Dr. Antoine Van Proeyen, *Promoteur*	KU Leuven
Prof. Dr. Mark Fannes	KU Leuven
Prof. Dr. Jean-Marc Gérard	UCL
Prof. Dr. Frederik Denef	KU Leuven
Prof. Dr. Ben Craps	VUB/Brussels
Prof. Dr. Benjamin Fuks	IPHC/Strasbourg
Prof. Dr. Gustavo Burdman	USP/São Paulo

May 2012

The present manuscript is the result from a cooperation programme between the Katholieke Universiteit Leuven and the Université Catholique de Louvain.

Acknowledgements

"*In the vastness of space and the immensity of time, it is my joy to share a planet and an epoch with you.*" [Carl Sagan]

I would like to express my endless gratitude to everyone who has helped me to obtain my PhD in Belgium!

A very special thank you for my supervisors Prof. Fabio Maltoni and Prof. Antoine Van Proeyen who have inspired me, encouraged me and believed in me during this entire journey. Fabio, it is indescribable how much I have learned from you! Thank you for your incredible enthusiasm, dedication and for guiding me through every stage. The passion you have for this field is contagious, and it has certainly infected me! Toine, I will be always thankful for the opportunity you have given me when you accepted me as your "half-student"! Thank you for your careful supervision and for the several valuable discussions and advices!

During the past four years, I had the pleasure to experience a joint PhD programme between two Belgian universities which have one time in history been one: Katholieke Universiteit Leuven (KU Leuven) and Université Catholique de Louvain (UCL). This unique experience has enabled me to work with twice as much inspiring researchers and to make twice as much friends!

I would like to show my appreciation to all professors from the ITF at KU Leuven and the CP3 at UCL, with whom I had many valuable discussions. A special thanks to Prof. Jean-Marc Gérard who has taught me so much, and to Prof. Eduardo Cortina who has kindly assisted me when I was acclimatizing to my new life in Belgium!

A kind thank you to my jury members and to all my scientific collaborators with whom I had the chance to work with and learn so much from. Thank you Claude Duhr and Benjamin Fuks for greatly assisting me during the initial stage of my research.

Thank you Xavier Calmet for all the advices and the encouragement for working with gravitons! Thank you Prof. Kaoru Hagiwara and Qiang Li for your kindness and your constant willingness to support and teach me! Thank you Olivier, Céline, Pierre and Simon for your incredible assistance and patience when explaining me methods and codes. A big thanks also to the MadGraph and FeynRules teams.

To complete my scientific collaboration through all regions of Belgium I had also the pleasure to work with the phenomenological group created at the Vrije Universiteit Brussels in 2010. I would like to thank enormously Dr. Kentarou Mawatari, Prof. Ben Craps, and Bettina Oexl for this very fruitful collaboration, which has enriched my life as a researcher.

I would like to express my heartfelt gratitude to all ITF-members, whom have always made me feel at home! Special thanks to Anneleen and Filip who made the past four years so fun and bureaucratic and computational easy! Thanks Simi, Myriam, Eliran, Nick, Bert, Frederik, Hans, Soghra, Matthijs, Paul, Darya, John, Jean-Charles, Fernandos and all *ITF'ers* without whom these years would not have passed in a blink of an eye!

An affectionate thanks to all the CP3-members for your kindness and friendship. In particular thanks Elvira for your optimism and a so cheerful carpool! Thanks a lot Ginette, Carine, Vincent and Jérôme for your incredible support with all practical and computational matters! Thanks Marco, Antoine, Philippe, Maria, Michael, Mathieu, Elisa, Arnaud, Nicolas, Suzan, Lawrence, Simone and all friends from CP3 for such a joyful work-environment.

I would like to express a warm thanks also to all the friends I have made in Belgium, in particular to all *imec'ers* who have received me and shared so many happy moments with me!

A special thanks to the KU Leuven International Office, Mrs. Hilde Nijs and Mr. Edmundo Guzman who have enabled my doctoral studies through the KU Leuven SBA-Latin America grant, and helped me to stablish here in Belgium. This work is supported in part by the FWO - Vlaanderen, Project No. G.0651.11, and in part by the Federal Office for Scientific, Technical and Cultural Affairs through the "Interuniversity Attraction Poles Programme – Belgian Science Policy" P6/11-P.

Thank you Prof. Gustavo Burdman for the scientific motivation and the encouragement during my master studies in Brazil and for giving me the enormous support when I decided to come to Belgium. It was a great pleasure to work and to learn so much from you!

Acima de tudo um muito obrigada muito especial à toda a minha família por todo suporte que me deram todos estes anos, desde que eu escolhi esta profissão única! Obrigada ao meus pais, Gisela e Nelson, e aos meus irmãos, Lígia e Guilherme, por todo o carinho e pelo total apoio em todas as minhas decisões! Sem vocês eu com certeza não estaria aqui! Muito obrigada também aos meus avós Darly e Waldyr que acompanharam todos os momentos deste doutorado via skype! Obrigada Simone, Lau, Lu, Rafas, Bê, Henry, Maju, Bia, Livia, Lezey e Raquel por estarem sempre me incentivando e me dando força para continuar! Obrigada vó Marly, vô Zé, Mara, Paulinho, Flavia e Luiza por todo o apoio mesmo estando tão longe.

Um obrigada especial ao Pedro com quem falar de física é sempre um grande prazer! Muito obrigada Guerino, Marcia, Sandra, Marcelo, Ju e Miguel por todo carinho e companherismo durante todos estes anos.

A final and full-of-love-special thanks to my husband Mauricio who has always inspired me, supported me and has been on my side unconditionally! Mau, I do not have words to describe how much I thank you for making all my dreams come true! It has been an honour to share this amazing journey with you!

Priscila, May 2012

Abstract

The Standard Model of fundamental particles and their interactions is one of the most successful theories in physics. In particular, up to the weak scale (a few hundreds of GeV) it agrees to a great degree with a large set of experimental data. However, there are several theoretical reasons, such as the so-called "Hierarchy Problem", as well as experimental ones, such as the neutrino masses and the evidence for dark matter in the Universe, to expect that something new (particles and/or interactions) could lie at TeV scale. Hints and/or answer(s) to these fundamental questions will be provided by the Large Hadron Collider (LHC), a proton-proton collider running at high energies.

The present thesis aims to explore new physics at the LHC through phenomenological studies that employ simulations and computational tools to directly link theories with experimental data. In particular, the focus is on Beyond Standard Model theories that can incorporate a quantum description of gravity, such as extra dimensional theories, Supersymmetry and yet a simplified model where the constant of Newton is scale dependent. Phenomenological analyses are performed in which graviton and gravitino emission in combination with multiple jets are investigated at hadron colliders. Inclusive samples are generated by merging matrix element with parton shower descriptions, and validated by a comparison against next-to-leading order QCD calculations. Predictions for relevant observables at the LHC and Tevatron are obtained.

Résumé

Le Modèle Standard des particules élémentaires et des interactions fondamentales constitue une des théories les plus fructueuses en physique. En particulier, jusqu'à l'échelle éléctrofaible (quelques centaines de GeV), cette théorie est en excellent accord avec un grand nombre de résultats expérimentaux. Cependant, plusieurs raisons théoriques et expérimentales telles que le problème de la hiérarchie, celui de la masse des neutrinos ou de la matière noire laissent entrevoir de possibles extensions (particules et/ou interactions) à l'échelle du TeV. Des pistes pour répondre à ces questions fondamentales seront fournies par le *Large Hadron Collider* (LHC), un collisionneur proton-proton fonctionnant aux hautes énergies.

La présente thèse a pour objectif l'exploration de "nouvelle physique" au LHC sur base de simulations et d'outils informatiques permettant de relier directement la théorie aux données expérimentales. Dans ce cadre, un intérêt particulier est porté aux théories au-delà du Modèle Standard pouvant inclure une description quantique de la gravité, telles que des modèles avec des dimensions supplémentaires, la Supersymétrie, ou encore un modèle simplifié où la constante de Newton dépend de l'échelle. Des analyses phénoménologiques sont réalisées, dans lesquelles des processus d'émission de gravitons et de gravitinos accompagnés de jets multiples sont étudiés dans les collisionneurs hadroniques. Des échantillons inclusifs d'événements sont obtenus en combinant les descriptions selon l'élément de matrice et selon la gerbe partonique. Ils sont validés par la confrontation aux calculs à l'ordre suivant en théorie de perturbation de QCD. Des prédictions pour des observables appropriées au LHC et au Tevatron sont ainsi obtenues.

Samenvatting

Het standaard model van de fundamentele deeltjes en hun interacties is één van de meest succesvolle theorieën in de fysica. Meer bepaald, tot op de zwakke schaal (een paar honderd GeV) komt het met grote nauwkeurigheid overeen met een groot deel van de experimentele data. Maar er zijn enkele theoretische redenen, zoals het zogenaamde "Hierarchie Probleem", en ook experimentele redenen zoals de neutrino massa's en het bewijs voor donkere materie in het universum, om ook te verwachten dat iets nieuws (deeltjes en/of interacties) kan opduiken rond de TeV-schaal. Hints en/of antwoorden voor deze fundamentele vragen worden geleverd door de Large Hadron Collider (LHC), een proton-proton deeltjesversneller die op hoge energieën werkt.

Deze thesis heeft als doel de verkenning van nieuwe fysica aan de LHC, door fenomenologische studies die simulatie en computationele technieken gebruiken om theorie en experimentele data met elkaar te verbinden. In het bijzonder, ligt de focus op "Beyond Standard Model" theorieën die een kwantum beschrijving van gravitatie bevatten, zoals extra dimensionele theorieën, Supersymmetrie en ook nog een vereenvoudigd model waarin de constante van Newton schaalafhankelijk is. Fenomenologische analyses worden uitgevoerd, waarin graviton en gravitino emissie in combinatie met meervoudige jets worden onderzocht in hadron versnellers. Veelomvattende samples worden gegenereerd door het samenvoegen van matrix elementen met parton stortregen beschrijvingen, en gevalideerd door een vergelijking met op-één-natoonaangevende orde QCD-berekeningen. Voorspellingen voor relevante observabelen aan de LHC en Tevatron worden bekomen.

Contents

1 Introduction **3**

2 The Standard Model **7**

2.1 Symmetries, gauge theory and particle content 7

2.2 The Brout-Englert-Higgs mechanism 10

2.3 Experimental facts and Standard Model constraints 14

2.4 Why to go Beyond the Standard Model? 16

2.4.1 The Hierarchy Problem 17

2.4.2 Fermionic mass hierarchy 18

2.4.3 CP violation 20

2.4.4 Dark matter 20

3 Gravitation in Beyond Standard Model theories **25**

3.1 Gravity as a field theory 25

3.2 The theory with a scale-dependent M_{pl} 30

3.3 Extra Dimensions 34

3.3.1 Large Extra Dimensions 34

3.3.2 Warped Extra Dimensions 40

3.4 The graviton propagator 44

3.5 Graviton emission cross sections 48

4 The LHC and collision simulations **53**

4.1 Introduction to the LHC 53

4.2 Predictive methods at colliders 57

4.2.1 Kinematics and jet definitions 57

4.2.2 Next-to-leading order cross section contributions 61

4.3 Monte-Carlo collider simulations 64

4.3.1 Simulation tools 64

4.3.2 Matrix-element/parton-shower matching scheme 68

5 Phenomenology of graviton production **75**

5.1 Graviton emission in mono-jet searches 76

5.1.1 Mono-jet for the MGM theory 78

5.1.2 Mono-jet for the ADD theory 80

5.2 Graviton emission in multi-jet searches 82

5.2.1 Fully inclusive graviton production for the RS theory 84

5.2.2 Semi-inclusive analysis for graviton emission processes . . . 92

6 Gravitino production at the LHC **109**

6.1 Supersymmetry and the hierarchy problem 109

6.2 A brief introduction to the MSSM 111

6.2.1 Particle content of the MSSM 112

6.3 Supergravity: the goldstino and the gravitino 114

6.3.1 Gauge mediated supersymmetry breaking 114

6.3.2 The super-Higgs mechanism 116

6.3.3 The effective theory for light gravitinos 118

6.4 The phenomenology of gravitino emission 122

6.4.1 Parameter definitions 126

6.4.2 Checks and validations 127

6.4.3 Results 129

7 Epilogue **137**

7.1 Summary and conclusions 137

7.2 Outlook 140

A Massless graviton implementation **143**

A.1 HELAS routines modifications 143

A.1.1 TXXXXX 143

A.1.2 UIOXXX, UVVXXX, UIOVXX, UVVVXX 145

A.2 MGM model file 146

B New routines for ADD theories in MadGraph **149**

B.1 5-point vertices 149

B.2 Summation over the mass spectrum 154

C ALOHA **159**

C.1 Introduction 160

C.2 Automation of the method 160

C.3 ALOHA output 165

C.4 Checks and validation 166

C.4.1 Spin-2 validation checks 166

C.4.2 Goldstino validation checks 168

Chapter 1

Introduction

The Standard Model (SM) of fundamental particles and their interactions is one of the most successful theories in physics. It provides an astonishingly accurate description of phenomena in a wide range of scales. In particular, up to the weak scale (a few hundreds of GeV) it agrees to a great degree with the experimental data collected, also predicting the existence of a new scalar state, the Higgs particle, which, however, has so far eluded all searches[1].

There are several theoretical reasons, such as the so-called "Hierarchy Problem" and the "fermion mass hierarchy", as well as experimental ones, such as the neutrino masses and the evidence for dark matter in the Universe, to expect that "new physics" could lie at the TeV scale. Hints and/or answer(s) to these fundamental questions are expected to be provided very soon by the Large Hadron Collider (LHC), a proton-proton collider running at high-energies.

In particular, the search for a quantum field theory aiming at unifying gravity with the other three known forces of nature (electromagnetic, weak and strong forces) has been the main subject of several researches for many years. If the SM is not the complete picture, it may be possible to construct effective theories that incorporate gravity as a field theory. Higher dimensional theories have been an attempt of such scenarios since the beginning of the 20th century, when it was realized that the 5-dimensional generalization of the theory proposed by Einstein could describe both gravitational and electromagnetic interactions. However, because of the weak characteristic of gravity, inconsistencies arose when the mathematical theory was formulated. Such theories were therefore left aside until the appearance of the theories of *Supergravity* and *Superstrings* in the early 1970's.

More recent ideas using extra-dimensions have been proposed in the context of minimal extensions of the SM. These theories are created to address SM limitations, and

[1] The most recent results from the LHC and Tevatron experiments provide, however, the first experimental indications of its existence.

have a particular behaviour at high-energies. They however maintain all the low-energy features of the SM. The philosophy of such extra-dimensional theories lies in the idea that the SM is a 4-dimensional projection of a theory living in higher-dimensional space-time. Different scenarios have been built with such principles. We can cite for instance *theories with large extra dimensions* [1, 2, 3], and *theories with warped extra dimensions* [4, 5].

Furthermore, there are different extensions to the theory that are based on more effective approaches to include gravity. For example, general descriptions of 4-dimensional theories can account for gravitational interactions with SM particles through the existence of new particles living in a hidden sector [6, 7, 8, 9, 10, 11].

In addition, further extensions can be cited, such as *Supersymmetry*, which is based on symmetry principles rather than on extra-dimensions. Supersymmetric theories start from the assumption that there must exist an extra symmetry that transforms fermions into bosons, and vice-versa. As a consequence, all particles of the SM must have super-partners, *i.e.* particles that differ from SM particles by half a spin. Variations of such theories can predict, for example, the existence of the graviton particle, a hypothetical spin-2 particle that mediates the force of gravitation, and its super-partner, the spin-$3/2$ particle named gravitino.

The observation of new fundamental particles at hadron colliders can therefore be one indication of the existence of Beyond Standard Model (BSM) theories. Typically, each new physics model has its own characteristic predictions. Yet, it is often the case that very different theories might lead to similar signatures at colliders. This is the case, for example, with models that predict the existence of a dark matter candidate, weakly interacting, whose emission would just generate missing transverse energy in energetic multi-jet events. Gravitinos and neutralinos, predicted by supersymmetric theories, or gravitons, in specific variations of extra-dimensional models, are just a few examples of particles and models giving possibly equivalent signatures at the LHC.

With the LHC running, and a high luminosity being achieved, chances are that new physics will be emerging soon. However, the fact that so far no new particle has been detected, implies that more careful, accurate and dedicated studies will be needed. If evidence for new physics will emerge, it will be urgent yet certainly not trivial to understand its nature and to clearly identify it. The typical final states produced at the LHC involve a large number of jets, heavy-flavour quarks, missing energy and leptons. Therefore, such an overwhelming number of possible signs of new physics need a very careful understanding of the detector as well as an accurate modelling of the data themselves.

For this reason, precise simulation and computational tools play a key role in the current analyses. They have become indispensable in the effort of connecting theory with experimental data sets.

The possibility of automatically obtaining predictions at colliders from any BSM theory shows substantial progress. With such, it is possible to test and validate theories before an experimental analysis is performed. Tests and validations account for the specifications of the experiment and are very time consuming. This step already considerably reduces the number of theories suitable for correctly describing experimental data once these are at our disposal.

Until a few years ago, such possibility was not available. The implementation of complex BSM models in existing general purpose event generators was often a process susceptible to several calculation errors. That was because the derivation of Feynman rules to describe new interactions and their implementation into event generators depended on several aspects, going from convention definitions to computational difficulty. This situation has dramatically changed with the introduction of new simulation tools that can automatically link arbitrary lagrangians to a particular Monte-Carlo event generation that can be chosen by the user. Moreover, the development of several alternative simulation techniques (such as the merging procedure employed to match simulations performed by matrix element event generators with those obtained from the use of parton shower description) have substantially improved the precision of predictions at high energy hadron colliders. The evolution of such tools now provides a user-friendly manner to simulate BSM theories, and does not require a deep knowledge and/or strong computer skills to be applied.

The work presented in this thesis aims at performing phenomenological investigations at the LHC particularly focused on theories that incorporate gravity by means of a set of simulation tools and techniques developed for this purpose. We demonstrate how it is possible to perform complete phenomenological investigations that cover all the steps to link any theory with experiments. Furthermore, we explicitly show the particular efforts we have made for the development of automatic tools. As a natural step, we make use of such tools and design search strategies that can be applied in different studies, including those at a more experimental level.

This thesis is divided in five main chapters. In the following chapter, we present an introduction to the Standard Model and why extensions thereof are considered. In Chapter 3, gravitation as a quantum field theory is introduced as well as BSM theories that include the graviton particle. Theories with extra-dimensions and a particular theory, in which Newton's constant vary according to the effective scale of the theory, are considered. The Large Hadron Collider is introduced in Chapter 4, together with simulation techniques that will be employed through the present study. In Chapter 5, we present the main phenomenological analyses for graviton production at hadron

colliders. We consider the emission of one graviton in combination with jets. Finally, in Chapter 6, we introduce Supersymmetry and perform phenomenological investigations. Despite the large number of new particles predicted within this theory, we focus on the production of gravitino in combination with jets. Similar techniques to those applied for graviton production analyses are employed for the gravitino. We conclude with a complete comparison of all the results obtained, and an outlook.

The work presented in this thesis is based on the following publications:

- X. Calmet and P. de Aquino,
  Quantum Gravity at the LHC,
  Eur. Phys. J. C 68, 305-311 (2010) [arXiv: 0906.0363]
- X. Calmet, P. de Aquino and T. G. Rizzo,
  Massless versus Kaluza-Klein Gravitons at the LHC,
  Phys. Lett. B 682, 446-449 (2010) [arXiv: 0910.1535]
- N. D. Christensen, P. de Aquino, C. Degrande, C. Duhr, B. Fuks,
  M. Herquet, F. Maltoni and S. Schumann,
  A comprehensive approach to new physics simulations,
  Eur. Phys. J. C 71, 1541 (2011) [arXiv: 0906.2474]
- P. de Aquino, K. Hagiwara, Q. Li and F. Maltoni,
  Simulating graviton production at hadron colliders,
  JHEP 1106 132 (2011) [arXiv: 1101.5499]
- P. de Aquino, W. Link, F. Maltoni, O. Mattelaer and T. Stelzer
  ALOHA: Automatic Libraries Of Helicity Amplitudes for Feynman diagram computations.
  accepted for publication in Comp. Phys. Comm. (2012)
  [arXiv: 1108.2041]

The discussion of Chapter 6 is on-going work and it has not yet been submitted for publication:

- P. de Aquino, F. Maltoni, K. Mawatari, B. Oexl
  Jets plus missing energy in light gravitino production at the LHC.
  in preparation (2012).

Chapter 2

The Standard Model

The Standard Model (SM) is a successful description of particle physics nowadays. It is a quantum field theory that explains the dynamics of our universe through matter and forces. It incorporates three fundamental forces: the weak, the strong and the electromagnetic forces, and includes different types of particles.

Mainly, the SM states that all the matter is composed by fermionic fields interacting among each other via vector fields. In order to understand the field content of the SM, it is necessary to begin with the definition of the symmetry group.

2.1 Symmetries, gauge theory and particle content

Symmetries have always played an important role in physics. The creation of the SM has not followed a different path: it is a theory based on a local symmetry.

The first theorem of Noether assures that any differentiable symmetry of the action of a physical system leads to a corresponding conservation law [12]. Any conservation law of physics can be interpreted as resulting from the symmetries of a particular theory.

One example is the theory of Quantum Electrodynamics (or, QED). The invariance under local transformation implies the existence of gauge fields with specific properties. To demonstrate such remarkable consequence, let us begin by considering a free theory of fermions. The free lagrangian can be written as

$$\mathcal{L} = \bar{\psi}(i\gamma_\mu \partial^\mu - m)\psi, \tag{2.1}$$

with ψ being the spin-1/2 field, $\bar{\psi} = \psi^\dagger \gamma^0$, and γ^μ the Dirac matrices. The lagrangian is invariant under a global gauge transformation $\psi \rightarrow e^{-i\alpha}\psi$, with α a constant phase,

which implies the conservation of the Dirac current $j^\mu(x)$:

$$\partial_\mu j^\mu = 0; \;\; j^\mu = \bar{\psi}\gamma^\mu\psi. \tag{2.2}$$

However, Eq. (2.1) is not invariant under local gauge transformations, where now α depends on the space-time coordinates, and suggests that the derivative should be redefined as

$$\partial^\mu \rightarrow D^\mu \equiv \partial^\mu + iqA^\mu. \tag{2.3}$$

where A^μ is a vector field. The lagrangian (2.1) with the replacement $\partial^\mu \rightarrow D^\mu$ is now invariant under the following local transformations

$$\psi(x) \rightarrow \psi'(x) = e^{-i\alpha(x)}\psi(x), \tag{2.4}$$

$$A^\mu(x) \rightarrow A^{\mu\,\prime} = A^\mu(x) + \frac{1}{q}\partial^\mu\alpha(x), \tag{2.5}$$

and is finally given by

$$\mathcal{L} = \bar{\psi}\left(i\gamma_\mu\partial^\mu - m\right)\psi - q\,\bar{\psi}\,\gamma_\mu A^\mu\,\psi. \tag{2.6}$$

The second term has been derived from the imposition of local invariance. It describes the interaction of the fermionic matter ψ already existent on the theory, with the gauge field A^μ. Therefore, a theory that had in principle only matter fields, needs vector fields to provide interactions amongst fermions.

One could thus generalize this principle for all interactions, *i.e.* generate interaction terms for the weak, electromagnetic, strong (and later gravitational) forces through specific symmetries imposed on the theory. This is basically the idea for constructing the SM initially proposed by Glashow [13] and independently by Salam and Ward [14], extended later by Weinberg [15] and Salam [16]. Of course the complexity is larger than previously explained, since it works perfectly for abelian theories, however the world is not only described by them. Before going ahead, it is worth reminding that the SM of particle physics was created as a puzzle, and each piece was put together at different moments of History.

Initially, the electroweak theory was developed, and the gauge group $SU(2)_L \times U(1)_Y$ was used to relate electric charge with the isospin and the leptonic hypercharge of a particle. Besides matter fields, four gauge bosons are included due to the gauge symmetry: one triplet associated with the $SU(2)$ group and one singlet associated to the $U(1)$. The corresponding lagrangian, restricted to the leptonic fields, is given by

$$\mathcal{L} = \bar{L}\gamma^\mu D_\mu L + \bar{e}_R\gamma_\mu D'_\mu e_R - \frac{1}{4}W^{\mu\nu\,i}W^i_{\mu\nu} - \frac{1}{4}B^{\mu\nu}B_{\mu\nu} \tag{2.7}$$

where the covariant derivatives are defined by

$$\begin{aligned} D_\mu =& \partial_\mu + i\frac{g}{2}\sigma^i W_\mu^i + i\frac{g'}{2}B_\mu, \\ D'_\mu =& \partial_\mu + ig'B_\mu, \end{aligned} \tag{2.8}$$

and L is the isospin doublet that contains the left-handed neutrino and electron, e_R is the right-handed electron[1], σ^i are the Pauli matrices, and g and g' are the coupling constants. $W^i_{\mu\nu}$ and $B_{\mu\nu}$ are the field-strength tensors:

$$\begin{aligned} W^i_{\mu\nu} =& \partial_\mu W^i_\nu - \partial_\nu W^i_\mu - g\epsilon^{ijk}W^j_\mu W^k_\nu \\ B_{\mu\nu} =& \partial_\mu B_\nu - \partial_\nu B_\mu. \end{aligned} \tag{2.9}$$

The matter content of the world is not only formed by leptons but also by hadrons, and it has been discovered that hadrons are composed by quarks. The symmetry that relates the color charge in quarks is $SU(3)_c$. The SM is consequently defined to have $SU(3)_c \times SU(2)_L \times U(1)_Y$ as the gauged symmetry group. Each gauge boson field is associated to the generator of the algebra of each group. Therefore, eight coloured spin-1 particles associated to the $SU_c(3)$ gauge group exist and are also known as gluons. In addition, there are still the four un-coloured particles, $W^i_{\mu\nu}$ and $B_{\mu\nu}$ quoted previously, that will mix to form the massive $W^\pm$ and Z^0 gauge bosons and the massless photon.

In a nutshell, the final particle content of the SM is summarized in Fig. 2.1 [17]. The masses and most significant quantum numbers of each particle are stated in the figure.

One important piece of the SM, the scalar fields, has not yet been mentioned. It has been stated that conservation laws are a consequence of imposed symmetries. The SM theory is therefore based on gauge symmetries, and lagrangians are constructed from the assumption of massless fields. The mechanism to generate mass to the particles requires the existence of at least one scalar particle, the Brout-Englert-Higgs boson[2]. This is the so-called BEH mechanism [18, 19, 20], which will be explained in what follows.

[1] Right-handed neutrinos are not included in the theory.

[2] From the present moment on we shall abbreviate Brout-Englert-Higgs boson by Higgs boson, which is the usual shortened form used in the literature.

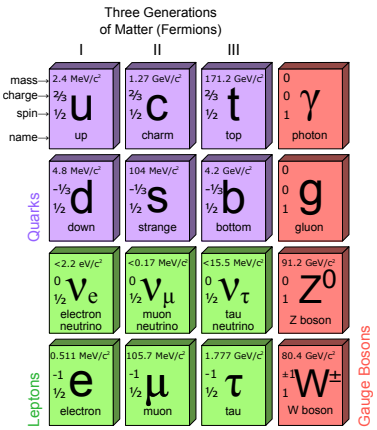

Figure 2.1: An illustration of the particle content of the Standard Model, excluding scalar fields. This is an interpretation of the periodic table of elements adapted to fundamental particle physics from [17].

2.2 The Brout-Englert-Higgs mechanism

It is known from Noether's theorem that symmetries imply conservation laws. It is a consequence of the invariance of both the lagrangian and the vacuum of a theory. However, there could be a situation where the lagrangian is invariant under a symmetry in which the vacuum is not. If such circumstance occurs, the symmetry is defined as to be broken, or hidden.

Consider for instance a scalar field ϕ whose lagrangian is given by [21]:

$$\mathcal{L}_\phi = \frac{1}{2}(\partial_\mu\phi)(\partial^\mu\phi) - V(\phi), \quad \text{with } V(\phi) = \frac{1}{2}\mu^2\phi^2 + \frac{1}{4}\lambda\phi^4, \tag{2.10}$$

where ϕ is real and $\lambda > 0$. The lagrangian is clearly invariant under the transformation $\phi \to -\phi$. When the vacuum expected value (vev) is calculated, two separated situations arise:

(a) If $\mu^2 > 0$, the vacuum is invariant under such symmetry,

$$\langle\phi\rangle_0 \equiv \langle 0|\phi|0\rangle = 0 \qquad (\mu^2 > 0). \tag{2.11}$$

(b) However, if $\mu^2 < 0$:

$$\langle\phi\rangle_0 = \pm\sqrt{\frac{-\mu^2}{2\lambda}} \equiv \pm\frac{v}{\sqrt{2}} \qquad (\mu^2 < 0). \tag{2.12}$$

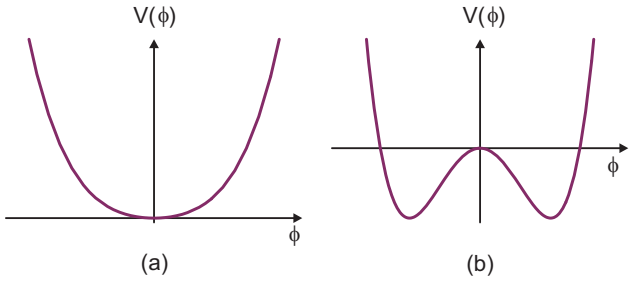

Figure 2.2: Potential $V(\phi)$ of Eq. (2.10) as a function of ϕ for the two situations presented: (a) with $\mu^2 > 0$ and (b) for $\mu^2 < 0$. For case (a), the minimum is at $\phi_0 = 0$ and for case (b) $\phi_0 = \pm v$, where the vacuum is degenerated.

The vacuum state in this case is degenerated, and it depends on the choice between $+v$ and $-v$.

Both situations are illustrated in Fig. 2.2. On the left side, the potential is shown as a function ϕ for $\mu^2 > 0$. As Eq. (2.11) revealed, only one vev is obtained. However, on the right, the plot of same potential is shown for the choice of $\mu^2 < 0$. Eq. (2.12) exhibits a degenerate vacuum state, displayed by the two local minimums in Fig. 2.2 (b).

We could therefore choose one state, for instance $\langle\phi\rangle_0 = +v$, and re-define the field in order for the vacuum to be at the origin:

$$\xi(x) \equiv \phi(x) - \langle\phi\rangle_0 = \phi(x) - v. \tag{2.13}$$

Now $\langle\xi\rangle_0 = 0$, and the lagrangian (2.10) becomes

$$\mathcal{L}_\xi = \frac{1}{2}(\partial_\mu\xi)(\partial^\mu\xi) - \lambda v^2\xi^2 - \lambda v\xi^3 - \frac{1}{4}\lambda\xi^4. \tag{2.14}$$

This is the lagrangian of a free scalar field ξ with mass term[3] $m_\xi = \sqrt{-2\mu^2}$. The symmetry was therefore hidden behind the primary definition of the field. By redefining the field ϕ it was possible to obtain the massive ξ. This concept is named *spontaneous symmetry breaking* and it illustrates the main mechanism used to generate the mass of fermionic and bosonic fields of the SM.

[3]Notice the mass is positive, since we are analysing the case where $\mu^2 < 0$.

In the SM, it is necessary to define a doublet composed of two complex scalar fields. Suppose the doublet ϕ can be defined in a Hermitian basis as [22, 23, 24]

$$\phi = \begin{pmatrix} \phi^+ \\ \phi^0 \end{pmatrix} = \frac{1}{\sqrt{2}} \begin{pmatrix} \phi_1 - i\phi_2 \\ \phi_3 - i\phi_4 \end{pmatrix} \tag{2.15}$$

The scalar lagrangian to be added to (2.7) will be similar to the one given in (2.10). However, in order to maintain the gauge invariance under $SU(2)_L \times U(1)_Y$, the covariant derivative (2.8) should be used:

$$\mathcal{L}_{BEH} = |D_\mu \phi|^2 - V(\phi). \tag{2.16}$$

In the new basis, the potential is

$$V(\phi) = \frac{1}{2}\mu^2 \left(\sum_{i=1}^{4} \phi_i^2 \right) + \frac{1}{4}\lambda \left(\sum_{i=1}^{4} \phi_i^2 \right)^2. \tag{2.17}$$

We can choose the position of the minimum as $\phi_1 = \phi_2 = \phi_4 = 0$ and $\phi_3 = v$, being v the Higgs vev. A new field h can be defined to be a radial excitation around the vev. The symmetry $SU(2)_L \times U(1)_Y$ is broken to $U(1)_{em}$ if we choose the specific value for the vev to be $\sqrt{-\mu^2/2\lambda}$. The field can thus be re-written as

$$\phi = \frac{1}{\sqrt{2}} \begin{pmatrix} 0 \\ v + h \end{pmatrix}, \tag{2.18}$$

The potential $V(\phi)$ of the lagrangian becomes

$$V_{BEH} = -\frac{1}{4}\lambda v^4 + \lambda v^2 h^2 + \lambda v h^3 + \frac{1}{4}\lambda h^4. \tag{2.19}$$

The second term indicates the mass of the Higgs field, $m_h^2 = 2v^2\lambda$. The third and the forth terms, *i.e.* the terms related to h^3 and h^4, indicate self-couplings of the Higgs boson.

The kinetic term of the lagrangian, $|D_\mu \phi|^2$ includes terms with the W_μ^i and B_μ fields,

$$\left| \left(i\frac{g}{2}\sigma^i W_\mu^i + i\frac{g'}{2}B_\mu \right) \phi \right|^2 = \frac{(v+h)^2}{8} \left[g^2 (W_\mu^1)^2 + g^2 (W_\mu^2)^2 + (-gW_\mu^3 + g' B_\mu)^2 \right]. \tag{2.20}$$

If four new vector fields are defined as:

$$Z_\mu^0 = \frac{1}{\sqrt{g^2+g'^2}}\left(gW_\mu^3 - g'B_\mu\right), \qquad W_\mu^\pm = \frac{1}{\sqrt{2}}\left(W_\mu^1 \mp iW_\mu^2\right), \tag{2.21}$$
$$A_\mu = \frac{1}{\sqrt{g^2+g'^2}}\left(g'W_\mu^3 + gB_\mu\right),$$

Eq. (2.20) can be written in terms of the new fields.The boson masses can be identified by the following terms of the lagrangian

$$m_W^2 W_\mu^+ W^{-\,\mu} + \frac{1}{2}\left(m_Z^2 Z_\mu Z^\mu + m_A^2 A_\mu A^\mu\right). \tag{2.22}$$

With the above expression, it is straightforward to find the masses related to the W_μ, Z_μ and A_μ fields [22]:

$$m_W = \frac{v\,g}{2}, \quad m_Z = \frac{v}{2}\sqrt{g^2+g'^2} \quad \text{and} \quad m_A = 0. \tag{2.23}$$

Notice however that covariant derivatives can now be written in terms of the new bosonic fields. Consequently, it is possible to re-write Eq. (2.8) in a more useful format, in terms of the electromagnetic coupling, given by

$$g_e = \frac{g\,g'}{\sqrt{g^2+g'^2}} \tag{2.24}$$

or in terms of the *weak mixing angle*,

$$g_e = g\sin\theta_w, \;\; \cos\theta_w = \frac{g}{\sqrt{g^2+g'^2}}, \;\; \text{and} \;\; \sin\theta_w = \frac{g'}{\sqrt{g^2+g'^2}}. \tag{2.25}$$

The mass of the $W^\pm$ and Z bosons are therefore related through the expression

$$m_W = m_Z\cos\theta_w. \tag{2.26}$$

As a result, all effects of $W^\pm$ and Z exchange processes (at tree level) can be exhibited as a function of the g_e, θ_w and m_W parameters.

Finally, to find the value for the vev v we can replace the expression found for the mass of the $W^\pm$ bosons in terms of the Fermi constant:

$$G_F = \sqrt{2}\,\frac{g^2}{8\,m_W^2} = \frac{\sqrt{2}}{2\,v^2}. \tag{2.27}$$

Because the Fermi constant is experimentally known with a very good accuracy, $G_F = 1.16637(1)\times 10^{-5}$ GeV^{-2} [25], the value for the Higgs vev can be deduced as $v \sim$

246 GeV. This is the value where the $SU(2)_L \times U(1)_Y$ is broken. However, because the parameter λ is not known, the mass of the Higgs boson cannot be predicted.

A similar mechanism is used to obtain the mass of the fermions. The invariant lagrangian that should be added to (2.7) can be exhibited as

$$\mathcal{L}_{yuk} = -\lambda_e \, \bar{L} \, \phi \, e_R - \lambda_d \, \bar{Q}_L \, \phi d_R - \lambda_u \, \bar{Q}_L \, \tilde{\phi} \, u_R + h.c. \tag{2.28}$$

where Q_L is the isospin doublet that contains the left-handed up and down quarks, u_R and d_R are the right-handed up and down quarks, $\tilde{\phi} = i\sigma_2\phi^*$, and σ_2 is one of the Pauli matrices. After spontaneous symmetry breaking, the mass of the fermions (except neutrinos) are generated as $m_f = \lambda_f v/2$, and neutrinos continue to be massless. The couplings λ_f are called Yukawa couplings [22], and are determined depending on the experimental values of fermionic masses.

2.3 Experimental facts and Standard Model constraints

As it has been stated, the SM is one of the most tested theories in physics. It has been experimentally investigated through different methods, and nowadays particle colliders are used for such task.

The final missing piece is, with no doubt, the experimental observation of the scalar sector of the SM through the Higgs particle. Very recent developments have been made in order to limit and constrain the mass of the Higgs particle using data from the Large Hadron Collider (LHC), the revolutionary proton-proton collider experiment situated in Switzerland. At this stage, we limit ourselves to display the most advanced SM results obtained from LHC data. A detailed description related to such collider will be presented in Chapter 4.

The LHC has started colliding protons for physics analyses in 2009, breaking energy records ever since. For more than a year starting in 2010, it has collided protons with a center-of-mass energy of 7 TeV, achieving a considerably high sensitivity. For this reason, many of the SM parameters have already been very precisely measured by the LHC. A summary of the most recent values due to electroweak constraints can be, for example,found in Reference [26]. As it has been stated, within the SM the only missing aspect is now the Higgs boson mass. However, it has been further constrained at the LHC by the end of 2011.

For a Higgs boson with a mass above 125 GeV, the search is dominated by bosonic modes, where Higgs decays to W^+W^- and ZZ. For lower masses, the most impor-

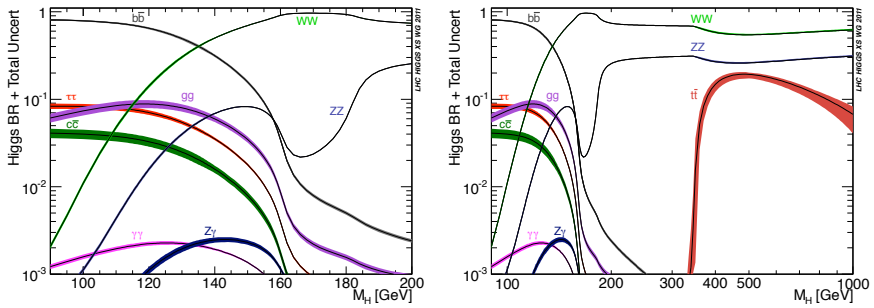

Figure 2.3: Higgs branching ratio for contributing decay channels as a function of the Higgs mass. These plots are made by the Higgs Working Group, extracted from [28].

tant channels are $b\bar{b}$, $\tau\tau$ and $\gamma\gamma$ [27]. This is explicitly displayed on Fig. 2.3 extracted from [28] that shows the Higgs branching ratio of each decay channel as a function of its expected mass.

The largest decay mode of the SM Higgs bosons is $h \rightarrow W^+W^-$. If the Higgs boson would have a mass between 160 GeV and 170 GeV, an excess would most probably (95% of confidence level) have already been observed by the Tevatron, proton-anti-proton hadron collider situated in the United States of America. Within the W^+W^- channel, purely leptonic ($h \rightarrow W^+W^- \rightarrow \ell\nu\ell\nu$) and semi-leptonic ($h \rightarrow W^+W^- \rightarrow \ell\nu qq$) decay modes are being searched at the LHC. The decay of the Higgs boson to a pair of Z bosons has also been very attractive due to the production of a very clean signal. If the Z boson would decay as $Z \rightarrow \ell\ell$, $h \rightarrow ZZ$ would produce 4ℓ signature, which is very uncommon for the SM, leading to very small background. The production of $h \rightarrow ZZ \rightarrow \ell\ell qq$ and $h \rightarrow ZZ \rightarrow \ell\ell qq$ are also being analysed. At the low mass region, direct analyses of $h \rightarrow \gamma\gamma$, $h \rightarrow b\bar{b}$ and $h \rightarrow \tau\tau$ are being taken care of by the collaborations of the LHC experiments.

Limits for the Higgs boson mass can therefore be set taking into account these analyses. Fig. 2.4 shows CMS[4] most recent results for the measurement of the rate σ/σ_{SM} (95% of confidence level), which is the excluded Higgs production cross section divided by the expected cross section based in the SM.

We can conclude from experimental analyses that the search for the Higgs boson might be close to the end. We have now a very thin mass gap where the Higgs could fit in. It is possible to notice from the right plot of Fig. 2.4 that an excess has been observed.

[4]CMS is one of the multi-purpose experiments of the LHC. More details will be given in Chapter 4.

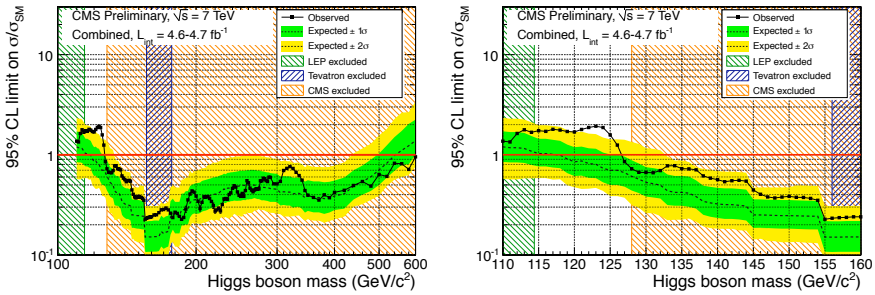

Figure 2.4: The combined 95% CL upper limits for the signal σ/σ_{SM} as a function of the Higgs boson mass. The dashed line is the median expected by the SM, the yellow and green bands, surrounding the dashed line, are the regions with 1σ and 2σ expected in the absence of a signal. The solid line exhibits the signal observed. The vertical green band is the exclusion gap imposed by LEP measurements, the blue band excluded by the Tevatron and the orange bands are the mass range excluded by the CMS collaboration on the present study. Both plots are extracted from [29].

However, it is yet very early to state whether it is related to the Higgs boson or it is only statistical fluctuations. The fact that both collaborations observe an excess in the same range for the mass of the Higgs, 120 GeV $< M_H <$ 130 GeV, it is a strong indication, which however can only be confirmed with analyses performed for a higher integrated luminosity.

We are living therefore in a historical moment for particle physics. If the Higgs is not discovered by the LHC very soon, the SM will not have a mechanism to explain the generation of mass for fermions and bosons. Fortunately, it has been shown that the LHC has strong indicators for a low mass Higgs boson of approximately 126 GeV. For the moment, only time can provide us these answers.

2.4 Why to go Beyond the Standard Model?

In the previous sections, it has been shown why the SM of particle physics is one of the most successful theories in physics, which explains with great accuracy the experimental data we have so far. However, the SM suffers from few shortcomings, which led theorists to believe there could be new physics lying at the TeV scale. Here, we present some of these issues, which will be addressed in further chapters by the introduction of extensions of the SM.

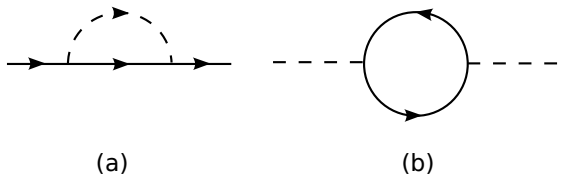

Figure 2.5: (a) Example of a fermionic loop on a scalar particle, (b) illustration of a scalar loop on a fermionic particle.

2.4.1 The Hierarchy Problem

Many features of the SM arise from the BEH mechanism, the procedure to generate masses for the particles observed. However, only calculations at the lowest level of perturbation theory, also known as tree-level contributions, have yet been discussed. In reality, radiative corrections to the mass of a particle should be computed when one-loop corrections to the propagator are considered.

Take for example a toy-theory with a single fermion ψ coupled to a massive scalar ϕ [30]. The lagrangian is given by

$$\mathcal{L}_\phi = i\,\bar{\psi}\gamma_\mu\partial^\mu\psi + |\partial_\mu\,\phi|^2 - m_s^2|\phi|^2 - \lambda_f\bar{\psi}\psi\phi. \tag{2.29}$$

As it has been done for the SM, we suppose the symmetry is spontaneously broken and the fermion obtains the mass $m_f = \lambda_f v/\sqrt{2}$ at the lowest order.

To compute corrections to the fermion mass within this toy-theory, it is necessary to consider one-loop contributions to the fermion propagator due to the scalar particle, as illustrated in Fig. 2.5 (a). The renormalized fermion mass is given by

$$m_f = m_f^{(0)} + \delta m_f \tag{2.30}$$

where $m_f^{(0)} = \lambda_f v/\sqrt{2}$, and the correction to the mass depends on the introduction of a cutoff Λ to the theory:

$$\delta m_f = -\frac{3\lambda_f^2 m_f}{64\pi^2}\log\frac{\Lambda^2}{m_f^2} + ... \tag{2.31}$$

where ... indicates terms that vanish when $\Lambda \to \infty$ or terms independent of the cutoff. Notice that the correction to the mass of the fermion depends explicitly on m_f. In the limit where the mass of the fermions are very small, the lagrangian (2.29) is invariant under chiral transformations. Therefore, decreasing the mass of the fermion increases

the symmetry of the theory. It is thus usually said that fermionic masses are protected by chiral symmetry.

Similarly, we could compute corrections to the scalar propagator due to the fermion loop, as shown on Fig. 2.5 (b). When this is done, the mass of the scalar obtains a δm_s correction, which can be written as:

$$\delta m_s^2 = -\frac{\lambda_f^2}{8\pi}\left[\Lambda^2 - 6\,m_f^2 \log\frac{\Lambda}{m_f} + 2\,m_f^2 + ...\right] \tag{2.32}$$

Differently from corrections for fermionic masses, the mass correction for a scalar particle is found to be quadratically divergent. For this reason, nothing can actually protect the mass of the scalar particle of having very large corrections. If we assume the theory to be valid until the Planck scale, *i.e.* scale at which quantum corrections to gravity become important, corrections to the scalar particles will be of such order of magnitude. Unless the mass of the particle and its correction are at most of the same order, the theory is considered to have a naturalness problem.

For the SM Higgs boson the same fact occurs. Obviously, corrections to the propagator due to all types of particles on the loop must be considered. However, the largest contributions come from fermionic loops, where quadratic divergences appear.

Since unitarity requires the Higgs boson to have a mass smaller than 1 TeV, quadratic divergences would indicate a large problem, considering corrections would have a much larger order of magnitude than the mass at lowest order. A counter term to cancel these quadratic divergences could solve the problem. However, such large cancellations would be highly un-natural. Conversely, one could adjust the cutoff down to 1 TeV. The result would be a theory that ceases to being valid at this energy scale. This is known as the *hierarchy problem*, and it is one of the reasons for which it is believed that new physics could indeed lie above the TeV scale.

2.4.2 Fermionic mass hierarchy

Another issue not well explained by the SM is related to the order of magnitude of the fermion masses. We have seen that fermionic lagrangian is defined by the Yukawa term, or Eq. (2.28), and they should acquire mass from spontaneous symmetry breaking. Concentrating on the quark terms, we have:

$$\mathcal{L}_{yuk}^{q} = -\lambda_d\,\bar{Q}_L\,\phi d_R - \lambda_u\,\bar{Q}_L\,\tilde{\phi}\,u_R + h.c, \tag{2.33}$$

which can be decomposed as

$$\mathcal{L}^q_{yuk} = \begin{pmatrix} \bar{u}'_R & \bar{c}'_R & \bar{t}'_R \end{pmatrix} \mathcal{M}_U \begin{pmatrix} u'_L \\ c'_L \\ t'_L \end{pmatrix} + \begin{pmatrix} \bar{d}'_R & \bar{s}'_R & \bar{b}'_R \end{pmatrix} \mathcal{M}_D \begin{pmatrix} d'_L \\ s'_L \\ b'_L \end{pmatrix} + h.c..$$

where we have used the *prime* notation to represent the weak eigenstates. However, there is no reason, in principle, for the matrices $\mathcal{M}_u = \frac{v}{\sqrt{2}}\,\lambda_u^{ij}$ and $\mathcal{M}_d = \frac{v}{\sqrt{2}}\,\lambda_d^{ij}$ to be diagonal. In fact, the weak eigenstates are linear superposition of mass eigenstates and the transformation can be given as

$$\begin{pmatrix} u' \\ c' \\ t' \end{pmatrix} = V_u \begin{pmatrix} u \\ c \\ t \end{pmatrix}, \quad \begin{pmatrix} d' \\ s' \\ b' \end{pmatrix} = V_d \begin{pmatrix} d \\ s \\ b \end{pmatrix} \tag{2.34}$$

where V_u and V_d are unitary matrices that diagonalize the mass matrices $\mathcal{M}_u$ and $\mathcal{M}_d$.

In the SM lagrangian, charged currents (processes intermediated by a charged particle, such as $W^{\pm}$) are proportional to

$$\begin{pmatrix} \bar{u}'_L & \bar{c}'_L & \bar{t}'_L \end{pmatrix} \gamma^\mu \begin{pmatrix} d'_L \\ s'_L \\ b'_L \end{pmatrix} = \begin{pmatrix} \bar{u}_L & \bar{c}_L & \bar{t}_L \end{pmatrix} (V_u^\dagger V_d) \gamma^\mu \begin{pmatrix} d_L \\ s_L \\ b_L \end{pmatrix} \tag{2.35}$$

while neutral currents are proportional to

$$\begin{pmatrix} \bar{u}'_L & \bar{c}'_L & \bar{t}'_L \end{pmatrix} \gamma^\mu \begin{pmatrix} d'_L \\ s'_L \\ b'_L \end{pmatrix} = \begin{pmatrix} \bar{u}_L & \bar{c}_L & \bar{t}_L \end{pmatrix} (V_u^\dagger V_u) \gamma^\mu \begin{pmatrix} d_L \\ s_L \\ b_L \end{pmatrix}. \tag{2.36}$$

Notice that $V_u^\dagger V_u = 1$, and there is no flavour mixing terms (at tree level) for neutral currents. However, flavour changing terms appear for charged currents coming from the CKM matrix defined to be $V_{CKM} = V_u^\dagger V_d$ [21].

Experimentally, the CKM matrix is constrained and its parameters are defined according to the observed mass values for the fermions. It has been also realized that the CKM matrix follows a hierarchy and can be parametrized following the Wolfenstein parametrization [31].

In principle there is no natural explanation for the hierarchy observed in the CKM matrix. This can be related to the hierarchy observed in the experimental values obtained for the mass of the fermions. In particular, note that fermionic masses are generated

from the same mechanism. It is therefore un-natural to obtain masses with so different order of magnitude. For instance the ratio $m_{\mathrm{electron}}/m_{\mathrm{top}}$ is of the order of 3×10^{-6}. This issue is usually known as the *fermionic mass hierarchy*, and it could be one more indication of new physics at the TeV scale.

2.4.3 CP violation

CP symmetry is the combination of charge (C) conjugation and parity (P) symmetries. These symmetries state that the laws of physics must be the same if:

- charge is conjugated, *i.e.* particles are replaced by anti-particles;
- parity is exchanged, *i.e.* left-handed particles are replaced by right-handed particles.

Both symmetries hold for electromagnetic interactions. It has been discovered however that they can be separately violated for weak interactions [32, 33]. The CP symmetry has been proposed to solve the problem of individual C and P violations, with the statement that the CP should be the real symmetry between matter and anti-matter.

Violation of CP has been experimentally discovered in 1964 by Cronin and Fitch [34, 35], through experiments made with K^0. Later on, CP violation in B mesons has also been observed [36, 37, 38].

The main question regarding the subject nowadays is why is the strong force CP-invariant? The QCD lagrangian contain one term that could be responsible for a possible CP violation. This term is set to zero due to the non-existence of such events. The issue is also known as *strong CP problem*, and presents one more evidence for new physics at TeV scale. Besides, CP violation is often used to explain the unbalance of matter/anti-matter of the Universe.

The most famous solution has been proposed by Peccei and Quinn [39, 40]. This theory postulates the existence of a new particle named axion, generated from the spontaneous symmetry breaking of a new symmetry. We shall explain more about this particle in what follows.

2.4.4 Dark matter

A different indication of new physics at the TeV scale is the evidence of dark matter existence. Dark matter is defined to be an undetermined type of matter that does not

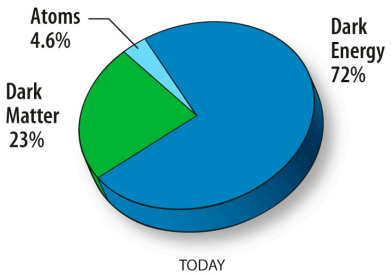

Figure 2.6: WMAP data shows that the content of the present Universe is formed by 4.6% of baryonic matter, *i.e.* atoms that compose planets and stars; 23% of dark matter; and 72% by dark energy, subject not discussed within this study. Dark energy should be different from dark matter, and responsible for the experimentally observed acceleration of the Universe. These images are created by and belong to the NASA / WMAP Science Team [43].

emit or reflect electromagnetic radiation. In fact, the subatomic composition of this new type of matter is not yet known, neither are its interactions.

The first evidence was postulated by Jan Oort in 1932, in a study related to the search of orbital velocities of stars in the Milky Way. In 1933, when calculating orbital velocities of galaxies and clusters, Fritz Zwicky discovered that part of the mass expected by his calculations was missing, and denominated it dark matter [41].

Nowadays, several observations have confirmed dark matter evidence [42]. For instance, analyses combining galaxy cluster dynamics, supernova data and Cosmic Microwave Background (CMB) radiation with Big Bang nucleosyntesis are good indicators for its existence. Besides, precise measurements have been performed and recently confirmed the existence of dark matter at larger scales than the size of galaxies and clusters. It is believed that approximately 5% of the known matter in the Universe is formed of atoms, while 23% is dark. A relation of the matter content of the Universe as of today, extracted from WMAP results, are displayed on Fig. 2.6 [43].

In principle, dark matter could be formed of either baryonic, non-baryonic content or yet by a combination of both. It could consist of planets, black-holes or even burnt-out stars in the galatic halo, for example. These are so-called MACHOS, *i.e.* massive compact halo objects, and are the most probable constituent of the dark matter if it is found to be formed of baryonic content [44].

Nevertheless, there are reasons to believe that dark matter could not consist of only baryonic content. Studies have shown that there is more dark matter in the Universe than the maximum number that can be calculated. The theory of Big Bang nucleosyn-

tesis and acoustic peaks in the CMB can be used to accurately determine the fraction of baryons in the Universe, and therefore to predict how much dark matter is expected to be baryonic. For this reason, it is widely believed that a significant part of the dark matter content is likely to be exotic, *i.e.* composed by non-baryonic content.

From the SM of particle physics, only the neutrino would fill in all the requirements to be a non-baryonic dark matter candidate. Since it does not carry electric charge and it interacts very weakly to the particles of the SM, the cross section for neutrino production is very small. However, the mass density of neutrinos in the Universe has been calculated and is not enough to explain the matter fraction of the cosmic average density. Besides, there are studies of galaxies structure affirming that neutrinos with a very small mass cannot be entirely responsible for the measured dark matter composition. As a solution, there could exist different types of neutrinos not yet observed, such as sterile neutrinos, to account for part of the dark matter content. In this case, clearly new physics is expected.

There are usually three categories to separate possible non-baryonic dark matter content: i) hot dark matter, which encompass theories with sterile neutrinos, ii) warm dark matter and iii) cold dark matter. These categories are related through the velocity of propagation of the particles, rather than their actual temperature. Particles moving ultra relativistically fit in the first category, particles moving relativistically fit in the second category and finally, particles moving at classical velocities are categorized as cold dark matter.

Different (and most probable) options are available. If dark matter is non-baryonic and not formed by neutrinos, it should be composed by new particle(s). The most common suggestions are axions and WIMPs (or weakly interacting massive particles).

The axion is the hypothetical particle postulated by Peccei and Quinn to solve the strong CP problem that appears in QCD [39, 40], as explained previously. They are supposed to be scalar particles generated from the spontaneous symmetry breaking of a new symmetry.

WIMPs are massive particles, predicted by some theories Beyond the Standard Model (BSM), *i.e.* theory extensions to the SM. Examples of such theories are supersymmetry or theories with extra dimensions, both to be detailed on subsequent chapters. Candidates for WIMPs should interact only via the weak or gravitational forces, and not through the strong force. These are for example the neutralino or the gravitino in different variations of supersymmetric (SUSY) theories. SUSY theories not only predict a stable particle to be the dark matter candidate, but also solve several other issues presented here (for example the hierarchy problem). It is therefore one of the most studied BSM theories giving rise to different branches. More details on SUSY theories will be presented in Chapter 6. Finally, WIMPs candidates could also be

for example new and unpredicted particles coupled to the SM only via gravitational interaction.

All the options briefly discussed here to find the best candidate for dark matter largely indicate the existence of new constituents of fundamental particles. Moreover, an extended version of the SM would be necessary to incorporate such exotic particles. If this is true, chances are that these particles will be at the LHC energy range. Therefore, hints of new physics existence could appear very soon.

Chapter 3

Gravitation in Beyond Standard Model theories

It has been shown that the SM is a successful theory that unifies three forces of Nature. However, general relativity is still left apart, and for many years several analyses seeking a general unification have been made. Throughout this chapter we shall briefly present the standard description used to quantize gravity, and assemble a quantum field theory that unifies all forces. The intention is also to display the limitation of the standard quantum gravity theory and introduce how new theories could well address SM shortcomings.

3.1 Gravity as a field theory

Initially, to introduce gravity to the theory, one could start from the renowned Einstein–Hilbert action for gravity [45]:

$$S_{gravity} = \int d^4x \sqrt{-g} \left[\frac{R}{\kappa^2} \right] \tag{3.1}$$

where $\kappa^2 = 16\pi G_N$, $g = \det[g_{\mu\nu}]$, $g_{\mu\nu}$ is the metric tensor and the curvature scalar $R = g^{\mu\nu} R_{\mu\nu}$. The Ricci tensor is defined as

$$R_{\mu\nu} = \partial_\nu \Gamma^\lambda_{\mu\lambda} - \partial_\lambda \Gamma^\lambda_{\mu\nu} + \Gamma^\sigma_{\mu\lambda} \Gamma^\lambda_{\nu\sigma} - \Gamma^\sigma_{\mu\nu} \Gamma^\lambda_{\lambda\sigma} \tag{3.2}$$

where,

$$\Gamma^\lambda_{\alpha\beta} = \frac{g^{\lambda\sigma}}{2} \left(\partial_\alpha g_{\beta\sigma} + \partial_\beta g_{\alpha\sigma} - \partial_\sigma g_{\alpha\beta} \right). \tag{3.3}$$

Varying $S_{gravity}$ will result in the Einstein field equation [46,47]:

$$R^{\mu\nu} - \frac{1}{2}\, g^{\mu\nu}\, R = -\frac{\kappa^2}{2}\mathcal{T}^{\mu\nu}, \tag{3.4}$$

where $\mathcal{T}^{\mu\nu}$ is the matter energy-momentum tensor.

For a quantum theory of gravity, it is necessary to consider quantum fluctuations for the gravitational field. One possibility generally chosen is:

$$\begin{aligned} g_{\mu\nu} &= \eta_{\mu\nu} + \kappa\, h_{\mu\nu} \\ g^{\mu\nu} &= \eta^{\mu\nu} - \kappa\, h^{\mu\nu} + \kappa^2\, h^{\mu}_{\lambda}\, h^{\lambda\nu} + ... \end{aligned} \tag{3.5}$$

where the flat space is represented by the metric $\eta_{\mu\nu} = \mathrm{diag}(1, -1, -1, -1)$. Notice we work using *natural units*, *i.e.* $\hbar = c = 1$. If one applies Eq. (3.5) in (3.1), the action can usually be expanded in orders of κ and takes the form:

$$S_{grav} = \int d^4x\, \sqrt{-g}\, \left[\mathcal{L}^0_{grav} + \mathcal{L}^1_{grav} + \mathcal{L}^2_{grav} + ...\right] \tag{3.6}$$

where

$$\begin{aligned} \mathcal{L}^0_{grav} &= \frac{\mathcal{R}}{\kappa^2}; \\ \mathcal{L}^1_{grav} &= \frac{h_{\mu\nu}}{\kappa}\left(\frac{1}{2}\eta^{\mu\nu}\mathcal{R} - \mathcal{R}^{\mu\nu}\right); \\ \mathcal{L}^2_{grav} &= \frac{1}{2}\,\partial_\alpha h_{\mu\nu}\,\partial^\alpha h^{\mu\nu} \;-\; \frac{1}{2}\,\partial_\alpha h\,\partial^\alpha h \;+ \partial_\alpha h\,\partial_\beta h^{\alpha\beta} - \partial_\alpha h_{\mu\beta}\,\partial^\beta h^{\mu\alpha} \\ &\quad + \mathcal{R}\left(\frac{1}{4}h^2 - \frac{1}{2}h_{\mu\nu}h^{\mu\nu}\right) + \left(\frac{1}{2}h^{\lambda}_{\mu}h_{\nu\lambda} - h h_{\mu\nu}\right)\mathcal{R}^{\mu\nu}. \end{aligned} \tag{3.7}$$

where indices are raised/lowered with $\eta_{\mu\nu}$ and in which $\mathcal{R} = \eta^{\mu\nu}\mathcal{R}_{\mu\nu}$, and $\mathcal{R}_{\mu\nu} = R_{\mu\nu}$ with $g_{\mu\nu} \to \eta_{\mu\nu}$.

We are looking for a quantum theory to unify gravity with the other three forces of Nature, or in other terms, to incorporate gravity in the SM. For this reason, besides the graviton lagrangian we should consider all the other types of fields:

$$S(\phi, \psi, A_\mu) = \int d^4x\, \sqrt{-g}\, \mathcal{L}(\phi, \psi, A_\mu), \tag{3.8}$$

where the action S can be the action for either a scalar field ϕ, or a fermionic field ψ, or yet a vectorial field A_μ.

As it has been performed for the gravity action, it is necessary to consider quantum fluctuations in the action above. As a consequence, an interaction term between the

gravity field and the SM field is obtained:

$$S = \int d^4x \left(-\frac{\kappa}{2}\right) h_{\mu\nu}\mathcal{T}^{\mu\nu}, \tag{3.9}$$

where $\mathcal{T}_{\mu\nu}$ is the energy-momentum tensor corresponding to the matter content of the theory, *i.e.*,

$$\mathcal{T}_{\mu\nu}(\phi,\psi,A_\mu) = \left(-\eta_{\mu\nu}\,\mathcal{L}(\phi,\psi,A_\mu) + 2\frac{\delta\mathcal{L}(\phi,\psi,A_\mu)}{\delta g^{\mu\nu}}\right)\Bigg|_{g^{\mu\nu}=\eta^{\mu\nu}}. \tag{3.10}$$

The final action for a quantum theory of gravity, where SM fields can couple to the quantum field of gravity, should contain therefore a total lagrangian which is the sum of Eqs. (3.1) and (3.9). The inclusion of matter in combination with Eq. (3.4) results in the total lagrangian that can be re-written as:

$$\begin{aligned} S = \int d^4x \Bigg[\Bigg(&\frac{1}{2}\,\partial_\alpha h_{\mu\nu}\,\partial^\alpha h^{\mu\nu} \;-\; \frac{1}{2}\,\partial_\alpha h\,\partial^\alpha h \;+\partial_\alpha h\,\partial_\beta h^{\alpha\beta} \\ &-\partial_\alpha h_{\mu\beta}\,\partial^\beta h^{\mu\alpha}\Big) - \left(\frac{\kappa}{2}h_{\mu\nu}\mathcal{T}^{\mu\nu}\right)\Bigg], \end{aligned} \tag{3.11}$$

where the first term is also known as the Fierz-Pauli lagrangian [48] and we take $\mathcal{R} = 0$.

Consider for example the action of a scalar field:

$$S_\phi = \int d^4x\,\sqrt{-g}\,\frac{1}{2}\left[g^{\mu\nu}\partial_\mu\phi\partial_\nu\phi - m^2\phi^2\right]. \tag{3.12}$$

Using the expansion of $g^{\mu\nu}$ in Eq. (3.12), we obtain:

$$S_\phi = \int d^4x\,\left[\frac{1}{2}\left(\partial_\mu\phi\partial^\mu\phi - m^2\phi^2\right) - \frac{\kappa}{2}\,h_{\mu\nu}\,\mathcal{T}_\phi^{\mu\nu}\right], \tag{3.13}$$

with

$$\mathcal{T}^\phi_{\mu\nu} \equiv \partial_\mu\phi\partial_\nu\phi - \frac{1}{2}\eta_{\mu\nu}\left(\partial_\rho\phi\partial^\rho\phi - m^2\phi^2\right). \tag{3.14}$$

From Eqs. (3.13) and (3.14) we can therefore construct Feynman diagrams related to the interaction between scalar fields and the graviton tensor represented by $h_{\mu\nu}$ in these equations.

We can similarly apply the same technique for fermions and vectors in order to obtain the interaction vertex between these particles and the graviton field. We thus consider

$C_{\mu\nu\rho\sigma}$	$= \eta_{\mu\rho}\eta_{\nu\sigma} + \eta_{\mu\sigma}\eta_{\nu\rho} - \eta_{\mu\nu}\eta_{\rho\sigma}$;
$D_{\mu\nu\rho\sigma}(k_1,k_2)$	$= \eta_{\mu\nu}k_{1\sigma}k_{2\rho} - [\eta_{\mu\sigma}k_{1\nu}k_{2\rho} - \eta_{\mu\rho}k_{1\sigma}k_{2\nu} + \eta_{\rho\sigma}k_{1\mu}k_{2\nu} + +(\mu\to\nu)]$;
$E_{\mu\nu\rho\sigma}(k_1,k_2)$	$= \eta_{\mu\nu}(k_{1\rho}k_{1\sigma} + k_{2\rho}k_{2\sigma} + k_{1\rho}k_{2\sigma}) - -[\eta_{\nu\sigma}k_{1\mu}k_{1\rho} - \eta_{\nu\rho}k_{2\mu}k_{2\sigma} + (\mu\to\nu)]$;
$F_{\mu\nu\rho\sigma\lambda}(k_1,k_2,k_3)$	$= \eta_{\mu\rho}\eta_{\sigma\lambda}(k_{2\nu} - k_{3\nu}) + \eta_{\mu\sigma}\eta_{\rho\lambda}(k_{3\nu} - k_{1\nu}) + + \eta_{\mu\lambda}\eta_{\rho\sigma}(k_{1\nu} - k_{2\nu}) + (\mu\to\nu)$;
$G_{\mu\nu\rho\sigma\lambda\delta}$	$= \eta_{\mu\nu}\eta_{\rho\sigma}\eta_{\lambda\delta} - \eta_{\mu\nu}\eta_{\rho\delta}\eta_{\sigma\lambda} + [\eta_{\mu\rho}\eta_{\nu\delta}\eta_{\lambda\sigma} + + \eta_{\mu\lambda}\eta_{\nu\sigma}\eta_{\rho\delta} - \eta_{\mu\rho}\eta_{\nu\sigma}\eta_{\lambda\delta} - \eta_{\mu\lambda}\eta_{\nu\delta}\eta_{\rho\sigma} + (\mu\to\nu)]$.

Table 3.1: Definition of the parameters $C_{\mu\nu\rho\sigma}$, $D_{\mu\nu\rho\sigma}$, $E_{\mu\nu\rho\sigma}$, $F_{\mu\nu\rho\sigma\lambda}$ and $G_{\mu\nu\rho\sigma\lambda\delta}$ using the notation introduced in Ref. [49].

the generic action that include vectors and fermions,

$$S = \int d^4x\sqrt{-g}\,\left[e\,\bar{\psi}\,i\,\gamma^\mu\,D_\mu\psi\,-\,\frac{1}{4}\,F_{\mu\nu}\,F^{\mu\nu}\right], \tag{3.15}$$

where e is the vierbein, ψ is the fermionic field, and $F_{\mu\nu}$ is the electromagnetic tensor that contains the vector field A_μ. In addition, we consider quantum fluctuations specified by Eq. (3.5). Writing the lagrangian expression to be compatible with Eq. (3.9), the energy-momentum tensor for vector and fermionic fields are

$$\begin{aligned}
\mathcal{T}^V_{\mu\nu} &= \frac{1}{4}\eta_{\mu\nu}F^{\rho\sigma}F_{\rho\sigma} - F_\mu^{\ \rho}F_{\nu\rho} \qquad (3.16)\\
\mathcal{T}^\psi_{\mu\nu} &= -\eta_{\mu\nu}\left(\bar{\psi}\,i\,\gamma^\rho D_\rho\psi - m\bar{\psi}\,\psi\right) + \frac{1}{2}\bar{\psi}\,i\,\gamma_\mu D_\nu\psi + \\
&\quad + \frac{1}{2}\bar{\psi}\,i\,\gamma_\nu D_\mu\psi + \frac{1}{2}\eta_{\mu\nu}\partial^\rho(\bar{\psi}\,i\,\gamma_\rho\psi) - \frac{1}{4}\partial_\mu(\bar{\psi}\,i\,\gamma_\nu\psi)\frac{1}{4}\partial_\nu(\bar{\psi}\,i\,\gamma_\mu\psi).
\end{aligned}$$

As a result, it is possible to obtain the total Feynman rules for the present theory. These rules describe the effective theory in which a graviton field couples to the usual vector, fermion and scalar fields. They are summarized in Fig. 3.1.

We can see from Fig. 3.1 that if gravity couples to the SM fields, it is very weakly coupled. In fact, Eq. (3.9) reveals that the interaction is proportional to the square

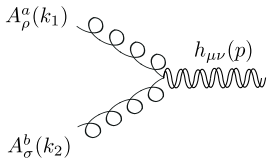

$$= i\,\frac{\kappa}{2}\delta^{ab}\left[(k_1\cdot k_2)\,C_{\mu\nu\rho\sigma} + \right.$$
$$\left. + \; D_{\mu\nu\rho\sigma} + \xi^{-1}E_{\mu\nu\rho\sigma}\right]$$

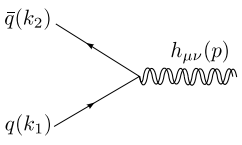

$$= -\,i\,\frac{\kappa}{8}\left[\gamma^\mu\,(k_1-k_2)_\nu - \right.$$
$$\left. - \gamma^\nu\,(k_1-k_2)_\mu \;-2\,\eta_{\mu\nu}\,(\not{k}_1 - \not{k}_2)\right]$$

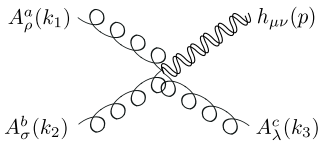

$$= g\,\frac{\kappa}{2}f^{abc}\left[C_{\mu\nu\rho\sigma}\,(k_1-k_2)_\lambda \right.$$
$$+ C_{\mu\nu\rho\lambda}\,(k_3-k_1)_\sigma +$$
$$\left. + C_{\mu\nu\sigma\lambda}\,(k_2-k_3)_\rho + F_{\mu\nu\rho\sigma\lambda}\right]$$

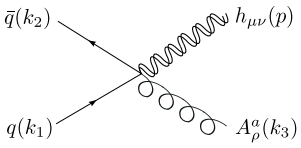

$$= i\,g\,\frac{\kappa}{4}\,T^a\left[C_{\mu\nu\rho\sigma} - \eta_{\mu\nu}\eta_{\rho\sigma}\right]\gamma^\sigma$$

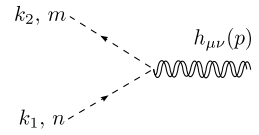

$$= -i\,\frac{\kappa}{2}\left[m^2\,\eta_{\mu\nu} + C_{\mu\nu\rho\sigma}\,k_1^\rho k_2^\sigma\right]$$

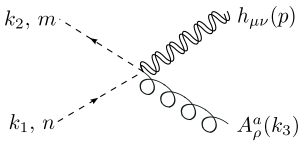

$$= i\,g\,\frac{\kappa}{2}C_{\mu\nu\rho\sigma}\,(k_1+k_2)^\sigma\,T^a_{mn}$$

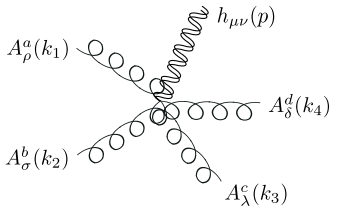

$$= i\,g^2\,\frac{\kappa}{2}\left[f^{eac}f^{edb}G_{\mu\nu\rho\sigma\lambda\delta} + \right.$$
$$\left. f^{eab}f^{ecd}G_{\mu\nu\rho\lambda\sigma\delta} + f^{ead}f^{ebc}G_{\mu\nu\rho\sigma\delta\lambda}\right]$$

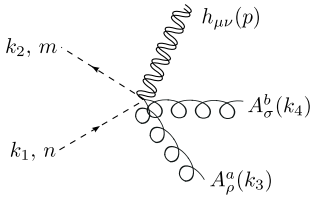

$$= -i\,g^2\,\frac{\kappa}{2}C_{\mu\nu\rho\sigma}\left\{T^a, T^b\right\}_{mn}$$

Figure 3.1: Feynman rules for a theory containing general spin-0, spin-1/2, spin-1 and spin-2 fields, described by the lagrangian summarized in Eq. (3.9). The notation is coherent with [49], and the parameters $C_{\mu\nu\rho\sigma}$, $D_{\mu\nu\rho\sigma}$, $E_{\mu\nu\rho\sigma}$, $F_{\mu\nu\rho\sigma\lambda}$ and $G_{\mu\nu\rho\sigma\lambda\delta}$ are defined in Table 3.1.

root of Newton's constant, or in other terms, to the inverse of the Planck mass. The interaction of the graviton with the SM fields will therefore be so small that it would be very hard to be tested by collider experiments.

Nevertheless, the problem for quantizing gravity is more extensive. When computing quantum corrections to the graviton propagator, we account for loop diagrams. To calculate quantum corrections at one-loop, we need to consider the lagrangian to quadratic order. When this is done, because gravity coupling is dimension-full, *i.e.* proportional to κ, and taking into account the non-linear nature of the theory, divergences appear that cannot be re-absorbed by any fundamental parameters that we have introduced. Because of the dimension-full coupling and explicit powers of momentum in the self coupling of the graviton, divergences gets worse as more loops are considered. It is believed therefore that the physics we know ceases to being valid above the Planck scale, when quantum corrections become important.

The dream of unifying gravity with all three forces of nature is not yet reached, however we have seen that progress has been made for the understanding of the underlying theory. Currently, one promising approach is to treat relativity as an effective field theory [45, 50]. Quoting J. Donoghue in Ref. [45]: "*Since small quantum fluctuations at ordinary energies behave normally in perturbation theory, it is natural to try to separate these quantum corrections from the problematic (and most likely incorrect) high energy fluctuations. Effective field theory is the tool to accomplish this separation.*"

Different extensions to the SM aiming to treat this problem using the effective field theory approach have been proposed. This is the case for example of the theories suggested by G. Dvali *et al* [6, 7, 8] and by X. Calmet *et al* [9, 10, 11]. Additionally, other BSM theories that intend to address different SM issues (such as the hierarchy problem or indirect signs of dark matter) may also achieve the unification of all the forces of Nature, including gravity. The following sections will present an overview of some particular SM extensions and describe their solution to the issues cited above.

3.2 The theory with a scale-dependent M_{pl}

The Planck scale M_{pl} is generally treated as the fundamental scale of a theory. This is consequence to the fact that this is the scale where quantum gravitational effects become important. However, it could happen that these effects become large at a much smaller scale, such as the TeV scale. Consequences would thus be several. The trivial outcome would be that standard theories would not be any longer valid above this scale and extensions would have be considered.

The primary extension we shall present is the consequence of a presumed renormalization of the Newton's constant, or in other terms, the Planck mass [11].

It is known that the Newton' s constant is inversely proportional to the Planck mass:

$$G_N = \frac{1}{M_{pl}^2}, \text{ or, } \frac{\kappa}{2} = \frac{\sqrt{8\pi}}{M_{pl}} = \frac{1}{\overline{M}_{pl}}. \tag{3.17}$$

where $\overline{M}_{pl} \equiv M_{pl}/\sqrt{8\pi} \sim 2.4 \times 10^{18}$ GeV is the reduced Planck mass. Recall that the action of a general field coupled to gravity is given by Eq. (3.9). If we consider a generic massless scalar field, the resulting action shall be the combination of Eqs. (3.1) and (3.12):

$$S = S_{grav} + S_{\phi} = \int d^4x \sqrt{-g} \left[\frac{R}{\kappa^2} + \frac{1}{2} g^{\mu\nu} \partial_\mu \phi \partial_\nu \phi \right]. \tag{3.18}$$

Expanding $g_{\mu\nu}$ according to Eq. (3.5), the resultant action should be the sum of Eqs. (3.6) and (3.13). However, notice that Newton's constant is incorporated by definition in the expansion through the parameter κ. If this dependence is isolated from $h_{\mu\nu}$, the expansion becomes simply

$$g_{\mu\nu} = \eta_{\mu\nu} + h_{\mu\nu}. \tag{3.19}$$

The leading order term of the lagrangian displayed in Eq. (3.18) can be displayed as:

$$\frac{R}{\kappa^2} \sim \frac{1}{\kappa^2} h \,\Box\, h = \frac{h}{\kappa} \,\Box\, \frac{h}{\kappa}. \tag{3.20}$$

Since κ was not absorbed in the definition of small fluctuations, loop correction to the propagator of the graviton could be re-interpreted as a renormalization to Newton's constant.

In order to be more precise and consistent with the example we have been employing, consider our toy theory with a scalar field coupled to gravity. The graviton propagator must receive 1-loop corrections from the scalar particle in the loop, as illustrated in Fig. 3.2. Neglecting the index structure, the graviton propagator including the 1-loop correction, can be displayed as

$$P_{grav}(q) \sim \left[\frac{i}{q^2\,\kappa^2} + \frac{i}{q^2\,\kappa^2} \Sigma \frac{i}{q^2\,\kappa^2} + ... \right]. \tag{3.21}$$

However, similarly to what has been done to calculate the Higgs boson mass corrections, it is found that the integral included in Σ is quadratically divergent. The authors of [11] proposed to absorb this part into the redefinition of Newton's constant,

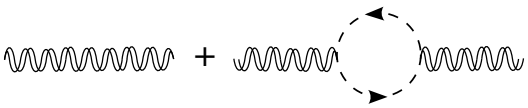

Figure 3.2: Illustration of the graviton propagator and its one-loop correction due to the existence of scalar fields coupled to gravity in the theory.

obtaining:

$$\frac{1}{G_N^{ren}} = \frac{1}{G_N^{bare}} + \frac{c}{16\pi^2}\,\Lambda^2, \tag{3.22}$$

where G_N^{ren} is the renormalized constant measured by experiments, c is a new parameter, and Λ is the ultraviolet cutoff.

If the Planck mass is scale-dependent, then the true scale at which quantum effects become important is $\mu_\star$:

$$G_N(\mu_\star) \sim \mu_\star^{-2}. \tag{3.23}$$

Requesting G_N^{ren} to be of the order of the Planck scale, $G_N^{bare}(\Lambda) \sim \Lambda$ and the ultraviolet cutoff of the order of $\mu_\star$, results on $c \sim \mathcal{O}(10^{32})$.

If we now assume the possibility that spin-1/2 and spin-1 particles also couple to gravity[1] [51, 52], and compute the total number of particles required to generate the Planck scale from the fundamental scale $\mu_\star$, we obtain:

$$\mu_\star^2 = \frac{M_{pl}^2}{1 + N_l/96\pi^2} \tag{3.24}$$

where $N_l = N_\phi + N_\psi - 4N_V$, N_ϕ is the number of scalar fields in the theory, N_ψ is the number of fermion fields and N_V vectorial fields.

Eq. (3.24) indicates that roughly 10^{32} light particles coupled to gravity (within a new hidden sector), are necessary to address the hierarchy problem and generate the Planck scale from the fundamental scale, here assumed to be the electroweak scale. In principle, this observation may appear to be excessively strong. However, more generally accepted theories, such as the theory with Large Extra Dimensions [1,2,3] also predict the existence of a large number of new particles, as we shall confirm in Section 3.3.

[1] Consider the simplest lagrangian to describe such theory, where the coupling with fermions is treated with the vierbein formalism and the vectorial coupling employs the traditional field strength tensor.

The effective lagrangian

A main consequence of the theory presented above is that there must exist a large number of particles coupled to gravity through a hidden sector. Because the theory contains a massless graviton, from the present moment on, we shall refer to it as *massless graviton model*, or MGM for short. To obtain the effective lagrangian of the theory, one must proceed by defining the action of each field and couple it to the gravity by considering quantum fluctuations for the metric. Eq. (3.8) exhibits explicitly the procedure.

Feynman rules have been calculated for a general theory with spin-2 particles coupled to SM fields. They are displayed in Fig. 3.1. For the MGM theory, each SM particle that couples to gravity within the hidden sector shall follow these rules. If one integrates over the total number of new particles, the effective scale of the theory can reach the electroweak scale through the scale dependence of Newton's constant. Therefore, Eq. (3.23) can be translated to the Planck scale,

$$\overline{M}_{pl}(\mu_\star) \sim \mu_\star, \quad \text{with } \overline{M}_{pl} = M_{pl}/\sqrt{8\pi}. \tag{3.25}$$

As a consequence, the MGM theory will have the same Feynman rules as displayed in Fig. 3.1, with (3.25) included in the κ parameter. Because $M_{pl}(\mu_\star) \sim \mu_\star$, the gravity coupling to the SM fields becomes important at the electroweak scale once $\mu_\star$ is chosen to be $\mathcal{O}$(TeV).

We therefore have a complete theory that incorporates the gravity force, and in which all types of fields can only couple to gravity through a hidden sector. Now, graviton-related processes can have reasonably large cross sections at colliders, and they need to be taken into account. Cross-sections and decay-rates based on this particular theory can be calculated in order to impose limits for its parameters taking into consideration electroweak constrains.

It is important however to stress that this is an effective theory, and we have calculated vertices up the first order of $h_{\mu\nu}$. It signifies that there is at most one graviton field at each vertex. We can start by computing cross-section at colliders for processes with one graviton emission, as for example, *proton + proton* $\rightarrow$ *gluon + graviton*. This calculation shall be performed in Section 3.5, followed by full phenomenological analyses at the LHC. In addition, we shall compare these cross sections calculated for the MGM theory against cross sections computed based on different BSM theories. With this aim, an introduction for different BSM theories that contain spin-2 particles are presented below.

3.3 Extra Dimensions

Theories with extra spatial dimensions to work as an extension to the SM theory, have become extremely popular in the last decade. However, these ideas are not new. They have started to appear in the beginning of the 20th century just after Einstein's theory of relativity had been formulated.

The first idea was proposed by Theodor Kaluza, a german physicist, who studied the consequences of the theory of relativity of Einstein assuming a 5-dimensional space-time metric, instead the usual four. For his own surprise, Kaluza discovered that it was possible to unify Einstein's theory of gravitation with Maxwell's electromagnetism by the addition of one dimension [53]. A few years later, Oskar Klein reformulated the theory proposed by Kaluza and demonstrated that very small and compact spatial extra dimensions could exist. However, these theories predict that gravity should be very weakly coupled to SM fields, and for this reason they were, for a very long time, left aside.

In the search for unified theories, in the earlies 80's, these ideas started to re-born and gave rise to different types of new theories, from strings to extra-dimensional theories, the latter being the subject we will now focus on.

Theories with extra dimensions start from the idea that we could live in a world described by more than 4 dimensions. However, different from string theories, where in total 10 or 11 dimensions are required, the assumption is that only a small number of extra-dimensions are added to the usual four. The idea is to look for an extension to the SM by adding very small and compact extra dimensions.

What would be the 4-dimensional consequences of having a D-dimensional space-time? This was one of the questions asked by N. Arkani-Hamed, S. Dimopoulos and G. Dvali, authors of the first proposition to employ Kaluza and Klein calculations for the search of a SM extension. Nowadays, this theory is also known as ADD theory [1, 2, 3], or theory with *large extra dimensions*, name originated from the prediction related to the size of the radius of the extra dimension. Several branches of extra dimensional theories have been developed ever since. We can cite for instance the theory with *warped extra dimensions*, proposed by L. Randall and R. Sundrum [4, 5]. Both SM extensions are discussed in the following sections.

3.3.1 Large Extra Dimensions

Arkani-Hamed, Dimopoulos and Dvali have proposed to use the framework of extra dimensions in principle to address the hierarchy problem. It is known that there are at

least two significant energy scales in nature: the Planck scale, where quantum corrections related to gravity become relevant; and the electroweak scale, where masses of the SM particles lie. One of the key motivations for creating extensions to the SM theory is, as explained previously, the large value for the ratio M_{pl}/M_{ew}. Although the electroweak scale has been well tested by recent experiments, it is not easy to explore the gravitational sector due to the large order of magnitude of the M_{pl} scale.

For this reason, the fundamental scale of the SM theory has been assumed to be M_{pl}. However, similarly to what has occurred to the MGM theory, a reinterpretation of some parameters could bring the value for the fundamental scale down to the electroweak scale, and the naturalness of the theory would be recovered.

Consider a D-dimensional theory, where $D = 4 + \delta$ and δ is the number of extra dimensions. Einstein's action for gravity is now,

$$S_{gravity} = \int d^4x\, d^\delta y \sqrt{-\hat{g}} \left[\frac{R}{\kappa_D^2} \right]. \tag{3.26}$$

where x^μ are the usual 4-dimensional coordinates, y are the extra-dimensional coordinates and $\hat{g}$ is the higher dimensional metric corresponding to g. If one impose the so-called KK reduction, *i.e.* if we integrate the action over the extra dimensional coordinate and impose that the 4-dimensional action should be the same as Eq. (3.1), we obtain a relation between κ and κ_D. This relation is clearer when written in terms of the Planck constant:

$$M_{pl}^2 \sim M_D^{(2+\delta)}\, V_\delta \tag{3.27}$$

where V_δ is the volume formed by the extra dimensional space, proportional to the radius of the extra dimension(s).

The fundamental scale of the theory is now M_D and can be of the order of the electroweak scale, according to Arkani-Hamed, Dimopoulos and Dvali's philosophy. The Planck scale is consequently generated by the fundamental scale through the volume of the un-observed extra dimensions.

Values of the radius of the extra dimensions R are related to the Planck mass according to Eq. (3.27). If the fundamental scale is chosen to be of the order of 1 TeV, a theory with one extra dimension, *i.e.* $\delta = 1$, is excluded, since $R \sim 10^{11}$ m. For $\delta = 2$, $R \sim 0.2$ mm, which is within experimental limits (low gravity experiments) [54]. For this reason, from now on we consider ADD theories with $\delta \geq 2$.

A realistic model

Now, it is clear that it would be possible to address the hierarchy problem within the framework of extra dimensional theories. We can therefore proceed to present a realistic theory where gravity couples to SM fields.

It is usual to name the full dimensional space as the *bulk*, and the 4-dimensional space as the *brane*. For this reason, theories with extra dimensions are also known as brane-world models. We shall also make use of these terms.

The first concern should be the accessibility of the fields to the extra dimensional coordinate. If a general field ϕ is free to propagate through the bulk, the consistent action should be [54]

$$S_{bulk} = \int d^4x\, d^\delta y\, \sqrt{-\hat{g}}\, \mathcal{L}_\phi\,(x, y)\,. \tag{3.28}$$

Rather, if the field must be constrained on the 4-dimensional brane,

$$S_{brane} = \int d^4x\, d^\delta y\, \sqrt{-\hat{g}}\, \mathcal{L}_\phi\,(x)\ \delta^\delta(y - y_0). \tag{3.29}$$

To find out the consequences of a general field propagating in the bulk, consider once again a toy-theory described by a generic scalar field coupled to gravity. Now the space-time is 5-dimensional and the scalar field is free to propagate through the bulk.

The relevant action for such theory is

$$S^D_\phi = \int d^4x\, dy\, \sqrt{-\hat{g}}\, \frac{1}{2}\left[g^{MN}\partial_M\phi\partial_N\phi - m^2\phi^2\right], \tag{3.30}$$

being y the coordinate of the extra dimension, and the upper case indices running through all the dimensions, *i.e.* $M,\ N = 0,\ 1,\ 2,\ 3,\ 5$.

The compactness of the manifold is revealed by the periodicity of the field

$$\phi(x^\mu,\, y) = \phi(x^\mu,\, y + 2\pi R), \tag{3.31}$$

and a Fourier expansion can be employed:

$$\phi(x^\mu, y) = \frac{1}{\sqrt{2\pi R}}\varphi_0(x) + \sum_n \frac{1}{\sqrt{\pi R}}\left[\varphi_n \cos\left(\frac{ny}{R}\right) + \hat{\varphi}_n \sin\left(\frac{ny}{R}\right)\right]. \tag{3.32}$$

To apply the KK reduction, we must integrate the 5-dimensional action and relate it to the known 4-dimension action for a scalar field. Introducing Eq. (3.32) in the

5-dimensional action and integrating it over y, we obtain

$$S_\phi^D = \frac{1}{2}\int d^4x \left\{ \sum_{n=0}^{\infty} \left(\partial^\mu \varphi_n \partial_\mu \varphi_n + m_n^2 \varphi_n^2\right) + \sum_{n=1}^{\infty} \left(\partial^\mu \hat{\varphi}_n \partial_\mu \hat{\varphi}_n + m_n^2 \hat{\varphi}_n^2\right) \right\} \tag{3.33}$$

where $m_n^2 = m^2 + \frac{n^2}{R^2}$. Eq. (3.12) is the corresponding 4-dimensional action to (3.33). Comparing both equations, we can deduce that the higher dimensional scalar field is observed in the effective theory as an infinite tower of fields with masses m_n. These excited modes will be named KK excitations, referring to the calculation first performed by Kaluza and Klein.

The consequence of a field free to propagate in the bulk is thus the appearance of a tower of 4-dimensional fields with the same quantum numbers but increasing masses.

In order to visualize how such consequence would be possible, we shall make an analogy with a lower-dimensional theory. Consider the three-dimensional sphere illustrated in Fig. 3.3 (a). How could one describe it in a two-dimensional theory?

The sphere could, for instance, be characterized as a sum of an infinite number of 2-dimensional circles, located in the vicinity of each other, as displayed in Fig. 3.3 (b). These circles should have different radii, forming the sphere when placed alongside.

The KK-excited modes of the scalar field could be interpreted following the same concept. In this sense, the zero-mode field could be identified with the SM field. The subsequent modes should therefore exist with higher masses. Because the D-dimensional space-time metric considered is flat, the expansion of the field has been performed in terms of trigonometric functions. Therefore, the mass separation between two successive KK modes is $1/R$ for the ADD theory.

The concept of having a D dimensional object projected into the $D-1$ dimension is also known as compactification. It can be applied for any type of field, (*i.e.* for spin-0, spin-1/2, spin-1 and spin-2 fields) provided that it propagates through the bulk. The consequence will consistently be the same: the reduced theory will have a similar spectrum with larger degeneracy.

The effective theory

In the ADD theory, only the graviton field is allowed to propagate through the bulk while the SM fields are kept in the 4-dimensional brane. The theory has been extensively discussed by several authors [49,55,56]. Here we summarize how to obtain the 4-dimensional effective theory starting from the D-dimensional action.

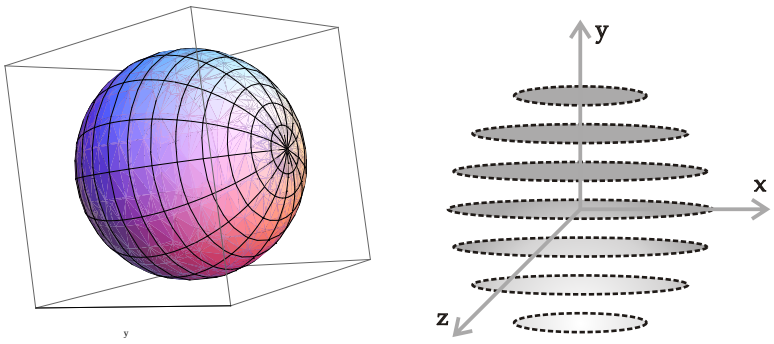

Figure 3.3: 3-dimensional spheres represented by the infinite sum of the 2-dimensional circles along the y-axis. The left sphere has been constructed using the software Mathematica®.

Eq. (3.28) describes the action of a particle propagating in the bulk. Therefore, in the ADD theory, this is the action of the graviton. Quantum fluctuations for the metric must be adapted to the higher dimensional space-time:

$$g_{MN} = \eta_{MN} + \kappa_D \, h_{MN}. \tag{3.34}$$

The lagrangian of a particle in the brane is given by Eq. (3.29), where now ϕ should refer to the SM fields. The energy momentum tensor has also to be defined in D-dimensions, and when the gravity field is weak it becomes:

$$T_{MN} = T_{\mu\nu} \, \eta^{\mu}_{\ M} \, \eta^{\nu}_{\ N} \, \delta^{\delta}(y). \tag{3.35}$$

In 4-dimensions, Eq. 3.9 determined the effective coupling of the graviton with a SM field. In D-dimensions, the corresponding lagrangian is given by:

$$\mathcal{L}^{D}_{int} = \frac{\kappa_D}{2} h_{MN} \, T^{MN} \tag{3.36}$$

In order to start the dimensional reduction, assume the extra dimension is compactified in a torus. By doing so, the higher dimensional volume can be approximated as $V_\delta \sim (2\pi R)^\delta$, and the graviton field, which is periodic $h_{\mu\nu}(y) = h_{\mu\nu}(y + 2\pi R)$, allows for the expansion

$$h_{MN}(x^\mu, \, y) = \sum_n \frac{h^{(n)}_{MN}(x^\mu)}{\sqrt{V_\delta}} e^{iny/R}. \tag{3.37}$$

Applying the expansion (3.37) in the total action, and performing the KK reduction, the part of the lagrangian proportional to the graviton field should be

$$\mathcal{L}_{int} = \frac{\kappa}{2} \sum_n h_{\mu\nu}^{(n)} T^{\mu\nu}, \tag{3.38}$$

in addition to an extra term related to the dilaton field, which we will not focus on within the present study.

The zero mode of the graviton field should be massless and coupled to the SM particles proportionally to the inverse of the Planck mass, giving rise to the weak nature of gravity as we know it. The following KK modes should be massive, and the mass splitting between consecutive modes[2] should be $\Delta m = 1/R$.

Notice the similarity between the lagrangian obtained for the 4-dimensional massless graviton (MGM) model presented in Section 3.2 and the effective lagrangian of a higher dimensional graviton described by Eq. (3.38). For a generic coupling constant, both lagrangians are equivalent. The Feynman rules for the ADD theory can thus be identified with the rules specified in Fig. 3.1. The difference lies in two factors: i) for the MGM theory only one massless graviton is predicted, while for the ADD theory also a tower of massive gravitons is expected; ii) for the MGM theory, the coupling constant is scale dependent and can be of the order of the electroweak scale because of the existence of a large number of invisible particles that can only feel the gravitational force. Conversely, for the ADD theory, the effective scale can reach the TeV scale due to the existence of extra dimensions, which results in the prediction of the KK tower of the graviton.

As it has already been stated, the mass value for each KK excited mode is proportional to $|n|/R$. Therefore, the mass splitting between two successive modes is so small that it cannot be measured. It would require a large number of states in order for the mass splitting to be at experimental range. In other words, a large number of KK modes of the graviton would be necessary to compensate the factor $1/M_{pl}$ coming from each interaction vertex. Therefore, for cross section and decay rates calculations, it is more relevant to obtain the contribution of the sum over all the KK states. One can thus integrate the number of KK-modes between $|n|$ and $|n| + dn$ [56]. The total number will be given by

$$dN = \left[\frac{2\,\pi^{\delta/2}}{\Gamma(\delta/2)}\right] |n|^{\delta-1} dn = \left[\frac{2\,\pi^{\delta/2}}{\Gamma(\delta/2)}\right] \frac{M_{pl}^2}{M_D^{2+\delta}} \frac{m^{\delta-1}}{8\,\pi} dm \tag{3.39}$$

using that $m = |n|/R$ and Eq. (3.27) to relate the higher dimensional radius R with M_{pl} and M_D. As consequence, the cross section calculation for graviton production

[2]Here we assume a flat higher dimensional space-time metric.

will have an extra integration over the KK mass states.

$$\frac{d^2\sigma}{dt\,dm} = \left[\frac{2\,\pi^{\delta/2}}{\Gamma(\delta/2)}\right] \frac{M_{pl}^2}{M_D^{2+\delta}} \frac{m^{\delta-1}}{8\,\pi} \frac{d\sigma_m}{dt}, \tag{3.40}$$

where $d\sigma_m/dt$ is the differential cross section for producing one KK graviton of mass m.

In the next chapter we shall compute cross sections for producing KK graviton(s) at the LHC, and compare them with results obtained by taking into account different BSM models such as the MGM or the RS model, which will be presented in the succeeding section. We can, nevertheless, already state that the dependence of the cross section on M_{pl} can be replaced by M_D when the emission of the full tower of graviton is being considered. Similarly to the MGM theory, the ADD theory predicts therefore graviton emission processes at the LHC energy reach.

3.3.2 Warped Extra Dimensions

Several branches of extra-dimensional theories have been suggested since ADD was first proposed. Various scenarios can be created by considering different particles in the bulk, or different higher dimensional space-time metric. Within this line of thought, L. Randall and R. Sundrum have proposed an alternative to the ADD scenario to address the hierarchy between the electroweak and Planck scales [4, 5]. They suggested a theory with 5-dimensional space-time that could be described by the total metric

$$ds^2 = g_{MN}\,dx^M\,dx^N, \tag{3.41}$$

where again upper case indices represent the full set of coordinates or $M,\, N = 0,\, 1,\, 2,\, 3,\, 5$, and

$$g_{MN} = \begin{pmatrix} g_{\mu\nu} & 0 \\ 0 & 1 \end{pmatrix} = \begin{pmatrix} e^{-2k|y|}\eta_{\mu\nu} & 0 \\ 0 & -1 \end{pmatrix}. \tag{3.42}$$

Eq. (3.41) can also be written as

$$ds^2 = e^{-2\,k\,|y|}\,\eta_{\mu\nu}\,dx^\mu\,dx^\nu - dy^2, \tag{3.43}$$

where x^μ are the usual 4-dimensional coordinates, k is of the order of the Planck scale and y is the fifth-dimensional coordinate.

We shall start as customary, by writing the 5-dimensional action for gravity in the bulk:

$$S_{gravity} = \int d^4x\, dy \sqrt{-\hat{g}} \left[\frac{R}{\kappa_5^2} \right]. \tag{3.44}$$

where $\kappa_5 = \sqrt{16\pi}/M_5$ is the higher dimensional coupling and $\hat{g} = det[g_{MN}]$. Employing Eq. (3.42) in $\hat{g}$, we obtain the relation $\sqrt{-\hat{g}} = e^{-4k|y|}$.

For the authors, although the 4-dimensional space-time is flat, the exponential factor works as a warping factor for the total metric. The symmetry S^1/Z_2 is applied, *i.e.* the periodicity of the fifth dimension is used to identify both $y \leftrightarrow y + 2\pi R$ and $y \leftrightarrow -y$. Both extremity points of the orbifold, $y = 0$ and $y = \pi\, R$, do not transform under the Z_2 symmetry [57].

In principle, only gravity will be allowed to propagate through the bulk while other fields must be localized at one of the branes. We can thus choose $y = 0$ as the initial point and define the action at each 4-dimension brane, located at the orbifold fixed points $y = 0$ and $y = \pi\, R$:

$$\begin{aligned} S_{vis} &= \int d^4x \sqrt{-g_{vis}}\, \mathcal{L}_{vis} & g_{\mu\nu}^{vis} &\equiv g_{\mu\nu}(x^\mu, \pi\, R) \\ S_{hid} &= \int d^4x \sqrt{-g_{hid}}\, \mathcal{L}_{hid} & g_{\mu\nu}^{hid} &\equiv g_{\mu\nu}(x^\mu, 0) \end{aligned} \tag{3.45}$$

From these equations, we obtain $g_{\mu\nu}^{hid} = \eta_{\mu\nu}$, whereas $g_{\mu\nu}^{vis} = e^{-2k\pi R}\, \eta_{\mu\nu}$.

In order to understand the consequences of this exponential factor, let us suppose the Higgs field is locked in the visible brane, *i.e.* localized at $y = \pi R$. The Higgs action is:

$$S_{vis}^{higgs} = \int d^4x \sqrt{-g_{vis}} \left[g_{vis}^{\mu\nu} D_\mu H^\dagger D_\nu H - \lambda \left(|H|^2 - v_0^2 \right)^2 \right]. \tag{3.46}$$

Applying $g_{\mu\nu}^{vis} = e^{-2k\pi R}\, g_{\mu\nu}$, and re-defining the Higgs field as $H \rightarrow e^{k\pi R} H$, we obtain

$$S_{vis}^{higgs} = \int d^4x \left[\eta^{\mu\nu} D_\mu H^\dagger D_\nu H - \lambda \left(|H|^2 - e^{-2k\pi R}\, v_0^2 \right)^2 \right]. \tag{3.47}$$

Notice the exponential factor redefines the symmetry-breaking scale, which is now

$$v = e^{-k\pi R} v_0. \tag{3.48}$$

We can therefore conclude that the theory proposed by Randall and Sundrum predicts that any mass parameter at the visible brane is exponentially reduced from its absolute

value at the hidden brane. If we assume the natural scale of the theory to be M_{pl} at the hidden brane, we can require the visible brane to have masses of the order of the electroweak scale. This requirement constrains the product $kR \sim 12$, and address to the hierarchy problem in a very natural manner.

In order to obtain the relation between the Planck scale M_{pl} and the effective scale M_5, one should perform the dimensional reduction in the action (3.44). Identifying the resulting action with the 4-dimension action, we obtain:

$$M_{pl}^2 = M_5^3 \left[\frac{1 - e^{-2k\pi R}}{k}\right]. \tag{3.49}$$

From (3.49) it is clear that M_{pl} depends strongly on the limit kR. It results that the huge gap between the Planck scale and the electroweak scale exists due to the warping factor of the 5-dimensional metric. However, different from the ADD theory, the fundamental scale of the RS theory is still the Planck scale, and is reduced to the TeV scale at the brane localized at $y = \pi R$.

A realistic model

In order to know how the exponential factor of the metric will influence the dimensional reduction, consider a 5-dimensional scalar field ϕ allowed to propagate in the bulk [58, 59, 60]. The relevant action is again

$$S_\phi^{5d} = \int d^4x\, dy\, \sqrt{-\hat{g}}\, \frac{1}{2}\left[g^{MN}\partial_M\phi\,\partial_N\phi - m^2\phi^2\right], \tag{3.50}$$

which can be written, considering Eq. (3.43), as:

$$S_\phi^{5d} = \int d^4x\, dy\, e^{-4k|y|}\, \frac{1}{2}\left[e^{2k|y|}\,\partial_\mu\phi\,\partial^\mu\phi + \partial_5\phi\,\partial^5\phi - m^2\phi^2\right]. \tag{3.51}$$

Using the periodicity of the field with the symmetry imposed, we can expand the scalar field as

$$\phi(x^\mu, y) = \frac{1}{\sqrt{\pi R}}\sum_n \varphi^n(x^\mu)\, f_n(y). \tag{3.52}$$

If $f_n(y)$ are chosen to satisfy both:

$$\frac{1}{2\pi R}\int_{-\pi R}^{\pi R} dy\, e^{-2kR} f_n(y) f_m(y) = \delta_{nm}, \quad \text{and,} \tag{3.53}$$

$$\left[-e^{2k|y|}\partial_5(e^{-4k|y|}\partial_5) + m_\phi^2 e^{-2k|y|}\right] f_n(y) = m_n^2\, f_n(y), \tag{3.54}$$

equation (3.51) becomes

$$S_{\phi}^{5d} = \frac{1}{2}\sum_{n}\int d^4x \left[\eta^{\mu\nu}\partial_\mu\varphi_n\partial_\nu\varphi_n - m_n^2\varphi^2\right]. \tag{3.55}$$

Notice that the zero-mode, or $n = 0$, represents the action of a scalar field in the usual 4-dimensional theory. Eq. (3.55) is therefore the dimensionally reduced action.

The solution of Eq. (3.54) is

$$f_n(y) = \frac{e^{2k|y|}}{N_n}\left[J_\alpha(\frac{m_n e^{k|y|}}{k}) + \beta(m_n)Y_\alpha(\frac{m_n e^{k|y|}}{k})\right], \tag{3.56}$$

where J_α and I_α are Bessel functions of order α, $\alpha = \sqrt{4 + \frac{m^2}{k^2}}$, m_n are the masses of each KK state and the coefficients N_n and $\beta(m_n)$ are determined by normalization and the boundary conditions in the branes:

$$\phi(x^\mu, y)\mid_{y=0,\,\pi R} = 0 \qquad\qquad \partial_5\phi(x^\mu, y)\mid_{y=0,\,\pi R} = 0. \tag{3.57}$$

Therefore,

$$\beta(m_n) = -\frac{2\,J_\alpha(\frac{m_n}{k}) + \frac{m_n}{k}\,J'_\alpha(\frac{m_n}{k})}{2\,Y_\alpha(\frac{m_n}{k}) + \frac{m_n}{k}\,Y'_\alpha(\frac{m_n}{k})}. \tag{3.58}$$

Due to the warping factor of the metric, the KK mass states m_n do not increase linearly as happens for the ADD theory. They can be calculated and given by [60]

$$m_n \simeq \left(n + \frac{\alpha}{2} - \frac{3}{4}\right)\pi k e^{-\pi kR}, \tag{3.59}$$

for $m_n \ll k$, $kR \gg 1$ and $n = 1,\, 2,\, 3,\, \ldots$.

Once more, the consequence of a 5-dimensional field propagating in the bulk is the appearance of the KK tower. However, for RS theories, two successive KK mass states are not separated linearly, but their separation depends on the exponential factor of the metric.

The effective theory

In order to obtain the effective theory, let us assume that only gravity can propagate in the bulk. The SM fields must be constrained in the 4-dimensional brane localized at $y = \pi\, R$. The action of gravity and SM fields are given by Eqs. (3.44) and (3.45).

The graviton field must be expanded as it has been performed for ϕ in Eq. (3.52), and fluctuations of the metric must be taken into account:

$$g_{\mu\nu} = e^{-2k|y|}\,\eta_{\mu\nu} + h_{\mu\nu}. \tag{3.60}$$

Imposing (3.60) in (3.44) and (3.45) we obtain the interacting lagrangian of the graviton and the SM fields:

$$\mathcal{L} = \frac{\kappa}{2}\,h^{(0)}_{\mu\nu}T^{\mu\nu} - e^{-k\pi R}\,\frac{\kappa}{2}\,h^{(1)}_{\mu\nu}T^{\mu\nu}. \tag{3.61}$$

The massless graviton, localized at the hidden brane, couples to SM fields proportionally to the Planck mass, whereas the first KK mode can couple to the SM fields proportionally to the TeV scale, accounting for their localization at the visible brane. The zero mode of the graviton can therefore be identified as the massless graviton predicted by usual quantum gravity, whereas the first mode can have a mass of the order of the TeV scale. The mass of the n-th mode of the graviton is given by [61]:

$$m_n = k\,x_n\,e^{-k\pi R} \tag{3.62}$$

where x_n are the roots of the Bessel function of order 1 (for example $x_1 = 3.8317$).

Once more, due to the similarity of Eqs. (3.61) and (3.9), the Feynman rules for KK modes of the graviton coupled to the SM fields are exhibited in Fig. 3.1. However, the generic coupling displayed in Fig. 3.1 is now given by $e^{-k\pi R}/\overline{M}_{pl}$ for the coupling of the first mode of the graviton with the SM fields. Notice that because of the exponential factor present in this coupling, RS theories are considered to be much more strongly interacting than ADD theories with large extra dimensions.

3.4 The graviton propagator

We have presented so far a complete overview of BSM theories featuring spin-2 particles, from 4-dimensional theories to extra dimensional theories. Further ahead, we shall display the phenomenology of these theories at hadron colliders. We are lacking therefore only an analytical discussion on the graviton propagator, which is one of the factors differentiating massless graviton theories to the ones containing massive spin-2 particles. We shall follow the formalism presented in [62] to derive the spin-2 propagators. Nevertheless, the reader could check [63, 64] for the derivation of the propagator in full details.

To obtain the graviton propagator, we start from the Fierz-Pauli lagrangian [48] for massive spin-2 particles:

$$S_{grav} = \int d^4x \left[\frac{1}{2}\,\partial_\alpha h_{\mu\nu}\,\partial^\alpha h^{\mu\nu} - \frac{1}{2}\,\partial_\alpha h\,\partial^\alpha h + \right. \\ \left. + \partial_\alpha h\,\partial_\beta h^{\alpha\beta} - \partial_\alpha h_{\mu\beta}\,\partial^\beta h^{\mu\alpha} + \frac{1}{2} m^2 (h_{\mu\nu}\,h^{\mu\nu} - h^2) \right]. \tag{3.63}$$

The last term is related to the mass of spin-2 particles and the relative -1 coefficient between $h_{\mu\nu}\,h^{\mu\nu}$ and h^2 is an assumption named *Fierz-Pauli tuning* [62]. There is no known symmetry that imposes such choice. However, the Fierz-Pauli tuning is usually employed to prevent the theory from containing scalar ghosts.

If (3.63) is integrated by parts, the action/lagrangian can be re-written as

$$S_{grav} = \int d^4x\, \frac{1}{2}\, h_{\mu\nu}\, \mathcal{O}^{\mu\nu,\alpha\beta}\, h_{\alpha\beta}, \tag{3.64}$$

where $\mathcal{O}^{\mu\nu,\alpha\beta}$ is given by

$$\mathcal{O}^{\mu\nu,\alpha\beta} = \left(\frac{1}{2}\eta^{\mu\alpha}\eta^{\nu\beta} + \frac{1}{2}\eta^{\mu\alpha}\eta^{\nu\beta} - \eta^{\mu\nu}\eta^{\alpha\beta} \right) (\Box - m^2) + \partial^\mu\partial^\mu\eta^{\alpha\beta} + \\ \partial^\alpha\partial^\beta\eta^{\mu\nu} - \frac{1}{2}\left(\partial^\mu\partial^\alpha\eta^{\nu\beta} + \partial^\mu\partial^\beta\eta^{\nu\alpha} + \partial^\nu\partial^\alpha\eta^{\mu\beta} + \partial^\nu\partial^\beta\eta^{\mu\alpha} \right),$$

and satisfies the symmetries

$$\mathcal{O}^{\mu\nu,\alpha\beta} = \mathcal{O}^{\nu\mu,\alpha\beta} = \mathcal{O}^{\mu\nu,\beta\alpha} = \mathcal{O}^{\alpha\beta,\mu\nu}. \tag{3.65}$$

To extract the graviton propagator, we should apply the quantum prescription and move to the momentum space. The propagator will be the operator $\mathcal{P}_{\alpha\beta,\sigma\lambda}$ which satisfies the relation

$$\mathcal{O}^{\mu\nu,\alpha\beta}\mathcal{P}_{\alpha\beta,\sigma\lambda} = \frac{i}{2}\left(\delta^\mu_\sigma\delta^\nu_\lambda + \delta^\nu_\sigma\delta^\mu_\lambda\right). \tag{3.66}$$

For Eq. (3.65) that is

$$\mathcal{P}_{\mu\nu,\alpha\beta} = \frac{i}{p^2+m^2}\left[\frac{1}{2}\left(\eta_{\mu\alpha} + \frac{p_\alpha p_\beta}{m^2}\right)\left(\eta_{\nu\beta} + \frac{p_\nu p_\beta}{m^2}\right) \right. \\ + \frac{1}{2}\left(\eta_{\mu\beta} + \frac{p_\mu p_\beta}{m^2}\right)\left(\eta_{\nu\alpha} + \frac{p_\nu p_\alpha}{m^2}\right) \\ \left. - \frac{1}{3}\left(\eta_{\mu\nu} + \frac{p_\mu p_\nu}{m^2}\right)\left(\eta_{\alpha\beta} + \frac{p_\alpha p_\beta}{m^2}\right) \right]. \tag{3.67}$$

To derive the massless propagator we follow a similar prescription. We start from Eq. (3.63) in the limit where $m \to 0$. We can again integrate it by parts obtaining:

$$S_{grav} = \int d^D x \, \frac{1}{2} \, h_{\mu\nu} \, \mathcal{E}^{\mu\nu,\alpha\beta} \, h_{\alpha\beta}, \tag{3.68}$$

where $\mathcal{E}_{\mu\nu,\alpha\beta} = \mathcal{O}_{\mu\nu,\alpha\beta}|_{m\to 0}$.

However, now it is necessary to fix the gauge in order to obtain the propagator. The most common choice is the *de Donder gauge*:

$$\partial^\mu h_{\mu\nu} - \frac{1}{2}\partial_\nu h = 0, \tag{3.69}$$

which is achieved by adding the gauge fixing term for the lagrangian:

$$\mathcal{L}_{gf} = \left(\partial_\sigma h^\sigma_{\ \mu} - \frac{1}{2}\partial_\mu h\right) \, g^{\mu\nu} \, \left(\partial_\sigma h^\sigma_{\ \nu} - \frac{1}{2}\partial_\nu h\right). \tag{3.70}$$

Notice we use $h^\alpha_{\ \alpha} \equiv h$.

The total lagrangian is given by the sum of the gravitation and the gauge fixed lagrangians:

$$\mathcal{L} = \mathcal{L}_{grav} + \mathcal{L}_{gf} \equiv \frac{1}{2} \, h_{\mu\nu} \, \tilde{\mathcal{O}}^{\mu\nu\alpha\beta} \, h_{\alpha\beta}. \tag{3.71}$$

with

$$\tilde{\mathcal{O}}^{\mu\nu,\alpha\beta} = \frac{1}{2} \, \Box \, \left(\eta^{\mu\alpha}\eta^{\nu\beta} + \eta^{\mu\beta}\eta^{\nu\alpha} - \eta^{\mu\nu}\eta^{\alpha\beta}\right). \tag{3.72}$$

To obtain the propagator, we once more go to the momentum space and apply the quantum prescription. We obtain simply:

$$\tilde{\mathcal{P}}_{\mu\nu,\alpha\beta} = \frac{i}{q^2} \left[\frac{1}{2} \, \left(\eta^{\mu\alpha}\eta^{\nu\beta} + \eta^{\mu\beta}\eta^{\nu\alpha} - \eta^{\mu\nu}\eta^{\alpha\beta}\right)\right]. \tag{3.73}$$

When the massless (3.73) and massive (3.67) propagators are compared, one can realize a difference in the last term, which appears even in the limit where $m \to 0$:

$$\tilde{\mathcal{P}}_{\mu\nu,\alpha\beta} \neq \lim_{m\to 0} \mathcal{P}_{\mu\nu,\alpha\beta} = \frac{i}{q^2} \left[\frac{1}{2} \, \left(\eta^{\mu\alpha}\eta^{\nu\beta} + \eta^{\mu\beta}\eta^{\nu\alpha} - \frac{2}{3}\,\eta^{\mu\nu}\eta^{\alpha\beta}\right)\right]. \tag{3.74}$$

This is the famous *van Dam-Veltman discontinuity* [65, 66].

To understand how such discontinuity arises, let us consider the study made by Dicus *et al* in Ref. [67]. They have performed a full analysis on the graviton propagator both for the massive and the massless cases.

First, consider an off-shell graviton particle. If the graviton is massless, it has the usual five polarization tensors ($J = 2,\ J_z = 0, \pm 1, \pm 2$) in addition to the ($J = 0$) component:

$$\tilde{\mathcal{P}}^{\mu\nu,\alpha\beta} \sim \sum_{\lambda=\pm 2,\pm 1,0} \epsilon^{\mu\nu}(2,\lambda)\, \epsilon^{\alpha\beta\,\star}(2,\lambda) - \epsilon^{\mu\nu}(0,0)\, \epsilon^{\alpha\beta\,\star}(0,0). \tag{3.75}$$

However, an on-shell massless graviton has only transverse components:

$$\tilde{\mathcal{P}}^{\mu\nu,\alpha\beta} \sim \sum_{\lambda=\pm 2} \epsilon^{\mu\nu}(2,\lambda)\, \epsilon^{\alpha\beta\,\star}(2,\lambda). \tag{3.76}$$

The authors of Ref. [67] affirm that besides the cancellation of ($J = 2,\ J_z = \pm 1$) components, the ($J = 2,\ J_z = 0$) is cancelled by ($J = 0$), leaving only ($J = 2,\ J_z = \pm 2$) components.

However, a massive graviton does not have the ($J = 0$) component:

$$\mathcal{P}^{\mu\nu,\alpha\beta} \sim \sum_{\lambda=\pm 2,\pm 1,0} \epsilon^{\mu\nu}(2,\lambda)\, \epsilon^{\alpha\beta\,\star}(2,\lambda). \tag{3.77}$$

Thus, when the zero-mass limit of Eq. (3.77) is considered, the ($J = 2,\ J_z = \pm 1$) and ($J = 2,\ J_z = 0$) components are cancelled, but the ($J = 0$) component remains.

Therefore, the discontinuity arises from the fact that a virtual massless graviton has a component with zero angular momentum ($J = 0$), that serves to cancel the ($J = 2,\ J_z = 0$) component when the graviton is on-shell, whereas the massive graviton does not have the ($J = 0$) component at all.

It is clear now that theories containing massless gravitons should be treated separately from theories comprising massive such particles. In this context, the similarity of the Feynman rules between the MGM theory and extra dimensional theories disappear at the propagator level. One could therefore investigate if the discontinuity of the graviton propagator can also been seen at the cross section level.

With this question in mind, we have analytically computed cross sections of graviton emission processes for both cases: emission of a massless graviton and emission of a massive graviton, taking the limit where $m \to 0$. This will be the subject of the next section.

3.5 Graviton emission cross sections

On Section 3.1, we have shown the Feynman rules for a general theory in which SM fields are coupled to the graviton field. These rules are displayed in Fig. 3.1, considering a generic coupling presented through the parameter κ. We shall now use these rules to analytically calculate cross sections for graviton emission processes in addition to quarks and gluons.

The production of quarks and gluons recoiling against a graviton G can arise from the parton sub-processes $q + \bar{q} \to G + g$, $q + g \to q + G$, $\bar{q} + g \to \bar{q} + G$, and $g + g \to g + G$. Primarily, we have calculated the leading order contributions at the parton level for a theory featuring a massless graviton. Regarding the notation, we use $\tilde{G}$ for the massless, and non-tilded G for the massive spin-2 particles. For simplicity, at this stage, we treat all quarks as being massless. The sum over the polarizations of the graviton is given by Eq. (3.76). We have found that the polarization and color averaged cross section for $q + \bar{q} \to g + \tilde{G}$ is given by

$$\frac{d\sigma(q\,\bar{q} \to g\,\tilde{G})}{d\cos\theta} = \frac{\kappa^2\,\alpha_s}{72}\left(\frac{s^2 + 2t^2 + 2\,t\,s}{s^2}\right), \tag{3.78}$$

where $\alpha_s = g_s^2/4\pi$, g_s is the strong coupling constant, κ is given on Eq. (3.17), s and t are the Mandelstam variables: $t = -1/2s(1 - \cos\theta)$, and θ is the angle between the beam and the visible final particle. The cross sections for $q + g \to q + \tilde{G}$ and $\bar{q} + g \to \bar{q} + \tilde{G}$ are given by

$$\frac{d\sigma(q\,g \to q\,\tilde{G})}{d\cos\theta} = -\frac{\kappa^2\,\alpha_s}{192}\left(\frac{2\,s^2 + 2\,s\,t\,+\,t^2}{s\,t}\right). \tag{3.79}$$

The corresponding matrix element can be obtained using crossing symmetry from that of the transition $q+\bar{q} \to \tilde{G}+g$. These cross sections can be deduced from [68]. Finally we also obtain the cross section for $g + g \to g + \tilde{G}$ which is given by

$$\frac{d\sigma(g\,g \to g\,\tilde{G})}{d\cos\theta} = -\frac{3\,\kappa^2\,\alpha_s}{128}\left(\frac{s^2 + st + t^2}{s\,\sqrt{t\,(s+t)}}\right)^2. \tag{3.80}$$

Note that the calculations can be simplified tremendously by the realization that the graviton is on-shell and thus any contraction of the style $T^{\mu\nu}q_\mu$ vanishes, where $T^{\mu\nu}$ is the energy momentum tensor and q_μ is the momentum of the graviton.

Subsequently, we have computed the differential cross section contributions for a theory featuring a massive graviton. Now, the sum over the polarizations of the graviton is given by Eq. (3.77), the massive graviton propagator. We have obtained the following respective results. The cross section for $q + \bar{q} \to g + G$ is given by:

$$\begin{aligned}\frac{d\sigma(q\,\bar{q} \to g\,G)}{d\cos\theta} &= \frac{\kappa^2\,\alpha_s}{144}\frac{1}{1-m^2/s}\Bigg[(2-\frac{4ut}{(s-m^2)^2})\left(1+(\frac{m^2}{s})^4\right)+\\ &+\left(2\frac{(s-m^2)^2}{4ut}-5+4\frac{4ut}{(s-m^2)^2}\right)\frac{m^2}{s}\left(1+(\frac{m^2}{s})^2\right)+\\ &+6\left(\frac{u-t}{s-m^2}\right)^2(\frac{m^2}{s})^2\Bigg], \end{aligned} \tag{3.81}$$

where s, t, u are the Mandelstam variables, and $t, u = -1/2s(1 - m^2/s)(1 \mp \cos\theta)$. The cross section for $q + g \to q + G$ can be obtained from this expression by crossing $s \leftrightarrow t$:

$$\begin{aligned}\frac{d\sigma\,(q\,g \to q\,G)}{d\cos\theta} &= \frac{\kappa^2\alpha_s}{384}\frac{(-t/s)(1-m^2/s)}{(1-m^2/t)^2}\Bigg[(2-\frac{4us}{(t-m^2)^2})\left(1+(\frac{m^2}{t})^4\right)\\ &+\left(2\frac{(t-m^2)^2}{4us}-5+4\frac{4us}{(t-m^2)^2}\right)\frac{m^2}{t}\left(1+(\frac{m^2}{t})^2\right)+\\ &+6\left(\frac{s-u}{t-m^2}\right)^2(\frac{m^2}{t})^2\Bigg]. \end{aligned} \tag{3.82}$$

As in the massless case, the cross section for $\bar{q} + g \to \bar{q} + G$ is also the same as that of $q + g \to q + G$. For the process $g + g \to g + G$, we find

$$\begin{aligned}\frac{d\sigma(gg \to gG)}{d\cos\theta} &= \frac{3}{256}\frac{\kappa^2\alpha_s}{(1-m^2/s)(1-\cos^2\theta)}\Bigg[(3+\cos^2\theta)^2\left(1+(\frac{m^2}{s})^4\right)\\ &-4(7+\cos^4\theta)\frac{m^2}{s}\left(1+(\frac{m^2}{s})^2\right)+\\ &+6(9-2\cos^2\theta+\cos^4\theta)(\frac{m^2}{s})^2\Bigg]. \end{aligned} \tag{3.83}$$

If we take the limit where $m \to 0$ of Eqs. (3.81), (3.82) and (3.83), we obtain the same results as Eqs. (3.78), (3.79) and (3.80) respectively. The discontinuity existent

for the propagator of a spin-2 particle vanishes at cross section level when processes with an on-shell graviton are considered.

The smoothness of this limit has been pointed out in several references, including [55]. Particularly, Mirabelli *et al* have pointed out that due to helicity conservation, only the polarization modes that correspond to the massless graviton are produced in the reaction being analysed. However, in order to understand theoretically the smoothness of this limit, we have carried out a small calculation that verifies it for the $q\bar{q} \to gG$ process. The validation follows.

From Eqs. (3.73) and (3.67) it is possible to obtain the relation

$$\lim_{m\to 0} \mathcal{P}_{\mu\nu,\alpha\beta} = \tilde{\mathcal{P}}_{\mu\nu,\alpha\beta} + \frac{1}{6}\eta_{\mu\nu}\eta_{\rho\sigma}. \tag{3.84}$$

On the calculation of the cross section of the process specified, the difference between both calculations (using massless or a massive graviton in the $m \to 0$ limit) lies on the amplitude $|\mathcal{M}|^2$. Therefore, the corresponding relation to Eq. (3.84) between amplitudes computed for each case can be written as

$$\begin{aligned} \lim_{m\to 0} \sum_{pol} \left|\mathcal{M}_{\mu\nu,\alpha\beta}\right|^2 &= \lim_{m\to 0} \mathcal{M}^*_{\mu\nu}\, \mathcal{P}^{\mu\nu,\alpha\beta}\, \mathcal{M}_{\alpha\beta} = \\ &= \tilde{\mathcal{M}}^*_{\mu\nu}\, \tilde{\mathcal{P}}^{\mu\nu,\alpha\beta}\, \tilde{\mathcal{M}}_{\mu\nu} + \frac{1}{6}\tilde{\mathcal{M}}^{*\,\mu}_{\mu}\, \tilde{\mathcal{M}}_{\alpha}^{\ \alpha} = \\ &= \sum_{pol} \left|\tilde{\mathcal{M}}_{\mu\nu,\alpha\beta}\right|^2 + \frac{1}{6}\left|\tilde{\mathcal{M}}_{\mu\ ,\alpha}^{\ \mu\ \alpha}\right|^2, \end{aligned} \tag{3.85}$$

where $\mathcal{M}_{\mu\nu,\alpha\beta}$ is the amplitude calculated using a massive graviton and $\tilde{\mathcal{M}}_{\mu\nu,\alpha\beta}$ using a massless graviton.

To obtain a smooth limit at the cross section level, the second term of Eq. (3.85) should be zero:

$$\left|\tilde{\mathcal{M}}_{\mu\ ,\alpha}^{\ \mu\ \alpha}\right|^2 \equiv 0. \tag{3.86}$$

To verify the smoothness of the limit we check that Eq. (3.86) is indeed true for the particular processes we are interested in. Take for example $q\bar{q} \to gG$. Four Feynman diagrams contribute for such process, which are illustrated in Fig. 3.4.

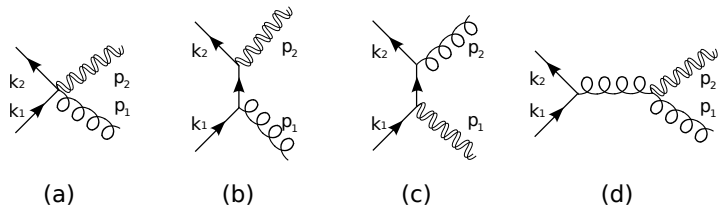

Figure 3.4: Illustration of the four Feynman diagrams contributing for the process $q\bar{q} \to gG$. The straight lines represent a quark or an anti-quark, the curly line represents the gluon and the double-curly line the graviton.

Calculating the amplitude for the first diagram, we obtain:

$$\begin{aligned}\mathcal{M}^{(a)} &= \frac{ig_s\kappa}{4}\,\bar{v}\,\gamma^\beta T^a\,u\,(C_{\mu\nu\alpha\beta}-\eta_{\mu\nu}\eta_{\alpha\beta})\,\epsilon_a^\alpha\epsilon^{\mu\nu} = \\ &= -\frac{3ig_s\kappa}{2}\,\bar{v}\,\gamma_\alpha T^a\,u\,\epsilon_a^\alpha.\end{aligned} \tag{3.87}$$

From the amplitude of the second diagram:

$$\begin{aligned}\mathcal{M}^{(b)} &= \frac{ig_s\kappa}{8}\frac{1}{(k_2-p_1)^2}\,\bar{v}\,[\gamma_\mu(-2k_2+p_1)_\nu+\gamma_\nu(-2k_2+p_1)_\mu \\ &\quad -2\eta_{\mu\nu}(-2\not{k}_2+\not{p}_1)]\,(\not{k}_2-\not{p}_1)\gamma_\alpha T^a\,u\,\epsilon_a^\alpha\epsilon^{\mu\nu} = \\ &= \frac{3ig_s\kappa}{4}\,\bar{v}\,\gamma_\alpha T^a\,u\,\epsilon_a^\alpha.\end{aligned} \tag{3.88}$$

Similarly, for the third diagram:

$$\mathcal{M}^{(c)} = \frac{3ig_s\kappa}{4}\,\bar{v}\,\gamma_\alpha T^a\,u\,\epsilon_a^\alpha. \tag{3.89}$$

And finally the forth:

$$\begin{aligned}\mathcal{M}^{(d)} &= \frac{ig_s\kappa}{2}\,\bar{v}\gamma_\beta T^a\frac{1}{2k_1k_2}\,[-p_2\,(p_1+p_2)C_{\mu\nu\alpha\beta}+ \\ &\quad +D_{\mu\nu,\alpha\beta}(-p_2,p_1+p_2)+\xi^{-1}E_{\mu\nu,\alpha\beta}(-p_2,p_1+p_2)]\,u\,\epsilon_a^\alpha\epsilon^{\mu\nu} = \\ &= \frac{ig_s\kappa}{2}\,\bar{v}\,\gamma_\beta T^a\,u\frac{1}{s}\left[\frac{s}{2}(-2\eta_{\alpha\beta})+(-s)\eta_{\alpha\beta}\right]\epsilon_a^\alpha = 0.\end{aligned} \tag{3.90}$$

It is now trivial to verify that the sum of all contributing diagrams is zero, exactly as expected from Eq. (3.86). If one follows the same strategy and computes $|\mathcal{M}|^2$ for the additional processes that can produce one graviton, the smooth limit is always obtained. Even for massive quarks in the initial/final state a similar calculation has been carried out and the smooth limit prevailed.

To conclude, it would be significant to notice that the expressions for the cross sections displayed within the present study can be applied for the MGM and extra dimensional theories if the correct effective coupling are considered. For instance, for the MGM theory, Eqs. (3.78), (3.79) and (3.80) can describe correctly the theory if the general κ parameter is replaced by the effective parameter set in Eq. (3.25). Similarly, the strategy can be applied to relate Eqs. (3.81), (3.82) and (3.83) with the ADD theory.

Our subsequent goal is to investigate how to distinguish between MGM and ADD theories through phenomenological analyses at colliders, and moreover, if we can still identify signs of such theories considering the expected SM background. This will be the starting point for Chapter 5 following an introduction to hadron colliders and phenomenological simulations which will be presented in the next chapter.

Chapter 4

The LHC and collision simulations

The Large Hadron Collider (or LHC for short) was built to smash protons at a very high center-of-mass energy, in order to test predictions of different theories in particle physics and to confirm the existence of the Higgs boson.

For the comparison between experimental data against theory predictions, simulations play a crucial role. In order to correctly make predictions of the consequences of particular BSM theories, it is necessary to use simulation tools. These packages can reproduce events expected at the hadron collider, which can be used to compare with real data. In this chapter, we thus present an overview of both the LHC itself and methods used to simulate events at hadron colliders. There are numerous references on this subject. We, however, shall base our discussion and follow the structure presented in Refs. [69, 70, 24].

We begin with an introduction of the LHC and its characteristics. Further ahead we present Monte-Carlo simulations of collisions and conclude by defining matrix element/parton shower merging schemes, which will be substantially employed in the following chapters for phenomenological analyses of new physics emissions.

4.1 Introduction to the LHC

The LHC was constructed at the "Organisation européenne pour la recherche nucléaire" (CERN) near Geneva, in the tunnel which previously comprised the LEP experiment, the Large Electron-Positron collider that ran up to the year 2000.

The LHC tunnel has 27 km of circumference, is buried approximately 100 meters under ground and is designed to collide protons with a maximum center-of-mass energy

of 14 TeV. Collisions have started in the end of 2009, rapidly achieving the center-of-mass energy record of 2.36 TeV, exceeding even limits established by the Tevatron[1].

On March, 2010, the LHC started colliding protons with $\sqrt{s} = 7$ TeV, beating its own previous record, and achieving the final center-of-mass energy established for the first run.

To reach such colliding energy, the proton beam has to go through several acceleration steps, which are shown pictorially in Fig. 4.1 [71]. First, protons are produced in the LINAC, and accelerated to 1.4 GeV in the Booster. They are subsequently accelerated at the PS (proton synchrotron), and pass to the SPS to achieve the energy of 450 GeV. They finally move to the main ring to gain their final energy (at the current stage 3.5 TeV each proton) and collide within one of the four main detectors: the Compact Muon Solenoid (CMS), the Toroidal LHC Apparatus (ATLAS), the LHCb or yet the Large Ion Collider Experiment (ALICE). The first two detectors are called "general-purpose" experiments. The LHCb is oriented towards analyses on the b-quark sector, CP violation and rare decays. ALICE however has been designed to focus on heavy ion physics and the study of quark-gluon plasma.

In a nutshell, the goal for colliding protons is to test theories of fundamental interactions and their building blocks. Based on theoretical models we can predict chances of obtaining specific final states from the collision of two protons. With the LHC data, we are able to verify if theoretical expectations are actually fulfilled. With cross sections provided by theoretical calculations based on specific models, it is possible to compute the quantity of such events are expected at the detector using the specifications for the collider. In reality, the complexity for linking experimental data with theoretical expectations is higher. However, we try to summarize the main aspects which will be employed within this study in what follows.

The rate of collisions R and the luminosity $\mathcal{L}$ are related through the value for the cross-section σ that can be calculated for a particular process:

$$R = \frac{dN}{dt} = \mathcal{L}\,\sigma. \tag{4.1}$$

Here, $\frac{dN}{dt}$ is the number of events produced per second.

[1]The Tevatron is located at the Fermi National Accelerator Laboratory, and was built to collide protons and anti-protons with a center-of-mass energy limit of approximately 2 TeV. It has worked from 1983 until September of 2011, having many important discoveries on its list of achievements (including the discovery of the top quark in 1995). The large number of breakthroughs made by the Tevatron enabled the proposition of a even stronger particle collider, the LHC.

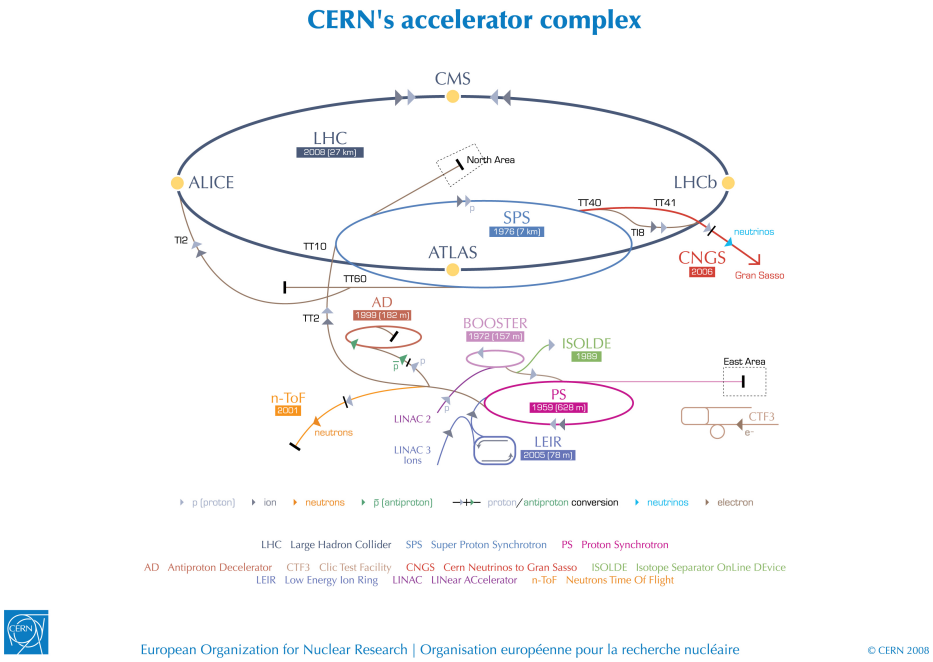

Figure 4.1: The LHC accelerator complex at CERN [71].

For different experimental reasons, detectors cannot observe all events produced. We should thus account for the efficiency for observing a particular process. We obtain

$$N_{events} = \sigma \times L \times \mathcal{E}, \quad \text{for} \quad L = \int \mathcal{L}\, dt, \tag{4.2}$$

where N_{events} is the total number of events produced, L is the integrated luminosity provided by the experiment and $\mathcal{E}$ is the efficiency of observing such process.

The choice of building a proton collider was made aiming the achievement of high luminosities. The luminosity is controlled by the parameters of the experiment, the process however should be parameter independent. Anyhow, because the proton is composed by partons, one should consider parton distribution functions (also known as PDFs) to the computation of inclusive cross sections, considering the combination of different initial partons.

The cross-section for a hard scattering process with two hadrons in the initial state [72] is

$$\sigma(P_1, P_2) = \sum_{i,j} \int dx_1\, dx_2\, f_i(x_1, \mu^2)\, f_j(x_2, \mu_F^2)\, \hat{\sigma}_{ij}\left(p_1,\, p_2,\, Q^2/\mu_F^2, Q^2/\mu_R^2\right)$$

(4.3)

where P_1 and P_2 are the four-momenta of the initial hadrons and p_1 and p_2 are the four-momenta of the partons present in the hard interaction. They are related by

$$p_1 = x_1 P_1 \quad \text{and} \quad p_2 = x_2\, P_2. \tag{4.4}$$

The quark or gluon distribution functions at a factorization scale μ_F are exhibited by $f_{i,j}$. The factorization scale can be qualitatively described as the resolution of the hadron which is being tested [73]. Q^2 is the characteristic scale of the scattering, and μ_R is the renormalization scale. The parton-level cross section for the process envisaged to be analysed is $\hat{\sigma}_{ij}$ and depends on Q as well as on the choice of the factorization and renormalization scales.

From Eq. (4.4) it is trivial to observe that partons only carry a fraction of the four-momentum of the initial hadron, resulting on a parton-level center-of-mass energy $\sqrt{\hat{s}}$ smaller than the total proton-proton $\sqrt{s}$ energy. They are related by $\tau \equiv x_1\, x_2 = \hat{s}/s$, where $\hat{s} = (p_1 + p_2)^2$ and $s = (P_1 + P_2)^2$. We can define a new quantity, the differential parton luminosity, as:

$$\frac{dL_{i,j}}{d\tau} = \frac{1}{\tau}\frac{1}{(1+\delta_{i,j})}\int_0^1 dx_1\, dx_2\, [x_1 f_i(x_1) x_2 f_j(x_2) + (1 \to 2)]\, \delta(\tau - x_1 x_2). \tag{4.5}$$

The cross-section will thus be given by:

$$\sigma(s) = \sum_{i,j}\int_{\tau_0}^1 \frac{d\tau}{\tau}\left[\frac{1}{s}\frac{dL_{i,j}}{d\tau}\right][\hat{s}\hat{\sigma}_{i,j}], \tag{4.6}$$

where the sum is performed over all pairs of partons.

If one chooses the set of parton distribution function to be used, it is possible to obtain the differential luminosity $\frac{1}{s}\frac{dL_{i,j}}{d\tau}$ as a function of the partonic center-of-mass energy. Examples of such plots are shown in Fig. 4.2, extracted from Quigg *et al* [74]. At the LHC with $\sqrt{s} = 14$ TeV, we find that, in general, processes produced from a gluon-gluon initial state contribute more significantly than quark-quark or quark-gluon initial states. Therefore, processes having significant contribution at the Tevatron collider may not be equally relevant at the LHC.

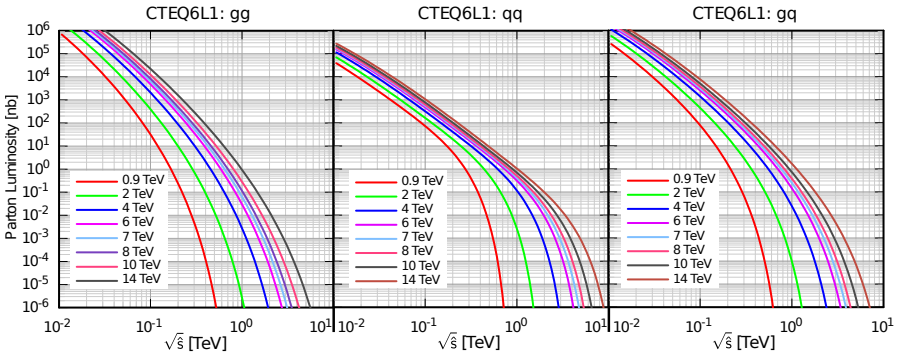

Figure 4.2: Parton luminosities $\frac{1}{s}\frac{dL_{i,j}}{d\tau}$ for processes with gluon-gluon (gg) , quark-quark (qq) and quark-gluon (qg) in the initial state as a function of the partonic center-of-mass energy. Plots extracted from Ref. [74], computed using the CTEQ6L1 PDF [75].

4.2 Predictive methods at colliders

In order to correctly predict the consequences of a particular theory at colliders, it is necessary to define which observable one should focus on. In this section, we thus introduce the relevant observables for the present study.

4.2.1 Kinematics and jet definitions

Typically, in a collider experiment, the two incoming beams are assumed to be in opposite directions on the z-axis. The polar angle is θ and the azimuthal angle is ϕ. At hadron colliders, the incoming beams have a spectrum of longitudinal momenta determined by the PDFs. The center-of-mass of the incoming partons is usually boosted in comparison to the center-of-mass of the incoming hadron. Therefore, it can be useful to define final states in terms of variables proportional to longitudinal observables.

Let us start by defining the transverse momentum p_T of a particle. The four-momentum of a particle can be written as

$$p^\mu = (E,\, p_x,\, p_y,\, p_z). \tag{4.7}$$

The transverse momentum is defined to be

$$p_T = \sqrt{p_x^2 + p_y^2} = p\,\sin\theta. \tag{4.8}$$

Similarly we can define the transverse mass and transverse energy:

$$m_T = \sqrt{p_T^2 + m^2}, \quad E_T = E \sin\theta. \tag{4.9}$$

Two further observables that will be largely employed within our phenomenological investigations are the missing transverse energy and the missing transverse momentum of an event:

$$\vec{\not{E}}_T = -\sum_{visible} \vec{E}_T, \quad \text{and} \quad \vec{\not{p}}_T = -\sum_{visible} \vec{p}_T \tag{4.10}$$

which can be constructed from the sum of the transverse energy/momentum of visible particles within the event. This quantity is one of the smoking-gun observables at the LHC, since many new physics signatures are expected to have large $\not{E}_T$.

Other significant observables are the rapidity y,

$$y = \frac{1}{2}\ln\left(\frac{E+p_z}{E-p_z}\right) = \tanh^{-1}\left(\frac{p_z}{E}\right), \tag{4.11}$$

and the pseudo-rapidity η,

$$\eta = -\ln\tan\left(\frac{\theta}{2}\right). \tag{4.12}$$

In the coordinate system presented above, θ is not Lorentz invariant, however, the pseudo-rapidity is. In the limit where $m \to 0$, the rapidity and the pseudo-rapidity of a particle are the same. It is also interesting to point out that we can calculate the pseudo-rapidity of an outgoing particle even not knowing its mass.

Notice also that the four-momentum of a particle can be written in terms of the transverse mass, the rapidity, and the azimuthal angle:

$$p^\mu = (m_T \cosh y,\, p_T \sin\phi,\, p_T \cos\phi,\, m_T \sinh y). \tag{4.13}$$

Up to this stage we have only defined observables related to incoming or outgoing particles. However, sometimes we cannot completely experimentally differentiate outgoing particles. That is the case for light quarks and gluons, which due to color confinement, hadronize before being detected. These hadronic final states are usually numerous and appear as an agglomerate of particles, called *jet of hadrons*. An illustration of the relation between parton-level outgoing particles and jets, *i.e.* hadronic final states, is represented in Fig. 4.3, extracted from [76].

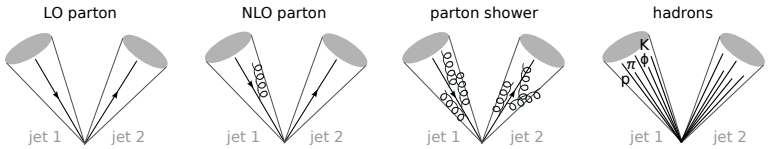

Figure 4.3: Illustration of the relation between partonic final states and hadronic final states, which gives identical jets in all the cases. Figure based on [76].

To associate the hadronic final state with the most probable parton-level particle, it is necessary to define the jet. However, the reconstruction of a jet is not unique and it can vary depending on the parameters chosen. One should specify at least which are the particles belonging to the jet, and how to combine their momenta. These choices of parameters compose what is called as a jet definition. There are algorithms created to this aim, also referred as clustering algorithm. These are separated in two main classes: cone algorithms, and sequential recombination algorithms. The first is based on the idea that the energy flow of the vertex is not modified by the branching[2] of the parton. It is a "top-down" approach in the sense that the algorithm defines the size of the jet based on one main particle. Sequential recombination algorithms, use a "bottom-up" approach, in which two particles are combined in one, sequentially, until only one particle (containing all the information of the others) is left. More details of each algorithm is given below. For more details, we refer to Refs. [76, 77].

Cone algorithms were the first type of jet algorithms proposed intended for the treatment of outgoing particles from e^+e^- collisions [78]. It starts by classifying all the (final) particles according to their p_T. The particle with the highest p_T is defined as the central particle. The algorithm draws a cone of radius R around the central particle, in terms of the pseudo-rapidity η and the azimuthal angle ϕ:

$$\Delta R = \sqrt{(\Delta\eta)^2 + (\Delta\phi)^2} \tag{4.14}$$

where $\Delta\eta = \eta_i - \eta_c$ and $\Delta\phi = \phi_i - \phi_c$, in which i is the index referred to the i-th particle, and c to the central particle. Subsequently, the algorithm uses all the particles in the cone, and find the direction of the sum of the momenta of these particles. If the sum is the same as the momenta of the central particle, a stable cone is obtained. Otherwise, the sum of the momenta (of the particles) of the cone is made the new central particle and the iteration re-starts until the cone is found to be stable. Once the cone is stable, all the particles inside the cone can be removed from the list of particles of the event. The iteration stops once all the particles are identified as belonging to a specific cone.

[2]Once a parton is emitted, it can multiply and emit other partons. These are usually soft, or collinear partons, which can be approximately reproduced in perturbation theory. A more precise explanation is given further ahead within this chapter.

The major disadvantage of using such kind of algorithm is the use of the p_T of the particles to decide what will be the first central particle. The problem is that the transverse momentum is not a collinear safe observable, and it could lead to divergences. One could then use cone algorithms that do not rely on one particle to be the central, but perform several tries in which all particles are once central. Several stables cones would be obtained in this case, and an optimized merge would be done defining the jet. These types of cone algorithms avoid collinear divergences, but are not infra-red safe. A full solution to both problems was found and nominated *Seedless Infrared Safe Cone algorithm* [79], being the main cone algorithm used nowadays.

Sequential recombination algorithms have a different strategy. They are based on a definition of "distance" between jets rather than a cone. The first algorithm using sequential combination was also developed for e^+e^- collisions and called the k_T *algorithm* [80]. In this case, a distance between two particles (i and j) is defined as:

$$y_{ij} = \frac{2\min\left(E_i^2, E_j^2\right)(1-\cos\theta)}{Q^2}, \tag{4.15}$$

where E is the energy of the particles, Q is the scale of the hard-scattering and θ is the angle separation between both particles. The two particles with the smallest distance, measured in terms of y_{ij}, are recognized and combined together giving rise to a "pseudo-particle". This strategy is repeated until the pseudo-particle and all the other particles in the event are separated by a larger distance than y_{cut}. When this happens, the pseudo-particle is determined as the jet.

The algorithm was adapted later on for hadron collisions [81, 82]. The distance between particles i and j can be fixed in terms of the ΔR:

$$d_{ij} = \frac{\min\left(p_{Ti}^2, p_{Tj}^2\right)\Delta R_{ij}^2}{R^2}, \tag{4.16}$$

where ΔR is defined similarly to the cone algorithm. It is also necessary to define the beam distance:

$$d_{iB} = p_{Ti}^2. \tag{4.17}$$

Now, the algorithm searches for the smallest distance, either d_{ij} or d_{iB}. If the smallest distance is the one separating both particles i and j, the algorithm works as explained previously combining both to a pseudo-particle. Otherwise, the particle i is removed from the list of particles and the jet is defined. This algorithm is very often employed to define a jet. We will make use of it in our phenomenological analyses.

A branch from the k_T algorithm also very commonly used as of today is the so-called *anti-k_T algorithm* [83]. Both k_T and anti-k_T algorithms have similar strategies, the

difference lies on the distance definition. In this case, d_{ij} and d_{iB} are defined as:

$$d_{ij} = \frac{1}{\max\left(p_{Ti}^2, p_{Tj}^2\right)} \frac{\Delta R_{ij}^2}{R^2}, \qquad (4.18)$$
$$d_{iB} = \frac{1}{p_{Ti}^2}.$$

Once we have selected one method for defining a jet, it can be treated as an unique particle. We can thus define observables that are related to jets, such as the H_T. From the same class of the $\not{E}_T$observable, the H_T is defined as the sum of the p_T of all the jets of an event:

$$H_T = \sum_{i=jets} \left|\vec{p}_T^{\,i}\right|. \qquad (4.19)$$

The H_T is an observable widely used in experimental searches due to its power on measuring the scale of the visible p_T of an event.

As the parton center of mass energy increases, hadron collision events with large jet multiplicities become more probable. As a result, accurate simulations require to correctly account for the presence of QCD radiation, which might modify predictions for these relevant observables that we have just presented. For specific processes, it is important therefore to account for extra orders in α_S when calculating cross section contributions. Subsequently, we demonstrate the necessity of such contributions.

4.2.2 Next-to-leading order cross section contributions

The expression (4.3) is obtained through perturbative QCD. One can obtain cross section contributions of specific processes up to the lowest order in α_S. To achieve more accurate results, one should compute higher orders contributions. These can be calculated considering the addition of one extra particle (quarks, or gluons) to the process being evaluated. The first two additional orders in α_S are usually named next-to-leading order (NLO) and next-to-next-to leading order (NNLO) contributions.

Take for instance the production of a Z boson [76]. The leading order term is $pp \to Z$. Eq. (4.3) for this leading process is given by

$$\sigma(P_1, P_2) = \sum_{i,j} \int dx_1\, dx_2\, f_i(x_1, \mu^2)\, f_j(x_2, \mu^2)\, \hat{\sigma}_{ij\to Z}^{(0)}. \qquad (4.20)$$

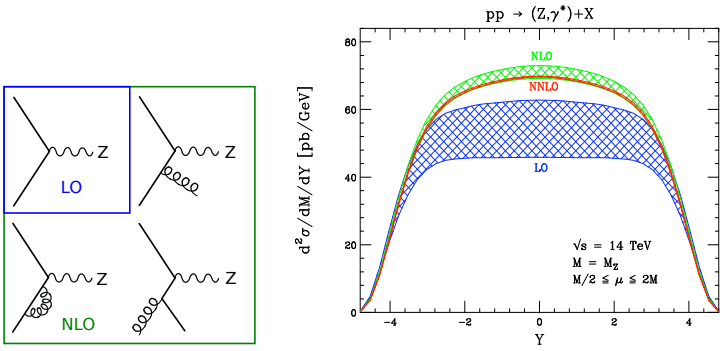

Figure 4.4: On left: LO and NLO diagrams for $pp \rightarrow Z$ production. In the right: Rapidity plot from [84].

To add the NLO term, besides taking loops into account, it is necessary to consider extra quarks and gluons produced in addition to the Z boson. The additional term is given by $pp \rightarrow Z + X$, where X is the emitted particle. A pictorial view of the process is presented in Fig. 4.4 (left). Accounting for the NLO contribution, the cross section is given by:

$$\sigma(P_1, P_2) = \sum_{i,j} \int dx_1\, dx_2\, f_i(x_1, \mu^2)\, f_j(x_2, \mu^2) \left[\hat{\sigma}^{(0)}_{ij\rightarrow Z} + \alpha_S(\mu_R)\, \hat{\sigma}^{(1)}_{ij\rightarrow Z+X}\right]. \tag{4.21}$$

In the previous sections, we have verified that the expected rate of observation of a process is related to its cross section, which is linked to observables such as the transverse momentum or the rapidity of a particle. The inclusion of higher order corrections on cross section calculations will thus increase the accuracy of results obtained for these relevant observables. This can be seen for example in the calculation of the Drell-Yan cross section for the Z boson decaying into a pair of leptons.

Consider the $q\bar{q} \rightarrow \ell^+\ell^-$ process, mediated by a Z boson and a photon. The tree-level cross section can be calculated [72]:

$$\hat{\sigma}(q\bar{q} \rightarrow \ell^+\ell^-) = \frac{4\pi\alpha^2}{9\hat{s}} \left(Q_q^2 - 2Q_q V_\ell V_q \xi_1(\hat{s}) + (A_\ell^2 + V_\ell^2)(A_q^2 + V_q^2)\xi_2(\hat{s})\right), \tag{4.22}$$

where $\hat{s} = (p_1 + p_2)^2$, p_1 is the four-momentum of the quark, p_2 is the four-momentum of the anti-quark, Q_f is the charge of the fermion, $V_f = T_f^3 - 2Q_f \sin\theta_w$, $A_f =$

T_f^3, $T_f^3 = +1/2$ for the up-quark/neutrino families and $T_f^3 = -1/2$ for down-quark/electron families. ξ_1 and ξ_2 are defined to be:

$$\xi_1(s) = \left(\frac{\sqrt{2}G_F M_Z^2}{16\pi\alpha}\right) \frac{s(s-M_Z^2)}{(s-M_Z^2)^2+\Gamma_Z^2 M_Z^2} \tag{4.23}$$
$$\xi_2(s) = \left(\frac{\sqrt{2}G_F M_Z^2}{16\pi\alpha}\right)^2 \frac{s^2}{(s-M_Z^2)^2+\Gamma_Z^2 M_Z^2}$$

where G_F is the Fermi constant, α is the electromagnetic coupling, M_Z and Γ_Z are the mass and width of the Z boson.

The differential lepton pair cross section $d\hat{\sigma}/dM_{\ell\ell}^2$ can be calculated, and from Eqs. (4.3) and (4.4) we know that $\hat{s} = x_1 x_2 s$. Accounting for the different parton probabilities, the differential cross section is given by

$$\frac{d\sigma}{dM_{\ell\ell}^2} = \int_0^1 dx_1 dx_2 \sum_q \left[f_q(x_1) f_{\bar{q}}(x_2) + f_{\bar{q}}(x_1) f_q(x_2)\right] \frac{d\hat{\sigma}}{dM_{\ell\ell}^2}. \tag{4.24}$$

To find the consequences of NLO corrections to a relevant observable, it is possible to find the double differential cross section as a function of the rapidity distribution. Eq. (4.11) can be written in terms of the parton momentum fraction:

$$y = \frac{1}{2}\log\left(\frac{x_1}{x_2}\right), \text{ and consequently } x_1 = \sqrt{\tau}\, e^y, \; x_2 = \sqrt{\tau}\, e^{-y}, \tag{4.25}$$

where $\tau = M_{\ell\ell}^2/s$. The tree-level double differential cross section is thus

$$\frac{d^2\sigma}{dM_{\ell\ell}^2 dy} = \frac{\sigma_0}{3s} \sum_q f_q(x_1) f_{\bar{q}}(x_2) + f_{\bar{q}}(x_1) f_q(x_2). \tag{4.26}$$

Once the next-to-leading order is considered, the double-differential cross section will have an extra order in α_S and divergences should be eliminated for the calculation to be finite. This is possible through different regularization schemes chosen [72]. For the process being considered, the (double differential) rapidity distribution is obtained for the LO, NLO and NNLO for instance by Anastasiou *et al* [84]. The plot in the right side of Fig. 4.4, extracted from the analysis of Ref. [84], exhibits such distribution. The bands are larger depending on the uncertainty of the calculation. These uncertainties are computed by varying both renormalization and factorization scales within $M_{\ell\ell}/2 < \mu < 2\, M_{\ell\ell}$, where $\mu = \mu_F = \mu_R$.

From Fig. 4.4 we can notice one feature of these corrections at LHC: the large σ_{NLO}/σ_{LO} factor, also known as the *K-factor*. Besides,

$$\frac{\sigma_{NNLO}}{\sigma_{NLO}} < \frac{\sigma_{NLO}}{\sigma_{LO}}. \tag{4.27}$$

A similar statement can be made concerning the uncertainty bands, (which decreases from LO to NNLO expectations) suggesting that even higher order corrections would have minimal relevance at the LHC energy scale.

Several tools exist to automatically compute cross sections at leading order of $2 \to n$ processes. These tools consider only tree-level diagrams, and the phase-space integration is performed in a region where results are finite. Tools to determine automatically NLO corrections have a complexity much larger. Because loop computations involve divergences, it is not so trivial to obtain NLO correction from numerical calculations. A lot of progress has already been made for the automation of such tools [85, 86, 87], however, we shall not employ this variation of simulation tools within the present studies as they are not yet completed or publicly available.

Nevertheless, leading order calculations have proven to give astonishing results. Distinct leading-order tools focused at different regions of phase-space have shown to be complementary providing overall very precise results when concerns the shape of relevant observables. Simulate events employing the correct tools is therefore the basis for obtaining accurate predictions at hadron colliders. Next, we present some of these tree-level tools, to subsequently introduce phenomenological analyses focused on graviton emission processes.

4.3 Monte-Carlo collider simulations

4.3.1 Simulation tools

Usually, hadron collisions can be separated mainly in two categories: hard and soft collisions. The difference lies on how separated the resulting partons are. Well separated partons belong to the first category, whereas collinear partons are included in the second. Likewise, hadron collisions can be simulated using mainly two approaches, which are suitable for each category presented above. The first is the matrix element technique, in which amplitudes are associated to a particular process, allowing for a cross-section calculation and event generation after the necessary integration over the phase-space. The second is the parton-shower description that simulates successive parton splitting, taking into account the emission of QCD radiation and, possibly, hard scatterings.

There are several Monte-Carlo software that can be used for both descriptions. For instance, SHERPA [88], CALCHEP [89], COMPHEP [90], MADGRAPH/MADEVENT [91, 92, 93, 94], ALPGEN [95], HELAC [96] or WHIZARD [97] are based on the matrix-element technique.

To exemplify how simulation within the matrix element technique works, let us use one of the above matrix element generator: MADGRAPH/MADEVENT. Initially, the process envisaged to be calculated should be specified, *i.e.* both initial and final state particles should be stated. The theory which is likely to be used for the computation of the processes has to be declared. As a result, MADGRAPH generates the Feynman diagrams and computes matrix element amplitudes at a randomly chosen point of phase-space using helicity amplitude routines. The implementation of helicity amplitudes and wave-functions have first been performed by the HELAS package [98, 99, 100, 101] and have recently been automatized [102], as describes Appendix C. These matrix element amplitudes are subsequently used by MADEVENT, which computes cross-sections (or decay widths) for the particularly chosen process, and generates simulated events for hadron colliders.

This approach is very flexible due to the fact that, in principle, any theory or model of particle physics can be used within the code, once it has been implemented in the event generator. However, the description is only valid at determined regions of phase-space, where final-state partons are very well separated from each other.

When protons collide at high energies, there is a large probability that partons will continue basically in the same direction with small transverse momentum. There is however some probability that particles with large transverse momentum are generated from the collision. This is so-called hard scattering, and can be diagrammatically seen in Fig. 4.5. When the scattering is hard, calculations must be done using perturbative QCD [72]. The lowest order is the one used in matrix-element simulators described so far.

Nevertheless, soft processes are more likely to be generated. A emission is soft when the particle emitted has very a small fraction of the energy of the particle that emitted it. A particle defined to be collinear when the angle between two particles is very small, such as they seem to be almost collinear in the literal sense of the word.

In the limit where final-state partons are soft, or collinear, one has to take into account parton splitting and QCD radiation. These are also refereed as “underlying events” and encompass events with initial and final state radiations and interactions of remaining partons of the initial proton. In fact, when a collision happens, partons can interact with other produced partons (or partons reminiscent from the collision) by radiating quarks and gluons. These radiated particles can themselves interact with other partons

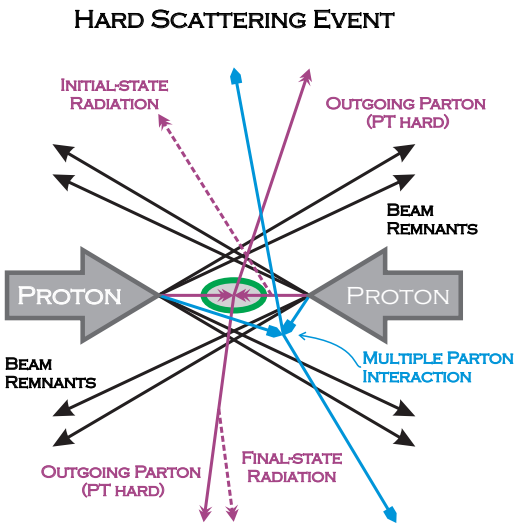

Figure 4.5: Pictorial view of a hard-scattering event at the LHC. Illustration based on Ref. [103].

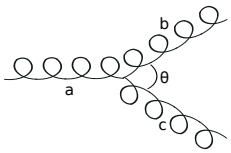

Figure 4.6: Illustration of a parton branching.

to produce their own QCD radiation. This forms a chain, or a shower of radiating quarks and gluons, also known as parton shower.

The parton shower approach is a treatment of QCD parton splitting which is a perturbative approximation and valid up to the order of some cut-off value. Above this value, which is usually fixed in terms of the p_T of the final particles, the probability of the splitting is low and the hard scattering approach is more suitable to describe such process. To briefly summarize how the parton shower approach works [72, 24], consider the parton branching illustrated in Fig. 4.6. The parton a splits into b and c. We assume that

$$t \equiv p_a^2 \gg p_b^2 \text{ and } p_c^2, \tag{4.28}$$

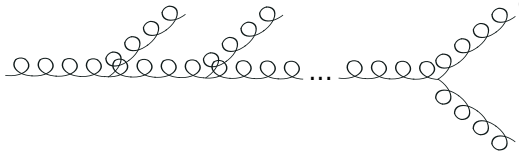

Figure 4.7: Illustration of sequential parton splitting.

where t is also known as the virtuality of the incoming parton. The separation angle between both outgoing partons is θ, and the energy fraction is z:

$$z = \frac{E_b}{E_a} = 1 - \frac{E_c}{E_a}. \tag{4.29}$$

In the soft and collinear limit, the cross section to describe a N-parton process (σ_N) is modified by the splitting of one parton as:

$$d\sigma_{N+1} = d\sigma_N \frac{\alpha_S}{2\pi} \frac{dt}{t} \hat{P}_{ba}(z) dz \tag{4.30}$$

where $\hat{P}$ is the Altarelli-Parisi splitting function [72]. As a consequence, sequential parton splitting can be simulated.

Suppose multiple parton branching, such as this represented in Fig. 4.7. It can be shown that the probability of a parton evolving from t' to t without resolvable radiation, *i.e.* without emitting other partons above a cutoff ϵ, is given by $\Delta(t)/\Delta(t')$, where $\Delta(t)$ is:

$$\Delta_i(t) \equiv \exp\left[-\sum_j \int_{t_0}^{t} \frac{dt'}{t'} \int_{\epsilon}^{1-\epsilon} dz \frac{\alpha_S(t)}{2\pi} \hat{P}_{ji}(z) \right]. \tag{4.31}$$

The $\Delta_i(t)$ is the probability summed over all possible processes $i \to j$. It is called Sudakov form factor and is the basis of Monte-Carlo simulation for the parton-shower approach. These algorithms employ the Sudakov form factor to control sequential splittings. They consider the probability of evolving from t_1 to t_2 without resolvable radiation:

$$\frac{\Delta(t_2)}{\Delta(t_1)} = \mathcal{R} \tag{4.32}$$

where $\mathcal{R}$ is a randomly generated number between $[0, 1]$. If the value of t_2 is smaller than Q^2, the next branching should have a fraction $z = x_2/x_1$ of the initial momentum and the next splitting should be generated. If this is the case, the probability

distribution for generating a fraction z of the initial momentum will be proportional to $(\alpha_s/2\pi)P(z)$, where $P(z)$ is the splitting function. Otherwise, no further splitting occurs. One can obtain the fraction of the initial momentum after a splitting by solving [72]:

$$\int_{\epsilon}^{x_2/x_1} dz \frac{\alpha_s}{2\pi} P(z) = \mathcal{R}' \int_{\epsilon}^{1-\epsilon} dz \frac{\alpha_s}{2\pi} P(z) \tag{4.33}$$

where $\mathcal{R}'$ is randomly generated number between $[0, 1]$, and ϵ is the cutoff for resolvable radiation.

This results on a cascade emission of partons up to the step where no more branching occurs. At this stage, partons are converted into hadrons following a hadronization description. This is used to simulate the creation of stable particles which will be the true observed final state at colliders. The hadronized particles will interact directly with the detector, and the resulting description is described as being "at detector level".

Different Monte-Carlo simulation tools are also available to simulate events following the parton shower and hadronization descriptions. These are for instance, PYTHIA [104], HERWIG [105], and ARIADNE [106].

The choice of which description to use is of course made depending on the process to be analysed. Collisions with a significantly low center-of-mass energy, processes that include few jets in the final state are very well described by using matrix-element simulation tools. However, as the parton center-of-mass energy increases, events with numerous jets in the final state become more likely. It is thus necessary to take into account the presence of QCD radiation using parton shower simulation. Because parton-shower approach underestimates the radiation of hard jets, the best solution is to use both descriptors at the same time. Nevertheless, some care is necessary in the limit where both tools are employed. At this region, one could consider the same event twice. For avoiding this problem one can use a matching, or merge scheme [107, 108, 109], which will consistently divide the space-space in two regions and specify the description to be used. A more detailed explanation on matching schemes is introduced in the following section.

4.3.2 Matrix-element/parton-shower matching scheme

The idea is to correctly simulate events using Monte-Carlo techniques and account for jets produced by initial state radiation. Generally, there are two ways of simulating $(N + 1)$-jet events: i) requesting a final state with N partons, where hard emissions could lead to the extra jet, or ii) from $(N + 1)$ partons final state, in which soft or collinear radiation evolved to generate the extra jets.

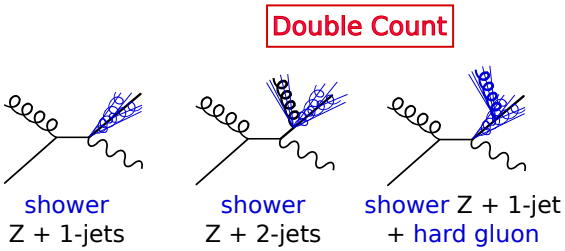

Figure 4.8: Pictorial example of a possible double counting of events with different multiplicities if the parton shower approach is considered at the same time as the matrix element technique without the employment of matching scheme. In the first diagram, it is shown one example for the production of a Z boson in association with one parton. The diagram in the middle exemplifies the production of a Z boson in addition to 2-partons final state. Finally the third diagram shows the production of a Z+1-parton process in which the parton radiates a hard-gluon, resulting on the same signature as the previous diagram.

As we have previously stated, the necessity of employing both prescriptions to simulate events with multiple jets in the final state comes from the fact they act at different regions of the phase-space. Parton shower descriptions are accurate for collinear/soft jet emission, but they can easily break down above a given scale where matrix element approach should be used. However, if both approaches are employed without some care, we could double count events with different multiplicities. One example of an event that could be double counted is illustrated in Fig. 4.8. The first diagram shows the production of a Z boson with one additional parton, which showers. The second diagram represents the Z boson produced with two partons in the final state. The third diagram however illustrates the production of a Z boson in addition to one parton which radiates and creates a hard gluon. Considering both approaches at the same time would double count events represented by the second and third diagrams. We have therefore to apply matching techniques in order to define, on an event-by-event basis, which prescription should be employed.

Different approaches have been proposed to merge the matrix element with parton shower descriptions. One can cite for instance the CKKW scheme [107, 108] and the MLM scheme [110, 111]. In general these procedures differ in three main aspects: the jet definitions used in the matrix element scheme, the employment of acceptance/rejection of the jet configuration and in the way that jets are vetoed inside the parton shower approach. Nevertheless, these approaches are based on a similar technique, which is basically to divide the phase-space into two regions. The separation between these regions, let us name it Q_{match}, should be expressed in terms of the

ΔR or p_T variables specified on the previous section, or of the k_T distance defined by Eqs. (4.16) and (4.17).

Here, we will focus on the MLM approach, using the software MADGRAPH/MADEVENT for matrix element simulations, and PYTHIA for the parton shower description. To be more precise, let us describe how the MLM description works. We use the k_T algorithm to cluster jets, and we shall follow strictly Refs. [111, 109].

The initial stage is to generate processes with N partons in the final state, *i.e.* to produce $pp \to X + N$-jets samples using the matrix element descriptor. They are defined following the kinematic cuts:

$$p_T > p_T^{min}, \quad |\eta| < \eta_{max}, \quad \Delta R_{ij} > R_{min}, \tag{4.34}$$

where p_T and $|\eta|$ are the transverse momentum and pseudo-rapidity of the final state partons and ΔR_{jj} is their minimal separation in the $(\eta,\, \phi)$ plane. The parameters with a subscript "min", or "max" are the generation parameters and must be the same for all N partons.

The tree structure is set according to the color-flow of the event, and the chosen scales of α_S, using the k_T value calculated at each vertex. The factorization scale for the parton densities is given by the hard scale of the process, *i.e.* $Q^2 = m_X^2 + p_{TX}^2$.

Subsequently, the shower is generated by the parton-shower descriptor and evolved up to the hard scale of the process, which was defined to be Q^2. A jet algorithm is then applied to the partons produced, specifying the final number of jets. These jets are determined by the following parameters: the cone size R_{clus}, the minimum transverse energy E_T^{clus} and the pseudo-rapidity η^{clus}. To be consistent with the division of the phase space, and to cover all the available range, it is necessary that $R_{clus} \geq R_{min}$, $\eta_{max}^{clus} \leq \eta_{max}$ and $E_T^{clus} \geq p_T^{min}$.

The matching scheme starts now. Beginning from the hardest parton, the closest jet in the $(\eta,\, \phi)$ plane is chosen. If the distance between the parton and the center of the jet is smaller than R_{min}, the jet is matched. This matching test is done in order to match each jet to a parton in the event. If that happens, the event is considered to be fully matched. Events which are not fully matched are rejected. Also, for events that pass the matching test, it is additionally required no extra jets to be present. That will avoid the double counting of the events that are already predicted, and more accurately described, by the $N + 1$ sample. However, for the highest parton multiplicity, these events are not rejected (considering no such $N + 1$ sample will be available), maintaining the full inclusiveness character of the sample.

It is valuable to state that the distribution of observables should not depend on the parameters defined on the scheme (such as R, η or Q_{match}). Moreover, the transition from one description to the other should be smooth.

The determination of the parameters used for the matching should depend on the process to be calculated. To demonstrate the utility of matching schemes, we shall present results for the process $pp \rightarrow Z + 0,\ 1,\ 2$-jets. We use this specific process, since it is one of the main background channels for the phenomenological analyses that we present for graviton emission. The Z boson could decay into a pair of neutrinos, and the signal expected would be missing transverse energy in addition to jets.

The first parameter we need to define is the matching scale. This is not a physical observable, therefore the results should not depend on it. However, the choice of such scale should be done smartly, in order to divide coherently the phase-space. If the cutoff is chosen too low, divergences in the matrix element simulation could appear. However, if the scale is chosen too high, there could be some regions where the parton shower would not be able to simulate events.

The intention is to have a smooth transition from one description to the other. The differential jet rate is the best variable to measure how smooth this transition may be. This variable is defined as the k_T scale at which an event passes from the $(N+1)$-jet to a N jet configuration while the algorithm cluster the showered partons. In reality, all the matching procedure do is to group showers according to the k_T scale chosen: if the jet is within the k_T distance, it belongs to a specific parton and grouped together with all the jets belonging to the same parton, otherwise it does not. In consequence, in a transition $N+1 \rightarrow N$, all the events with final number of jets smaller than $N+1$ should be below the cutoff, and events with multiplicity equal or larger than $N+1$ should lie above the scale chosen. In Fig. 4.9, we present differential jet rate plots for $pp \rightarrow Z + \ 0,\ 1,\ 2$ -jets, where we have used Q_{match} = 30 GeV, PYTHIA for the parton shower simulation and MADGRAPH/MADEVENT for the generation of events based on matrix element calculation. For the employment of the matching scheme as well as for the creation of the plots, we have made use of MATCHCHECKER [24], code designed for the interpretation of matching analyses.

The first graph of Fig. 4.9 shows the $1 \rightarrow 0$ differential jet rate. We can see that the curves of $Z + 1$-jet and $Z + 2$-jets samples are placed above the cutoff, while the $Z + 0$-jet sample is placed below. For $2 \rightarrow 1$, we have $Z + 2$-jets above the Q_{match} scale, while $Z + 0$-jet and $Z + 1$-jets situate below. One can see therefore in the three curves presented, the exact division where the straight pink line lies. In the left side of the line, mainly events are determined by parton shower approach, and in the right side using the description based on matrix element amplitudes. There is no need to

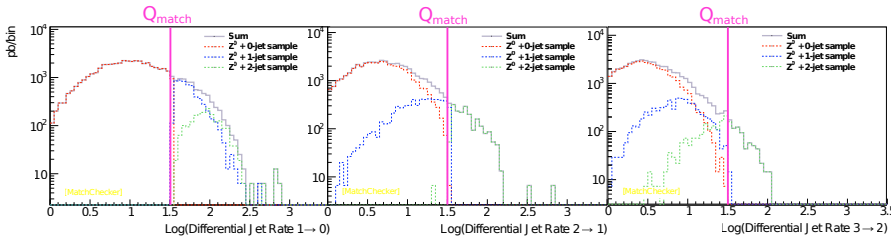

Figure 4.9: Differential jet rates for the process $pp \to Z + 0,\ 1,\ 2$-jets. The cutoff can be identified by the straight pink line. The curves in the left of the cutoff are produced using parton shower simulation. The curves in the right by matrix element simulation. Here, we can easily see the smoothness of the transitions.

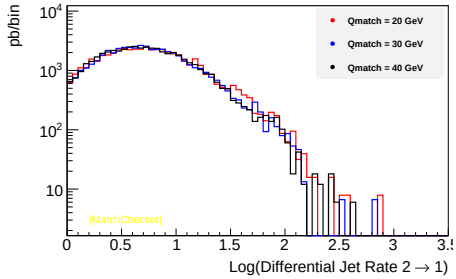

Figure 4.10: The choice of the Q_{match} scale should not modify the shape of any physical distribution. This statement is demonstrated in this plot of the differential jet rate of a $2 \to 1$ transition for different values of the Q_{match} scale. The curves shown are the final result, *i.e.* the sum of the contribution given by each multiplicity. The process being considered is $Z + 0,\ 1,\ 2$ jets.

focus at the $3 \to 2$ differential jet rate, because the transition is given fully by the parton shower.

As it has been stated, the choice of the Q_{match} scale should not modify overall results, *i.e.* the shape of the observed distributions. To prove this statement we show in Fig. 4.10 the differential jet rates for several choices of the cutoff scale. As expected, the curves lie above each other, predicting the same final result.

Finally, we can show distributions for some relevant observables. For instance Fig. 4.11 exhibits the differential cross section as a function of both the p_T of the Z boson (left) and the p_T of the highest energetic jet (right). One can easily see how parton shower and matrix element descriptions are complementary. At low values for the p_T, the

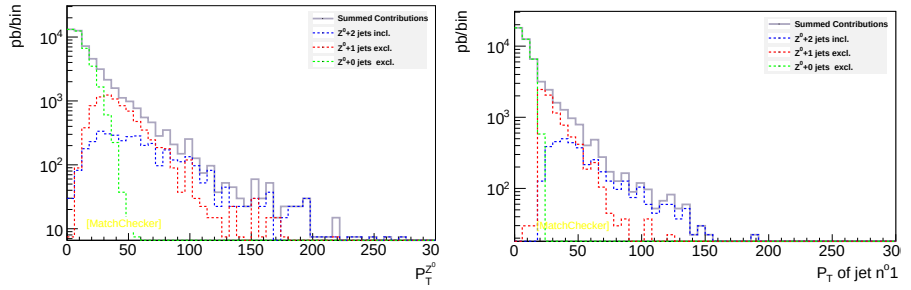

Figure 4.11: Differential cross section as a function of the p_T of the Z boson, left, and of the p_T of the highest energetic jet, in the right. The process being considered is $Z + 0,\ 1,\ 2$ jets, at the LHC with $\sqrt{s} = 14$ TeV, $Q_{match} = 20$ GeV and CTEQ6L1 PDF.

main contribution comes from lower multiplicities, basically computed through the parton shower description. As the energy increases, contributions from multiple jets in the final state become more significant and therefore matrix element description is more suitable to correctly account for them.

One substantial use of the matching technique is that it predicts very accurate shapes for distributions. The reason is that besides leading order processes being considered with the employment of the matrix element description, QCD radiation is taken into account within the parton shower approach. Therefore, even being a leading order simulation, the matching technique takes into account real emission processes. It therefore provides very precise shapes of the distributions comparable to NLO predictions. However, NLO calculation are still necessary for the prediction of the K-factors.

In order to verify how precise matching predictions are compared to NLO calculation for graviton emission processes, we have performed complete phenomenological analyses. Next chapter will therefore be focused on such phenomenological studies.

Chapter 5

Phenomenology of graviton production

In exact sciences, the word "phenomenology" is employed to relate empirical observations of phenomena with theories that attempt to describe it. This definition applies to particle physics as well. Comparison between theory and experiment is achieved through computer simulations. High-energy events are generated following the probability distributions expected from a theory, assuming certain initial conditions. Once the expectations of a particular theory are known, it is easy to test it and to constrain parameters.

The goal of this chapter is to perform phenomenological analyses on graviton emission processes at hadron colliders, taking into account theories which have been previously presented as a possible extension to the SM.

We start with an introductory analysis of graviton emission within processes with one jet in the final state [112, 113]. The events are characterized at colliders through its missing transverse energy signal. Two different theories are considered for such analysis: the theory with one massless graviton (MGM), and the theory with large extra dimensions (ADD), both presented in Chapter 3. The theory with warped extra dimensions (RS) is not expected to generate missing energy signature, since the first mode of the graviton should quickly decay into SM particles. Therefore, we do not consider it for this specific analysis.

We subsequently present a full phenomenological treatment of graviton emission within processes with multiple jets in the final state [114]. For the analysis, most types of theories predicting spin-2 particles are included and separated in three representative classes. Predictions of most relevant observables using different simulation methods are displayed, compared and validated against next-to-leading order QCD calculations.

5.1 Graviton emission in mono-jet searches

The specific four-dimensional model discussed in Chapter 3 is rather different at the theoretical level from the ADD extra dimensional model. Besides the fact that the graviton propagator has a different expression for each theory (due to the dependency of the propagator with the mass of the graviton), gravity could become strong in four dimensions if there would be a large hidden sector interacting gravitationally with the SM.

This large hidden sector could contribute to the renormalization group running of Newton's constant. In Chapter 3 we have shown that for approximately 10^{32} new particles, it would be possible to have $\overline{M}_{pl}(1\text{ TeV}) \sim 1$ TeV. For this reason, at the effective level of the theory, we could replace the coupling constant of Eq. (3.9) by the running Planck mass:

$$\frac{\kappa}{2} = \frac{1}{\overline{M}_{pl}(\mu_\star)}, \quad \text{and} \quad \overline{M}_{pl}(\mu_\star) \sim \mu_\star, \tag{5.1}$$

where $\mu_\star \sim 1$ TeV. The masses of the new particles determine the energy scale at which the running of Newton's constant starts. We could choose for example $m_i \sim 100$ GeV. If that is the case, most of the running of the Planck mass occurs at the order of 1 TeV. This suggests that the running of the reduced Planck mass could be effectively approximated by a step function:

$$\text{If } \mu < 1\text{ TeV}, \ \overline{M}_{pl}(\mu) = 2.4 \times 10^{18}\text{ GeV}, \tag{5.2}$$

$$\text{while for } \mu \geq 1\text{ TeV}, \ \overline{M}_{pl}(\mu) \sim 1\text{ TeV}. \tag{5.3}$$

As a result, the phenomenology expected for the MGM theory is very peculiar, since strong gravity breaks at the TeV scale for the MGM, while it does not for the ADD theory.

On the other hand, an infinite tower of KK excited modes of the graviton (coupled to the SM fields) are expected within the framework of the ADD theory. Subsequent modes of the graviton should have a mass gap of $1/R$, with R being the radius of the extra(s) dimension(s). For plausible values of R, excited modes of the graviton have a very compact discrete mass spectrum, *i.e.* subsequent modes should lie very tight to each other in absolute values of mass. In order to obtain an effective description of the full KK graviton tower, it is necessary to sum over all the states, or approximately, to integrate over the entire range of the mass spectrum. The mass integration is defined in Eq. (3.40), which results on the (expectation of) observation of one KK graviton with mass m.

In both theories, the graviton particle is expected to be identified at hadron colliders as transverse missing energy or momentum. Therefore, our first goal is to make a phenomenological analysis of processes that include invisible particles [112, 113]. A comparison of the signal against the SM expectation for missing energy, which is mainly translated into the production of pair of neutrinos, will give us a useful benchmark.

One extra motivation to the current phenomenological investigation has been presented in Section 3.4. We would like to investigate if there are phenomenological consequences of the propagator discontinuity, even if no discontinuity has been observed with analytical calculations at cross section level. For this reason, we have chosen to scrutinize graviton production in addition to one-jet in the final state, including all the processes discussed in Eqs. (3.78)−(3.83).

Mono-jet (*i.e.* 1-jet + missing energy) signature is one of the most familiar signal of several BSM theories, including both scenarios presented here. It will be crucial therefore to establish whether LHC could differentiate between theories. Moreover, in case of non-observation of mono-jet signals, one could use data from the LHC to constrain parameters of both theories. Particularly, it could set a limit on the value of the scale at which quantum gravitational effects become important.

The production of jets with large E_T in addition to a graviton G can emerge from the parton sub-processes $q + \bar{q} \to g + G$, $q + g \to q + G$, $\bar{q} + g \to \bar{q} + G$, and $g + g \to g + G$. To simulate and generate events for both theories, we use the matrix element description through the MADGRAPH/MADEVENT package. The ADD theory was implemented in MADGRAPH/MADEVENT version 4 by K. Hagiwara *et al* [99] and is supported by the package since 2008.

We follow the same strategy to implement the MGM theory according to our necessity. First, internally to the MADGRAPH code (or more precisely to the HELAS code), modifications in the graviton wave function routines are made in order to properly deal with massless spin-2 particles. In addition, helicity routines are modified and the massless spin-2 particle propagator is added to the code. Finally, a model file for the MGM is created (including particles, interactions and vertex definitions). In Appendix A the implementation is detailed, and checks and validation tests that have been accomplished are displayed.

The running of the Planck mass is implemented with a Heaviside step function in the cross section. The Planck mass for collisions at the parton level with $\sqrt{\hat{s}} > \mu_\star$ is given by $\overline{M}(\mu_\star) = \mu_\star$, and for less energetic parton level collisions we can approximate $M_{pl} \to \infty$. Because it is quadratic in energy, most of the running happens near to the scale in which gravity becomes strong, $\mu_\star$. Therefore, the approximation of the running of the Planck mass by a Heaviside step function can be very accurate.

The discussion begins with the results from predictions obtained by the MGM theory.

5.1.1 Mono-jet for the MGM theory

As explained, the graviton itself is not detectable and it appears as missing energy. One could think that if gravity becomes strong at the TeV scale, the Tevatron would have already felt its effect through Drell-Yan processes. However, in this scenario, the Drell-Yan process is extreme suppressed since virtual gravitons are decaying into the large hidden sector, and thus, the main signature would be that of the present analysis. Nevertheless, this is a very common signature. We expect the SM background to be dominated by the production of a Z boson (plus a single jet), with the Z decaying into pairs of neutrinos. We have therefore initially compared our predictions to the irreducible background process $pp(\bar{p}) \rightarrow \ \nu\,\bar{\nu}$ + jet [115, 116, 117] both for the LHC and Tevatron.

We display results for the number of events expected at the LHC in Fig. 5.1 and at the Tevatron in Fig 5.2. The analysis is made at the LHC for $\sqrt{s} = 14$ TeV with L=100 fb^{-1} of integrated luminosity and at the Tevatron for $\sqrt{s} = 1.96$ TeV with L= 1.1 fb^{-1}. The CTEQ6L1 PDF is employed. In order to have the background reduced, we choose a high-P_T cut and require the jet to be central:

$$\begin{aligned} \text{LHC:} \quad & p_T^{jet} > 500 \text{ GeV}, \quad |\eta^{jet}| < 3 \\ \text{Tevatron:} \quad & p_T^{jet} > 100 \text{ GeV}, \quad |\eta^{jet}| < 3. \end{aligned} \tag{5.4}$$

From Fig. 5.1 it is possible to deduce that there is a possibility for the LHC to identify signals of a massless graviton if $\mu_\star < 4$ TeV.

The distinctive indication of such theory would be the peak observed at $E_T^{miss} = \mu_\star/2$. The reason for this specific location of the peak is understood. Let us fix $\sqrt{\hat{s}} = M_0$, which is the invariant mass of the final state. The p_T of the jet, and in this case also the E_T, is $\frac{M_0}{2}\sin\theta$, where θ is the angle of the jet with respect to the beam. As θ varies, for any fixed M_0, the E_T changes and can be in the range $0 < E_T < M_0/2$. Now, let us concentrate on the cross section for the graviton emission processes. As M_0 increases, the cross section should diminish fast due to the reduced phase space and the rapid decrease in the parton densities. As a consequence, the cross section will have a maximum value when M_0 is minimum. However, in our case $M_0 \geq \overline{M}_{pl}(\mu_\star) \sim \mu_\star$ below which our cross section is zero by definition. This leads the E_T distribution to have a maximum at $\mu_\star/2$, as observed in both Figs. 5.1

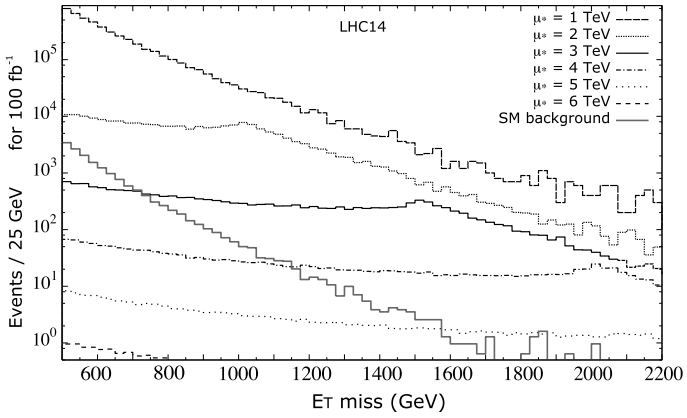

Figure 5.1: Number of events per bin considering a luminosity of $100\ fb^{-1}$. The background considered is $Z(\rightarrow \nu\bar{\nu})$ + jet. Figure extracted from [112].

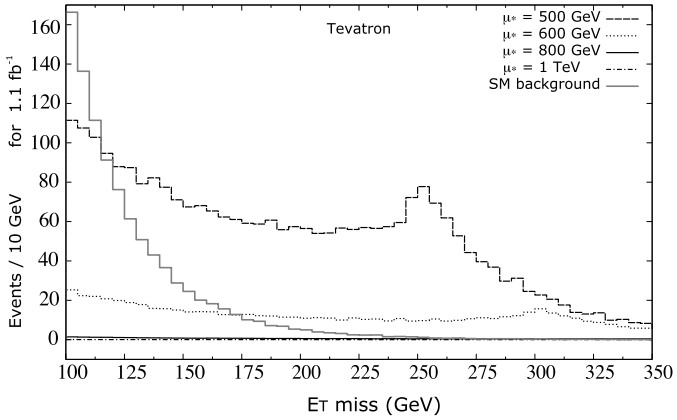

Figure 5.2: Number of events per bin at Tevatron considering a luminosity of $1.1\,fb^{-1}$. The background is $Z(\rightarrow \nu\bar{\nu})$ + jet. Notice that the y-axis is not displayed using a logarithmic scale in order to facilitate the analysis. Figure extracted from [112].

and 5.2. Therefore, the threshold is clearly a consequence from the imposition of the running of the Planck mass through the Heaviside step function.

From Fig. 5.2 we can infer that the Tevatron reach is quite limited. Combining results from the figure and these presented by the CDF Collaboration [117], we find that if $\mu_\star \simeq 500$ GeV, experimental hints should already have emerged at Tevatron. This limit is also obtained when cosmic rays data is used [118]. For $\mu_\star > 600$ GeV, we observe that it would be very hard to differentiate the MGM theory from the SM background.

We now present a comparative analysis of the results obtained with those predicted for the ADD theory at the LHC.

5.1.2 Mono-jet for the ADD theory

We employ two different techniques to simulate ADD at the LHC. Primarily, a modified version of the code developed by T. G. Rizzo for a different investigation [119] is adapted to the present analysis. Results are compared to a MADGRAPH/MADEVENT fully simulated sample. Same cuts given in Eq. (5.4) are used, and the PDF CTEQ6.6 [120] is applied.

The results of our direct comparison of the ADD predictions with those of the MGM theory assuming that $\overline{M}_{pl}(\mu_\star) = 1$ TeV can be found in Fig. 5.3. Here, we observe that both new physics models predict mono-jet E_T distributions which are reasonably different in shape. The decreasing curve from MGM mono-jet spectrum above the $\sqrt{\hat{s}} = M_\star$ threshold is lighter than the corresponding ADD distributions for any number of extra dimensions.

Comparing Figs. 5.1 and 5.3, we see the peak in the distributions associated with the MGM model, arise from the cross section threshold at $\sqrt{\hat{s}} = \mu_\star$, which are non-existent for the distributions associated with the ADD theory. In the latter case, the E_T distribution decreases monotonically, while the threshold in the MGM model cross section naturally leads to peak in these corresponding distributions. Therefore, the threshold would be the main point in distinguishing predictions of these two classes of models at the LHC. Moreover, because we have an indication of a cutoff in the cross section at a fixed value of $\sqrt{\hat{s}}$, this feature could allow us to extract the cutoff value directly from the LHC experimental data.

Notice from Fig. 5.3 that the parameters of the ADD theory are adjusted so that its curve starts at the same point as that of the MGM theory. This is done in order to fairly compare shapes of distributions obtained from both theories. A small difference

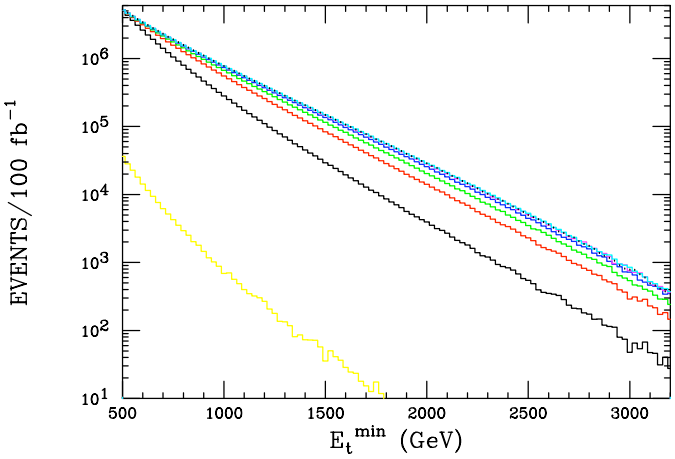

Figure 5.3: The number of mono-jet events expected as a function of the E_T^{min} distribution at the 14 TeV LHC, with L=100 fb^{-1} of integrated luminosity. A E_T^{min} cut of 500 GeV has been applied as well as the $|\eta^{jet}| < 3$ cut to require the jet to be central. The yellow histogram is the expected SM background ($Z \rightarrow \nu\bar{\nu}$), and the red and higher histograms are for the ADD model with the number of extra dimensions being 2,3,4, etc. The lower black curve is for the MGM model with $\mu_\star$=1 TeV. The parameters of the ADD curves are in each case adjusted by varying their associated Planck scale to produce the same result as does the MGM model at $E_T^{min} = 500$ GeV, in order to compare the relative shapes for these distributions. Figure extracted from [113].

between the black (MGM) and coloured curves (ADD) is observed. It is not a powerful difference that would allow to experimentally differentiate between both BSM theories. However, both curves lie above the background, and if observed, they would annunciate possible signals of new physics.

5.2 Graviton emission in multi-jet searches

We have analysed so far phenomenological consequences of graviton emission in combination with one parton level light jet. However, events with only one jet have a relatively low probability to appear at the LHC, considering its large center-of-mass energy. Besides, we have exclusively investigated graviton emission processes in which the signature is composed of invisible particles. There are however theories, such as the RS theory, that predict the decay of the spin-2 particle (into a pair of leptons for example).

Our subsequent goal is therefore to perform a complete analysis on graviton emission processes, including processes with more than one jet in the final state, and incorporating a full set of theories that contain different classes of spin-2 particles. Additionally, we aim on comparing our results against SM background expectations at the LHC and at Tevatron.

The search for this kind of new physics at the TeV scale is today among the major tasks of the LHC. Experimental analyses of such signatures require accurate simulations not only to design efficient signal selection strategies but also to extract information on new physics parameters, such as masses, coupling strengths, structures and spin.

The main idea is thus to include a wide class of models that involve spin-2 particles, such as:

- weakly coupled (Planck scale suppressed) massive graviton models, with infinite number of nearly continuously distributed KK modes of the graviton and the overall integrated effects are significant at the TeV scale, represented here by the ADD model;
- TeV scale massless graviton models, in which the graviton effects are negligible below the fundamental scale of quantum gravity, *i.e.* the TeV scale, due to the running of the gravitational constant, *e.g.*, in theories with many particles that interact with the SM particles only gravitationally. Represented here by the MGM theory;
- strongly coupled (TeV scale) massive graviton models, in which the graviton KK modes are widely separated. The lowest excitation gets mass at the TeV

scale and can decay into the SM particles within detectors. This class of theories is represented here by the RS model.

To show and validate the potential of MADGRAPH/MADEVENT implementation choose to study the most important signatures in representative models of the three classes above. For the ADD and MGM models the gravitons couple weakly to the SM particles and appear as invisible particles at colliders, as previously discussed. The main searching channel is $pp(\bar{p}) \rightarrow G + \mathrm{jet(s)}$, in which at least one accompanying hard jet is needed. For the RS model, resonance production $pp(\bar{p}) \rightarrow G$ is expected, with G decaying into e^+e^- or $\mu^+\mu^-$ for example. For completeness we additionally consider graviton in mono-jet channel to compare the RS model with the ADD and MGM results.

Several tools exist nowadays that are able to perform such simulations [121]. Here, we focus on MADGRAPH/MADEVENT, where a spin-2 particle implementation at the matrix element level exists [99]. In the appendix A we present the modifications made on such implementation to incorporate massless spin-2 particles. For the analysis with multiple jets in the final state, modifications in the massive spin-2 routines are still necessary in order to obtain a fully automatic event generator. First, MADGRAPH version 4 can only generate Feynman diagrams with up to 4-point vertices, and for this reason, diagrams containing 5-point vertex (*e.g.*, 4 gluons-graviton) have to be added by hand. Although it was fine for previous studies on graviton production with up to 2 jets [122, 123], it is inconvenient for graviton production with higher multiplicity jets. Secondly, gravitons are densely distributed in the ADD model and hence, it requires a special treatment for the propagator. These modifications have been successfully performed and are detailed in Appendix B.

As the parton center-of-mass energy increases, hadron collision events with large jet multiplicities become more probable. As a result, it is necessary that accurate simulations correctly account for presence of QCD radiation, which could modify leading order predictions for relevant observables.

Recall that in Chapter 4 it has been explained that there are mainly two approaches to simulate hadronic collisions: the matrix element technique and the parton shower approach. In parton shower MC programs like PYTHIA [104] and HERWIG [105], additional jets are usually obtained in the collinear and soft approximation. Hard and widely separated jets are poorly described in this approach. On the other hand, tree-level fixed order calculations can provide reliable predictions in the hard region, while failing in the collinear and soft limits. For this reason, to correctly take into account QCD radiation, matrix element simulators must be employed together with parton shower approach making use of matching description detailed in Section 4.3.2.

In this study, we use the k_T-MLM matching scheme implemented in MADGRAPH/ MADEVENT and interfaced to PYTHIA for parton shower and hadronization. In the k_T matching scheme, matrix element multi-parton events are produced with a minimum separation k_T cutoff, as described in Eq. (4.16) for $Q_{match} = Q^{\rm ME}_{\rm min}$. For every event, the final-state partons are clustered according to the k_T algorithm. Only clusterings corresponding to the Feynman diagrams provided by MADGRAPH are allowed. In order to closely mimic the behaviour of the parton shower, the k_T value for each clustering vertex corresponding to a QCD emission is used as renormalization scale for α_s in that vertex. For the central hard $2 \to 1$ or $2 \to 2$ process, the transverse mass $m_T^2 = p_T^2 + m^2$ of the particle(s) produced in the central process is used as a factorization scale, as well as a renormalization scale.

Subsequently, this event is passed to the parton shower MC simulator. Before hadronizing or decaying, the final partons are clustered into jets using the k_T algorithm with a jet cutoff of $Q_{match} > Q^{\rm ME}_{\rm min}$. The jets are then compared to partons. If d_{ij}(parton, jet) is smaller than the cutoff Q_{match}, they match. The event is only accepted is all the partons have matched with jets. For events with parton multiplicity smaller than the highest multiplicity, the number of jets must be equal to the number of partons.

Before establishing our phenomenological analyses, let us present one more detail of the current investigation. Our aim is equally to compare matched predictions against NLO calculations. For the RS theory, the leading order process is the zero-jet sample, since spin-2 particles should decay into a pair of leptons. For ADD and MGM theories, the leading order process is necessarily the 1-jet sample, because missing transverse energy cannot not be an observable if there is no visible particle to allow the invisible to be tagged. Therefore, we start by presenting the investigation carried out for RS models in fully inclusive samples for $pp \to G + n$-jets, where $n = 0, 1, 2$. Subsequently, exhibit a semi-inclusive analysis for $pp \to G + n$-jets, where $n = 1, 2, 3$, in which all three classes of theories presented above are investigated.

5.2.1 Fully inclusive graviton production for the RS theory

The first process to be explored is $pp \to G + X$, where the graviton will eventually decay into leptons. Let us start the discussion with the NLO-QCD corrections to such process.

NLO-QCD corrections

In Chapter 4 a brief discussion on NLO-QCD corrections to Z boson production within the SM has been presented. Currently, we follow the same strategy for the computation

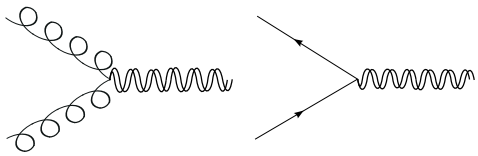

Figure 5.4: Leading order diagrams for the calculation of graviton emission. The curly lines represent a gluon, the straight lines a quark or anti-quark, and the double wavy line represents the graviton.

of NLO-QCD corrections to the production of a spin-2 particle within the RS theory. We begin with the process $P_1 + P_2 \rightarrow G + X$, where P_1 and P_2 are the initial hadrons, and X is an arbitrary hadronic final state.

The QCD hadronic cross section can be expressed as Eq. (4.20). To add NLO terms is necessary to consider loops and real emission of QCD radiation. Eq. (4.21) represents the cross section expression including first order terms.

The difference compared to the calculation presented in Section 4.2.2 is that for Z boson production only quark-anti-quark initial states are relevant, whereas for graviton production it is necessary to consider also the gluon-gluon initial state. Fig. 5.4 presents the diagrams relevant for the LO process, Fig. 5.5 shows real emission diagrams contributing for the NLO calculation and finally Fig. 5.6 exemplifies diagrams relevant for loop corrections. The diagrams contributing to first order corrections can be summarized as:

- $q + \bar{q} \rightarrow G + g$;
- $q + \bar{q} \rightarrow G$ (one-loop);
- $q + g \rightarrow G + q$;
- $\bar{q} + g \rightarrow G + \bar{q}$;
- $g + g \rightarrow G + g$;
- $g + g \rightarrow G$ (one-loop).

We can re-write Eq. (4.21) explicitly for graviton emissions [124, 125, 126]:

$$\sigma(P_1, P_2) = \sum_{i,j} \int dx_1\, dx_2\, f_i(x_1)\, f_j(x_2)\, \tau \left[\hat{\sigma}^{(0)}_{ij \rightarrow G} + a_S(\mu_R^2)\, \hat{\sigma}^{(1)}_{ij \rightarrow G+X} \right] . \quad (5.5)$$

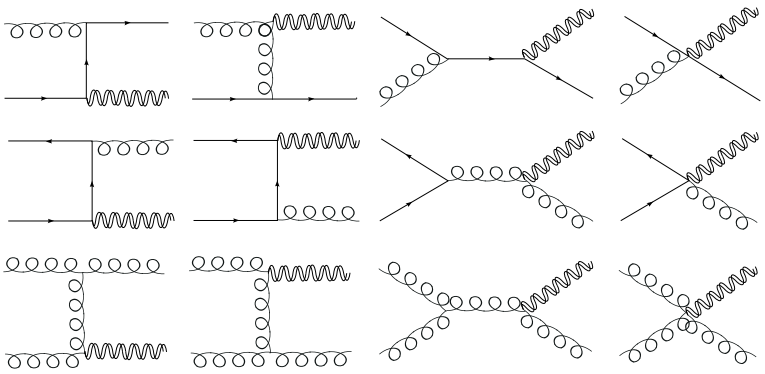

Figure 5.5: Real emission diagrams contributing for the NLO calculation of graviton emission process.

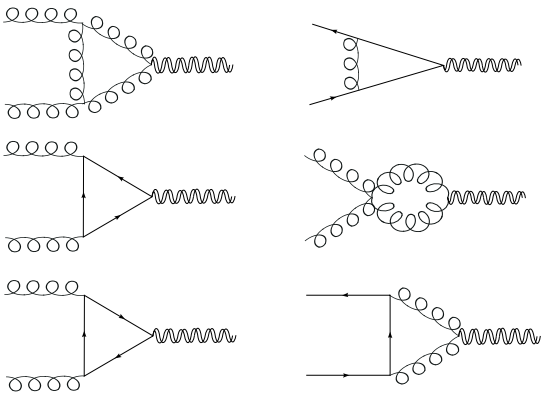

Figure 5.6: Loops diagrams contributing for the NLO calculation of graviton emission process.

where $\hat{\sigma}^{(0)}_{ij\to G} \equiv \sigma_0^{ij}\delta(1-z)$ is the Born partonic cross section, $a_S = \alpha_S/4\pi$ and $\hat{\sigma}^{(1)}_{ij\to G+X}$ are the contributions from loops and QCD emission. The scaling variables are:

$$\begin{aligned} &p_1 = x_1 P_1 && p_2 = x_2 P_2 \\ &s = (P_1+P_2)^2 && \hat{s} = (p_1+p_2)^2 \\ &\hat{s} = x_1 x_2 s = \tau s, && z \equiv \frac{M_G^2}{\hat{s}} = \frac{M_G^2}{\tau s} = \frac{\tau_0}{\tau}. \end{aligned} \tag{5.6}$$

For graviton emission we have:

$$\begin{aligned} \hat{\sigma}^{(0)}_{qq} =& \frac{\kappa^2\pi}{24}\delta(1-z); \qquad \hat{\sigma}^{(0)}_{gg} = \frac{\kappa^2\pi}{16}\delta(1-z); \\ \hat{\sigma}^{(1)}_{qq} =& \frac{2\pi\kappa^2}{9}\left[\left(-5+\frac{\pi^2}{3}+3\log\left(\frac{Q}{\mu_F}\right)\right)\delta(1-z) + 4\frac{1}{(1-z)_+}\log\left(\frac{Q}{\mu_F}\right) + \right. \\ & \left. 4\left(\frac{\log(1-z)}{1-z}\right)_+ - (1+z)\log\left(\frac{Q^2(1-z)^2}{\mu_F^2 z}\right) - \frac{2\log z}{1-z} + \frac{4}{3z} - \frac{4z^2}{3}\right]; \\ \hat{\sigma}^{(1)}_{qg} =& \frac{\pi\kappa^2}{48}\left[4\left(-\frac{7}{2}+\frac{4}{z}+z+z^2\right)\log\left(\frac{Q^2(1-z)^2}{\mu_F^2 z}\right) + 9 - \frac{12}{z} + 18z - 7z^2\right]; \\ \hat{\sigma}^{(1)}_{gg} =& \frac{3\pi\kappa^2}{16}\left[\left(-\frac{203}{9}+\frac{4\pi^2}{3}+\frac{44}{3}\log\frac{Q}{\mu_F}\right)\delta(1-z) + \frac{16}{(1-z)_+}\log\left(\frac{Q}{\mu_F}\right) + \right. \\ & + 16\left(\frac{\log(1-z)}{1-z}\right)_+ + 8(-2+\frac{1}{z}+z-z^2)\log\left(\frac{Q^2(1-z)^2}{\mu_F^2 z}\right) - 2 + \\ & \left. -\frac{22}{3z} + 2z + \frac{22z^2}{3} - \frac{8\log z}{1-z}\right] + \frac{\pi}{32}n_f\left[\frac{70}{9} - \frac{16}{3}\log\left(\frac{Q}{\mu_F}\right)\right]\delta(1-z); \end{aligned} \tag{5.7}$$

where n_f is the number of quark flavours considered and the "plus distribution" is defined as:

$$\int_0^1 dz\, h_+(z)\, f(z) = \int_0^1 dz\, h(z)\,(f(z) - f(1)) \tag{5.8}$$

For the computation of the NLO cross section, we implement a small code based on Eqs. (5.5) to (5.7). A change of variable is performed to facilitate the integration:

$$x_1 \equiv \sqrt{\tau}e^{y}; \quad x_2 \equiv \sqrt{\tau}e^{-y}; \quad \tau = x_1 x_2. \tag{5.9}$$

We find the jacobian and change the integration limits:

$$\int_{\tau_0}^1 dx_1 \int_{\tau_0/x_1}^1 dx_2 = \int_{\tau_0}^1 dz\,\frac{\tau_0}{z^2}\int_{\log\sqrt{\tau_0/z}}^{-\log\sqrt{\tau_0/z}} dy \tag{5.10}$$

m_G GeV	σ_{LO} (pb)	σ_{NLO} (pb)	K-factor
91	4.59×10^3	8.73×10^3	1.90
500	1.97×10^2	3.38×10^2	1.71
800	5.77×10^1	9.67×10^1	1.67
1000	2.99×10^1	4.95×10^1	1.65
1200	1.67×10^1	2.74×10^1	1.63
1500	0.78×10^1	1.25×10^1	1.61

Table 5.1: LO and NLO results for the integrated cross section of a graviton emission process within the RS theory at the LHC with center-of-mass energy of 14 TeV. The first mode of the graviton couples to the SM fields according to Eq. (3.9). Here, it is chosen $\frac{1}{\Lambda} = \frac{\kappa}{2} = 3$ TeV, $\mu_F = \mu_R = m_G$, n_f=5 and employed the CTEQ6L1 PDF [75].

For the leading order distribution, the integral is easy to solve. We present it therefore as a reference. For instance, the leading order contribution for the gluon-gluon initial state is exhibited in Eq. (5.7). The cross section is thus given by:

$$\sigma(gg/q\bar{q} \to G) = \frac{\kappa^2\pi}{16}\tau_0 \int_{\log\sqrt{\tau_0}}^{-\log\sqrt{\tau_0}} dy\, f_i(\sqrt{\tau_0 e^{y}}) f_j(\sqrt{\tau_0 e^{-y}}), \tag{5.11}$$

where $(i,j) = (g,g)$, $(q,\bar{q})$, $(\bar{q},q)$. The integral over partonic fractions presented just above are also named partonic luminosities.

As a result, we obtain the K-factor for graviton emission within the RS theory. Tables 5.1 and 5.2 display values for the K-factor calculated for different center-of-mass energy at the LHC. Notice that the factorization and renormalization scales are set to be the mass of the graviton.

The aim is now to obtain matching predictions for fully inclusive processes and compare the K-factor obtained, defined to be σ_{NLO}/σ_{LO}, with the normalization factor, or N-factor, defined to be $\sigma_{NLO}/\sigma_{match}$.

Matching predictions

For the matching scheme we have chosen to use $pp \to G + n$-jets where $n = 0, 1, 2$ ($n = 2$ samples are inclusive). The parameters employed for the RS theory are the same as for the NLO calculation. The analysis has been accomplished for: (a) the LHC with $\sqrt{s} = 14$ TeV and $m_G = 1$ TeV; (b) the LHC with $\sqrt{s} = 7$ TeV and $m_G =$

m_G GeV	σ_{LO} (pb)	σ_{NLO} (pb)	K-factor
91.2	1.61×10^3	3.21×10^3	1.99
500	2.62×10^1	4.61×10^1	1.76
800	5.24	8.73	1.67
1000	2.18	3.52	1.62
1200	0.99	1.56	1.57
1500	0.34	0.51	1.53

Table 5.2: LO and NLO results for the integrated cross section of a graviton emission process within the RS theory at the LHC with center-of-mass energy of 7 TeV. The first mode of the graviton couples to the SM fields according to Eq. (3.9). Here, it is chosen $\frac{1}{\Lambda} = \frac{\kappa}{2} = 3$ TeV, $\mu_F = \mu_R = m_G$, n_f=5 and employed CTEQ6L1 PDF [75].

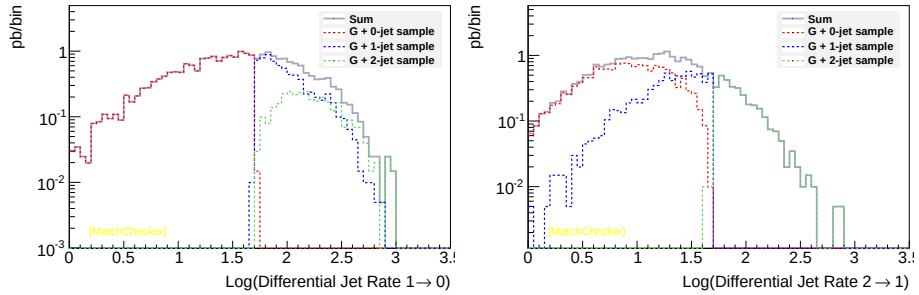

Figure 5.7: Differential cross section as a function of the differential jet rate for $2 \to 1$ and $1 \to 0$

500 GeV; (c) and for the Tevatron with $\sqrt{s} = 1.96$ TeV and both $m_G = 500$ GeV and (d) $m_G = 1$ TeV. At generation level we have employed $Q_{match} = 50$ GeV, and no cuts have been used.

First, we make sure the matching is properly working. To this aim we plot the differential $2 \to 1$ and $1 \to 0$ jet rates. Results for the LHC with $\sqrt{s} = 7$ TeV for a graviton with $m_G = 500$ GeV are displayed in Fig. 5.7. Notice the smoothness of the passage from when parton shower is employed to when the matrix element technique is used. All samples both for the Tevatron and the LHC have similar shapes for the differential jet rate and present as good smooth passage.

Subsequently, in order to exemplify the predicting capability of matching technique, we present the most relevant distributions at the LHC in Fig. 5.8. These plots exhibit the differential cross section as a function of its particular observable. The integrated

Tevatron					
m_G	σ_{LO} (pb)	σ_{NLO} (pb)	K-factor	σ_{match} (pb)	N-factor
500 GeV	1.039	1.416	1.36	1.059	1.34
1 TeV	0.020	0.031	1.55	0.021	1.52

Table 5.3: K-factor $\sigma_{(NLO)}/\sigma_{(LO)}$ and normalization factor $\sigma_{(NLO)}/\sigma_{match}$ for inclusive G production in the RS model at the Tevatron, from $p\bar{p} \to G$ NLO QCD calculations and parton shower matching with the matrix elements of $p\bar{p} \to G + n$ jet(s) with $n = 0, 1, 2$, $\Lambda = 3$ TeV, $m_G = 0.5$ and 1 TeV for $\sqrt{s} = 1.96$.

LHC					
m_G	σ_{LO} (pb)	σ_{NLO} (pb)	K-factor	σ_{match} (pb)	N-factor
500 GeV	26.238	46.155	1.76	24.642	1.87
1 TeV	23.803	40.316	1.69	24.362	1.65

Table 5.4: K-factor $\sigma_{(NLO)}/\sigma_{(LO)}$ and normalization factor $\sigma_{(NLO)}/\sigma_{match}$ for inclusive G production in the RS model at the LHC, from $pp \to G$ NLO QCD calculations and parton shower matching with the matrix elements of $pp \to G + n$ jet(s) with $n = 0, 1, 2$, $\Lambda = 3$ TeV, $m_G = 0.5$ and 1 TeV for $\sqrt{s} = 7$ and 14 TeV LHC, respectively.

cross sections can be calculated, and are displayed in Tables 5.3 and 5.4. We normalize matched cross sections with leading order values presented in Tables 5.2 and 5.1 for the corresponding values for the mass of the graviton, which are the underlined row. Results for both the K-factor (σ_{NLO}/σ_{LO}) and N-factor ($\sigma_{NLO}/\sigma_{match}$), as well as the cross sections obtained, are exhibited in Tables 5.3 and 5.4.

Observe that values for the K- factor are very close to the normalization factors (or N-factors, for short). In fact, the cross section after matching analysis is expected to be similar to the leading order computed for $pp \to G$. Leading order calculation already includes the production of extra radiation through the PDFs (parton distribution functions). However, matching calculation considers explicitly the production of extra jets in the final state, which leads to a modification on the behaviour of relevant observables, such as the missing P_T, pseudo-rapidity and H_T distribution. As a result, we expect that matched sample, normalized to NLO calculation, will produce better predictions for observables which involve extra radiation than a pure parton shower

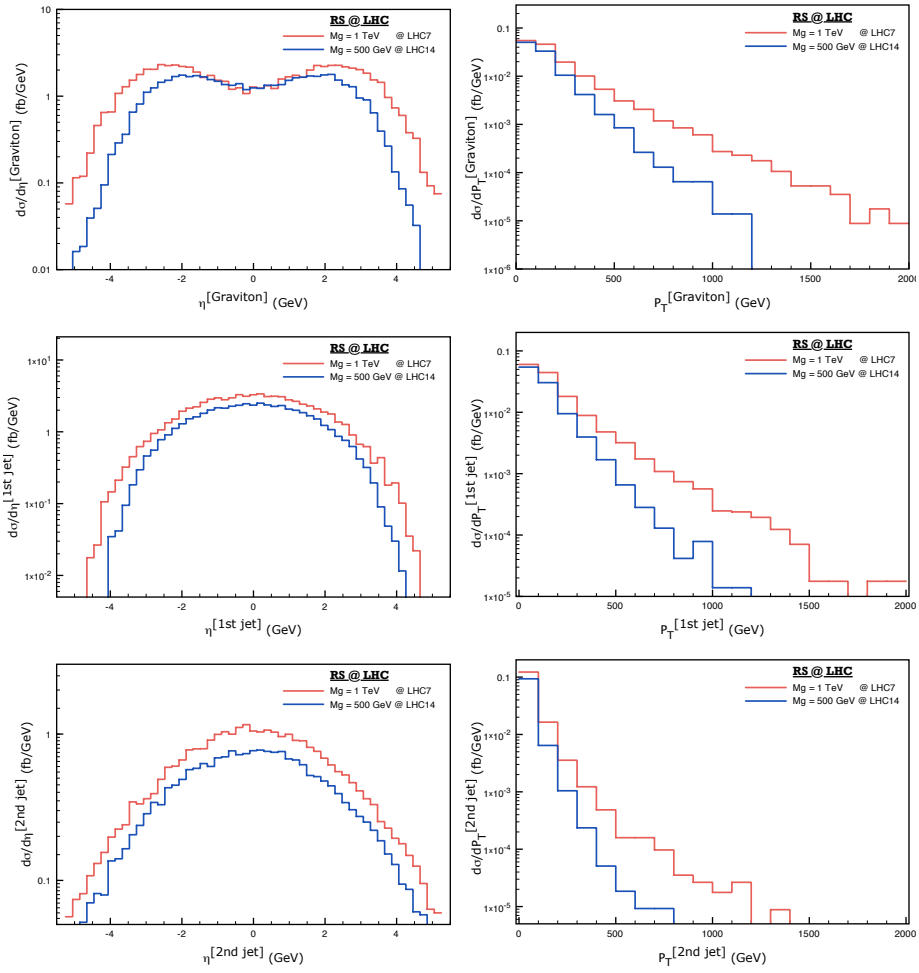

Figure 5.8: k_T-MLM matching results for a $pp \to G + n$-jets with $n = 0, 1, 2$ full inclusive sample of the RS model with $\Lambda = 3$ TeV. The matched results are given by the red and blue curves for $m_1 = 1$ TeV at the LHC with $\sqrt{s} = 14$ TeV, and $m_1 = 500$ GeV at the LHC with $\sqrt{s} = 7$ TeV, respectively. No cuts were applied in these samples.Figure extracted from [114].

approach. In order to verify such statement, we follow with a complete analysis of $pp \to G + n$-jets, in which the leading order process is now mono-jet, and the matching is performed up to 3-jets in the final state.

5.2.2 Semi-inclusive analysis for graviton emission processes

For different classes of theories, such as the ADD and MGM, it is more interesting to explore missing energy signature in combination with jets. We present therefore a similar investigation to these of the previous section. However, the leading order process should currently be the emission of one graviton in addition to one jet. An example of such diagrams are presented in Fig. 3.4 for the quark-anti-quark initial state. Similar diagrams exist for the gluon-quark and gluon-gluon initial states.

As previously performed, we consider a general theory containing a graviton that couples to the SM fields following Eq. (3.9) and in which the Feynman rules are displayed in Fig. 3.1. We summarize the relation between the general parameter κ (explicitly revealed in the lagrangian) and the effective scale of the three representative classes of theories currently being analysed:

$$\begin{aligned} &\text{MGM theory} && \frac{1}{\Lambda} \equiv \frac{\kappa}{2} = \frac{1}{\overline{M}_{pl}(\mu_\star)} \sim \frac{1}{\mu_\star} \\ &\text{ADD theory} && \frac{1}{\Lambda} \equiv \frac{\kappa}{2} = \frac{1}{\overline{M}_{pl}} \\ &\text{RS theory} && \frac{1}{\Lambda} \equiv \frac{\kappa}{2} = \frac{e^{+kR\pi}}{\overline{M}_{pl}} \end{aligned} \tag{5.12}$$

For the ADD model, one extra integration over KK the mass spectrum is performed according to Eq. (3.40), which results the effective scale to be of the TeV order.

The implementation of the running of the Planck mass for the MGM theory has been performed during the generation of the events. The technique to implement the running has changed from the analysis exhibited in Section 5.1. Previously, we had applied a cut on $\sqrt{\hat{s}}$. However, now we have extra jets in the final state. When these extra jets are soft/collinear, we could get non-physical enhancements below the threshold, which would have nothing to do with the Q^2 of the scattering. A solution would be to apply a cut in all partonic Mandelstam variables: $\sqrt{\hat{s}}$, $\sqrt{-\hat{t}}$ and $\sqrt{-\hat{u}}$. The problem is that cuts on $\sqrt{-\hat{t}}$ and $\sqrt{-\hat{u}}$ are not physical, and could spoil the infra-red divergence cancellation when NLO corrections are calculated. We have thus decided to apply a minimum cut of $\mathrm{H}_T^{\min} > \overline{M}(\mu_\star) \sim \mu_\star$ in the sum of transverse momentum of the jets, which is stronger than the combination of the cuts on Mandelston variables. In

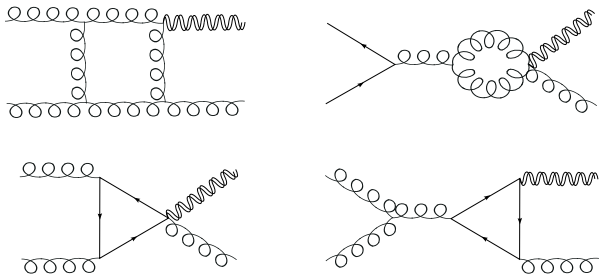

Figure 5.9: Example of loop diagrams contributing for NLO calculation of the process $pp \to gG$.

other words, a Heaviside step function-like behaviour is still added to the cross section. However, now for collisions with $H_T < \overline{M}(\mu_\star) \sim \mu_\star$, gravity contributions are so weak that the cross section can be approximated to zero.

To fix the parameters related to the theories, we consider the up-to-date experimental constraints for each representative class [116, 127, 117, 128, 129, 130]. For the ADD model, we choose $\Lambda = 5$ TeV at the LHC, $\Lambda = 1$ TeV at the Tevatron, with $\delta = 2, 4, 6$. For the MGM model, we set $\overline{M}(\mu_\star) \sim \mu_\star = 1$ TeV and 2 TeV. For the RS model, we take $m_G = 1$ TeV and 100 GeV, with $\Lambda = 3$ TeV. The latter value chosen for the mass of the graviton is clearly excluded by experimental searches. We have decided to employ it in order to check how RS theory behaves at low graviton mass limit. The idea is to check that no strange behaviour comes from the discontinuity of the propagator.

NLO-QCD corrections

We present the NLO corrections to $pp \to G\,j + X$. Such calculation has been performed by several authors, including [122]. Here, we summarize the main aspects.

The NLO calculation for the cross section consists on computing loops and real QCD emission, as presented in the previous section. The leading order contributions are now the diagrams represented in Fig. 5.5. Examples of loop diagrams contributing for this specific calculation are presented in Fig. 5.9. Again, we can separate the calculation in three parts: the computation of virtual corrections, real emission contributions and the collinear term. Virtual correction arises from the interference of the born and one-loop amplitudes. Real-emission contributions appear from the production of a QCD light jet, and the collinear term is the finite reminder of the factorization of collinear singularities into the PDFs.

The authors of [122] have created a code to compute NLO corrections for graviton emission considering the ADD theory. In [114], we have employed and extended their code to compute NLO corrections accounting for the three classes of theories.

Concerning the parameters chosen for the calculation, in order to suppress SM backgrounds in LHC graviton searches [115] we require:

$$\not{p}_T > 500 \text{ GeV}, \quad |\eta^{jet}| < 4.5, \quad \text{and} \quad p_T^{jet} > 50 \text{ GeV}. \tag{5.13}$$

Jets are defined by the k_T algorithm, with the resolution parameter set to D=0.6. At the Tevatron, we require

$$\not{p}_T > 120 \text{ GeV}, \quad |\eta^{jet}| < 1.0, \quad \text{and} \quad p_T^{jet} > 150 \text{ GeV}, \tag{5.14}$$

following the settings considered in a recent CDF study [116, 117]. Notice p_T^{jet} is the minimum p_T required for the leading jet. Here, all jets are defined by the k_T algorithm with $D = 0.7$, and are required to satisfy $|\eta_j| < 3.6$ and $p_T^j > 20$ GeV. A second jet with $p_T > 60$ GeV is vetoed.

Again, the SM background considered is the irreducible $pp \to \nu_\ell \bar{\nu}_\ell$ + jets. The idea is to use the background as a reference curve. A detailed experimental search would have to consider other types of processes for the SM background, such as the production of W boson decaying to a lepton and a neutrino, where the lepton is not tagged.

For the LO/NLO calculations, CTEQ6L1/6M PDFs are employed together with the corresponding values for the strong coupling α_S. The renormalization and factorization scales are set to the transverse momentum of the graviton p_T^G. We vary the scales in the range between $p_T^G/2$ and $2p_T^G$ to show the uncertainties related to the scales.

On Tables 5.5 and 5.6 we display LO and NLO values obtained for the integrated cross section at the LHC and at Tevatron. The K-factor is calculated and also exhibited.

In addition, we have computed the differential cross section as a function of the following distributions:

(a) Transverse missing energy (for ADD and MGM theories) or transverse energy of the graviton (for RS theory);

(b) Transverse momentum of the first and second highest energetic jets;

(c) Pseudo-rapidity of the the graviton;

(d) Pseudo-rapidity of the first and second highest energetic jets;

(e) The H_T distribution, which is defined by Eq. (4.19).

Before showing and interpreting results obtained for each relevant observable, let us describe the implementation of the matching scheme.

Matching predictions

Similarly to the NLO calculations, we analyse $pp \to G{+}n$-jets, where $n = 1, 2, 3$ with the leading order process being $n = 1$. We employ MADGRAPH/MADEVENT for the parton-level generation, and shower using the PYTHIA package. In the event generation with MADGRAPH/MADEVENT, CTEQ6L1 PDF [75] is employed, which fixes the values of α_S at the Z mass. The choices of renormalization and factorization scales are defined to be the transverse mass of the graviton.

The calculation of the cross section as well as the event generation is performed using the following matching scales:

$$\begin{array}{lll} \text{LHC} & Q^{\rm ME}_{\rm min} > 45\,\text{GeV}, & Q_{match} > 50\,\text{GeV} \\ \text{Tevatron} & Q^{\rm ME}_{\rm min} > 20\,\text{GeV}, & Q_{match} > 30\,\text{GeV}. \end{array} \tag{5.15}$$

In Tables 5.5 and 5.6 we display the obtained matched values for the integrated cross section at the LHC and at Tevatron. The N-factor is calculated and exhibited in order to allow the comparison against the K-factor previously computed.

Comparative analysis and interpretation of the results

Let us start the discussion with a comparative analysis of the values obtained for the K-factor against N-factor. Tables 5.5 and 5.6 exhibit both values for the three classes of theories and parameters specified in the beginning of this section. Notice we do not observe consistent values at the Tevatron as we observe at the LHC. Recall the settings used to compute such numbers:

k_T-MLM matching calculation:

- Process: $pp \to G + n$-jets, $n = 1,\ 2,\ 3$.
- Scales: $\mu_F = \mu_R = \sqrt{p_T^2 + m_G^2}$
- PDF: CTEQ6L1

	LHC				
	σ_{LO} (fb)	σ_{NLO} (fb)	K-factor	σ_{match} (fb)	N-factor
ADD $\delta = 2$	1.67×10^2	2.76×10^2	1.65	1.35×10^2	2.05
ADD $\delta = 4$	3.83×10^1	6.22×10^1	1.62	2.67×10^1	2.33
ADD $\delta = 6$	1.45×10^1	2.36×10^1	1.63	9.47×10^0	2.49
MGM 1 TeV	2.27×10^3	1.08×10^4	1.86	6.89×10^3	1.56
MGM 2 TeV	7.19×10^1	1.52×10^2	2.11	9.24×10^1	1.64
RS 1 TeV	9.65×10^2	1.59×10^3	1.65	7.98×10^2	1.99
RS 100 GeV	4.72×10^3	8.51×10^2	1.80	4.70×10^3	1.81

Table 5.5: Integrated cross section, K-factor σ_{NLO}/σ_{LO} and N-factor $\sigma_{NLO}/\sigma_{match}$ for semi-inclusive G production at the LHC with $\sqrt{s} = 14$ TeV, from $pp \to G$ NLO QCD calculations and parton shower matching with the matrix elements of $pp \to G + n$ $-$jet(s) with $n = 1, 2, 3$. For the ADD theory, the effective scale is set as 5 TeV, and δ is the number of extra dimensions. For the MGM theory, 1 Tev and 2 TeV stand for the values chosen for $\mu_\star$. We consider $\Lambda = 3$ TeV for the RS theory, in which the mass of the first mode of the graviton is either $m_G = 0.1$ or $m_G = 1$ TeV respectively.

	Tevatron				
	σ_{LO} (fb)	σ_{NLO} (fb)	K-factor	σ_{match} (fb)	N-factor
ADD $\delta = 2$	5.22×10^2	6.39×10^2	1.22	2.66×10^2	2.40
ADD $\delta = 4$	1.82×10^2	1.77×10^2	0.97	7.16×10^1	2.47
ADD $\delta = 6$	8.24×10^1	6.91×10^1	0.83	3.59×10^1	1.92
RS 1 TeV	1.91×10^{-1}	1.20×10^{-1}	0.62	6.17×10^{-2}	1.95
RS 100 GeV	2.31×10^2	3.37×10^2	1.46	1.95×10^2	1.73

Table 5.6: Integrated cross section, K-factor σ_{NLO}/σ_{LO} and N-factor $\sigma_{NLO}/\sigma_{match}$ for semi-inclusive G production at the Tevatron with $\sqrt{s} = 1.96$ TeV, from $p\bar{p} \to G + j$ NLO QCD calculations, and parton shower matching with the matrix elements of $pp \to G + n$ $-$jet(s) with $n = 1, 2, 3$. For the ADD theory, the effective scale is set as 1 TeV, and δ is the number of extra dimensions. There is no reason for the computation with the MGM theory, since it has been proved not possible to be detected at the Tevatron. We consider $\Lambda = 3$ TeV for the RS theory, in which the mass of the first mode of the graviton is either $m_G = 0.1$ or $m_G = 1$ TeV respectively.

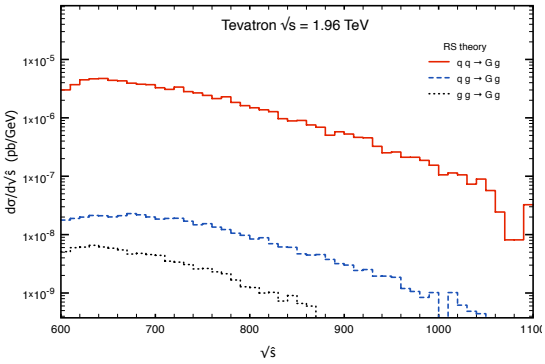

Figure 5.10: The differential cross section as a function of the partonic center-of-mass energy $\sqrt{\hat{s}}$ for the process $p\bar{p} \to Gg$ considering the RS theory at the Tevatron. This plot demonstrates separately each sub-process contribution. The analysis is performed with $m_G = 1$ TeV, $\Lambda = 3$ TeV and the cuts: $p_T^{\text{jet}} > 150$ GeV and $|\eta^{\text{jet}}| < 1$.

NLO/LO calculation:

- Process: $pp \to G + 1$-jet (+ 1 jet for NLO).
- Scales: $\mu_F = \mu_R = p_T^G$
- PDF: CTEQ6L1/CTEQ6M

In Chapter 4 we have seen that depending on the collider, different processes can have different differential luminosity contributions. From Fig. 4.2 it is possible to realize that at the LHC the sub-process that contribute the most for graviton emission is $gg \to Gg$. At Tevatron this is not true. From Fig. 5.10 we can see that the most contributing sub-process is $q\bar{q} \to Gg$, which carries a large Bjorken $|x|$ (equal or larger than 0.5). For large values of $|x|$, the valence quarks, which are dominating, become smaller at NLO. This results in a NLO PDF different from the LO PDF. Notice that in our calculation, we have employed NLO PDF for NLO calculation, and LO PDF for LO calculation. If we also take into account the difference in α_S used to compute NLO and LO cross sections, it will be reasonable to obtain a smaller value for the NLO cross section. This is the cause for such small values obtained for the K-factor at Tevatron.

Now, let us concentrate on the N-factors for the Tevatron samples. Notice they are of order 2 for a heavy graviton, due to the factorization and renormalization scales chosen for the NLO/LO and matching calculation. For light graviton production, no

	$\sigma(\mu_F = \mu_R = p_T^G)$	$\sigma(\mu_F = \mu_R = m_T^G)$	Ratio
LHC	0.957 pb	0.803 pb	1.19
Tevatron	0.203 fb	0.087 fb	2.33

Table 5.7: Results for the integrated cross section obtained from the LO process $pp \to Gg$ within the RS theory for $m_G = 1$ TeV and $\Lambda = 3$ TeV. At the LHC it has been employed $p_T^{\rm jet} > 500$ GeV, and $|\eta^{\rm jet}| < 5$ cuts and at Tevatron $p_T^{\rm jet} > 150$ GeV, and $|\eta^{\rm jet}| < 1$. The PDF is set to CTEQ6L1.

difference at the cross section level is expected because the scales chosen for k_T-MLM matching and NLO/LO are similar, *i.e.* $\left(p_T^G\right)^2 \simeq (m_T^G)^2 = (p_T)_G^2 + m_G^2$. However, for heavy graviton $\left(p_T^G\right)^2 < (m_T^2)^2$.

This can be easily observed if we perform a brief validation check in which we compute values for the LO cross section of the process $pp \to Gg$ within the RS theory. The idea is to employ these two different scales in the calculation both at the LHC and Tevatron, and compare results obtained. The cuts applied within the analysis are the following:

$$\begin{array}{lllll} \text{LHC} & p_T^{\rm jet} > 500 \text{ GeV}, & |\eta^{\rm jet}| < 5, & \text{CTEQ6L1}. \\ \text{Tevatron} & p_T^{\rm jet} > 150 \text{ GeV}, & |\eta^{\rm jet}| < 1, & \text{CTEQ6L1}. \end{array} \tag{5.16}$$

Table 5.7 presents the outcome. At the LHC we have a factor of approximately 1.2 for the ratio $\sigma(p_T^G)/\sigma(m_T^G)$. At Tevatron this ratio is much higher: 2.3. Notice that the ratio between both scales can be interpreted as N-factor/K-factor ratio of our real analysis.

From both Tables 5.5 and 5.6 we obtain N-factor/K-factor ~ 1.2 for the LHC, and a larger ratio of approximately 2.5 at the Tevatron for the heavy graviton cases. These results demonstrate the reason why we obtain different values for the K-factor and N-factor for the current semi-inclusive analysis. They also demonstrate the consistency of our results.

Distributions of relevant observables

Figs. 5.11 to 5.16 exhibit the differential distributions for the comparison between NLO-QCD calculation and matrix element-parton shower matching.

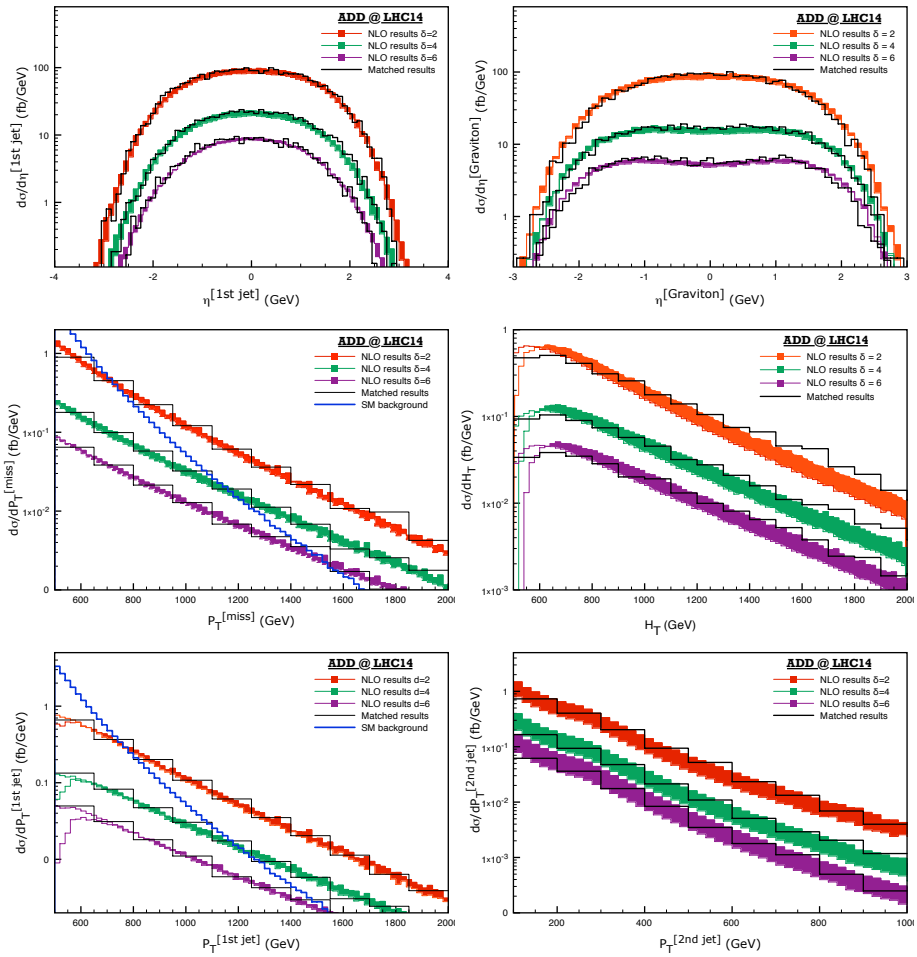

Figure 5.11: NLO/matching comparison for the ADD model at the LHC ($\sqrt{s} = 14$ TeV) with $\Lambda = 5$ TeV. The NLO results are given by the red, green and purple bands for $\delta = 2, 4, 6$, respectively. Matched results are given by the black curves in which we employ the same parameters as the for the NLO. The dominant $Z \rightarrow \nu\bar{\nu}$ background is also shown as a reference by the blue curve. The k_T-MLM matched curves are normalized by the NLO results, and the normalization factors can be found in Table 5.5. Figure extracted from [114].

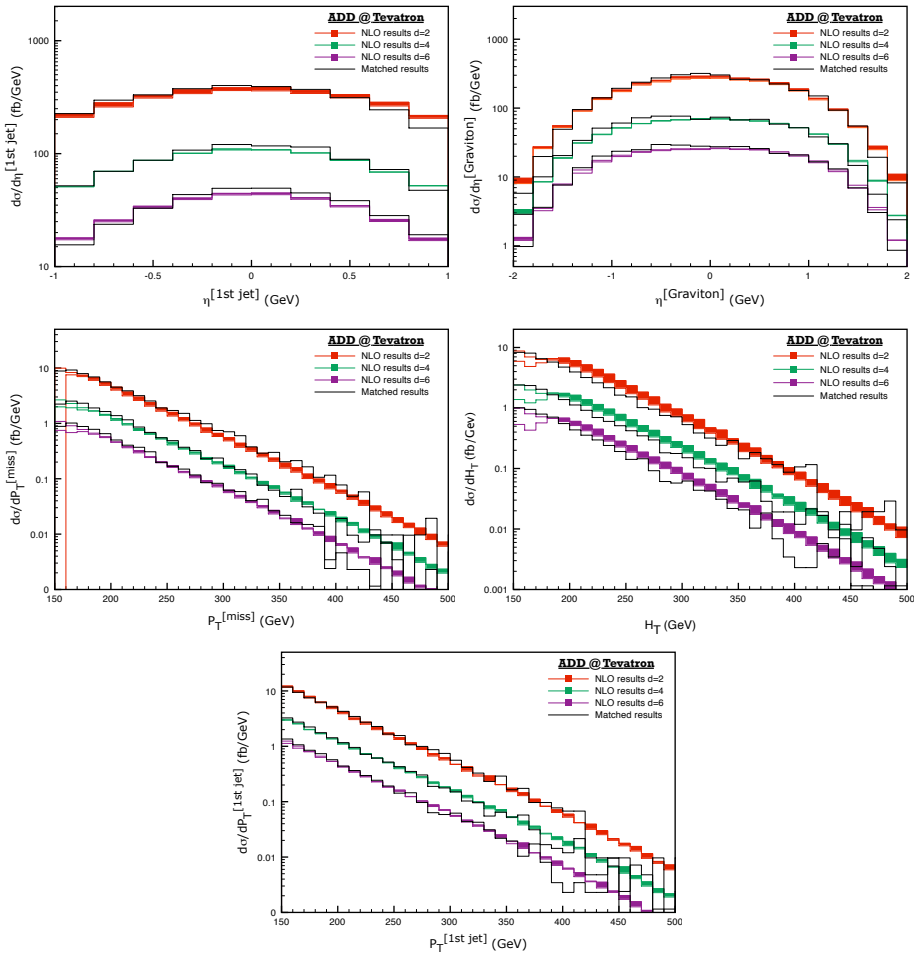

Figure 5.12: NLO/matching comparison for the ADD model at the Tevatron ($\sqrt{s} = 1.96$ TeV) with $\Lambda = 1$ TeV for $\delta = 2, 4, 6$. The matched curve is normalized by the NLO results and the normalization factors can be found in Table 5.6. Figure extracted from [114].

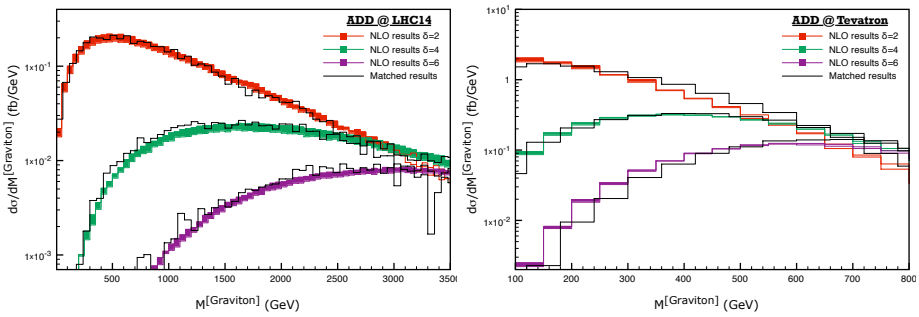

Figure 5.13: Graviton mass distribution at the LHC (left) and Tevatron (right) for the ADD model with $\delta = 2, 4, 6$, respectively. The NLO results are shown by the red, green and purple bands, and the matched ones are shown by the black curves. Figure extracted from [114].

We start with a discussion of the results of the ADD theory. From Fig. 5.11, one can immediately see that the shapes obtained with NLO and k_T-MLM matching agree quite well for the pseudo-rapidity of the leading jet and the graviton and for the transverse missing p_T. For the p_T distributions of the first jet, the agreement is satisfactory for large $p_T \gtrsim 800$ GeV region, while for $p_T \sim 500$ GeV, NLO curves quickly decrease and become unreliable. That is due to the cut on the minimum $\not{p}_T$, which leads to inconsistency on p_T^{1stjet} lower bound at LO and NLO calculations, while the matching technique gives reliable results. The same argument also applies for H_T distributions when $H_T \sim 500$ GeV. However, at large $H_T \gtrsim 1500$ GeV, the k_T-MLM matching tends to give harder distributions, because the contributions from the matrix elements of $G + 3$ partons are also included, while this is not true for NLO.

Fig. 5.12 presents similar results for the Tevatron. Because the energy scale of the Tevatron is much smaller, the agreement is in general much better.The reason is that the contribution from more hard jet emission included with matching does not play an important role for such low center-of-mass energy.

Finally, recall that the infinite sum of KK gravitons in the ADD model has been considered as an extra integral over the mass states. The mass of the experimentally expected graviton would therefore be given by a distribution instead of one specific value. In Fig. 5.13 we show the results for the graviton mass distribution. If the mass of the graviton would be an observable, one could easily constrain the number of extra dimensions using these distributions. That is because the average for the graviton mass depends on the number of extra dimensions. The larger it is the mass, more extra dimensions are predicted.

Fig. 5.14 presents results for the MGM model at the LHC. Similar distributions for the Tevatron are out of reach for $\overline{M}(\mu_\star) = 1,\ 2$ TeV (and excluded for smaller values), therefore the corresponding results are not shown. We apply here the running of the Planck mass cut: $\mathrm{H}_T^{\mathrm{min}} > \overline{M}(\mu_\star)$. One can see a turning point in the distributions of the leading or second jet p_T and transverse missing p_T due the cut. The NLO and matched results agree quite well on shapes for distributions of pseudo-rapidity of the leading jet and graviton, transverse missing p_T and H_T of the jets. For the second jet p_T distribution, k_T-MLM matching gives a considerably different shape when compared to the NLO calculation, especially for $\overline{M}(\mu_\star) = 2$ TeV case. For the leading jet distribution, the NLO and matched results for the LHC agree well for large $p_T \gtrsim \overline{M}(\mu_\star)/2$, while for $p_T \lesssim \overline{M}(\mu_\star)/2$, the NLO curves are unreliable, again due to the inconsistency on p_T^{1stjet} lower bound at LO and NLO calculations.

Finally, Figs. 5.15 and 5.16 present results for the RS model at the LHC and Tevatron. This analysis aims at a fare comparison between all classes of models. In reality, RS graviton is expected to decay and graviton distributions would have to be re-drawn as a functions of its decay products. However, theoretically, distributions of the graviton should be similar to the ones obtained by the system formed by its decay products. Therefore, we can use all distributions (displayed in Figs. 5.15 and 5.16) in a comparative analysis against ADD and MGM theories.

Here, the agreement between the NLO and matched results is again much better at the Tevatron than the LHC for the same reasons pointed for the ADD theory. Also, k_T-MLM matching tends to give harder H_T distributions especially for large $H_T \gtrsim 1500$ GeV due to the fact one extra jet is considered for matching when compared to NLO calculation.

To conclude, allow us to perform one final analysis. In multi-jet final states, observables exist that can be subject to large NLO QCD corrections at TeV scales [131]. The H_T or the P_T of the leading jet distributions are examples of such observables. They are sensitive to the opening of new channels with new kinematic topologies at NLO, which are enhanced by parton distribution effects or by special kinematic configurations (leading to large logarithm terms). One could imagine that higher order corrections would be dominant and for this reason not trust the perturbative series. In fact, one can easily show that this is not the case for more inclusive quantities. This behaviour is due to the choice of the specific observable. In any case, the effects in some specific region of the phase space can be large and need to be accounted for. Here, we show that samples with multiple jets in the final-state with k_T-MLM matching provide a reliable description also of this kind of effects.

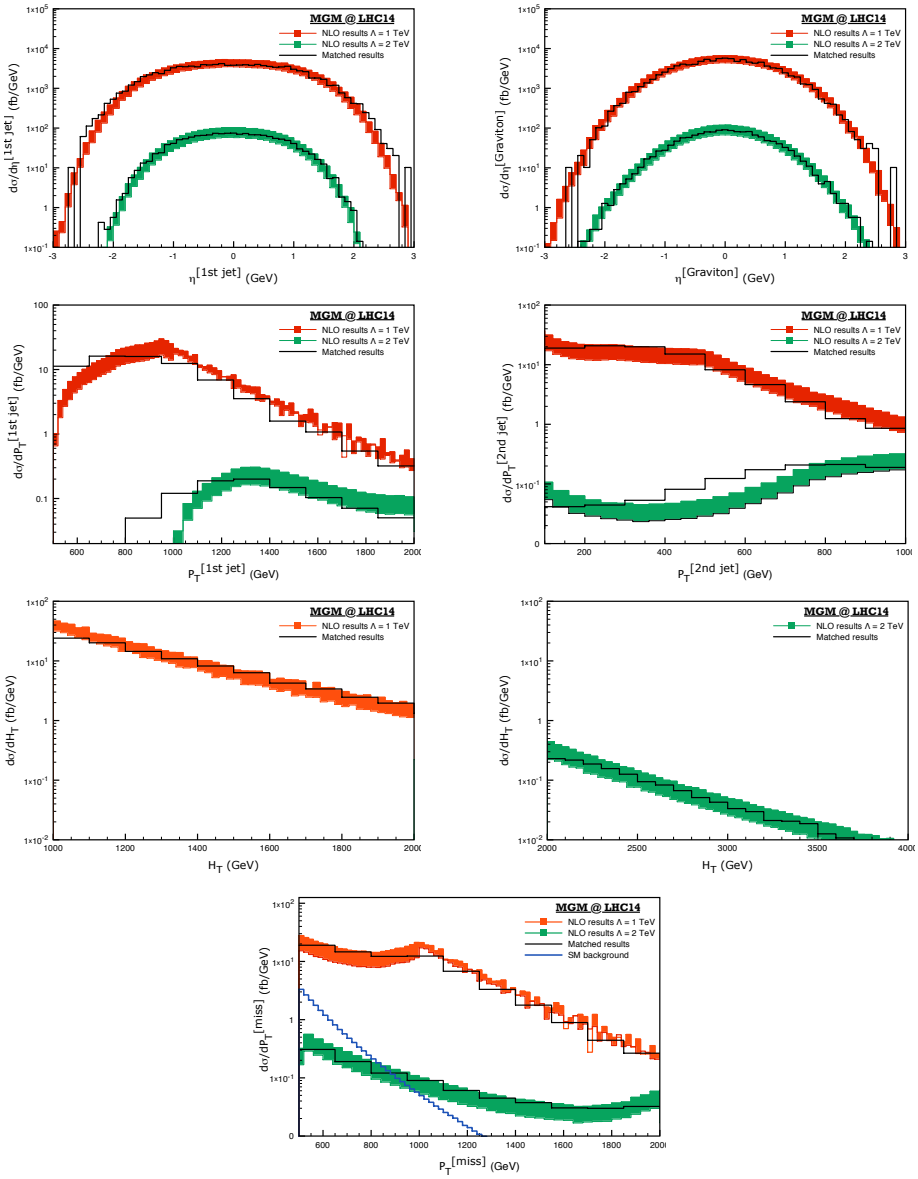

Figure 5.14: NLO/matching comparison for the MGM model at the LHC. The NLO results are given by the red and green bands for $\overline{M}(\mu_\star) = 1, 2$ TeV, respectively. The matched results are given by the black curves with the same parameters as for the NLO ones. The dominant $Z \to \nu\bar{\nu}$ background is also shown as a reference by the blue curve on the $\not{p}_t$ distribution. The k_T-MLM matched curves are normalized by the NLO results, and the normalization factors can be found in Table 5.5. Figure extracted from [114].

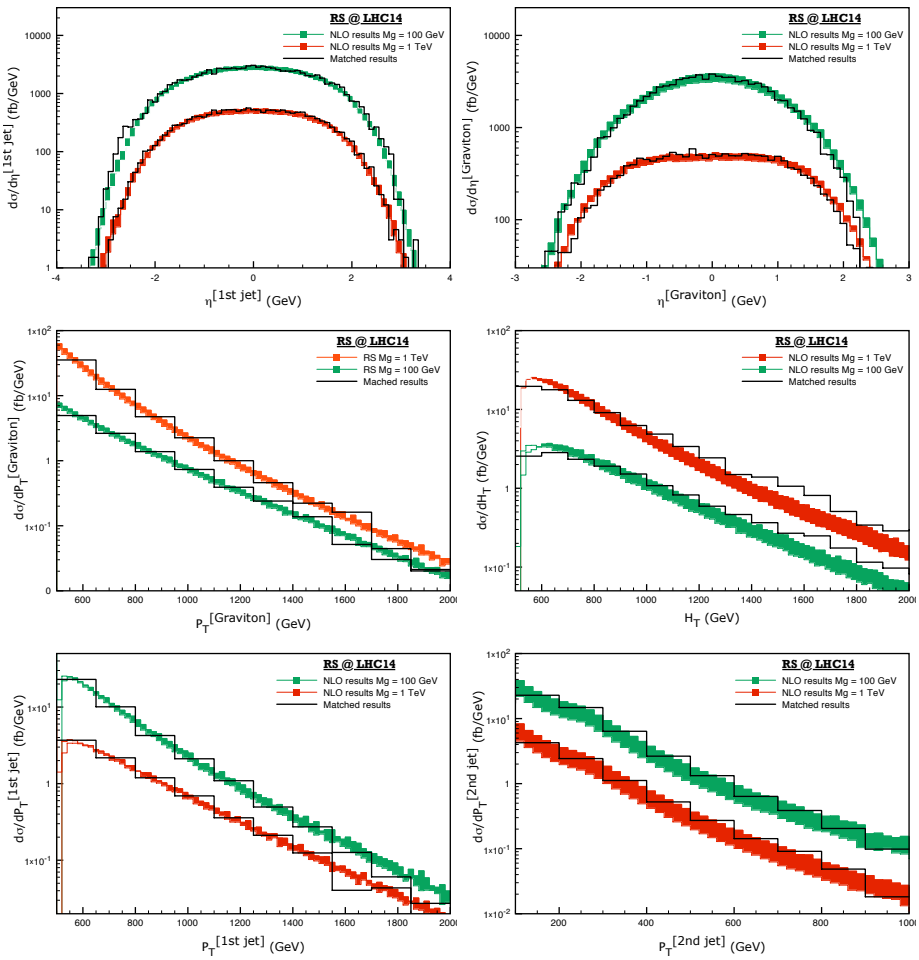

Figure 5.15: NLO/matching comparison for the RS model at the LHC with $\Lambda = 3$ TeV. The NLO results are given by the red and green bands for $m_G = 1$ TeV and 100 GeV respectively. The matched results are given by the black curves with the same parameters as for the NLO ones. Matched curves are normalized by the NLO results, and the normalization factors can be found in Table 5.5. Figure extracted from [114].

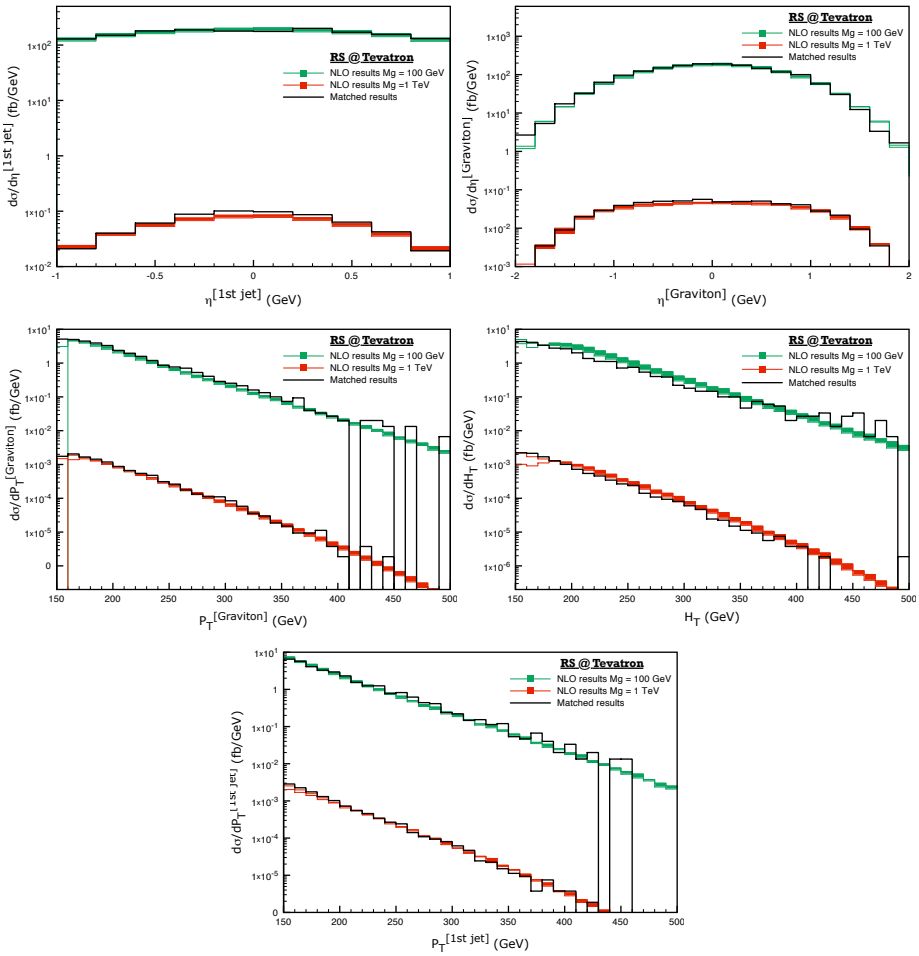

Figure 5.16: NLO/matching comparison for the RS Model at the Tevatron with $\Lambda = 3$ TeV, for $m_G = 100$ TeV and 1 TeV, respectively. The matched curve is normalized by the NLO results and the normalization factors can be found in Table 5.5. Figure extracted from [114].

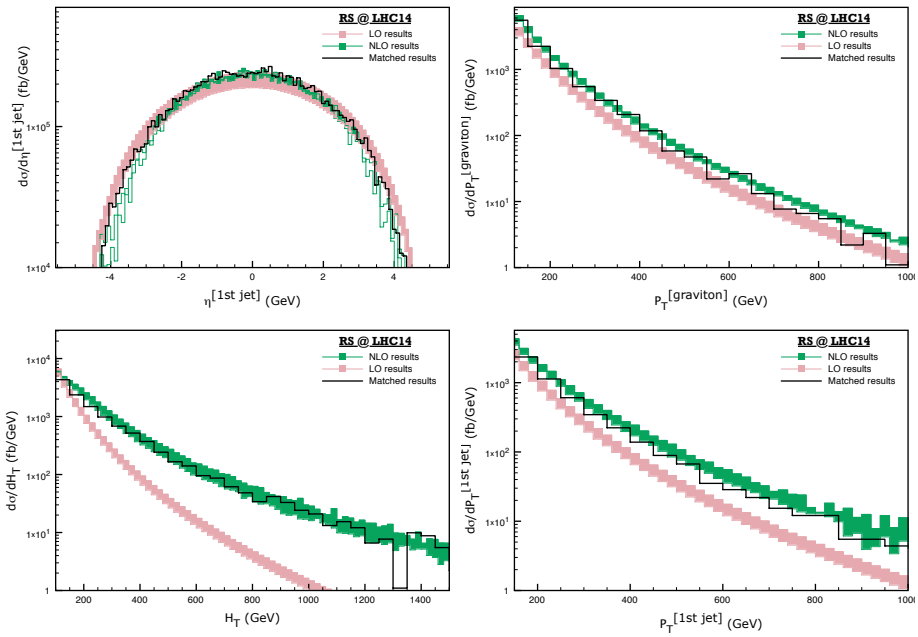

Figure 5.17: NLO/matching comparison for the RS Model at the LHC with $m_G = 100$ GeV and $\Lambda = 3$ TeV with jet cuts $|\eta_{\rm jet}| < 4.5$ and $p_T^{\rm jet} > 50$ GeV, and graviton cut $p_T^G > 50$ GeV. Here we show the appearance of very large K-factors explicitly observed in some observables such as the $p_T^{\rm 1st jet}$ and H_T distributions. Figure extracted from [114].

In Fig. 5.17 we display some illustrative plots. For simplicity, we consider the RS model at the LHC with $\Lambda = 3$ TeV and $m_G = 100$ GeV, with jet cuts $|\eta_{\rm jet}| < 4.5$ and $p_T^{\rm jet} > 50$ GeV, and graviton cut $p_T^G > 50$ GeV. Comparing the LO and NLO curves, it is possible to notice the appearance of very large K-factors, especially at large p_T^G, leading jet p_T and H_T. As a result, we can see that the matched samples describe extremely well the NLO shapes.

Let us now summarize the main aspects and findings within the current study. We have presented a detailed comparison between predictions from NLO QCD calculations and the tree level matrix-element matching with parton showers in the context of three representative theories featuring a graviton: ADD, RS and MGM. This study validates and motivates the use of a fully automatized event generator such as MADGRAPH/MADEVENT including spin-2 particles and multi-parton jet matching for LHC simulations.

In ADD and MGM theories, the graviton appears as missing energy while in RS model it may be observed through its decay products. The fully inclusive samples have been normalized to the corresponding NLO inclusive total cross sections for producing $G + X$, which has been presented in details. Subsequently, key distributions for the most relevant observables involving one or more jets have been compared to those obtained by the NLO calculation $G+\mathrm{jet}+X$. We have observed a complete agreement in shape, as well as in normalization, between the distributions obtained with NLO and k_T-MLM matching calculations at the LHC. At Tevatron, values obtained for the normalization factors are very different from K-factors. This could be explained by the distinct PDFs used for NLO and MLM-matching calculations in addition to the scale definitions employed for each analysis. Finally, we note that observables which are sensitive to the number of jets, such as the H_T are better described by the matched sample than a fixed-order calculation.

Chapter 6

Gravitino production at the LHC

In Chapter 2 we have presented several reasons to expect new physics at the TeV scale. One of these is the *hierarchy problem*, explained in Section 2.4.1. Supersymmetric theories can naturally solve such issue, and at the same time, shed some light on different SM shortcomings, providing for example candidates suitable for being a dark matter particle.

We start with a simple description of how quadratic divergences arise in the SM, and the possible solution for the hierarchy problem provided by Supersymmetric theories. We subsequently characterize such theories and describe some of its main branches. Finally, phenomenological analyses for the production of specific super-particles are exhibited.

6.1 Supersymmetry and the hierarchy problem

In the SM, quadratic divergences emerge when corrections to the Higgs propagator are calculated. More precisely, in Section 2.4.1 we have demonstrated such calculation for a toy-model containing one fermion and one scalar particle. Recall that the correction of the mass of a scalar particle from fermionic loops is given by Eq. (2.32). For a theory with N_f identical fermions, we have:

$$\delta m_s^2 = -\frac{\lambda_f^2 N_f}{8\pi}\left[\Lambda^2 - 6m_f^2 \log\frac{\Lambda}{m_f} + 2m_f^2 + ...\right] + \mathcal{O}\left(1/\Lambda^2\right), \tag{6.1}$$

where δm_s^2 is the correction for the mass of the scalar particle. In the SM, the Higgs receives such corrections from fermionic particles in the loop. Notice that these corrections are quadratically divergent, causing the hierarchy problem.

One could think, however, that new and not-yet-observed particles exist, and must be taken into account when corrections to the Higgs mass are computed.

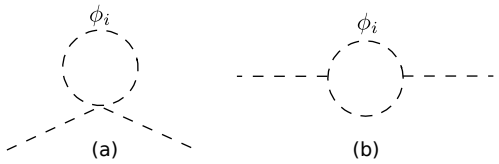

Figure 6.1: Illustration of loop corrections from new scalars on the calculation of the Higgs propagator.

Assume a SM-like theory, where fermions are coupled to the scalar field ϕ:

$$\mathcal{L}_f = -\lambda_f \bar{\psi}\psi\phi \tag{6.2}$$

The symmetry is broken and we take $\phi = (v+h)/\sqrt{2}$, being h the Higgs boson. Suppose for instance that a number N_s of new scalar fields ϕ_i exist, where $i = 1,\ 2, ..., n$. They couple to the Higgs field following the lagrangian [132, 133, 134, 30]:

$$\mathcal{L} = \sum_i^n\ |\partial_\mu \phi_i|^2 - m_{\phi_i}^2 |\phi_i|^2 - \lambda_s |h|^2 |\phi_i|^2 - 2v\lambda_s h |\phi_i|^2. \tag{6.3}$$

Notice that for simplicity, the coupling λ_s is the same for new scalar fields.

When computing corrections to the Higgs from the loops of new particles, as illustrated on Fig. 6.1, again divergences are encountered. Contributions from the quartic coupling, which are exhibited in Fig. 6.1 (a), are:

$$\left[\delta m_h^2\right]_{(a)} = -\frac{\lambda_s N_s}{16\pi^2}\left[\Lambda^2 - \sum_i 2\, m_{\phi_i}^2 \log\left(\frac{\Lambda}{m_{\phi_i}}\right)\right] + \mathcal{O}\left({}^{1}\!/_{\Lambda^2}\right). \tag{6.4}$$

Combining Eqs. (6.1) and (6.4) we already observe that if we chose $N_f = 2N_s$ and $-\lambda_s = \lambda_f^2$, the quadratic term in Λ cancels. The sign difference between corrections computed from the fermionic and scalar fields on the loop enable such cancellation.

Contributions from the diagram displayed in Fig. 6.1 (b), can be written as

$$\left[\delta m_h^2\right]_{(b)} = -\frac{\lambda_s^2 v^2 N_s}{16\pi^2}\left[-1 + \sum_i 2\, \log\left(\frac{\Lambda}{m_{\phi_i}}\right)\right] + \mathcal{O}\left({}^{1}\!/_{\Lambda^2}\right). \tag{6.5}$$

Combining all contributions, we observe a complete cancellation of the divergences if we appropriately choose the coupling constants and the masses for the new scalars

and SM fermions to be the same:

$$\delta m_h^2 = \frac{\lambda_f^2 N_f}{4\pi^2}\left[(m_f^2 - m_s^2)\log\left(\frac{\Lambda}{m_s}\right) + 3\,m_f^2\log\left(\frac{m_s}{m_f}\right)\right] + \mathcal{O}\left(1/\Lambda^2\right), \quad (6.6)$$

where we have assumed $N_f = 2N_s$, $\lambda_f^2 = -\lambda_s$ and $m_{\phi_i} = m_s$. Therefore, if we have a theory with two scalar particles associated with each fermion existing in the SM, no divergences are encountered. In other words, the problem of quadratic divergences of the SM is solved if the theory becomes *Supersymmetric*.

In a Supersymmetric theory, new scalar fields are associated with SM fermionic fields, and new fermionic fields are associated with the existing (SM) bosonic fields. In the next section we present an introduction to the Minimal Supersymmetric Standard Model (MSSM) and specify the particle spectrum of the theory. Here, we have briefly demonstrated how the addition of new particles could generate the cancellation of divergences that appear on the calculation of corrections for the mass of the Higgs boson.

6.2 A brief introduction to the MSSM

Supersymmetry, or SUSY for short, is a symmetry that transforms bosonic states into fermionic states and vice-versa. It is therefore an operator Q which performs the transformations:

$$Q\,|Boson\rangle = |Fermion\rangle\,, \quad Q\,|Fermion\rangle = |Boson\rangle\,. \quad (6.7)$$

The operator Q must be an anti-commuting spinor. For generating a consistent SUSY theory with chiral fields (necessary due to the existence of SM fermions), Q and its hermitian conjugate $Q^\dagger$ must satisfy the following algebra [135]:

$$\{Q, Q^\dagger\} \propto P^\mu; \quad \{Q, Q\} = \{Q^\dagger, Q^\dagger\} = 0; \quad [P^\mu, Q] = [P^\mu, Q^\dagger] = 0. \quad (6.8)$$

P^μ is the four-momentum generator of space-time translations.

In the SM, we identify elementary particles with irreducible representations of the Poincare group. The irreducible representations of the SUSY algebra are not particles, but *supermultiplets* that contain both the SM corresponding fields and its *superpartners*. Therefore, field members of the same supermultiplet should have equal masses and be in the same representation of the gauge group.

Superfield	SU(3)	SU(2)	U(1)	Particle content	
				SM-like	super-partner
$\hat{Q}$	3	2	$\frac{1}{3}$	$\begin{pmatrix} u_L \\ d_L \end{pmatrix}$	$\begin{pmatrix} \tilde{u}_L \\ \tilde{d}_L \end{pmatrix}$
$\hat{U}$	$\bar{3}$	1	$-\frac{4}{3}$	$\bar{u}_R$	$\tilde{u}_R^*$
$\hat{D}$	$\bar{3}$	1	$\frac{2}{3}$	$\bar{d}_R$	$\tilde{d}_R^*$
$\hat{L}$	1	2	-1	$\begin{pmatrix} \nu_L \\ e_L \end{pmatrix}$	$\begin{pmatrix} \tilde{\nu}_L \\ \tilde{e}_L \end{pmatrix}$
$\hat{E}$	1	1	2	$\bar{e}_R$	$\tilde{d}_R^*$
$\hat{G}^a$	8	1	0	g^a	$\tilde{g}^a$
$\hat{W}^i$	1	3	0	W^i	$\tilde{w}^i$
$\hat{B}$	1	1	0	B	$\tilde{b}$
$\hat{H}_u$	1	2	$+1$	$\begin{pmatrix} H_u^+ \\ H_u^0 \end{pmatrix}$	$\begin{pmatrix} \tilde{H}_u^+ \\ \tilde{H}_u^0 \end{pmatrix}$
$\hat{H}_d$	1	2	-1	$\begin{pmatrix} H_d^0 \\ H_d^- \end{pmatrix}$	$\begin{pmatrix} \tilde{H}_d^0 \\ \tilde{H}_d^- \end{pmatrix}$

Table 6.1: The particle content of a minimal supersymmetric theory. In the first block, we present the chiral supermultiplets of the MSSM. Super-partner of the SM fermions are named sfermions (*i.e.*, sup, sdown, selectron, etc). The first generation of SM fermions are shown, while the existence of the second and third generations are implicit. In the second block, we present vector multiplets with their particle content: the SM gauge bosons and their corresponding super-partners name gluino, wino and bino. Finally, in the third block the Higgs content of MSSM is exhibited.

6.2.1 Particle content of the MSSM

The Minimal Supersymmetric Standard Model, or MSSM, retains this name because it respects the same gauge symmetries of the SM: $SU(3) \times SU(2) \times U(1)$. The particles necessary to construct such theory are the same as these of the SM, in addition to their super-partners.

A summary of the supermultiplets with symmetries explicitly displayed and their corresponding particle content is exhibited on Table 6.1. Chiral supermultiplets are only specified for the first generation. The existence of the second and third generations is implicit.

As a consequence of the SUSY transformation, SM fermionic particles should have scalar super-partners (both included in the chiral supermultiplet), and SM bosonic particles should have fermionic super-partners (included in the vector supermultiplet). Furthermore, super-partners should have the same mass and quantum numbers as their corresponding SM particle. For example, the super-partner of the electron, the selectron, should have a mass of approximately 0.51 MeV and have the same electric charge as the electron. If it existed, it should have already been detected. Because as of today none of these super-partners have been experimentally observed, if the world is supersymmetric, SUSY must be broken.

In the SM, fermionic masses are generated from yukawa terms as it is exhibited in Eq. (2.28). However, the term $-\lambda_u \bar{Q}_L \tilde{\phi} u_R$ is not allowed in SUSY theories, since the superpotential should only involve superfields with left-handed fermion components and not their conjugates in order to prevent from chiral anomalies[1] [134, 136]. To create such term, which is relevant for the generation of the mass of part of the SM fermions, another Higgs doublet is necessary to be added to the supersymmetric lagrangian. Therefore, the MSSM theory has two Higgs doublets: $\hat{H}_u$ and $\hat{H}_d$. The most general super-potential can be described by [135]:

$$W = \hat{\bar{U}} \mathrm{y}_u \hat{Q} \hat{H}_u - \hat{\bar{D}} \mathrm{y}_d \hat{Q} \hat{H}_d - \hat{\bar{E}} \mathrm{y}_e \hat{L} \hat{H}_d + \mu \hat{H}_u \hat{H}_d, \tag{6.9}$$

where all the gauge and family indices are suppressed. Other gauge invariant terms could be part of the super-potential. However, these would violate lepton and/or baryon number conservation. A new symmetry, R-parity, is therefore imposed in the MSSM:

$$P_R = (-1)^{3(B-L)+2s}, \tag{6.10}$$

where B and L are the baryon and lepton numbers, s is the spin of the particle and P_R is the quantum conserved quantity. Terms in the lagrangian are only allowed if the product of the P_R of all the fields (within the specific term) is $+1$. One can check that this is always true for each term of Eq. (6.9). Notice all the SM particles and the Higgs bosons have $P_R = +1$, while all the super-partners have $P_R = -1$.

The consequences of the introduction of R-parity are several. For instance, since every vertex of the theory necessarily has an even number of super-particles, they will always be produced in pairs. Therefore, the lightest super-particle (LSP) should be stable and is thus a good candidate for dark matter. As one can see, through the

[1] To obtain chiral fermions in SUSY theories, right-handed fermion fields are defined to be the complex-conjugate of the left-handed fermion fields ($\phi_{j\,R} = \phi_L^{j}$). Similarly, their scalar super-partners are defined to be their complex-conjugate (ϕ_j^* and ϕ^j). Since the super-potential only involves ϕ^j, one Higgs doublet will not generate mass for all the particle spectrum related to the SM.

imposition of the R-parity symmetry, the MSSM provides a natural solution for the dark matter problem of the SM.

From Eq. (6.9), it is possible to write the classical scalar potential for the Higgs [135]:

$$\begin{aligned} V = &\left(|\mu|^2 + m_{H_u}^2\right)\left(|H_u^0|^2 + |H_u^+|^2\right) + \left(|\mu|^2 + m_{H_d}^2\right)(|H_d^0|^2 + |H_d^-|^2) + \\ &+ \frac{(g^2 + g'^2)}{8}\left(|H_u^0|^2 + |H_u^+|^2 - |H_d^0|^2 - |H_d^-|^2\right)^2 + \\ &+ \frac{g^2}{2}|H_u^+ H_d^{0*} + H_u^0 H_d^{-*}|^2 + \left[b\left(H_u^+ H_d^- - H_u^0 H_d^0\right) + c.c.\right]. \end{aligned} \tag{6.11}$$

Notice we have two couplings g and g', and the potential should give raise to v_u and v_d, the vev of both $\hat{H}_u$ and $\hat{H}_d$.

One can count the degrees-of-freedom of the theory. Before the symmetry breaking, the theory contains two complex Higgs fields, summing eight degrees-of-freedom. When the symmetry is broken, SM gauge fields absorb three degrees-of-freedom to become massive. Five degrees are left to "new fields" that arise from the Higgs boson: two charged Higgs $H^{\pm}$; a CP-odd neutral Higgs A^0; and two CP-even neutral Higgs h and H.

As a result from the SUSY symmetry breaking, higgsinos and gauginos mix giving rise to: i) four supersymmetric neutral mass eigenstates, the neutralinos; and ii) two charged mass eigenstates, the charginos. A summary of the particle content (mass eigenstates) is presented in Table 6.2.

6.3 Supergravity: the goldstino and the gravitino

6.3.1 Gauge mediated supersymmetry breaking

As of today, there is no dynamical way to break SUSY which is completely adequate. Supersymmetry is usually broken by hand, and several mechanisms exist to enable spontaneous breaking. Here we briefly discuss the so-called *gauge mediated SUSY breaking* (GMSB) scenario.

In these types of models, a small extension to MSSM is necessary. It is assumed that SUSY breaking occurs in a hidden sector, also known as the *secluded sector*. The SM particles and their super-partners are fixed in the *visible sector*. The communication between both sectors are made through the particles contained in the *messenger sector*,

Names	spin	Mass eigenstates
Higgs bosons	0	h^0, H^0, A^0, $H^\pm$
squarks	0	$\tilde{u}_R$, $\tilde{u}_L$, $\tilde{d}_R$, $\tilde{d}_L$
		$\tilde{s}_R$, $\tilde{s}_L$, $\tilde{c}_R$, $\tilde{c}_L$
		$\tilde{t}_1$, $\tilde{t}_2$, $\tilde{b}_1$, $\tilde{b}_2$
sleptons	0	$\tilde{e}_R$, $\tilde{e}_L$, $\tilde{\nu}_e$
		$\tilde{\mu}_R$, $\tilde{\mu}_L$, $\tilde{\nu}_\mu$
		$\tilde{\tau}_1$, $\tilde{\tau}_2$, $\tilde{\nu}_\tau$
neutralinos	$1/2$	$\tilde{\chi}_1^0$, $\tilde{\chi}_2^0$, $\tilde{\chi}_3^0$, $\tilde{\chi}_4^0$
charginos	$1/2$	$\tilde{\chi}_1^\pm$, $\tilde{\chi}_2^\pm$
gluino	$1/2$	$\tilde{g}$

Table 6.2: The particle content (mass eigenstates) of the MSSM [135] explicit for the SUSY and the Higgs sectors. Notice the gauge eigenstates of the third generation of quarks and leptons are different from the mass eigenstate, therefore these are represented with numerical indices.

usually being one singlet field in addition to fields with $SU(3)_L \times SU(2)_L \times U(1)_Y$ quantum numbers. Soft SUSY breaking terms[2] arise from loop interactions involving the messenger particles. This is convenient because it provides an automatic and natural suppression of terms with flavour change neutral currents and CP-violation, which are strongly constrained by experiments.

In the MSSM the supersymmetry breaking is introduced explicitly. Goldstone bosons are thus generated, and are eaten to give mass to bosons. For global SUSY, the broken generator is fermionic, so the Goldstone boson in this case should have spin-1/2 and is usually named *goldstino*.

The goldstino is the eigenstate of the fermion mass matrix in which the eigenvalue is zero. The derivation of the goldstino interacting lagrangian depends on the supercurrent conservation and it is independent from the details of how the supersymmetry breaking is communicated to the visible sector [135, 137, 138]. We shall not discuss more theoretical aspects of the theory, it is enough to know that the appearance of the goldstino is provided by the breaking of a global symmetry. If SUSY is a local symmetry, the *gravitino* will be the field associated to the invariance of such symmetry.

[2] Soft breaking terms are these added to the MSSM lagrangian (in order to enable spontaneous symmetry breaking) that do not create new divergent contributions to the mass of the scalar particles such as the Higgs.

6.3.2 The super-Higgs mechanism

The SUSY theory invariant under local transformations is named *Supergravity* [139, 140, 141, 142]. In this type of theories, the gravitino has spin $3/2$ and is the super-partner of the graviton.

In order to see explicitly how local symmetry necessarily implies gravity, let us consider the lagrangian of a scalar field ϕ and its fermionic super-partner χ [143]:

$$\mathcal{L} = -(\partial^\mu \phi^*)(\partial_\mu \phi) - \frac{1}{2}\overline{\chi}\gamma^\mu \partial_\mu \chi. \tag{6.12}$$

The lagrangian is invariant under global transformations:

$$\begin{aligned} &\phi \rightarrow \phi + \epsilon\chi, \\ &\chi \rightarrow \chi - i\,\sigma^\mu\,\bar{\epsilon}\,\partial_\mu \phi, \end{aligned} \tag{6.13}$$

but is not invariant under local transformations $\epsilon \rightarrow \epsilon(x)$. To maintain the invariance, a field has to be introduced (similarly to what happens in the SM, where gauge fields A_μ are generated from the invariance of a local symmetry). An extra term $\mathcal{L}_K$ must thus be added to the lagrangian:

$$\mathcal{L}_K = \frac{1}{M_{pl}}\, K^\alpha_\mu\, \psi^\mu_\alpha, \tag{6.14}$$

where $K^\alpha_\mu \equiv -\partial_\mu \phi^* \chi^\alpha - i/2\,\chi^\beta (\sigma_\mu \bar{\sigma}^\nu)^\alpha_\beta\, \partial_\nu \phi^*$, and ψ is a Majorana fermion with spin-$3/2$ that transforms like

$$\psi^\mu_\alpha \rightarrow \psi^\mu_\alpha + M_{pl}\, \partial^\mu \epsilon_\alpha. \tag{6.15}$$

The problem is that the sum of both lagrangians $\mathcal{L} + \mathcal{L}_K$ is not yet invariant. It has an extra contribution which is proportional to the energy-momentum tensor. However, this contribution can be cancelled if we add the term $\mathcal{L}_g$:

$$\mathcal{L}_g = -g_{\mu\nu} T^{\mu\nu}. \tag{6.16}$$

The transformation of the tensor field is

$$g_{\mu\nu} \rightarrow g_{\mu\nu} + \frac{1}{M_{pl}} \overline{\psi}_\mu \gamma_\nu \epsilon, \tag{6.17}$$

which demonstrates that any locally SUSY theory must include gravity. For the MSSM, we have shown that chiral supermultiplets contain fermions and their super partners, and vector supermultiplets contain gauge bosons and gauginos. When super-

gravity is considered, the theory also has the gravity supermultiplet, which contains the graviton and the gravitino: $(g_{\mu\nu}, \psi)$.

Before the supersymmetry breaking, the gravitino is massless. To become massive, it absorbs the goldstino and obtain spin $\pm 1/2$ components. This is the corresponding to the Higgs mechanism of the SM, and for this reason is named super-Higgs mechanism. The mass of the gravitino depends on how supersymmetry is broken.

Usually, the mass of the gravitino can be estimated following from dimensional analysis [135]. Let $\langle F \rangle$ be the vev of scalar fields responsible for supersymmetry breaking. We thus expect the mass of the gravitino to be:

$$m_\psi \sim \frac{\langle F \rangle}{\overline{M}_{pl}}, \tag{6.18}$$

since m_ψ must vanish when SUSY is restored, $\langle F \rangle \to 0$.

Heretofore, we have avoided to introduce explicitly the SUSY lagrangian because of its complexity. However, since gravitino interactions will be necessary to subsequent phenomenological analyses, we briefly introduce the interaction lagrangian of the gravitino, and show that the dimensional analysis for the mass of the gravitino is adequate. We further demonstrate how to obtain the Feynman rules related to the gravitino and verify the gravitino/goldstino correspondence. This summary is based on Refs. [143, 144, 145, 146, 98]

Let us start writing the terms in the supergravity lagrangian where the mass term for the gravitino arises. The supergravity lagrangian depends on arbitrary real functions of scalar fields ϕ_i^* and ϕ_j with $i, j = 1, ..., n$. It is called the Kähler function:

$$G(\phi^*, \chi) = K(\phi^*, \chi) + \ln |W(\phi)|^2, \tag{6.19}$$

where K is the Kähler potential and W is the super-potential[3]. The part of the lagrangian that include terms for the gravitino is given by:

$$\frac{1}{\sqrt{-g}}\,\mathcal{L} = \frac{i}{2} e^{G/2} \bar{\psi}_\mu \bar{\sigma}^{\mu\nu} \psi_\nu + \frac{i}{\sqrt{2}} e^{G/2} G_i \bar{\psi}_\mu \gamma^\mu \chi^i - \frac{1}{2} e^{G/2} (G_{ij} + G_i G_j) \bar{\chi}^i \chi^j \tag{6.20}$$

where

$$G_i \equiv \frac{\partial G}{\partial \phi_i}, \quad G_{ij} \equiv \frac{\partial^2 G}{\partial \phi_i \partial \phi_j}, \quad \text{and} \quad g = det(g_{\mu\nu}). \tag{6.21}$$

[3] See Ref. [142] for more details.

The $\overline{M}_{pl}$ is momentarily set to 1 to simplify the format of Eq. (6.20). The second term specifically shows the mix of the gravitino and the goldstino η,

$$\eta = G_i \chi^i. \tag{6.22}$$

We can redefine the fields, where the gravitino is now ψ':

$$\psi' = \psi - \frac{i}{3\sqrt{2}}\gamma_\mu \eta - \frac{\sqrt{2}}{3} e^{G/2} \partial_\mu \eta. \tag{6.23}$$

Eq. (6.20) is thus:

$$\frac{1}{\sqrt{-g}}\,\mathcal{L} = \frac{i}{2} e^{G/2} \bar{\psi}'_\mu \bar{\sigma}^{\mu\nu} \psi'_\nu - \frac{e^{G/2}}{2}\left(G_{ij} + \frac{1}{3} G_i G_j\right) \bar{\chi}^i \chi^j, \tag{6.24}$$

from which we obtain the mass of the gravitino: $e^{G/2}$. Recovering the $\overline{M}_{pl}$ dependency, the mass of the gravitino[4] is:

$$m_\psi = e^{G/2}\overline{M}_{pl} = e^{K/2}\frac{|W|}{\overline{M}_{pl}}. \tag{6.25}$$

One can observe from Eq. (6.24) that the gravitino ψ' absorbs the goldstino η and obtain mass. We can thus conclude that the dimensional analysis giving rise to Eq. (6.18) is adequate. Once auxiliary fields F^i

$$F^i = e^{G/2}\frac{1}{G^{ij*}} G_{j*} \tag{6.26}$$

obtain a vevs, the symmetry is broken, and gravitinos obtain mass.

Now we have seen that spontaneous supersymmetry breaking can occur. We shall not discuss in details the mechanism to generate it, rather, we are interested in how the theory presents (in the visible sector) after symmetry breaking.

6.3.3 The effective theory for light gravitinos

From this moment on, we use the supermultiplets in the four-components notation. We follow the notation presented in Ref. [144]. The four-component spinors can be constructed from two-component spinors. For the gravitino Ψ, gaugino λ and chiral

[4] From now on we drop the *prime* index: $\psi' \to \psi$.

fermions $\chi_{L,R}$ we have:

$$\Psi_\mu^{(M)} = \begin{pmatrix} \psi_\mu \\ \overline{\psi}_\mu \end{pmatrix}, \qquad \overline{\Psi}_\mu^{(M)} = \left(\psi_\mu \;\; \overline{\psi}_\mu\right), \tag{6.27}$$

$$\lambda^{(M)} = \begin{pmatrix} \lambda \\ \overline{\lambda} \end{pmatrix}, \qquad \overline{\lambda}^{(M)} = \left(\lambda \;\; \overline{\lambda}\right), \tag{6.28}$$

$$\chi_R^{(D)} = \begin{pmatrix} \chi \\ 0 \end{pmatrix}, \qquad \overline{\chi}_L^{(D)} = \left(0 \;\; \overline{\chi}\right), \tag{6.29}$$

where $^{(M)}$ stands for Majorana and $^{(D)}$ for Dirac. The fields satisfy either the Majorana or Dirac conditions depending on the given index. From now on we drop the $^{(M)}$ and $^{(D)}$ indices to simplify the notation.

The term in the supergravity lagrangian for the massive free gravitino, considering the mass term given by Eq. (6.25), is given by [144]:

$$\mathcal{L}_\Psi = -\frac{1}{2}\epsilon^{\mu\nu\rho\sigma}\overline{\Psi}_\mu\gamma_5\gamma_\nu\partial_\rho\Psi_\sigma - \frac{m_\Psi}{4}\overline{\Psi}_\mu\left[\gamma^\mu,\gamma^\nu\right]\Psi_\nu. \tag{6.30}$$

The polarization tensor for a gravitino with momentum p, is [147]:

$$\Pi_{\mu\nu}(p) = \sum_\lambda \Psi_\mu^\lambda(p)\overline{\Psi}_\nu^\lambda(p) = \tag{6.31}$$

$$= -\left(\not{p} + m_\Psi\right)\left(g_{\mu\nu} - \frac{p_\mu p_\nu}{m_\Psi^2}\right) - \frac{1}{3}\left(\gamma^\mu + \frac{p_\mu}{m_\Psi}\right)\left(\not{p} - m_\Psi\right)\left(\gamma^\nu + \frac{p_\nu}{m_\Psi}\right),$$

where the sum over the four gravitino helicities ($\lambda = \pm 1/2, \pm 3/2$) is performed.

Because we will be interested on the phenomenology of gravitino production at the LHC, the energy scale of gravitino production will be much larger than the gravitino mass. The polarization tensor can thus be simplified as [147]:

$$\Pi_{\mu\nu}(p) = -\not{p}\, g_{\mu\nu} + \frac{2}{3}\not{p}\frac{p_\mu p_\nu}{m_\Psi^2}, \tag{6.32}$$

where the first term corresponds to the $\lambda = \pm 3/2$ helicity states and the second to $\lambda = \pm 1/2$. We will discuss this equation in details further ahead.

The interaction terms of the gravitino are defined through the supercurrent J_μ by:

$$\mathcal{L} = -\frac{i}{2\overline{M}_{pl}}\Psi_\mu J^\mu + h.c. \tag{6.33}$$

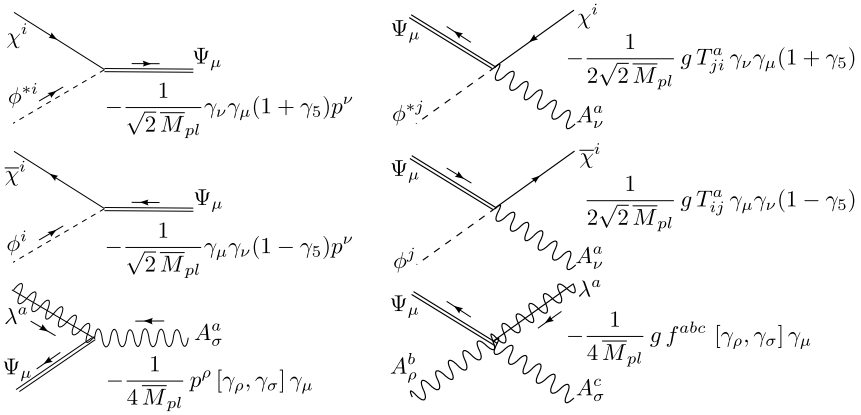

Figure 6.2: Feynman rules for the gravitino interactions.

The supercurrent enables interactions of the gravitino with all the other fields. Although the supergravity lagrangian contains many interaction terms for the gravitino, the only relevant terms[5] for our phenomenological studies will be the following:

$$\mathcal{L} = -\frac{1}{\sqrt{2}\,\overline{M}_{pl}} D_\nu\phi^{*i}\,\overline{\Psi}_\mu\gamma^\nu\gamma^\mu\chi^i_R - \frac{1}{\sqrt{2}\,\overline{M}_{pl}} D_\nu\phi^i\,\overline{\chi}^i_L\gamma^\mu\gamma^\nu\Psi_\mu - \\ -\frac{i}{8\,\overline{M}_{pl}}\overline{\Psi}_\mu\,[\gamma^\nu,\gamma^\sigma]\,\gamma^\mu\lambda^a F^a_{\nu\sigma}. \tag{6.34}$$

where $D_\nu\phi^i = \partial_\nu\phi^i + ig\,A^a_\nu\,T^a_{ij}\,\phi^j$, T_{ij} is the generator of the gauged Lie group, ϕ is the scalar field present in the chiral multiplet, $\chi_{L/R}$ are chiral fermions and λ are gauginos.

The Feynman rules for gravitino interactions arise from the lagrangian (6.34) and are shown in Fig. 6.2. A comprehensive derivation of the lagrangian and Feynman rules related to the gravitino and some discussions can be found for example in Refs. [144, 146, 142, 148].

Gravitinos obtain mass from (absorbing) goldstinos after SUSY breaking. The longitudinal modes of gravitinos arise from the two helicity state components of the goldstinos. As a result, gravitinos will have in total four helicity states. Eq. (6.31) presents the polarization tensor of an external gravitino. For the case where $\sqrt{s} \gg m_\Psi$ Eq. (6.32) shows that the polarization tensor can be explicitly separated in terms of $\lambda = \pm 3/2$ and $\lambda = \pm 1/2$ [147, 144, 146]. From this equation, one can realize that there is

[5] Other terms are irrelevant for the present analysis because we will consider processes at the LHC energy scale, which is much smaller than the scale at which quantum gravity corrections become important (M_{pl}).

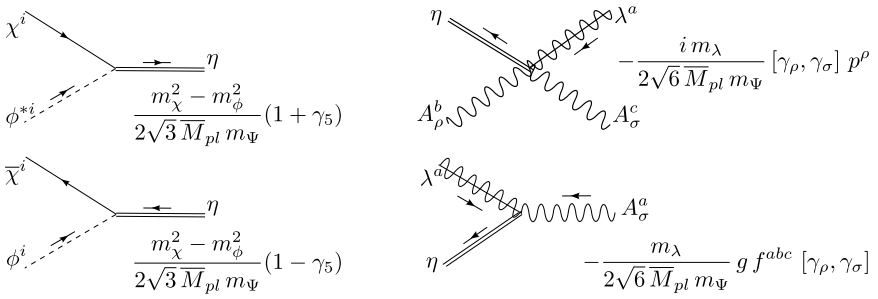

Figure 6.3: Feynman rules for the goldstino interactions.

a correspondence between the gravitino and goldstino lagrangians. The interacting lagrangian of the goldstino with matter can be obtained by the following substitution [149, 150, 145]:

$$\Psi_\mu \to \sqrt{\frac{2}{3}}\frac{1}{m_\Psi}\partial_\mu \eta. \tag{6.35}$$

where η is the spin-1/2 goldstino field. Considering that we are interested in processes with a light external gravitino, it is possible to use the relation $\partial\!\!\!/\eta = 0$. Furthermore, because in supergravity high energy behaviours cancel out the total amplitude of a process (with one external gravitino), the derivatives on ϕ, χ and λ can be replaced by the masses of the corresponding fields [144]. One can thus obtain the final interacting lagrangian of the goldstino:

$$\mathcal{L}_\eta = i\frac{m_\phi^2 - m_\chi^2}{\sqrt{3}\,m_\Psi\,\overline{M}_{pl}}\overline{\eta}\,\chi_R\,\phi^* - i\frac{m_\lambda}{8\sqrt{6}\,m_\Psi\overline{M}_{pl}}\overline{\eta}\,[\gamma^\mu,\gamma^\nu]\,\lambda^a F^a_{\mu\nu} + h.c. \tag{6.36}$$

and derive the Feynman rules, illustrated on Fig. 6.3. When the center-of-mass energy is higher than the mass of the gravitino, the gravitino is mainly composed by $\pm 1/2$ helicity states. Therefore, at the LHC, it is sufficient to consider the Feynman rules of goldstinos.

Our goal is to continue to analyse processes that could be observed at the LHC through the missing energy signature in combination with jets. Several such studies employing SUSY theories have already been extensively performed. However, searches for the gravitino in the final state have not been largely explored due to limitations of simulation tools. A recent implementation of gravitinos and goldstinos in MADGRAPH/MADEVENT [100,98] has changed the situation. In collaboration with the au-

thors we have been able to perform a phenomenological study on gravitino/goldstino[6] production with multiple jets in the final state, which we present in what follows.

6.4 The phenomenology of gravitino emission

We have seen that in the context of supergravity theories, gravitinos are massive fields, super-partner of the graviton. In some variations of such theories, these are super-light particles, however not exactly massless [151, 152].

Similarly to what has been presented in Chapter 5, we are interested in the missing energy signature in combination with jets. The gravitino, being the LSP, is expected to be invisible. In addition, because SUSY particles are always produced in pairs[7], we consider the production of two gravitinos. Therefore, we now focus mainly on the process $p\,p \rightarrow \tilde{G}\,\tilde{G} + n$-partons, where now $\tilde{G}$ represents the gravitino[8]. For simplicity yet being exhaustive, we will consider $n = 3$ as the maximum number of partons.

We consider a simplified model with the Feynman rules explicitly defined in Fig. 6.3. The particle content is reduced, focused for the present study. Only the SM quarks and gluons coupled to the gravitino/goldstino and the gluino will contribute significantly. Cross sections related to graviton production at the LHC are suppressed by the Planck mass. For this reason, graviton production does not contribute for the present study.

However, super-light gravitino production can become relevant, since the cross section is proportional to the inverse of the gravitino mass. From Fig. 6.3, we observe the interaction vertices of the gravitino at the LHC energy scale. Different combinations can be considered to form processes in which the gravitino is one of the products of a proton-proton collision. Here, we concentrate on scenarios where the gluino is the NLSP. Sub-processes that contribute most significantly to our analysis are illustrated in Fig. 6.4. They are summarized as:

- *Gluino-gravitino associated production*:

$$pp \rightarrow \tilde{G}\,\tilde{g} \rightarrow \tilde{G}\,\tilde{G}\,g + \text{extra partons}; \tag{6.37}$$

[6] From this moment on, we will refer to it as the phenomenological study of the production of gravitinos, which we have shown to be the same as the production of goldstinos in the low energy limit.

[7] We consider R-parity conserving theories.

[8] Within the present study we consider processes in which at least one gravitino decays from a gluino, as illustrated in Fig. 6.4.

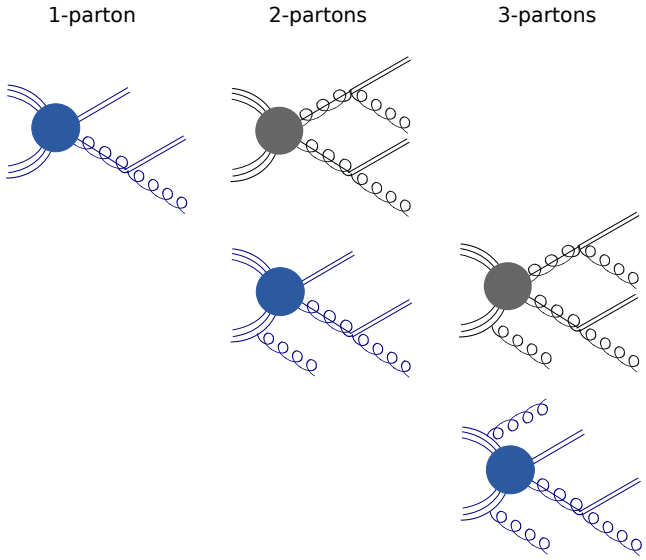

Figure 6.4: Example of processes contributing to $pp \to \tilde{G}\tilde{G}+$ jets. The three-lines initial state represents a proton. The double-straight-line on the final state represents a gravitino. The curly line is a gluon, and the curly-line crossed by a straight line represents the gluino. The filled circle symbolizes that all the processes that can possibly generate such final state are included in the illustration of the diagram. Notice that the diagrams are separated in columns characterized by the number of final state partons. The diagonals represent matched diagrams. The second diagram of the last column is not matched in order for the highest multiplicity to be the same for both processes.

- *Double-gluino resonance*:

$$pp \to \tilde{g}\,\tilde{g} \to \tilde{G}\,g\,\tilde{G}\,g + \text{extra partons}. \tag{6.38}$$

The first sub-process will be often referred hereby as "gluino-gravitino associated production", and the second as "double gluino resonance". In principle, the zero-jet process should also exist, in which two gravitinos are directly produced. However, here we specifically focus on processes with at least one gluino, which decays producing the gravitino.

The decay width of a gluino ($\tilde{g}$) to a gravitino ($\tilde{G}$) and a gluon (g) is given by [98,144]:

$$\Gamma_{\tilde{g}\to\tilde{G}g} = \frac{m_{\tilde{g}}^5}{48\pi\overline{M}_{pl}^2 m_{\tilde{G}}^2}. \tag{6.39}$$

Notice that the decay width depends both of the gravitino and the gluino mass. For a fixed value of the gravitino mass, the decay width rapidly increases with the increase of the the gluino mass.

Let us explore first the cross sections of each sub-process presented above. However, because we consider $Br(\tilde{g} \to \tilde{G}g) = 1$, it is enough to compute the $2 \to 2$ sub-processes that give rise to $pp \to \tilde{G}\tilde{g}$ and $pp \to \tilde{g}\tilde{g}$.

We can now start by estimating the cross section for $pp \to \tilde{g}\tilde{G}$. One has to consider all the three possible initial states: pair of gluons, quark-anti-quark and quark-gluon (anti-quark-gluon). Each vertex including gravitino is inversely proportional to the gravitino mass. The result is thus inversely proportional to the square of the gravitino mass:

$$\sigma(pp \to \tilde{g}\tilde{G}) \propto \frac{1}{m_{\tilde{G}}^2}, \tag{6.40}$$

which has several consequences for our analysis. Eq. (6.40) also depends on the gluino mass. However, each sub-process has a different dependency on $m_{\tilde{g}}$, and for this reason it is not explicitly written. Fig. 6.5 exhibits the cross section dependency on the gluino mass for a fixed value for the gravitino mass. An exact calculation of the amplitudes and cross section for each sub-process can be found for instance in [153].

Similarly, the cross section for producing a pair of gluinos can be calculated. As expected, it does not depend on the mass of the gravitino, since no interacting vertex

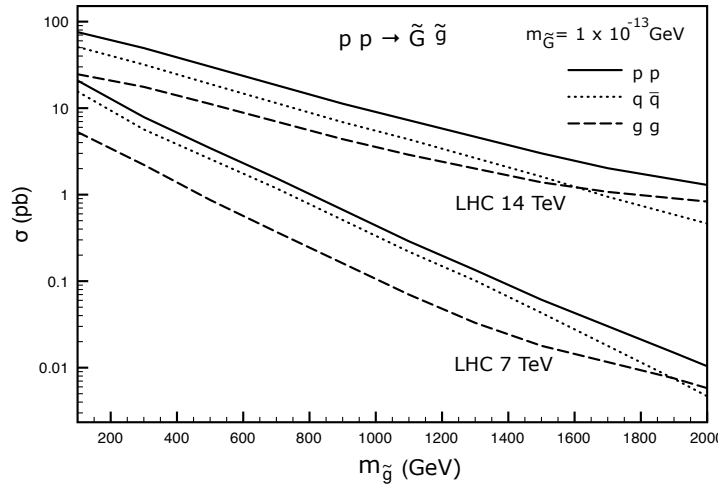

Figure 6.5: Cross section of $pp \to \tilde{g}\tilde{G}$ at the LHC separated for each contributing subprocess. To obtain the curves, we have employed MADGRAPH/MADEVENT with CTEQ6L1 PDF. The mass of the gravitino is fixed at 10^{-13} GeV, the mass of the squarks at 3 TeV and $\mu = \mu_R = \mu_F = (m_{\tilde{G}} + m_{\tilde{g}})/2 \sim m_{\tilde{g}}/2$.

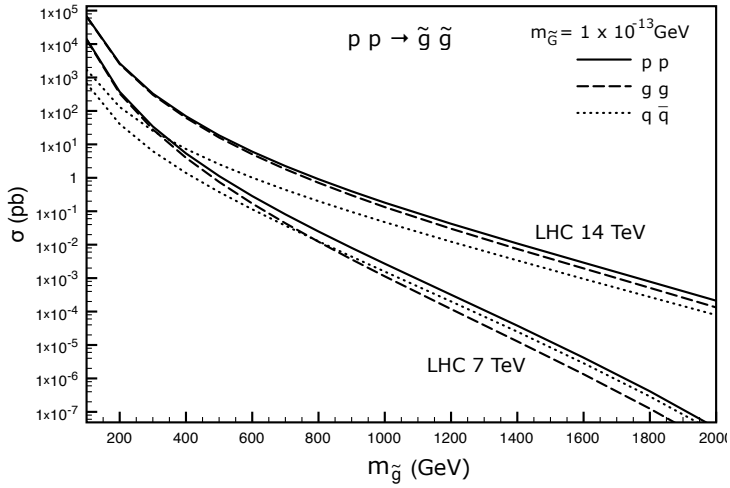

Figure 6.6: Total cross section of $pp \to \tilde{g}\tilde{g}$ separately in $gg \to \tilde{g}\tilde{g}$, $q\bar{q} \to \tilde{g}\tilde{g}$ contributing sub-processes. To obtain the curve we have employed MADGRAPH/MADEVENT with CTEQ6L1 PDF, fixed the mass of squarks at 3 TeV, the mass of the gravitino at 10^{-13} GeV and $\mu = \mu_R = \mu_F = m_{\tilde{g}}$.

with the gravitino exists. Fig. 6.6, illustrates the dependency of the cross section on the gluino mass.

The cross sections of both sub-processes have a particularity. If we fix the gluino mass, the cross section for the double-gluino resonance is determined. However, the cross section for gluino-gravitino associated production process varies depending also of the mass of the gravitino. For analysing processes with two gravitinos and jets in the final state, one has to take into account contributions from both sub-processes. The mass of the gravitino determines therefore which sub-process contribution is dominant.

In principle, it would be necessary to divide the simulation of $pp \rightarrow \tilde{G}\tilde{G} + n$-jets in three stages: simulation of dominant gluino-gravitino production, simulation of dominant double-gluino resonance; and the simulation of equally contributing sub-processes. However, the matching technique automatically accounts for both sub-processes at the same time, independent of the region of the parameter space. This is one substantial advantage of using such technique. There is therefore no need for simulating each sub-process separately, and we can thus treat the whole parameter space at once.

Our aim is therefore to perform a complete analysis on gravitino production in combination with jets, in which we make use of the matching technique presented on previous chapters. We know that apart from normalization issues, the employment of the matching technique can correctly predict the shape of relevant observables and can cover all regions of the parameter space.

6.4.1 Parameter definitions

In the present analysis, the gluino mass is fixed at 800 GeV, value chosen based on recent experimental searches [154]. The gravitino mass is selected according to the three cases below:

$$\text{Case A.} \quad \sigma(pp \rightarrow \tilde{g}\tilde{g}) < \sigma(pp \rightarrow \tilde{G}\tilde{g}) \tag{6.41}$$

$$\text{Case B.} \quad \sigma(pp \rightarrow \tilde{g}\tilde{g}) \approx \sigma(pp \rightarrow \tilde{G}\tilde{g}) \tag{6.42}$$

$$\text{Case C.} \quad \sigma(pp \rightarrow \tilde{g}\tilde{g}) > \sigma(pp \rightarrow \tilde{G}\tilde{g}) \tag{6.43}$$

We observe from Eq. (6.42) that the value for the gravitino mass in "case B" ($m^B_{\tilde{G}}$) is selected as to fix $\sigma(pp \rightarrow \tilde{g}\tilde{G}) \approx \sigma(pp \rightarrow \tilde{g}\tilde{g})$. We define one heavier and one lighter gravitino, as stated by Eqs. (6.41) and (6.43), referred here as "case A" and "case C".

Their masses and cross sections are related to case B as:

$$\begin{aligned} m^A_{\tilde{G}} &= \frac{1}{n}\, m^B_{\tilde{G}}, & \sigma_A(pp \to \tilde{g}\tilde{G}) &\approx \frac{1}{n^2}\, \sigma(pp \to \tilde{g}\tilde{g}), \\ m^C_{\tilde{G}} &= n\, m^B_{\tilde{G}}, & \sigma_C(pp \to \tilde{g}\tilde{G}) &\approx n^2\, \sigma(pp \to \tilde{g}\tilde{g}), \end{aligned} \tag{6.44}$$

For our investigation we take $n = 3$, *i.e.*, $m^A_{\tilde{G}} = 1 \times 10^{-13}$ GeV, $m^B_{\tilde{G}} = 3 \times 10^{-13}$ GeV and $m^C_{\tilde{G}} = 9 \times 10^{-13}$ GeV.

The SUSY model with gravitinos has been implemented in the FeynRules package [155], and we make use of such implementation [156]. It can be used by MADGRAPH/MADEVENT version 5 thanks to the UFO and ALOHA packages [157, 102] which translate the Feynman rules obtained from FeynRules into a universal output that can be used by event generators, such as MADGRAPH/MADEVENT. In particular, we have worked for the development of the ALOHA package, which is detailed in the Appendix C.

The complete analysis is performed for the LHC with $\sqrt{s} = 14$ TeV and we employ the CTEQ6L1 PDF. No cut is used for the generation of events, except for a minimum jet p_T:

$$p_T > 20\,\mathrm{GeV}. \tag{6.45}$$

For the matching technique, we employ the k_T-MLM scheme, use MADGRAPH/MADEVENT version 5 [92] for the matrix element simulation and PYTHIA for parton shower and hadronization. We choose $Q_{match} = 100$ GeV, for jet clustering we use the anti-k_T-algorithm with $R = 0.5$ [158], and impose a cut in the minimum p_T of the jets:

$$p_T > 50\,\mathrm{GeV}. \tag{6.46}$$

6.4.2 Checks and validations

Before displaying the results for a specific analysis, it is crucial to validate the implementation. Since we have two distinct sub-processes contributing separately for the final cross section, such checks are indispensable.

The first check is made as a separate study. First, we consider both sub-processes with one extra jet, *i.e.* $pp \to \tilde{G}\tilde{G}+n$-jets, with $n = 1,\ 2$ jets for gluino-gravitino associated production and $n = 2,\ 3$ jets for double-gluino resonance. We employ the parameters presented above and make use of the matching technique. We plot the distributions for different relevant observables. To check the validity of our implementation, besides

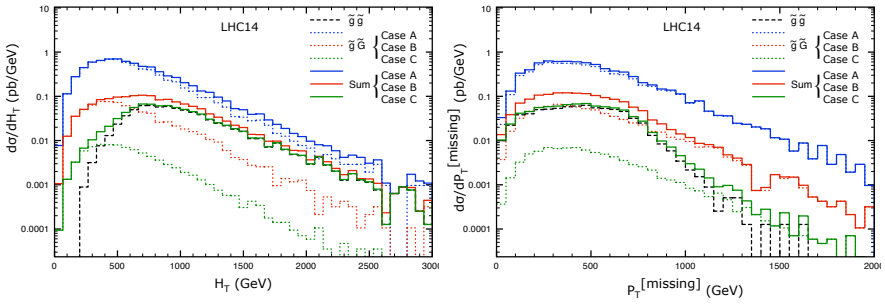

Figure 6.7: Differential cross section as a function of the H_T (left) and $\not{p}_T$ (right). Here we exhibit separately the contributions of both $pp \to \tilde{g}\tilde{g}$ and $pp \to \tilde{G}\tilde{g}$ sub-processes that are included in the evaluation of $pp \to \tilde{G}\tilde{G}j+$ 1 extra jet. The sum of the contributions agree with matched sample. We employ a $p_T^{\rm jet} > 20$ GeV cut, and the results are for the LHC with $\sqrt{s}$=14 TeV.

the total matched simulation, we can separately simulate the contribution of each sub-process: $\sigma_{\tilde{G}\tilde{g}}$ and $\sigma_{\tilde{g}\tilde{g}}$. We can check therefore, that the sum of both contributions agree with the overall matched distribution.

These plots are interesting to demonstrate the contribution of each sub-process for the three sets of parameters chosen. For example, Fig. 6.7 presents the differential cross section as a function of the H_T (left), and of the $\not{p}_T$ (right). We can observe that for case C, the double-gluino resonance dominates, as requested in Eq. (6.43), and the sum of the contributions is very similar to this specific sub-process. For case A the opposite happens: the sum of the contributions is mainly given by the gluino-gravitino production, as Eq. (6.41) show. Finally, for case B, we can check that both contributions are equally relevant.

Different from NLO calculations, the matching technique only considers real-emission contributions. For high-energy collisions processes with initial/final state radiation become most likely and the matching technique can treat correctly these real contributions. However, virtual corrections are not considered, which are needed to cancel the infrared divergences that could arise in the calculation of real QCD-emission corrections. Therefore, with the employment of the matching technique, we can obtain the correct shape for the distributions of the differential cross section, but we cannot predict the K-factors needed to correctly rescale the final cross section:

$$d\sigma(\tilde{G}\tilde{G} + \text{jets}) = K_{\tilde{g}\tilde{g}}\, d\sigma(\tilde{g}\tilde{g} + \text{jets}) + K_{\tilde{g}\tilde{G}}\, d\sigma(\tilde{g}\tilde{G} + \text{jets}). \tag{6.47}$$

We thus assume $K_{\tilde{g}\tilde{g}} \sim K_{\tilde{G}\tilde{g}} \sim 1$ in the following studies.

6.4.3 Results

We now consider $pp \to \tilde{G}\tilde{G} + 1, 2, 3$-jets. The relevant diagrams are illustrated in Fig. 6.4 separately in columns for 1-jet, 2-jets and 3-jets contributions. These diagrams exemplify the main sub-processes existent. Notice that diagrams with no initial-state-radiation (ISR) are illustrated in the first line, with one ISR in the second line and two ISR in the third line. Therefore, diagrams that should be matched are represented in the diagonals.

Because there are two distinct sub-processes relevant for the analysis, PYTHIA cannot automatically correctly set the highest jet multiplicity. The reason is that the leading order contribution for each sub-process has different multiplicity. It is necessary therefore to define the number of additional jets as an input of the analysis. We have set it to be one, which removes the explicit contributions of the second diagram of the last column of Fig. 6.4 that has two radiated jets.

The irreducible background is given by the matched sample of $pp \to \nu\bar{\nu} + n$-jets, where n can be 0, 1, 2 and 3. To simulate the background we have used a cut in the missing E_T,

$$\not{E}_T > 200 \text{ GeV}, \tag{6.48}$$

in order to improve the statistics in the high energy region.

Fig. 6.8 collects the results obtained, in which we display the differential cross section as a function of:

(i) the p_T of the leading jet;

(ii) the p_T of the second highest jet;

(iii) the $\not{p}_T$;

(iv) the H_T.

From Fig. 6.8 (i) and (ii), one can immediately see that the shapes for cases A, B and C are similar, and the curves differ mainly in overall magnitude. However, shapes for the $\not{p}_T$ and H_T distributions are slightly different in the high-energy region. Case A tends to give harder distributions than cases B and C. This is due to the most contributing sub-process of each sample. In case A, the dominant contribution comes from the gluino-gravitino associated production, and in case C from the double-gluino resonance. The $\not{p}_T$ is a combination of the p_T of both gravitinos. In case A, one gravitino

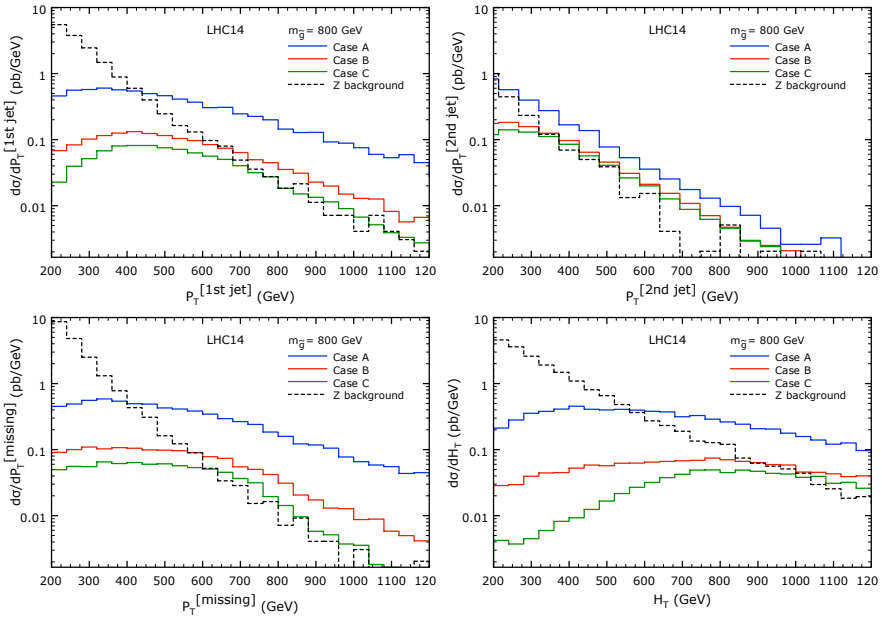

Figure 6.8: Differential cross section as a function of the relevant observables. The signal is $pp \to \tilde{G}\tilde{G} + n$-jets with $n = 1, 2, 3$. The mass of the gluino is 800 GeV, and the mass of the gravitino is 1×10^{-13} GeV in case A, 3×10^{-13} GeV in case B and 9×10^{-13} GeV in case C. The irreducible background, $pp \to \nu\bar{\nu} + n$-jets with $n = 0, 1, 2, 3$, is shown for reference. The simulation is performed using the k_T-MLM matching technique at the LHC with $\sqrt{s} = 14$ TeV and CTEQ6L1 PDF.

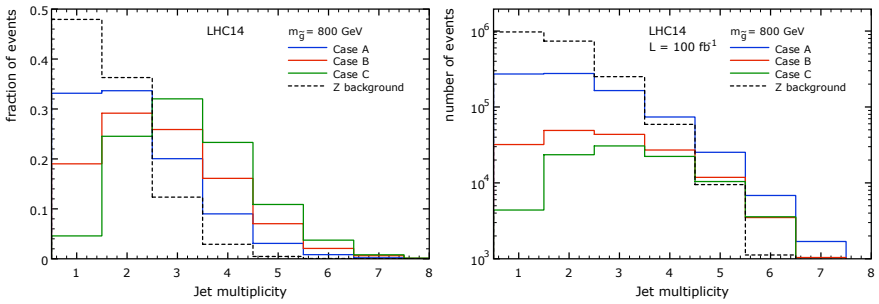

Figure 6.9: In the left, the fraction of events (N_{events}/N_{total}) for different multiplicities in each sample is displayed. In the right, the final number of events expected as a function of the jet multiplicities is shown. The signal is $pp \to \tilde{G}\tilde{G} + n$-jets with $n = 1, 2, 3$. The mass of the gluino is 800 GeV, and the mass of the gravitino is 1×10^{-13} GeV in case A, 3×10^{-13} GeV in case B and 9×10^{-13} GeV in case C. The irreducible background, $pp \to \nu\bar{\nu} + n$-jets with $n = 0, 1, 2, 3$, is shown for reference. The simulation is performed using the k_T-MLM matching technique at the LHC with $\sqrt{s} = 14$ TeV, $L = 100$ fb^{-1} and CTEQ6L1 PDF.

is directly produced and the other comes from the decay of the gluino. In case C, both gravitinos come from the decay of the gluino. A more detailed analysis related to the kinematics is performed further ahead, when we present the correlation between relevant observables.

In Fig. 6.8 we also display the irreducible background curve as reference. The curves for cases A and B lie above the background distribution and could thus indicate signs of new physics at the LHC. However, for case C more complete analyses are necessary.

One indication of new physics and of the dominant sub-process contribution can be given by the jet rates. Case A, gluino-gravitino associated production, has one hard-jet in addition to extra jets coming from QCD radiation. Case C, double-gluino resonance, has two hard-jets and contributions from radiated extra jets. Therefore, it is expected that the number of events with one jet is larger for case A than for case C, being case B intermediate. This is what we observe in the left graph of Fig. 6.9. Moreover, distinct behaviours are noticed for each sample. The background has the shape of decreasing stairs, where most of the events have 1-jet, while signal exposes a peak. The position of the peak varies for the signal samples. Case A has a similar number of events with 1 and 2-jets. The peak is at events with 2-jets for case B, and in case C the maximum is reached for events with 3-jets. If signals of new physics are observed at the LHC, one could therefore use the shape of jet multiplicities to differentiate between theories, and/or to constrain parameters. However, the right plot of Fig. 6.9 exhibits the expected number of events as a function of the jet multiplicities for the

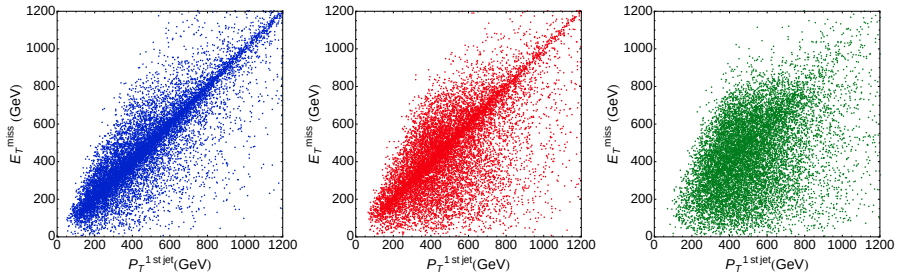

Figure 6.10: Scatter plots for cases A, B and C. These illustrate the correlation between the p_T of the leading jet and the $\not{p}_T$. For case A, in which gravitino-gluino production is dominant, most of the points are distributed following a straight diagonal line. For case C however, where double-gluino resonance is dominant, points are spread into an ellipsoid region around the $\not{p}_T = p_T^{\rm 1stjet}$ diagonal.

present analysis (in which we use $L = 100$ fb^{-1}), showing the difficulty in observing any signal when accounting for the background.

In order to curb the background, we investigate the correlation between observables. One interesting result is exhibited in Fig. 6.10. These are scatter plots with $p_T^{\rm 1stjet}$ and the $\not{p}_T$ distribution in both axes, in which each point represents one event. The three different cases considered are displayed.

For case A, where gluino-gravitino production is dominant, points are concentrated around the main $p_T^{\rm 1stjet} = \not{p}_T$ diagonal. This is expected since for this process, the hard-jet is the gluon decayed from the gluino. Extra jets in events with more than one jet are most likely to have been generated from QCD radiation, which results in jets with a reasonably low p_T. In this case, the gravitino directly produced has a fairly high p_T, larger than that of the gravitino decayed from the gluino. The tendency is therefore to obtain the hard-jet approximately *back-to-back*[9] with the missing energy, which results in events concentrated in the diagonal region as we observe from the left plot of Fig. 6.10.

For case B, we have both sub-processes equally contributing. We can thus observe an intertwine behaviour between cases A and C. Fig. 6.10 shows the evolution of the contributions from gluino-gravitino dominant production to double-gluino resonance, and how it affects the p_T of the particles involved.

For case C, the main contribution comes from the double-gluino resonance, in which we have two hard-jets. Now, the probability is larger for both gluinos to be back-to-back, and the p_T of the leading and the second jets are likely to be of the same order of

[9] Jets are defined to be back-to-back when they have equal momenta but opposite directions.

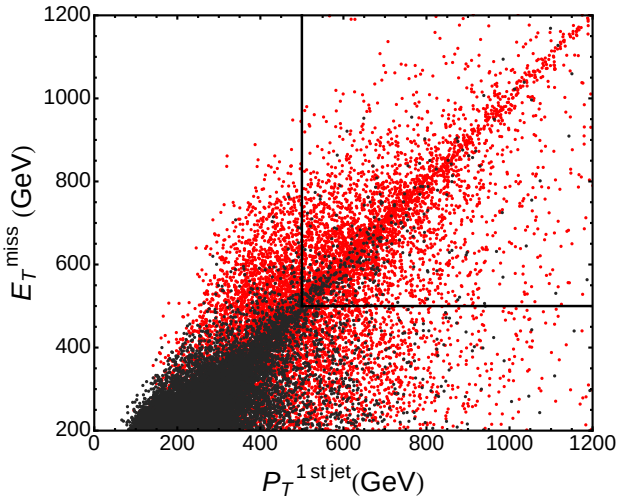

Figure 6.11: Scatter plot of the signal $pp \to \tilde{G}\tilde{G} + 1, 2, 3$-jets (case B), in red, and the background $pp \to \nu\bar{\nu} + 0, 1, 2, 3$-jets, in black. Each point represents one event. Here, we can easily see that the background is concentrated in the small p_T^{1stjet} and $\not{p}_T$ region. To reduce the background we have applied the cuts specified by Eq. (6.49), *i.e.* we only accept events in the region represented by the upper black box.

magnitude, but opposite directions. A similar argument can be used for both gravitinos produced in combination with each hard-jet. However, we cannot distinguish between the gravitinos, as the missing energy is experimentally obtained from visible particles. Since the missing p_T is a combination of the p_T of both gravitinos, in this case, there is a larger probability that they will (partially) cancel each other. The tendency is therefore to have events more spread around the diagonal, with the high $p_T^{1\text{stjet}}$ and low $\not{p}_T$ region populated. That is what we observe in the third plot of Fig. 6.10.

To reduce the background we use scatter plots to search for the most populated region with signal events and scarcely any background events. Fig. 6.11 shows the background superimposed to the signal - case B (equally contributing sub-processes). We can thus impose the following cut

$$\not{p}_T > 500 \text{ GeV}, \quad p_T^{1\text{stjet}} > 500 \text{ GeV}, \tag{6.49}$$

which is represented by the grey lines in Fig. 6.11. The differential cross section as a function of the relevant observables, accounting for the cuts given by Eq. 6.49, are collected in Fig. 6.12.

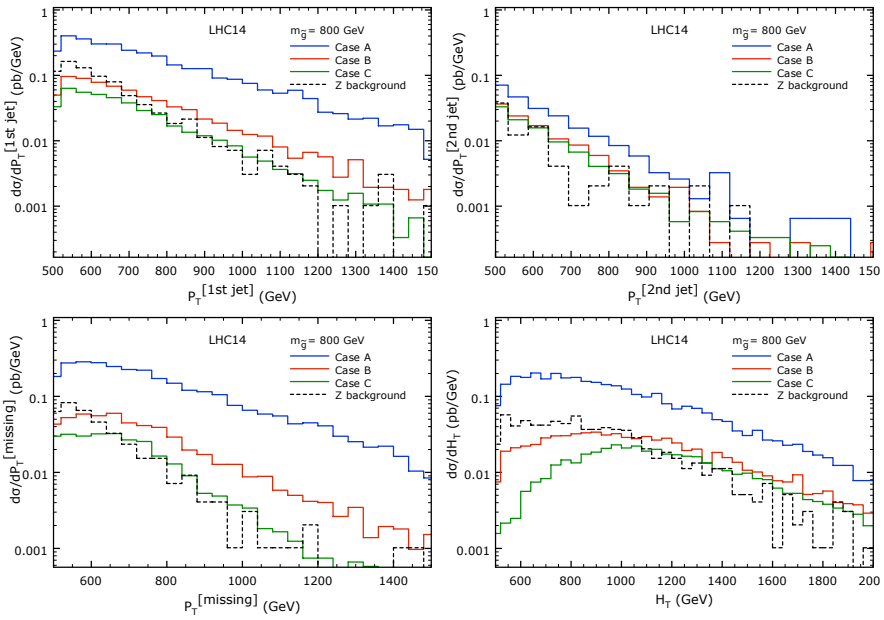

Figure 6.12: Differential cross section as a function of the relevant observables after cuts: $\not{p}_T > 500$ GeV and $p_T^{\mathrm{1st\,jet}} > 500$ GeV. The signal is $pp \to \tilde{G}\tilde{G} + n$-jets with $n = 1, 2, 3$. The irreducible background, $pp \to \nu\bar{\nu} + n$-jets with $n = 0, 1, 2, 3$, is shown for reference. The mass of the gluino is 800 GeV, and the mass of the gravitino is 1×10^{-13} GeV in case A, 3×10^{-13} GeV in case B and 9×10^{-13} GeV in case C. The simulation is performed for the LHC with $\sqrt{s} = 14$ GeV.

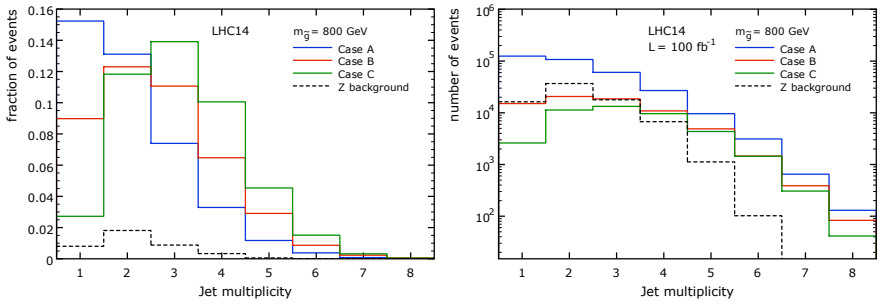

Figure 6.13: In the left, we show the ratio of events $N_{events(AC)}/N_{total(BC)}$ for different multiplicities in each sample, where $N_{events(AC)}$ is the number of events after the imposition of the cuts specified in Eq. 6.49 and $N_{total(BC)}$ is the total number of events before the application of any cut. In the right, the final number of events expected as a function of the jet multiplicity is displayed. The signal is $pp \to \tilde{G}\tilde{G}+n$-jets with $n = 1,\ 2,\ 3$. The irreducible background, $pp \to \nu\bar{\nu} + n$-jets with $n = 0,\ 1,\ 2,\ 3$, is shown for reference. The mass of the gluino is 800 GeV, and the mass of the gravitino is 1×10^{-13} GeV in case A, 3×10^{-13} GeV in case B and 9×10^{-13} GeV in case C. The simulation is performed for the LHC with $\sqrt{s} = 14$ GeV and $L = 100$ fb^{-1}.

From Fig 6.12 we observe that consequences for the observables related to the p_T of the particles do not change considerably at the high p_T region with the application of the cuts. One could possibly observe signals of new physics for cases A or B, however the curve for case C still runs together with the background.

Nevertheless, Fig. 6.11 shows that applying the cuts specified in Eq. (6.49) should remove most of the background. We can thus plot the fraction of events observed after such cuts as a function of the jet rate. From the left plot of Fig. 6.13 we observe that most of the background is removed, whereas a great part of the signal remains. The shape of the distributions change from before the imposition of cuts. The background distribution has now a peak for events with 2-jets, and the distribution for case A obtains the decreasing stair shape. Let us stress that the left plot of Fig. 6.13 only confirms that a great part of the background is removed. However, it is the plot with number of events as a function of the jet multiplicity, in the right, that can show us the distributions fairly compared. We observe that case A is possibly be detectable at the LHC. For cases B and C, an excess at higher multiplicities (more than 4 jets) could be indication of new physics.

To summarize, the main difficulty of the present analysis lies in the fact that two different sub-processes are substantially relevant. Normally, they would have to be considered separately and a careful analysis would be necessary to gather all the contri-

butions into one final result. This process would be susceptible to unintentional errors due to several reasons, such as an under/overestimation of one of the sub-processes for example. A significant upshot of our technique is therefore the ability of treating both sub-processes at once, at any region of the parameter space.

If signals of new physics emerge at the LHC as an excess of events with high jet multiplicities, more refined analyses will be necessary to identify the theory and constrain parameters. Essentially, a complete control of jet parameters are required, since jet rate distributions can dramatically change if one parameter is modified. Nevertheless, once jet parameters are dominated, and the mass of the gluino is fixed, one could use jet multiplicities to constrain the mass of the gravitino. We observe that different peaks in Fig. 6.13 could allow us to set limits in the mass of the gravitino, and identify what sub-process is dominant.

The mass of the gluino must be fixed in order for the analysis with the jet rates to be useful. At the LHC gluinos, being the NLSP, could be identified through different signatures. Within the strategy of the present study, gluinos should decay into one jet and one gravitino, which is the invisible particle. Therefore, gluinos could be identified through analyses that use the distributions of the differential cross section as a function of the p_T of the leading jet. Because of the kinematics of the processes being considered, the peak observed in the signal distributions should lie approximately at $m_{\tilde{g}}/2$. This is what we observe in Fig. 6.8. For case C, where double-gluino resonance is dominant, the peak is clearly at $p_T^{\mathrm{1stjet}} = 400$ GeV. For case A the determination of the peak is more difficult, because the dominant contribution is the gluino-gravitino associated production, but still possible. As we have stated, once the mass of the gluino is fixed, one can use the shape of jet rate distributions as an indication of the mass of the gravitino.

Chapter 7

Epilogue

7.1 Summary and conclusions

The SM describes very accurately the experimental data we have so far, however, chances are high that signs of new physics will appear soon at the LHC. Several BSM theories have been proposed as an alternative to the SM at high energies. If the theory extension could incorporate gravity in the quantum description of Nature, one of the greatest puzzles of particle physics would be unravelled. Theories with such attributes are therefore specially interesting. One can cite for example higher dimensional theories, such as large extra dimensions or warped extra dimensions. Another option are 4-dimensional theories with a separate sector that contains many particles that do not interact with the SM particles through the usual weak, strong and electromagnetic forces. One example is the massless graviton model presented in Chapter 3. There are also theory extensions that allow for extra symmetries, such as supersymmetry and supergravity, both introduced in Chapter 6.

Given the large number of existing scenarios, it will certainly not be trivial to determine the nature of new physics once it emerges at high energy hadron colliders. Simulations, and search strategies will thus play a key role in the determination of such theories, and moreover, in the treatment of new physics. Therefore, the necessity of general simulation tools that quickly predict experimental observables have become essential. Furthermore, the demand for new search strategies has substantially increased with the advance of computer technology and simulation tools aimed at the treatment of particle physics focused on theory extensions to the SM.

The present work has been intended to accomplish a complete phenomenological analysis at hadron colliders of BSM theories that incorporates gravitational interactions. To this aim, the development of new simulation tools and search strategies has been necessary, and performed. We have carried out an analysis that covers all the steps to

go from a theoretical framework to the experimental observables expected at hadron colliders.

The format of this thesis has also followed the "theories → experiments path". We have started with an brief introduction followed by an overview of the SM and some of the open questions that we hope to be (partially) answered by the LHC. In the third chapter, we have introduced theory extensions to the SM that contains graviton particles. A rather theoretical description has been presented, in which we show the difference between theories that include massive gravitons to these with massless gravitons. In particular, it has been highlighted that the propagator of such particles has a unique behaviour when the limit from a massive to a massless graviton is considered.

The connection to a more experimental point-of-view has started with the calculation of differential cross sections for graviton production at hadron colliders. We have considered different types of theories, containing both massive and massless gravitons. We have observed that the unique behaviour of the propagator of such theories, known as the van Dam-Veltman discontinuity, does not appear at cross section level. This is an interesting consequence, since the opposite would be expected. We cannot therefore use the discontinuity of the graviton propagator as hint for the determination of the mass of the graviton particle if it is observed at the LHC or at future colliders, and more phenomenological analyses are necessary.

The proximity to more experimental searches has increased in Chapter 4, when we have presented the LHC and defined observables. Very energetic particles are the consequences of high energy collisions, such as these happening at the LHC. When the center-of-mass energy increases, final-state full of jets become more likely. Therefore, it is a natural choice to study signatures that predict numerous particles as a result from the collision.

For this reason, in Chapter 5, we have focused on graviton production in combination with jets. We have started with a simple phenomenological investigation of processes with one graviton and one jet at the LHC. We have used the Monte-Carlo event generator MADGRAPH/MADEVENT for the simulation of events, which included recent implemented helicity routines for correctly treating massive spin-2 particles. We have manually implemented the helicity routines needed by massless spin-2 particles, and the MGM model within the event generator. With such implementations, MADGRAPH/MADEVENT has become complete in terms of spin-2 particles, *i.e.* could automatically generate events for any type of spin-2 particles. Results for this particular analysis have been obtained as a function of relevant observables at the LHC, and compared to the expected SM background.

However, at the LHC larger number of jets in the final state are expected. Therefore, despite the significant results obtained with the mono-jet analysis, more realistic in-

vestigations needed to be performed. Because the emission of QCD radiation needs to be taken into account when multiple jets are the final product of a collision, different types of tree-level simulation descriptions should be used simultaneously: the matrix element approach and the parton-shower description. To this aim, modifications in the routines used by MADGRAPH/MADEVENT were necessary. We have performed such modifications, and used the merge/matching technique to investigate graviton production in inclusive multi-jet samples at hadron colliders.

A very general analysis has been carried out. Since the development of the routines used by MADGRAPH/MADEVENT has been made aiming on the automatic generation of events involving spin-2 particles, we could investigate the differences/similarities between three main classes of theories that contain the graviton particle. In the ADD and MGM theories, the graviton appears as missing energy, while in RS model it may be observed through its decay products.

We have checked and validated the robustness of matching results with a comparison against next-to-leading order simulation of graviton + jet production. The fully inclusive samples have been normalized to the corresponding NLO inclusive total cross sections for producing G + X. Key distributions for the most relevant observables involving one or more jets have then been compared to those obtained by the NLO calculation G + jet + X. The overall agreement in shape as well as in normalization between the NLO observables and these obtained by making use of the matching technique is excellent. In particular, notice that a unique normalization factor (the one normalizing the overall inclusive sample) suffices to describe not only the shape but also the normalization of jet distributions. It demonstrates that the use of matched samples in experimental analyses is straightforward and accurate. We therefore make use of such technique once more in Chapter 6. Finally, we have seen that observables which are sensitive to the number of jets, such as the H_T, are better described by the matched sample than a fixed-order calculation.

Since we are interested in the missing energy signature generated from theories that include gravitational interactions, supersymmetry within the context of simplified models of supergravity should be taken into account. Such theories comprise gravitino particles, which are spin-$3/2$ particles, super-partner of the graviton. In some variations of supersymmetric theories, gravitinos are super-light, invisible particles, whose productions can become relevant at hadron colliders. In Chapter 6 we thus consider the production of two gravitinos in multi-jet final states.

To obtain the predictions for relevant experimental observables, we have made use of the matching technique, which takes into account simultaneously hard and soft jets. Because two different sub-processes separately contribute for our analysis, the use of the matching tool has been a major advantage. It has not only facilitated and prevented us from errors, but has also saved substantial computational time. That is due to the

fact that we do not need to simulate each sub-process separately, nor worry about the region of the parameter space that a particular sub-process is dominant.

Results obtained for gravitino production are encouraging. We have observed that, if such new physics signs are detected at the LHC, one could use observables related to the p_T of the jets and/or $\not{p}_T$ to estimate the value for the mass of the gluino. Once this is fixed, jet multiplicities allow us to predict the mass of the gravitino, and the leading contributing sub-process.

The methods and ideas employed in the course of the present research are at the cutting edge in high-energy phenomenology. We have helped to develop and advance tree-level simulation tools and search strategies to easily connect theory with experimental observables. With them, we have performed a complete analysis on processes involving missing energy signature for theories that incorporate the gravitational force. We now look forward to their use in the current and forthcoming searches at hadron collider.

7.2 Outlook

The advancement of simulation methods and computer technology have defined the beginning a new era for the phenomenology of particle physics. Phenomenological investigations, are now essential for the search of BSM theories, and hints of their existence may appear very soon at the LHC. With the large number of possible SM extensions, it is necessary to know in advance the best strategy to identify new particles and connect them with the most favourable theory which these particles could belong to.

For this reason, simulation tools and the search strategies developed and employed here can be very fruitful for future researches. First, the implementation of spin-2 helicity routines can be used by MC event generators to simulate processes containing such particles. Several BSM theories can be considered, where similar analyses to those presented in Chapters 5 and 6 can be performed. Moreover, phenomenological investigations could be modified and extended to more model-independent approaches.

The automation of helicity routines necessary for calculating the matrix element associated with any new model presents an indispensable step completed towards the effort to connect theory with experimental data. Any theory can now be easily implemented into a MC event generator, accounting that the implementation of helicity routines are no longer restricted to the same Lorentz structures as these of the SM. Obtaining predictions for experimental observables (considering tree-level calculations)

has become feasible for anyone, from a person with a more theoretical background to someone with a more experimental point of view. There are several theories that could be implemented and studied with the employment of such tool. For instance, there are extra dimensional theories with SM-like particles propagating in the bulk, different SM extensions based on specific symmetries, as well as simplified models focused on the treatment of new particles.

One example of the use of these tools would be a signature-based research aiming the discovery of a new particle. The idea would be to consider, in a model-independent manner, all the channels that could result in a particular signature. Similarly to the investigation that has been performed for the graviton production in Chapter 5, where we consider three representative classes of theories that could produce a graviton, we could concentrate in final states that include any type of invisible particles and build a strategy to differentiate theories using final observables. One goal would be the identification of the observable(s) that best discriminate classes of theories.

A consequence of the non-observation of new physics so far, is the realization that some processes need more accurate predictions than these that can be provided by LO calculations. Since a few years ago, a huge effort is being made for the development of both the automatic NLO computations, and the MC event generators that take into account such corrections. Recent ideas, in addition to the advancement of simulation techniques and machines, enabled the creation of such NLO simulation tools, which are however still in (the final stage of) development [87, 86, 85]. Once NLO event generators are available, an "accuracy revolution" will begin, and we will have the possibility of performing several phenomenological investigations. In particular, we could extend the analysis made here for mono-jet graviton production at NLO, and obtain the prediction for the relevant observables with larger precision and, most importantly, the correct normalization for the cross section.

Although NLO predictions provide accurate results for the cross section, it is still necessary to consider QCD emission and an hadronization description to correctly predict observables at the detector level. The LO matching/merge description described in Chapter 4, and employed in Chapters 5 and 6, is interesting because it considers the best features of both approaches. A novel description combining NLO event generation and parton-shower description have been developed [159, 160, 161, 162, 163, 164] and great progress has been made since their actual conception. Another idea would therefore be the use of such tool to perform similar investigations to these presented in the course of this work. With the use of such tools, one could obtain the distribution of relevant observables with the correct shapes and cross section normalization.

Finally, more severe investigations will be necessary to constrain parameters of BSM theories with the LHC data once they are available. Simulation tools and search/ identification strategies will help to accelerate this process and enable more theories

to be looked into simultaneously. There is certainly still a long way ahead, when it comes to interpreting and understanding results that will soon be provided by the LHC, but that can also be the reason why the next years may be the most fun and exciting years for modern particle physics!

Appendix A

Massless graviton implementation

Here, we detailed present the implementation of massless graviton routines within MADGRAPH/MADEVENT. Initially, we alter helicity routines (HELAS) for spin-2 particles in order to handle massless particles. We subsequent create a model file for the particular theory described on chapter 3. All information characterizing implementation follows.

A.1 HELAS routines modifications

The HELAS routines for massive spin-2 particles have been implemented by K. Hagiwara et al [99] in 2008. A summary of the routines can be found on Table A.1. In order to have massless spin-2 particles in MADGRAPH/MADEVENT , we have modified the tensor wave function subroutine `TXXXXX`, and four subroutines for the off-shell tensor were added to the former implementation.

A.1.1 TXXXXX

This subroutine computes the graviton tensor wave function, namely $\epsilon^{\mu\nu}(p,\lambda)$ and $\epsilon^{\mu\nu}(p,\lambda)^*$ in terms of the graviton four-momentum p and its helicity λ.

Vertex	Inputs	Output	Subroutine
SST	SST	Amplitude	SSTXXX
	ST	S	HSTXXX
	SS	T	USSXXX
FFT	FFT	Amplitude	IOTXXX
	FT	F	FTIXXX, FTOXXX
	FF	T	UIOXXX
VVT	VVT	Amplitude	VVTXXX
	VT	V	JVTXXX
	VV	T	UVVXXX
FFVT	FFVT	Amplitude	IOVXX
	FVT	F	FVTIXX, FVTOXX
	FFT	V	JIOTXX
	FFV	T	UIOVXX
VVVT	VVVT	Amplitude	VVVTXX
	VVT	V	JVVTXX
	VVV	T	UVVVXX
VVVVT	GGGGT	Amplitude	GGGGTX
	GGGT	G	JGGGTX
	GGGG	T	UGGGGX

Table A.1: Summary of Spin-2 HELAS routines extracted from [99].

The helicity states of the graviton can be expressed by

$$\begin{aligned}
\epsilon^{\mu\nu}(p,\pm 2) =& \epsilon^{\mu}(p,\pm)\epsilon^{\nu}(p,\pm) \\
\epsilon^{\mu\nu}(p,\pm 1) =& \frac{1}{\sqrt{2}}\left[\epsilon^{\mu}(p,\pm)\epsilon^{\nu}(p,0) + \epsilon^{\mu}(p,0)\epsilon^{\nu}(p,\pm)\right] \\
\epsilon^{\mu\nu}(p,0) =& \frac{1}{\sqrt{6}}\left[\epsilon^{\mu}(p,+)\epsilon^{\nu}(p,-) + \epsilon^{\mu}(p,-)\epsilon^{\nu}(p,+) + 2\epsilon^{\mu}(p,0)\epsilon^{\nu}(p,0)\right],
\end{aligned} \tag{A.1}$$

where $\epsilon^{\mu}(p,\lambda)$ is the vector boson wave function, already pre-defined on the HELAS convention. For completeness it is important to state here that the spin-2 wave functions are traceless, transverse, orthogonal and symmetric, obeying therefore the fol-

lowing relations:

$$\begin{aligned} &\epsilon^{\mu}{}_{\mu}(p,\lambda) = 0, && \epsilon^{\mu\nu}(p,\lambda)\epsilon_{\mu\nu}(p,\lambda')^* = \delta_{\lambda\lambda'} \\ &\epsilon^{\mu\nu}(p,\lambda) = \epsilon^{\nu\mu}(p,\lambda) && p_\mu\epsilon^{\mu\nu}(p,\lambda) = p_\nu\epsilon^{\mu\nu}(p,\lambda) = 0 \end{aligned} \tag{A.2}$$

The sum of helicity states for the graviton is introduced on the routines to be given by

$$\sum_{\lambda=\pm 2} \epsilon_{\mu\nu}(p,\lambda)\epsilon_{\alpha\beta}(p,\lambda)^* = \tilde{\mathcal{P}}_{\mu\nu,\alpha\beta}(p), \tag{A.3}$$

where $\tilde{\mathcal{P}}_{\mu\nu\alpha\beta}$ is the massless graviton propagator defined on equation (3.73). While the massive graviton has five helicity states of polarization, the massless spin-2 particles will only have two physical states. The sum of polarization for the massless graviton is therefore modified on the routines to set $\lambda = \pm 1,\ 0$ to zero allowing only $\lambda = \pm 2$ to contribute.

A.1.2 UIOXXX, UVVXXX, UIOVXX, UVVVXX

These subroutines compute off-shell tensor currents `U` by the `FFT`, `VVT`, `FFVT`, and `VVVT` vertices respectively. The main modification here was the inclusion of the zero mass graviton propagator to be the one showed in equation (3.73) for the massless case.

The `UIOXXX` routine computes the bi-spinor spin-2 current from the flowing-in and flowing-out fermions calculated by the `FFT` vertex. The flowing-in `FI` and flowing-out `FO` fermions are defined to be arrays which contain their four-momenta:

$$\texttt{FI} = \begin{pmatrix} p_I^0 \\ p_I^1 \\ p_I^2 \\ p_I^3 \end{pmatrix}, \quad \texttt{FO} = \begin{pmatrix} p_o^0 & p_o^1 & p_o^2 & p_o^3 \end{pmatrix}. \tag{A.4}$$

The output is a complex array defined by

$$T^{\alpha\beta} = g_t \frac{\tilde{\mathcal{P}}^{\mu\nu\alpha\beta}}{q^2} \texttt{FO}\left[-\eta_{\mu\nu}(\not{p}_I + \not{p}_o - 2m_f) + \gamma_\mu(p_I + p_o)_\nu + \gamma_\nu(p_I + p_o)_\mu\right] \texttt{FI}$$

where q is the four-momentum related to the massless propagator, $g_t = \frac{1}{4\Lambda}$ and Λ is the effective scale of the model. For the MGM theory, $\Lambda = \overline{M}_{pl}(\mu_\star) \sim \mu_\star$.

The UUVXXX is the subroutine that computes an off-shell spin-2 current from the two flowing-out vector bosons calculated by the VVT vertex. The graviton output is the complex array:

$$T^{\alpha\beta} = g_t \frac{\tilde{\mathcal{P}}^{\mu\nu\alpha\beta}}{q^2} \left[(m_V^2 + p_I \cdot p_o) C_{\mu\nu\rho\sigma} + D_{\mu\nu\rho\sigma}(p_I, p_o) + \right. \\ \left. + \xi^{-1} E_{\mu\nu\rho\sigma}(p_I, p_o) \right] V_I^\rho \, V_o^\sigma \tag{A.5}$$

where where q is the four-momentum related to the massless propagator, $g_t = \frac{1}{\Lambda}$, Λ is the effective scale of the model, and the parameters $C_{\mu\nu\alpha\beta}$, $D_{\mu\nu\alpha\beta}$ and $E_{\mu\nu\alpha\beta}$ are defined on Table 3.1.

The UIOVXX subroutine computes an off-shell spin-2 current calculated by the FFVT vertex. The graviton output complex array is given by:

$$T^{\alpha\beta} = g_t \frac{\tilde{\mathcal{P}}^{\mu\nu\alpha\beta}}{q^2} (\eta_{\mu\nu}\eta_{\rho\sigma} - C_{\mu\nu\rho\sigma}) \, \mathtt{FO} \left[V^\rho \gamma^\sigma \left(g_f^{(1)} P_L + g_f^{(2)} P_R \right) \right] \mathtt{FI}, \tag{A.6}$$

where q is the four-momentum related to the massless propagator, $g_t = \frac{1}{2\Lambda}$, Λ is the effective scale of the model, the parameter $C_{\mu\nu\alpha\beta}$ is defined on Table 3.1 and $g_f^{(1)}$ and $g_f^{(2)}$ are the SM FFV couplings. For example, if we have a quark-anti-quark-gluon-graviton vertex, $g_f^{(1)} = g_f^{(2)} = g_S$.

Finally, the UVVVXX subroutine computes an off-shell spin-2 current calculated by the VVVT vertex. The graviton tensor is given by

$$T^{\alpha\beta} = \frac{\tilde{\mathcal{P}}^{\mu\nu\alpha\beta}}{q^2} g_V \left[C_{\mu\nu\rho\sigma}(p_a - p_b)_\lambda + C_{\mu\nu\sigma\lambda}(p_b - p_c)_\rho + \right. \\ \left. + C_{\mu\nu\lambda\rho}(p_c - p_a)_\sigma + F_{\mu\nu\rho\sigma\lambda} \right] V_a^\rho \, V_b^\sigma \, V_c^\lambda, \tag{A.7}$$

where q is the four-momentum related to the massless propagator, $g_t = \frac{1}{\Lambda}$, Λ is the effective scale of the model, the parameters $C_{\mu\nu\alpha\beta}$ and $F_{\mu\nu\rho\sigma\lambda}$ are defined on Table 3.1 and g_V is the SM VVV coupling.

A.2 MGM model file

The model file was created for MADGRAPH/MADEVENT version 4. It contains all the information regarding particles, couplings and interactions and follows the structure presented on [99] for theories containing a massive spin-2 particle. A summary of the model content is presented below.

The particle content of the mode is similar to the SM, in addition to a massless tensor:

```
# This is a special data file which contains particles of the
# model. The format for entering new particles is:
# Name  anti_Name  Spin  Linetype  Mass  Width  Color Label PDG

   y        y       T        D     ZERO   ZERO    S     G    39
```

The graviton is represented by the letter `y`, and its PDG number is 39. The new coupling associated to the graviton particles are:

```
# The ordering of particles is very important.
# For FFV interactions, must use particles, not anti_particles.
#
# 3-particle vertices are entered as follows:
# particle1 particle2  particle3 coupling_name coupling_order
#
  g  g  y GTV QTD
  a  a  y GTV QTD
  z  z  y GTV QTD
  w- w+ y GTV QTD
  q  q  y GTF QTD
  l- l- y GTF QTD
  h  h  y GTS QTD
#
# 4-particle vertices are entered as follows:
# part1 part2 part3 part4 2xcoupling_names 2xcoupling_orders
#
  g  g  g y G   GTV  QCD QTD
  q  q  g y GG  GTFV QCD QTD
  qd qd a y GAD GTFV QED QTD
  qu qu a y GAU GTFV QED QTD
  l- l- a y GAL GTFV QED QTD
  qd qd z y GZD GTFV QED QTD
  qu qu z y GZU GTFV QED QTD
  l- l- z y GZL GTFV QED QTD
  vl vl z y GZN GTFV QED QTD
  qd qu w- y GWF GTFV QED QTD
  qu qd w+ y GWF GTFV QED QTD
  vl l- w+ y GWF GTFV QED QTD
  l- vl w- y GWF GTFV QED QTD
```

Here, all types of quarks are represented by `q`, up-quark family is `qu` and down-quark family is `qd`. For the leptons, electron, muon and tau are defined as `l-`, and the three types of neutrinos are represented by `vl`. The interaction order is the proportionality of the vertex with the g_S coupling for QCD, g_e coupling for QED, and g_t coupling for QTD, which is the new interaction defined for spin-2 particles. The couplings depend on the particles of the vertex.

The new couplings related to the spin-2 particle are `GTV`, `GTF` and `GTS`. They are defined to be:

$$\texttt{GTV} = \frac{1}{\Lambda}, \quad \texttt{GTS} = \frac{1}{2\Lambda}, \quad \texttt{GTF} = \frac{1}{4\Lambda} \tag{A.8}$$

where Λ is the effective scale of the theory.

Appendix B

New routines for ADD theories in MadGraph

B.1 5-point vertices

In chapter 3 we have obtained the Feynman rules and vertices for a theory with a general spin-2 particle coupled to the SM theory. These are exhibited on Figure 3.1.

We can check the existence of 5-point vertices, such as the ggggG vertex or the qqggG. Previously, MADGRAPH/MADEVENTversion 4 [91] did not have the automatic generation of 5-point diagrams, which was necessary for the correct evaluation of processes with more than 1 jet in the final state. Routines to automatic generate 5-point vertices have been implemented in collaboration with Q. Li [114]. Here we describe details of such implementation.

Recall that the ggggG vertex is described on Figure 3.1. It can be re-organized and written as:

$$\mathcal{L}_{\texttt{gggg}\texttt{T}} = -\,\texttt{GT}\,\texttt{GC}^2\, f^{abe} f^{cde}\, T^{\mu\nu *} \times \left[\frac{1}{4}\eta_{\mu\nu} g^{a,\rho *} g^{b,\sigma *} g^{c*}_{\rho} g^{d*}_{\sigma} - g^{b,\rho *} g^{a*}_{\mu} g^{c*}_{\nu} g^{d*}_{\rho}\right], \tag{B.1}$$

with the coupling constants $\texttt{GT} = -\frac{\kappa}{2}$ and $\texttt{GC} = g_s$. In HELAS such vertex can be encoded as `GGGGTX` computing the portion of the amplitude of the `ggggT` vertex from four gluon (`G`) polarization vectors and a tensor (`T`) boson wavefunction corresponding to the color structure $f^{abe}f^{cde}$, as it is illustrated on Figure B.1 (a).

In order to implement this vertex in MADGRAPH, which supports at most 4-point vertices, we reinterpret the scattering in the t, u and s channels of the non-propagating octet tensor boson t_A as an auxiliary particle. With t_A we can decompose the 5-point vertex into two 3-point vertices: ggt_A and $t_A t_A T$, which can then be generated

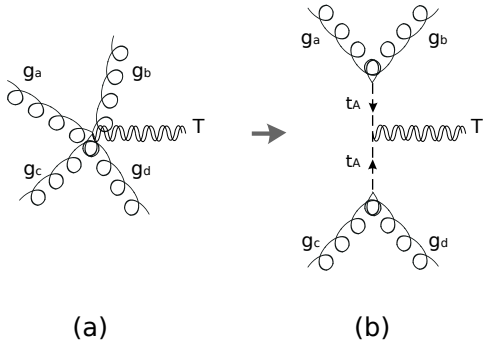

Figure B.1: Illustration of the decomposition of the 5-point vertex into two 3-point vertices to be automatically treated in MADGRAPH version 4.

by MADGRAPH automatically. The color structure of the vertex $f^{abe}f^{cde}$ is maintained. Figure B.1 illustrates the decomposition. Observe that we assign a flow to t_A, *i.e.* we treat t_A different from its antiparticle in MADGRAPH. The idea is to forbid the interaction of t_A and its antiparticle to avoid appearance of additional diagrams for $gg \to gg$.

In order to introduce the auxiliary particle t_A, several HELAS sub-routines have been modified and some have been created. Table B.1 presents a summary of all modifications. We follow with a full description of each routine.

GGGGTX

The subroutine `GGGGTX` computes the portion of the amplitude of the `ggggT` vertex from four `G`luon polarization vectors and a `T`ensor boson wavefunction corresponding to the color structure $f^{abe}f^{cde}$, which should be called as

$$\texttt{CALL GGGGTX}(\texttt{VA}, \texttt{VB}, \texttt{VC}, \texttt{VD}, \texttt{TC}, \texttt{GC}, \texttt{GT}\ ,\ \texttt{VERTEX}) \tag{B.2}$$

The inputs `VA(6)`, `VB(6)` and `VC(6)` are complex six-dimensional arrays which contain the `V`ector boson wavefunctions, and their momenta as

$$\begin{aligned}
p_a^\mu &= (\Re e\texttt{VA}(5), \Re e\texttt{VA}(6), \Im m\texttt{VA}(6), \Im m\texttt{VA}(5)),\\
p_b^\mu &= (\Re e\texttt{VB}(5), \Re e\texttt{VB}(6), \Im m\texttt{VB}(6), \Im m\texttt{VB}(5)),\\
p_c^\mu &= (\Re e\texttt{VC}(5), \Re e\texttt{VC}(6), \Im m\texttt{VC}(6), \Im m\texttt{VC}(5)).
\end{aligned}$$

Sub-routine	Summary
VVTCXX	computes the amplitude of the $\mathtt{gg}t_A$ vertex.
JVTCXX	computes the off-shell vector current J made from the interactions of a Vector gluon and an auxiliary Tensor boson by the $\mathtt{gg}t_A$ vertex.
UVVCXX	computes the off-shell tensor current U for the auxiliary tensor t_A, made from two flowing-out Vector gluons by the $\mathtt{gg}t_A$ vertex.
TTTXXX	computes the amplitude of the $t_A t_A$T vertex.
UTTAXX	computes the off-shell non-propagating tensor current U, made from the flowing-out graviton Tensor and the auxiliary Tensor by the $t_A t_A$T vertex.
UTTBXX	computes the off-shell graviton tensor current U, made from the two flowing-out auxiliary Tensors by the $t_A t_A$T vertex.

Table B.1: Summary of the HELAS sub-routines introduced for the implementation of the 5-point vertex in MADGRAPH extracted from [114].

The input TC(18) is a complex 18-dimensional array which contains the wavefunction of the Tensor boson:

$$\mathtt{T}^{\mu+1,\nu+1} = \mathtt{TC}(4\mu+\nu+1), \tag{B.3}$$

and its four-momentum as

$$p^\mu = (\Re e\mathtt{TC}(17), \Re e\mathtt{TC}(18), \Im m\mathtt{TC}(17), \Im m\mathtt{TC}(17)),$$

The output VERTEX is a complex number in units of GeV:

$$\mathtt{VERTEX} = -\mathtt{GT}\,\mathtt{GC}^2\, T^{\mu\nu}\, G_{\mu\nu,\rho\lambda\sigma\delta}\, V_A^\rho V_B^\sigma V_C^\lambda V_D^\delta \tag{B.4}$$

with $G_{\mu\nu,\rho\sigma\lambda\delta}$ given on Table 3.1, and we use the notation

$$\begin{aligned} V_A^\mu &= \mathtt{VA}(\mu+1),\ V_B^\mu = \mathtt{VB}(\mu+1), \\ V_C^\mu &= \mathtt{VC}(\mu+1),\ V_D^\mu = \mathtt{VD}(\mu+1). \end{aligned} \tag{B.5}$$

In order to insert automatically 5-point vertices in MADGRAPH, we introduce non-propagating colourless tensor boson t_A as an auxiliary particle. With t_A the portion

of the 5-point vertex with color structure $f^{abe}f^{cde}$ can be reduced automatically. After introducing particle t_A, several new HELAS subroutines were added. They are summarized on Table B.1, and can be called on the following way:

VVTCXX

This subroutine computes the amplitude of the $\mathtt{g}\mathtt{g}t_A$ vertex,

$$\texttt{CALL VVTCXX}(\texttt{VA}, \texttt{VB}, \texttt{TC}, \texttt{GC}, \texttt{VMASS , VERTEX})$$

VMASS represents the vector gluon mass which is zero (although it does not play any role here, we keep it as an input argument in accordance with the subroutine VVTXXX, for convenience of MADGRAPH). What we compute here is

$$\texttt{VERTEX} = \texttt{GC}\,\eta_{\mu\rho}\eta_{\nu\sigma}T^{\mu\nu}V_A^{\rho}V_B^{\sigma}. \tag{B.6}$$

JVTCXX

This subroutine computes an off-shell vector current J made from the interactions of a Vector gluon and an auxiliary Tensor boson by the $\mathtt{g}\mathtt{g}t_A$ vertex, and should be called as

$$\texttt{CALL JVTCXX}(\texttt{VC}, \texttt{TC}, \texttt{GC}, \texttt{VMASS}, \texttt{VWIDTH , JVTC})$$

The input VC(6) is the wavefunction and momentum of the gluon. The output JVTC(6) gives the off-shell vector current multiplied by the gluon propagator, which is expressed as a complex six-dimensional array:

$$\texttt{JVTC}(\alpha + \texttt{1}) = -\frac{GC}{q^2}\eta_{\alpha\mu}V^{\alpha}T^{\mu\nu}, \tag{B.7}$$

and

$$\texttt{JVTC}(\texttt{5}) = \texttt{V}(\texttt{5}) + \texttt{TC}(\texttt{17}), \tag{B.8}$$

$$\texttt{JVTC}(\texttt{6}) = \texttt{V}(\texttt{6}) + \texttt{TC}(\texttt{18}). \tag{B.9}$$

Here the momenta q are

$$q^{\mu} = (\Re e\texttt{JVTC}(\texttt{5}), \Re e\texttt{JVTC}(\texttt{6}), \Im m\texttt{JVTC}(\texttt{6}), \Im m\texttt{JVTC}(\texttt{5})).$$

UVVCXX

This subroutine computes an off-shell tensor current `U` for the auxiliary tensor t_A, made from two flowing-out `V`ector gluons by the $\mathtt{g}\mathtt{g}t_A$ vertex, and should be called as

`CALL UVVCXX(VA, VB, GC, VMASS, XM, XW , UVVC)`

The inputs `XM` and `XW` are two dummy arguments for which we keep them in accordance with the subroutine `UVVXXX`. The output `UVVC(18)` is a complex 18-dimensional array:

$$T^{\alpha\beta} = \mathtt{GC} V_A^\alpha V_B^\beta \tag{B.10}$$

for the first 16 components of `UVVC`, and

$$\mathtt{UVVC}(17) = \mathtt{VA}(5) + \mathtt{VB}(5), \tag{B.11}$$

$$\mathtt{UVVC}(18) = \mathtt{VA}(6) + \mathtt{VB}(6). \tag{B.12}$$

TTTXXX

This subroutine computes the amplitude of the $t_A \;\; t_A\mathtt{T}$ vertex, called as

`CALL TTTXXX(TC, T1C, T2C, GT, VERTEX)`

The inputs `T1C(18)` and `T2C(18)` are complex 18-dimensional arrays which contain the wavefunction and momenta for the auxiliary tensors. What we compute here is

$$\mathtt{VERTEX} = \mathtt{GT}\, T^{\mu\nu} T_1^{\rho\lambda} T_2^{\sigma\delta} G_{\mu\nu,\rho\sigma\lambda\delta}, \tag{B.13}$$

with $T_{1,2}$ defined from `T1C(18)` and `T2C(18)` as in equation (B.3).

UTTAXX

This subroutine computes an off-shell non-propagating tensor current `U`, made from the flowing-out graviton `T`ensor and the auxiliary `T`ensor by the $t_A \;\; t_A\mathtt{T}$ vertex, and should be called as

`CALL UTTAXX(TC, T1C, GT, UTTA)`

The output UTTA(18) is a complex 18-dimensional array:

$$T_A^{\alpha\beta} = \mathtt{GT}\,\eta^{\sigma\alpha}\eta^{\delta\beta}T^{\mu\nu}T_1^{\rho\lambda}G_{\mu\nu,\rho\sigma\lambda\delta} \tag{B.14}$$

for the first 16 components of UTTA, and

$$\mathtt{UTTA}(17) = \mathtt{T}(17) + \mathtt{T1}(17), \tag{B.15}$$
$$\mathtt{UTTA}(18) = \mathtt{T}(18) + \mathtt{T1}(18). \tag{B.16}$$

UTTBXX

This subroutine computes an off-shell graviton tensor current U, made from the two flowing-out auxiliary Tensors by the $t_A \;\; t_A$T vertex, and should be called as

CALL UTTBXX(T1C, T2C, GT, TMASS, TWIDTH, UTTB)

The inputs TMASS and TWIDTH are the graviton mass and width, m_T and Γ_T. The output UTTA(18) is a complex 18-dimensional array:

$$T^{\alpha\beta} = \mathtt{GT}\frac{-\mathcal{P}_{\mu\alpha,\nu\beta}}{q^2 - m_T^2 + im_T\Gamma_T}\,T_1^{\rho\lambda}T_2^{\sigma\delta}G_{\mu\nu,\rho\sigma\lambda\delta} \tag{B.17}$$

for the first 16 components of UTTB, and

$$\mathtt{UTTB}(17) = \mathtt{T1}(17) + \mathtt{T2}(17), \tag{B.18}$$
$$\mathtt{UTTB}(18) = \mathtt{T1}(17) + \mathtt{T2}(18). \tag{B.19}$$

Here q is the momentum of the off-shell tensor boson given in equations (B.18) and (B.19) as

$$q^\mu = (\Re e\mathtt{UTTB}(17), \Re e\mathtt{UTTB}(18), \Im m\mathtt{UTTB}(18), \Im m\mathtt{UTTB}(17)).$$

And $\mathcal{P}_{\mu\alpha,\nu\beta}$ is the polarization summation tensor (3.77) [99].

B.2 Summation over the mass spectrum

On chapter 2 it has been shown that for the ADD theory we expect to have an infinite number of spin-2 particles couples to the SM. Because their masses lie very close to each other experimental searches would hope to detect signs of gravity through the sum of such states.

The MC simulation would therefore have to perform an extra integral (accounting for all the KK modes of the graviton) for each point of the phase-space. The amplitude integration over the mass density function is specified on equation (3.40).

For virtual graviton exchange, the tower of KK graviton modes leads to the summation of their propagators, which is divergent since ADD is only an effective theory. It is possible to introduce a cutoff for the highest KK modes and replace the summation a factor on the effective scale, as it was first proposed by Han et al [49]. This was the method chosen for the implementation in MADGRAPH, which can be easily performed by setting the graviton mass to zero and the extra dimensional scale to be the same as the effective scale. Note however, that the propagator of the massive graviton is still employed here, and setting the mass of the graviton to zero has only been accomplished locally aiming on executing such trick.

Nevertheless, it is more complicated for graviton emission, because it is actually necessary to perform the integration described by equation (3.40). We have implemented the integration through the introduction of new vertices and two auxiliary dummy particles x_1 and x_2. These are massless colourless particles, in which the first is defined as a scalar, and the second a pseudo-tensor. MADGRAPH is subsequently modified to include a new particle type `P`, which is only involved in the interaction with graviton: $x_1 x_2$`T`.

For generate a process (exclusively for the ADD theory) in which a spin-2 particle is emitted, one should request for example $pp \to x_1 x_2 + X$, instead of $pp \to T + X$. The phase spaces are related by

$$d\Phi(x_1 x_2 + X) = \frac{dm_T^2}{16\pi^2} d\Phi(T + X)\,. \tag{B.20}$$

We can thus perform the mass integration with the help of the new HELAS subroutines for the $x_1 x_2$`T` vertex summarized in Table B.2.

PXXXXX

This subroutine stores the helicity and momentum of the auxiliary spin-2 `P`seudo-particle for further usage, and should be called as

`CALL PXXXXX(P, XM, NHEL, NST , PC)`

The input `P(0:3)` is a real four-dimensional array which contains the four-momentum p^μ of the pseudo particle, `NHEL` ($= \pm 2, \pm 1, 0$) specifies its helicity λ, `NST` specifies

Sub-routine	Summary
PXXXXX	stores helicity and momentum of the auxiliary particles x_1 and x_2.
TPSXXX	computes the amplitude of $x_1 x_2$T vertex from a set of parameters specified by the theory.
UPSXXX	computes an off-shell graviton tensor current U, made from the flowing-out auxiliary Scalar and Pseudo-particles, by the $x_1 x_2$T vertex.

Table B.2: Summary of new HELAS sub-routines introduced for the implementation of the KK mass integration in MADGRAPH/MADEVENT within the framework of the ADD model. Table extracted from [114]

whether the boson is in the final state (NST = 1) or in the initial state (NST = -1). XM is its mass but does not play any role here.

The output PC(18) is a complex 18-dimensional array, among which only the following matter, namely

$$\mathtt{PC(\ 1)} = \mathtt{NHEL}, \tag{B.21}$$

and

$$(\mathtt{PC(17)},\ \mathtt{PC(18)}) = \mathtt{NST}\,(\mathtt{P(0)} + i\mathtt{P(3)},\ \mathtt{P(1)} + i\mathtt{P(2)}). \tag{B.22}$$

TPSXXX

This subroutine computes the amplitude of the $x_1 x_2$T vertex, and should be called as

$$\mathtt{CALL\ TPSXXX(TC0, PC, SC, GP, TMASS0, TWIDTH,\ VERTEX)}$$

SC(3) is a complex three-dimensional array which contains the momentum for x_1. GP(1:2) here are not coupling constant, but contain the ADD model inputs:

$$\begin{aligned} \mathtt{GP(\ 1)} &= \Lambda + i\delta, \\ \mathtt{GP(\ 2)} &= M_{low} + iM_{up}, \end{aligned} \tag{B.23}$$

M_{low} and M_{up} are the lower and upper limits for graviton mass integration. TMASS0 (m_{T0} for below) is only temporarily used and got from the MG input file param_card.dat, while the real graviton mass m_T is defined as the invariant mass

of x1 and x2, *i.e.*,

$$m_T \equiv |q_1 + q_2|, \tag{B.24}$$

with q_1 and q_2 are the momenta of x_1 and x_2.

Also note the input `TC0` is indeed calculated from the other side of Feynman diagram, and contains the polarization summation tensor $\mathcal{P}_{\mu\nu\rho\sigma}$, which can be used to project out the real graviton wave function, due to the relations of the 5 helicity states of the tensor boson [99]:

$$\mathcal{P}_{\mu\nu,\alpha\beta}(p) = \sum_{\lambda=\pm 2,\,\pm 1,0} \epsilon_{\mu\nu}(p,\lambda)\epsilon_{\alpha\beta}(p,\lambda)^*, \tag{B.25}$$

and

$$\epsilon^{\mu\nu}(p,\lambda)\epsilon_{\mu\nu}(p,\lambda')^* = \delta_{\lambda\lambda'}, \tag{B.26}$$

with $p \equiv q_1 + q_2$, and the helicity λ is got from the pseudo-particle's wavefunction, or equation (B.21).

Now we can get the true graviton tensor wave function by calling the subroutine

$$\texttt{CALL TXXXXX}(\texttt{P}, m_T, \lambda, \texttt{+1}, \texttt{ TC}) \tag{B.27}$$

Finally, the output `VERTEX` is

$$\begin{aligned}\texttt{VERTEX} =& \frac{8\pi^2}{m_T}\rho(m_T)(p^2 - m_{T0}^2 + i m_{T0}\Gamma_T)T_{\mu\nu}T_0^{\mu\nu} \\ & \times \theta(m_T - M_{low})\theta(M_{up} - m_T),\end{aligned} \tag{B.28}$$

where θ represents the Heaviside step function. In equation (B.28), we include the mass density factor, the inverse graviton propagator, and the compensation factor for the decay phase space.

UPSXXX

This subroutine computes an off-shell graviton tensor current `U`, made from the flowing-out auxiliary `S`calar and `P`esudo-particles, by the x_1x_2`T` vertex, and should be called as

`CALL UPSXXX(PC, SC, GP, TMASS0, TWIDTH, UPS)`

The output UPS is a complex 18-dimensional array, which is indeed got simply by calling inside `UPSXXX`

`CALL TXXXXX(P,` m_T`, λ, +1, UPS)`. (B.29)

and including the step functions in equation (B.28).

Appendix C

ALOHA

Automatic Libraries Of Helicity Amplitudes for Feynman diagram computations

ALOHA is a package for the automation of the HELAS (HELicity Amplitude Subroutines) library [101] corresponding to the Feynman rules of any in quantum field theory Lagrangian.

From the input given by the Universal FeynRules Output (UFO) [157], ALOHA produces the complete set of routines, wave-functions and amplitudes, that are needed for the computation of Feynman diagrams. The code is written in `Python`, but the output language can be chosen by the user between `Python`, `C++` and `Fortran`. Here, we present how ALOHA works, and show a sample application implemented in the MADGRAPH 5 framework for theories containing spin-2.

C.1 Introduction

We have seen that due to the numerous quantity of possible BSM theories that could show up at the LHC, extensive efforts are being made to automate the process of going from the Lagrangian of a new theory, to simulating events that can be then compared with data. ALOHA is one important piece of that process with the ability to automatically create helicity amplitude routines necessary for calculating the matrix element associated with any new model. Such an ability will be useful to many groups writing custom generators, however, at present the greatest impact is on the recently released MADGRAPH 5 suite [92].

Helicity amplitudes methods [165, 166, 167, 168, 169, 170, 171] are a powerful way to evaluate the squared matrix element of any process. Several Monte-Carlo (MC) event generators, matrix-element based, use such routines already at the initial stage of the calculation.

The HELAS [101] library has been a particularly successful implementation of an helicity amplitude method for tree-level processes. Amplitudes are generated by initializing a set of external wavefunctions using their helicity and momenta. These wavefunctions are combined based on the particle interactions in the Lagrangian to determine the wavefunctions of the internal lines (propagators). Once all of the wavefunctions are determined, they are combined to calculate the complex number corresponding to the amplitude for the diagram. These amplitudes can then be added and squared to give the required result. The set of routines needed to calculate amplitudes for the SM at tree-level was released in the original HELAS and successfully employed for many phenomenological studies thereafter.

C.2 Automation of the method

ALOHA basically uses the same strategy as these of HELAS. These routines consists of three categories:

External particle routines: Wavefunction routines corresponding to each external leg of a Feynman diagram. They are computed for a given momentum and helicity. The type of the particle must be given as an input. The choices are: vector, scalar, tensor or incoming/outgoing fermion.

Wavefunction/Off-shell routines: The propagator wave function, which is generated when one leg of a vertex has no associated external wave-function. These routines return both the internal wavefunction and the momentum of the propagator.

Amplitude/On-shell routines: The amplitude routines, which is computed after all the legs of a diagram are associated to a wave-function. These can be used to compute the matrix-element of the diagram by the associated amplitude routines.

To illustrate how ALOHA works from the beginning, let us start with the one example of vertex produced by the UFO. The UFO output for the $e^+e^-\gamma$ vertex is:

```
FFV = Lorentz(name = 'FFV',
              spins = [ 2, 2, 3 ],
              structure = 'Gamma(3,2,1)')
```

The `spins` attribute contains the list of spins of each particle (present in the vertex) in the `2*S+1` scheme[1]. The `structure` property collects the analytical expression for the Lorentz structure in the vertex. The arguments of the Lorentz object refer to the particle associated with each index of the object. The list of available objects and the `Python` convention for different indices are explained in Table C.1.

The UFO convention requires that:

i. positive indices are linked to the particle numbers;

ii. all Lorentz indices should be listed before spin indices;

iii. all repeated indices should be summed with the appropriate matrix;

iv. and all momenta should be incoming.

From a given UFO model structure, ALOHA creates the analytical expression linked to the associated HELAS routine by contracting the expression with a set of wavefunctions.

Now, we exemplify how ALOHA works by relating a particular vertex produced by ALOHA and HELAS. The structure shown in the `FFV` python object introduced above is `Gamma(3,2,1)`.

[1] In the case of a fermion, the first particle is considered as an incoming fermion and the second as an outgoing fermion. For interactions containing more than two fermions, the convention is that the vertex should be defined for a given fermion flow. The outgoing fermion follows directly its associated incoming fermion.

Elementary Lorentz structures	
Charge conjugation matrix: C_{ab}	`C(a,b)`
Epsilon matrix: $\epsilon^{\mu\nu\rho\sigma}$	`Epsilon(`μ`,`ν`,`ρ`,`σ`)`
Gamma matrices: $(\gamma^{\mu})_{ab}$	`Gamma(`μ`, a, b)`
Gamma5 matrix: $(\gamma^{5})_{ab}$	`Gamma5(a,b)`
(Spinorial) Kronecker delta: δ_{ab}	`Identity(a,b)`
Minkowski metric: $\eta_{\mu\nu}$	`Metric(`μ`,`ν`)`
Momenta of particle N: p_N^{μ}	`P(`μ`,N)`
Right chiral projector: $\left(\frac{1+\gamma 5}{2}\right)_{ab}$	`ProjP(a,b)`
Left chiral projector $\left(\frac{1-\gamma 5}{2}\right)_{ab}$	`ProjM(a,b)`
Sigma matrices: $(\sigma^{\mu\nu})_{ab}$	`Sigma(`μ`,`ν`,a,b)`
Scalar wavefunction: ϕ_N	Scalar(N)
Spinor wavefunction: ψ_N^a	Spinor(a,N)
Vector wavefunction: ϵ_{μ}^N	Vector(μ,N)
Spin2 wavefunction: $T_N^{\mu,\nu}$	Spin2(μ,ν,N)

Table C.1: The greek indices stands for lorentz indices while the lower case latin indices stands for spin indices. The indices N stands for the label of the particle.

Amplitude/On-shell routine

The associated amplitude routine, which was previously named `IOV` by the HELAS convention, is now:

```
Spinor(2) * Gamma(3,2,1) * Spinor(1) * Vector(3)
```

which correspond to the analytical expression:

$$\texttt{FFV_0}(\psi_1, \psi_2, \epsilon_{3\,\mu}, g) = g * \bar{u}_2 \gamma^{\mu} v_1 \epsilon_{\mu}. \tag{C.1}$$

The analytical module of ALOHA expands Eq. (C.1) component by component. The result is written to a `C++`, `Python` or `Fortran` file, language chosen by the user. For instance, the Fortran output would be:

```
C     This File is Automatically generated by ALOHA
C     The process calculated in this file is:
C     Gamma(3,2,1)
C
```

```
 SUBROUTINE FFV1_0(F1,F2,V3,COUP,VERTEX)
 IMPLICIT NONE
 DOUBLE COMPLEX F1(*)
 DOUBLE COMPLEX F2(*)
 DOUBLE COMPLEX V3(*)
 DOUBLE COMPLEX COUP
 DOUBLE COMPLEX VERTEX

 VERTEX=COUP*((F2(1)*((F1(3)*((0,-1)*V3(1)+(0,1)*V3(4)))
$ +(F1(4)*((0,1)*V3(2)+V3(3)))))+((F2(2)*((F1(3)*((0, 1)
$ *V3(2)-V3(3)))+(F1(4)*((0,-1)*V3(1)+(0,-1)*V3(4)))))
$ +((F2(3)*((F1(1)*((0,-1)*V3(1)+(0,-1)*V3(4)))+(F1(2)
$ *((0,-1)*V3(2)-V3(3)))))+(F2(4)*((F1(1)*((0,-1)*V3(2)
$ +V3(3)))+(F1(2)*((0,-1)*V3(1)+(0,1)*V3(4)))))))))
 END
```

The convention for the naming of ALOHA's routines is denoted by `NAME_X`, where `NAME` is the name provided by UFO and `X` is either `0` for an amplitude routine or the number corresponding to the off-shell particle for a wavefunction routine.

Wavefunction/Off-shell routines

To produce the necessary off-shell routines, ALOHA loops over the list of particles and replaces the on-shell wavefunction with a propagator. For particle 1, the incoming spinor is replaced by a propagator, computing[2]:

```
Spinor(2)*Gamma(3,2,1)*SpinorPropagator(1)*Vector(3)
```

which is analogous to:

$$\texttt{FFV_1}(\psi_2, \epsilon_{3\,\mu}, g, m_1, \Gamma_1) = g * \bar{\psi}_2\, \gamma^\mu \cdot i \frac{\not{p} + m_1}{p^2 - m_1^2 + i m_1 \Gamma_1}\, \epsilon_{3\mu}. \tag{C.2}$$

`FFV_1` is the wavefunction of the first spinor, and would be `FOV` in the original HELAS language. The momentum for the propagator is computed by using conservation of momentum at the vertex.

Similarly, for the outgoing spinor, we have:

$$\texttt{FFV_2}(\psi_1, \epsilon_{3\,\mu}, g, m_2, \Gamma_2) = i\, \frac{\not{p} + m_2}{p^2 - m_2^2 + i m_2 \Gamma_2} \cdot i\, \gamma^\mu\, \psi_2\, \epsilon_{3\mu}. \tag{C.3}$$

[2]The propagator object is defined internally to ALOHA.

The syntax used by ALOHA reads:

```
SpinorPropagator(2)*Gamma(3,2,1)*Spinor(1)*Vector(3)
```

which can be related to the `FIV` routine in the original HELAS language.

Finally, ALOHA also creates the routine associated to the off-shell vector. This routine returns a vector wavefunction from a pair of incoming and outgoing fermion wavefunctions, and it is written by ALOHA as:

```
Spinor(2)*Gamma(3,2,1) Spinor(1)*VectorPropagator(3)
```

analogous to the analytic expression `FFV_3`, which would be `JIO` in the original HELAS language:

$$\texttt{FFV_3}(\psi_1, \psi_2, g, m_3, \Gamma_3) = \bar{\psi_2}\, i\, \gamma_\mu\, \psi_1 \cdot -i\, \frac{\eta^{\mu\nu} - \frac{p^\mu p^\nu}{m_3^2}}{p^2 - m_3^2 + i m_3 \Gamma_3}. \tag{C.4}$$

Following the original HELAS convention, it is used the unitary gauge for massive particles and the light cone gauge for massless particles.

External particle routines

ALOHA is not designed to create external particles routines, *e.g.*, `IXXXXX` and `OXXXXX` for incoming and outgoing fermions, `VXXXXX` for vectors, `SXXXXX` for scalars and `TXXXXX` for spin-2 particles. These from HELAS are used. There is a relatively small number of such routines needed, and for this reason is reasonable to use a static library. This is incorporated into the ALOHA package, and it is available in `Python`, `C++` and `Fortran` languages.

Two additional types of special routines are needed in order to cover the full range of routines required for any type of interaction (and model):

- **Conjugate Routines:** Required by the presence of majorana fermions and of fermion flow violation [172]. In the case of the previous example, the Lorentz expression would have to be replaced by:

```
C(-2,2)*Spinor(2)*Gamma(3,2,1)*
                        Spinor(1)*Vector(3) * C(3,-3)
```

To distinguish conjugate routines from the standard ones, ALOHA adds to their name the letter `C` followed by the number of the fermion pair that is conjugated. In this case the name of the conjugate routine would be `FFVC1_X` with `X` being either `0, 1, 2` or `3` depending on the number corresponding to the amplitude or off-shell particle. Note that `_1` (`_2`) returns the wavefunctions associated to the incoming (outcoming) fermion.

- **Multiple Couplings:** In the UFO scheme each Lorentz structure is associated to a single coupling. In practice, this means that some interactions are linked to more than one Lorentz structure. However, it is convenient for the readability and the compactness of the code to have one single routine per interaction. Therefore, ALOHA defines a series of wrapper functions which call different routines associated by their couplings. The name of these wrapper routines are the concatenation of the name of the associated routines combined by an underscore. If all of the associated routines start with the same prefix (with letter S, F, V, T) then this prefix is only kept the first time. For example, the wrapper function of `FFV1_X` and `FFV2_X` will be called `FFV1_2_X`.

In some cases, this method provides redundancy. Consider a four-Higgs-interaction. Due to the symmetry of the Lorentz structure, the four wavefunction routines will each have the same content. This type of symmetry is detected automatically by ALOHA and the computation is done only once. However, in order to simplify the work of the matrix element generator, all four routines are explicitly defined and have their own names. The first one is computed and the remaining three are written as an alias of the first one.

C.3 ALOHA output

The major advantage of ALOHA comes from using it in combination with a MC event generator. To this aim, ALOHA offers two options. The first is to use ALOHA as a standalone program. The user can call ALOHA from the shell:

```
./bin/aloha UFO_path[-f Fortran|Python|CPP][-o output_dir]
```

where `UFO_path` is the path to the UFO model directory, and the two possible arguments are

- the language in which the routine should be written (default is `Fortran`).
- the path for the output directory (which is by default `UFO_path/LANGUAGE`, where `LANGUAGE` can be either `Fortran`, `Python` or `C++`).

The second possibility is to internally link the ALOHA code to a MC event generator. This option is only possible for a generator written in `Python`, and is currently used by MADGRAPH version 5. For each process MADGRAPH requests a set of helicity routines, which is produced by ALOHA. This first implementation of ALOHA inside a matrix element generator played an essential role in fully validating the package.

C.4 Checks and validation

To validate ALOHA, we use two different versions of MADGRAPH to compute values for the square of the matrix element, given a specific phase-space point of a known process. We employ MADGRAPH version 4.4.44, which uses the original HELAS routines, and compare the results with those from MADGRAPH version 5.1.1.0, which uses the new ALOHA routines.

The comparison is made by specifying a point of phase space and a center-of-mass energy, after fixing properly the set of external parameters. The values for each matrix element squared are computed, and the difference is given by ΔD:

$$\Delta D = 2 \times \frac{|\mathcal{M}(\texttt{ALOHA})|^2 - |\mathcal{M}(\texttt{HELAS})|^2}{|\mathcal{M}(\texttt{ALOHA})|^2 + |\mathcal{M}(\texttt{HELAS})|^2}. \tag{C.5}$$

Due to effects of numerical precision, one can not expect exact agreement between the two codes. Instead, the test is considered to pass if values of the squared matrix element computed by ALOHA and HELAS agree to at least five orders of magnitude, *i.e.*, $\Delta D \leq 1 \times 10^{-5}$.

Such tests are carried out for different processes based on the Standard Model (SM), the Minimal Supersymmetric Model (MSSM) and the Randall-Sundrum type I (RS-I) model, the latter including spin-2 particles. Additional tests are made by checking gauge and Lorentz invariance of each process. We observe a great agreement for all processes, as exemplified in Table C.2 for the SM and the MSSM.

C.4.1 Spin-2 validation checks

We have seen that several models with extra dimensions have recently been proposed. Examples of such theories include the Large Extra Dimensional model (or ADD) [1,2,3] and Randall-Sundrum (RS) models [5,4]. These models contain spin-2 particles allowed to propagate through higher dimensional space-time that couple to the SM particles in a very particular way. To complement the implementation of the

SM processes		MSSM processes	
Process	ΔD	**Process**	ΔD
$e^+ e^- \to \gamma\,\gamma$	1.512×10^{-7}	$e_R^+ W^+ \to e_R^+ W^+$	5.544×10^{-8}
$e^- \bar{\nu}_e \to \gamma\, W^-$	4.541×10^{-8}	$H_2 W^+ \to H_3 W^+$	1.108×10^{-8}
$\gamma\, e^- \to \nu_e W^-$	4.545×10^{-8}	$e_L^+ W^- \to e_L^+ H^-$	5.285×10^{-9}
$b\ e^- \to b\ e^-$	7.310×10^{-8}	$\nu_e \bar{\nu}_e \to H^+ H^-$	6.214×10^{-9}
$e^+ \bar{\nu}_e \to e^+ \bar{\nu}_e$	3.911×10^{-8}	$e_L^+ \bar{\nu}_e \to e_L^+ \bar{\nu}_e$	5.987×10^{-8}
$e^+ Z \to \gamma\, e^+$	5.458×10^{-8}	$e^+ e_L^- \to s\nu_e \bar{\nu}_e$	1.792×10^{-9}
$\nu_e \bar{\nu}_e \to e^+ e^-$	7.164×10^{-8}	$e^+ e_R^- \to H^- x_1^+$	6.679×10^{-9}
$\nu_e W^- \to \gamma\, e^-$	4.545×10^{-8}	$e_L^+ e_L^- \to \mu^+ \mu^-$	1.984×10^{-9}
$\bar{\nu}_e Z \to \bar{\nu}_e Z$	$< 1.0\times10^{-10}$	$e_L^- x_1^+ \to H_2 \nu_e$	3.028×10^{-8}
$\gamma\, g \to t\, t$	7.528×10^{-8}	$s\nu_e x_1^- \to \nu_e W^-$	3.714×10^{-8}
$g\, t \to t\, Z$	3.173×10^{-8}	$H^- s\nu_e \to \nu_e x_1^-$	1.039×10^{-8}
$t\, t\ \to W^+ W^-$	1.833×10^{-8}	$e_R^+ H^- \to e_R^+ W^-$	7.992×10^{-9}
$b\ W^- \to b\ W^-$	6.291×10^{-9}	$x_1^+ x_1^+ \to x_1^+ x_1^+$	2.863×10^{-8}
$W^+ W^- \to Z\, Z$	1.666×10^{-7}	$H_2 x_1^- \to e^- s\bar{\nu}_e$	1.527×10^{-7}
$Z\, Z \to e^+ e^-$	1.162×10^{-7}	$e_L^- W^+ \to \gamma\, e^- x_1^+$	6.045×10^{-7}
$e^- W^- \to e^- W^- Z$	9.767×10^{-8}	$u_R W^- \to g\, u_R W^-$	5.029×10^{-9}
$\nu_e Z \to \gamma\, e^- W^+$	2.692×10^{-8}	$n_1 Z \to u_R \bar{u} Z$	8.805×10^{-10}
$u\, \bar{\nu}_e \to \gamma\, u\, \bar{\nu}_e$	1.179×10^{-7}	$\gamma\, e_L^- \to e^- s\nu_e \bar{\nu}_e$	4.001×10^{-9}
$t\, \bar{\nu}_e \to e^+ t\, W^-$	8.095×10^{-8}	$e^- x_1^+ \to \nu_e W^+ x_1^-$	3.355×10^{-7}
$\bar{\nu}_e W^+ \to b\, b\ e^+$	8.430×10^{-8}	$s\bar{\nu}_e x_1^+ \to e^+ \nu_e \bar{\nu}_e$	6.548×10^{-8}
$\gamma\, d \to d\, e^+ e^-$	6.045×10^{-8}	$e^+ x_1^- \to s\bar{\nu}_e u_R \bar{u}_R$	1.116×10^{-10}
$\bar{u}\, Z \to e^+ e^- \bar{u}$	3.816×10^{-8}	$n_1 s\nu_e \to \nu_e \nu_e \bar{\nu}_e$	2.176×10^{-9}
$d\, \bar{d} \to H\, \nu_e \bar{\nu}_e$	2.566×10^{-8}	$g\, u_L \to e^- e_R^+ u$	3.677×10^{-10}
$H\, Z \to g\, t\, t$	2.457×10^{-8}	$go\, go \to u_R \bar{u}_R Z$	1.089×10^{-7}
$t\, t\ \to u\, \bar{u}\, Z$	3.962×10^{-8}	$go\, u_R \to u\, Z\, Z$	1.526×10^{-10}
$t\, W^- \to e^- t\, \bar{\nu}_e$	4.744×10^{-8}	$\bar{u}\, \nu_e \to g\, s\nu_e \bar{u}_L$	1.233×10^{-8}
$b\, t\ \to \gamma\, b\, t$	7.409×10^{-8}	$e^+ u_L \to e^+ u_L Z$	1.542×10^{-8}
$t\ Z \to d\, \bar{d}\, t$	2.224×10^{-8}	$e_R^- \bar{u}_R \to e^- g\, \bar{u}$	2.204×10^{-7}
$b\ Z \to b\ Z\, Z$	8.196×10^{-8}	$e^- e_L^+ \to n_1\, u\, \bar{u}$	2.122×10^{-8}
$W^+ W^- \to d\, \bar{d}\, H$	9.519×10^{-8}	$\bar{\nu}_e \bar{\nu}_e \to e_L^+ \bar{\nu}_e x_1^-$	4.661×10^{-8}

Table C.2: Example of the results obtained by the validation tests for SM and MSSM processes.

RS processes	
Process	$\mathbf{\Delta}D$
$g\,u \to u\,y$	$< 1.0\times10^{-10}$
$b\,y \to b\,g$	$< 1.0\times10^{-10}$
$\bar{t}\,y \to g\,\bar{t}$	$< 1.0\times10^{-10}$
$g\,y \to t\,\bar{t}$	$< 1.0\times10^{-10}$
$g\,t \to t\,y$	$< 1.0\times10^{-10}$
$g\,g \to g\,y$	$< 1.0\times10^{-10}$
$\bar{t}\,y \to g\,g\,\bar{t}$	9.766×10^{-10}
$g\,g \to g\,g\,y$	3.979×10^{-10}
$b\,g \to b\,g\,y$	8.009×10^{-10}
$b\,\bar{b} \to b\,\bar{b}\,y$	1.864×10^{-9}
$\bar{b}\,\bar{t} \to \bar{b}\,\bar{t}\,y$	7.411×10^{-10}
$t\,\bar{t} \to b\,\bar{b}\,y$	1.928×10^{-10}

Table C.3: Example of the results obtained by the validation tests for RS processes.

ALOHA helicity routines, it is interesting to test and validate spin-2 routines comparing it to the HELAS implementation [99].

Using FEYNRULES, we implement a reduced version of the RS model [173]: it contains only the first mode of the spin-2 particle explicitly defined (which is denominated `y`), which couples to SM particles. Validation tests, similar to the ones presented above for the SM and MSSM, are performed. Approximately 500 $2 \to 2$ and 2000 $2 \to 3$ processes are tested, and some examples can be found in Table C.3. We obtain a full agreement between routines obtained with the use of HELAS and ALOHA.

C.4.2 Goldstino validation checks

Similarly to what has been performed for the SM, MSSM and RS theories, a simplified SUSY theory that includes goldstino interactions has been implemented in MADGRAPH/MADEVENT via the FEYNRULES package [156]. Since the goldstino is the helicity $\pm 1/2$ component of the gravitino, it can be treated by ALOHA. A comparison of the values of the matrix element squared obtained by ALOHA against these obtained with the use of HELAS [98, 100] has been performed. A full agreement is again obtained.

The next step is to add the treatment of spin-3/2 particles by ALOHA, which is not yet completed. However, since in Chapter 6 we have shown that goldstino particles are the relevant components of gravitino production at the LHC, for the phenomenological studies of gravitino emission (at the LHC) it is enough that MADGRAPH/MADEVENT handle goldstino particles.

Bibliography

[1] N. Arkani-Hamed, S. Dimopoulos, and G. Dvali, "Phenomenology, astrophysics, and cosmology of theories with submillimeter dimensions and TeV scale quantum gravity", *Physical Review D*, vol. 59, no. 8, p. 51, 1999, hep-ph/9807344.

[2] N. Arkani-Hamed, S. Dimopoulos, and G. Dvali, "The Hierarchy Problem and New Dimensions at a Millimeter", *Physics Letters B*, vol. 429, no. 3-4, p. 16, 1998, hep-ph/9803315.

[3] I. Antoniadis, "New dimensions at a millimeter to a fermi and superstrings at a TeV", *Physics Letters B*, vol. 436, no. 3-4, pp. 257–263, 1998, hep-ph/9804398.

[4] L. Randall and R. Sundrum, "A Large Mass Hierarchy from a Small Extra Dimension", *Physical Review Letters*, vol. 83, no. 17, p. 9, 1999, hep-ph/9905221.

[5] L. Randall and R. Sundrum, "An Alternative to Compactification", *Physical Review Letters*, vol. 83, no. 23, p. 9, 1999, hep-th/9906064.

[6] G. Dvali and M. Redi, "Black hole bound on the number of species and quantum gravity at CERN LHC", *Physical Review D*, vol. 77, no. 4, p. 15, 2008, 0710.4344.

[7] G. Dvali, "Black holes and large N species solution to the hierarchy problem", *Fortschritte der Physik*, vol. 58, no. 6, pp. 528–536, 2010, 0706.2050.

[8] G. Dvali, G. Gabadadze, M. Kolanović, and F. Nitti, "Scales of gravity", *Physical Review D*, vol. 65, no. 2, p. 51, 2001, hep-th/0106058.

[9] X. Calmet, M. Graesser, and S. Hsu, "Minimum Length from First Principles", *Int. J. Mod. Phys.*, vol. D14, pp. 2195–2200, 2005, hep-th/0505144.

[10] X. Calmet, M. Graesser, and S. Hsu, "Minimum Length from Quantum Mechanics and Classical General Relativity", *Physical Review Letters*, vol. 93, no. 21, pp. 19–22, 2004.

[11] X. Calmet, S. Hsu, and D. Reeb, "Quantum gravity at a TeV and the renormalization of Newton's constant", *Physical Review D*, vol. 77, no. 12, pp. 1–5, 2008.

[12] E. Noether, "Invariante Variationsprobleme", *Nachr. d. Konig. Gesellsch. d. Wiss. zu Gottingen*, no. Math-phys. Klasse, pp. 235–257, 1918.

[13] S. Glashow, "Partial-symmetries of weak interactions", *Nuclear Physics*, vol. 22, no. 4, pp. 579–588, 1961.

[14] A. Salam and J. Ward, "Electromagnetic and weak interactions", *Physics Letters*, vol. 13, no. 2, pp. 168–171, 1964.

[15] S. Weinberg, "A Model of Leptons", *Physical Review Letters*, vol. 19, no. 21, pp. 1264–1266, 1967.

[16] A. Salam, "Elementary Particle Theory", in *The Nobel Symposium n^o 8* (N. Svartholm, ed.), p. 367, Almqvist and Wiksell, Stockholm, 1968.

[17] MissMJ and E. Rusack, "The particle content of the Standard Model." `[http://cms.web.cern.ch/news/what-do-we-already-know]`.

[18] G. Guralnik, C. Hagen, and T. Kibble, "Global Conservation Laws and Massless Particles", *Physical Review Letters*, vol. 13, no. 20, pp. 585–587, 1964.

[19] P. Higgs, "Broken Symmetries and the Masses of Gauge Bosons", *Physical Review Letters*, vol. 13, no. 16, pp. 508–509, 1964.

[20] F. Englert and R. Brout, "Broken Symmetry and the Mass of Gauge Vector Mesons", *Physical Review Letters*, vol. 13, no. 9, pp. 321–323, 1964.

[21] S. F. Novaes, "Standard Model: An Introduction", p. 101, 2000, hep-ph/0001283.

[22] M. E. Peskin and D. V. Schroeder, *An Introduction To Quantum Field Theory*. Westview Press; Reprint edition, 1995.

[23] P. Langacker, "Introduction to the Standard Model and Electroweak Physics", 2009, 0901.0241.

[24] S. de Visscher, *Observability of an unconventional two-Higgs-doublet model at the LHC*. PhD thesis, Universite Catholique de Louvain, 2009.

[25] K. Nakamura, "Review of Particle Physics", *Journal of Physics G: Nuclear and Particle Physics*, vol. 37, no. 7A, p. 075021, 2010.

[26] M. Baak, M. Goebel, J. Haller, A. Hoecker, D. Ludwig, K. Moenig, M. Schott, and J. Stelzer, "Updated Status of the Global Electroweak Fit and Constraints on New Physics", p. 58, 2011, 1107.0975.

[27] W. Murray, "LHC Higgs Boson searches", 2012, 1201.4576.

[28] LHC Higgs Cross Section Working Group, S. Dittmaier, and Others, "Handbook of LHC Higgs Cross Sections: 2. Differential Distributions", *CERN-2012-002*, p. 275, 2012, 1201.3084.

[29] CMS Collaboration, "Combined results of searches for the standard model Higgs boson in pp collisions at sqrt(s) = 7 TeV", *submitted to Physics Letters B*, vol. 600, 2012, 1202.1488.

[30] S. Dawson, "Introduction to Electroweak Symmetry Breaking", pp. 1–83, 1999, hep-ph/9901280.

[31] L. Wolfenstein, "Parametrization of the Kobayashi-Maskawa Matrix", *Physical Review Letters*, vol. 51, no. 21, pp. 1945–1947, 1983.

[32] C. S. Wu, E. Ambler, R. W. Hayward, D. D. Hoppes, and R. P. Hudson, "Experimental Test of Parity Conservation in Beta Decay", *Phys. Rev.*, vol. 105, no. 4, pp. 1413–1415, 1957.

[33] T. D. Lee and C. N. Yang, "Question of Parity Conservation in Weak Interactions", *Phys. Rev.*, vol. 104, no. 1, pp. 254–258, 1956.

[34] D. Griffiths, *Introduction to Elementary Particles*. Wiley-VCH, 2008.

[35] J. H. Christenson, J. W. Cronin, V. L. Fitch, and R. Turlay, "Evidence for the 2π Decay of the K_2^0 Meson", *Physical Review Letters*, vol. 13, no. 4, pp. 138–140, 1964.

[36] B. Aubert and Babar Collaboration, "Measurement of CP-Violating Asymmetries in B0 Decays to CP Eigenstates", *Physical Review Letters*, vol. 86, no. 12, pp. 2515–2522, 2001.

[37] A. Abashian and Others, "Measurement of the CP Violation Parameter sin2ϕ1 in Bd0 Meson Decays", *Physical Review Letters*, vol. 86, no. 12, pp. 2509–2514, 2001.

[38] A. B. Carter and A. I. Sanda, "CP violation in B-meson decays", *Phys. Rev. D*, vol. 23, no. 7, pp. 1567–1579, 1981.

[39] R. D. Peccei and H. R. Quinn, "Constraints imposed by CP conservation in the presence of pseudoparticles", *Physical Review D*, vol. 16, no. 6, pp. 1791–1797, 1977.

[40] R. D. Peccei and H. R. Quinn, "CP Conservation in the Presence of Pseudoparticles", *Physical Review Letters*, vol. 38, no. 25, pp. 1440–1443, 1977.

[41] K. Freeman and G. McNamara, *In Search of Dark Matter (Springer Praxis Books / Space Exploration)*. Springer, 2006.

[42] L. Bergström, "Non-baryonic dark matter: observational evidence and detection methods", *Reports on Progress in Physics*, vol. 63, no. 5, pp. 793–841, 2000, hep-ph/0002126.

[43] NASA/WMAP Science team, "What is the Universe made of?", [http://map.gsfc.nasa.gov/universe/uni_matter.html].

[44] J. Silk, "Dark Matter", [http://astro.berkeley.edu/~mwhite/darkmatter/essay].

[45] J. Donoghue, "General relativity as an effective field theory: The leading quantum corrections", *Physical Review D*, vol. 50, no. 6, pp. 3874–3888, 1994, gr-qc/9405057.

[46] A. Zee, *Quantum Field Theory in a Nutshell*. Princeton University Press, 2003.

[47] S. Weinberg, *Gravitation and Cosmology: Principles and Applications of the General Theory of Relativity*. John Wiley & Sons, Inc., 1972.

[48] M. Fierz and W. Pauli, "On Relativistic Wave Equations for Particles of Arbitrary Spin in an Electromagnetic Field", *Proceedings of the Royal Society A: Mathematical, Physical and Engineering Sciences*, vol. 173, no. 953, pp. 211–232, 1939.

[49] T. Han, J. Lykken, and R.-J. Zhang, "Kaluza-Klein states from large extra dimensions", *Physical Review D*, vol. 59, no. 10, p. 28, 1999, hep-ph/9811350.

[50] J. Donoghue, "Leading quantum correction to the Newtonian potential", *Physical Review Letters*, vol. 72, no. 19, pp. 2996–2999, 1994, gr-qc/9310024.

[51] M. Atkins and X. Calmet, "On the unitarity of linearized General Relativity coupled to matter", *Physics Letters B*, vol. 695, no. 1-4, pp. 298–302, 2011.

[52] X. Calmet, "A review of Quantum Gravity at the Large Hadron Collider", p. 32, 2010, 1005.1805.

[53] T. Kaluza, "Zum Unitatsproblem der Physik.", *Berl. Ber.*, vol. 1921, pp. 966–972, 1921.

[54] A. Pérez-Lorenzana, "An introduction to extra dimensions", *Journal of Physics: Conference Series*, vol. 18, pp. 224–269, 2005, hep-ph/0503177.

[55] E. Mirabelli, M. Perelstein, and M. Peskin, "Collider Signatures of New Large Space Dimensions", *Physical Review Letters*, vol. 82, no. 11, pp. 2236–2239, 1999, hep-ph/9811337.

[56] G. Giudice and R. Rattazzi, "Quantum gravity and extra dimensions at high-energy colliders", *Nuclear Physics B*, vol. 544, no. 1-2, pp. 3–38, 1999, hep-ph/9811291.

[57] K. Agashe, "Extra Dimensions", in *Colliders and Neutrinos: The Window into Physics Beyond the Standard Model TASI 2006* (S. Dawson and R. N. Mohapatra, eds.), World Scientific Publishing Company, 2008.

[58] S. Dubovsky, V. Rubakov, and P. Tinyakov, "Brane world: Disappearing massive matter", *Physical Review D*, vol. 62, no. 10, p. 14, 2000, hep-th/0006046.

[59] W. Goldberger and M. Wise, "Bulk fields in the Randall-Sundrum compactification scenario", *Physical Review D*, vol. 60, no. 10, p. 8, 1999, hep-ph/9907218.

[60] T. Gherghetta and A. Pomarol, "Bulk Fields and Supersymmetry in a Slice of AdS", *Nuclear Physics B*, vol. 586, no. 1-2, p. 22, 2000, hep-ph/0003129.

[61] B. C. Allanach, K. Odagiri, M. J. Palmer, M. A. Parker, A. Sabetfakhri, and B. R. Webber, "Exploring Small Extra Dimensions at the Large Hadron Collider", *Journal of High Energy Physics*, vol. 2002, no. 12, pp. 039–039, 2002.

[62] K. Hinterbichler, "Theoretical Aspects of Massive Gravity", 2011, 1105.3735.

[63] R. Balian and J. Zinn-Justin, *Methods in Field Theory (Les Houches Summer School Proceedings)*. World Scientific Publishing Co Pte Ltd, 1981.

[64] R. P. Feynman, F. B. Morínigo, W. G. Wagner, and B. Hatfield, *Feynman lectures on gravitation*. Penguin Press Science Series, Penguin, 1999.

[65] H. Van Dam and M. Veltman, "On the mass of the graviton", *GRG*, vol. 3, no. 3, pp. 215– 220, 1972.

[66] H. Van Dam and M. Veltman, "Massive and Massless Yang-Mills and gravitational fields", *Nuclear Physics*, vol. 22, no. B, pp. 397–411, 1970.

[67] D. Dicus and S. Willenbrock, "Angular momentum content of a virtual graviton", *Physics Letters B*, vol. 609, no. 3-4, p. 5, 2004, hep-ph/0409316.

[68] B. R. Holstein, "Graviton physics", *American Journal of Physics*, vol. 74, no. 11, p. 1002, 2006, gr-qc/0607045.

[69] J. M. Campbell, J. W. Huston, and W. J. Stirling, "Hard interactions of quarks and gluons: a primer for LHC physics", *Reports on Progress in Physics*, vol. 70, no. 1, pp. 89–193, 2007, hep-ph/0611148.

[70] E. Halkiadakis, "Proceedings for TASI 2009 Summer School on "Physics of the Large and the Small": Introduction to the LHC experiments", p. 32, 2010, 1004.5564.

[71] C. Lefèvre, "Ilustration of the CERN accelerator complex.", `[http://cdsweb.cern.ch/record/1260465]`, 2008.

[72] R. K. Ellis, W. J. Stirling, and B. R. Webber, *QCD and collider physics*. Cambridge University Press, 2003.

[73] F. Maltoni, T. McElmurry, R. Putman, and S. Willenbrock, "Choosing the Factorization Scale in Perturbative QCD", p. 25, 2007, hep-ph/0703156.

[74] C. Quigg, "LHC Physics Potential vs. Energy: Considerations for the 2011 Run", *FERMILAB–FN–0913–T*, p. 33, 2011, 1101.3201.

[75] J. Pumplin, D. R. Stump, J. Huston, H.-L. Lai, P. Nadolsky, and W.-K. Tung, "New Generation of Parton Distributions with Uncertainties from Global QCD Analysis", *Journal of High Energy Physics*, vol. 2002, no. 07, pp. 012–012, 2002, hep-ph/0201195.

[76] G. P. Salam, "Elements of QCD for hadron colliders", no. June 2009, p. 56, 2010, 1011.5131.

[77] G. P. Salam, "Towards Jetography", p. 95, 2009, 0906.1833.

[78] G. Sterman, "Jets from Quantum Chromodynamics", *Physical Review Letters*, vol. 39, no. 23, pp. 1436–1439, 1977.

[79] G. P. Salam and G. Soyez, "A practical seedless infrared-safe cone jet algorithm", *Journal of High Energy Physics*, vol. 2007, no. 05, pp. 086–086, 2007, 0704.0292.

[80] S. Catani, Y. Dokshitzer, M. Olsson, G. Turnock, and B. R. Webber, "New clustering algorithm for multijet cross sections in e^+e^- annihilation", *Physics Letters B*, vol. 269, no. 3-4, pp. 432–438, 1991.

[81] S. Catani, Y. Dokshitzer, M. H. Seymour, and B. R. Webber, "Longitudinally-invariant k_T-clustering algorithms for hadron-hadron collisions", *Nuclear Physics B*, vol. 406, no. 1-2, pp. 187–224, 1993.

[82] S. D. Ellis and D. E. Soper, "Successive Combination Jet Algorithm For Hadron Collisions", *Physical Review D*, vol. 48, no. 7, p. 18, 1993, hep-ph/9305266.

[83] M. Cacciari, G. P. Salam, and G. Soyez, "The anti-k_t jet clustering algorithm", *Journal of High Energy Physics*, vol. 2008, no. 04, p. 12, 2008, 0802.1189.

[84] C. Anastasiou, L. Dixon, K. Melnikov, and F. Petriello, "High-precision QCD at hadron colliders: Electroweak gauge boson rapidity distributions at next-to-next-to leading order", *Physical Review D*, vol. 69, no. 9, 2004, hep-ex/0312266.

[85] G. Ossola, C. G. Papadopoulos, and R. Pittau, "CutTools : a program implementing the OPP reduction method to compute one-loop amplitudes", *Journal of High Energy Physics*, vol. 2008, no. 03, pp. 042–042, 2008, 0711.3596.

[86] R. Frederix, S. Frixione, F. Maltoni, and T. Stelzer, "Automation of next-to-leading order computations in QCD: the FKS subtraction", *Journal of High Energy Physics*, vol. 2009, no. 10, pp. 003–003, 2009, 0908.4272.

[87] V. Hirschi, R. Frederix, S. Frixione, M. Vittoria Garzelli, F. Maltoni, and R. Pittau, "Automation of one-loop QCD computations", *Journal of High Energy Physics*, vol. 2011, no. 5, p. 64, 2011, 1103.0621.

[88] T. Gleisberg, S. Hoeche, F. Krauss, A. Schaelicke, S. Schumann, and J. Winter, "SHERPA 1.alpha, a proof-of-concept version", *Journal of High Energy Physics*, vol. 2004, no. 02, p. 28, 2003, hep-ph/0311263.

[89] A. Pukhov, "CalcHEP 2.3: MSSM, structure functions, event generation, batchs, and generation of matrix elements for other packages", pp. 1–31, 2004, hep-ph/0412191.

[90] E. Boos, V. Bunichev, M. Dubinin, L. Dudko, V. Edneral, V. Ilyin, A. Kryukov, V. Savrin, A. Semenov, and A. Sherstnev, "CompHEP 4.4—automatic computations from Lagrangians to events", *Nuclear Instruments and Methods in Physics Research Section A: Accelerators, Spectrometers, Detectors and Associated Equipment*, vol. 534, no. 1-2, pp. 250–259, 2004, hep-ph/0403113.

[91] J. Alwall, P. Demin, S. de Visscher, R. Frederix, M. Herquet, F. Maltoni, T. Plehn, D. L. Rainwater, and T. Stelzer, "MadGraph/MadEvent v4: the new web generation", *Journal of High Energy Physics*, vol. 2007, no. 09, pp. 028–028, 2007, 0706.2334.

[92] J. Alwall, M. Herquet, F. Maltoni, O. Mattelaer, and T. Stelzer, "MadGraph 5: going beyond", *Journal of High Energy Physics*, vol. 2011, no. 6, p. 37, 2011, 1106.0522.

[93] T. Stelzer and W. Long, "Automatic generation of tree level helicity amplitudes", *Computer Physics Communications*, vol. 81, no. 3, pp. 357–371, 1994, hep-ph/9401258.

[94] F. Maltoni and T. Stelzer, "MadEvent: automatic event generation with MadGraph", *Journal of High Energy Physics*, vol. 2003, no. 02, pp. 027–027, 2003.

[95] M. L. Mangano, F. Piccinini, A. D. Polosa, M. Moretti, and R. Pittau, "ALPGEN, a generator for hard multiparton processes in hadronic collisions", *Journal of High Energy Physics*, vol. 2003, no. 07, pp. 001–001, 2003, hep-ph/0206293.

[96] A. Cafarella, C. G. Papadopoulos, and M. Worek, "Helac-Phegas: A generator for all parton level processes", *Computer Physics Communications*, vol. 180, no. 10, pp. 1941–1955, 2009, 0710.2427.

[97] W. Kilian, T. Ohl, and J. Reuter, "WHIZARD: Simulating Multi-Particle Processes at LHC and ILC", *The European Physical Journal C*, vol. 71, no. 9, 2007, 0708.4233.

[98] K. Mawatari and Y. Takaesu, "HELAS and MadGraph with goldstinos", *The European Physical Journal C*, vol. 71, no. 6, pp. 1–10, 2011.

[99] K. Hagiwara, J. Kanzaki, Q. Li, and K. Mawatari, "HELAS and MadGraph/MadEvent with spin-2 particles", *The European Physical Journal C*, vol. 56, no. 3, pp. 435–447, 2008, 0805.2554.

[100] K. Hagiwara, K. Mawatari, and Y. Takaesu, "HELAS and MadGraph with spin-3/2 particles", *The European Physical Journal C*, vol. 71, no. 1, pp. 1–14, 2011.

[101] H. Murayama, I. Watanabe, and K. Hagiwara, "HELAS: HELicity amplitude subroutines for Feynman diagram evaluations", KEK-91-11 [http://www-lib.kek.jp/cgi-bin/img_index?199124011], 1992.

[102] P. de Aquino, W. Link, F. Maltoni, O. Mattelaer, and T. Stelzer, "ALOHA: Automatic Libraries Of Helicity Amplitudes for Feynman diagram computations", p. 20, 2011, 1108.2041.

[103] R. C. Group, *Measurement of the inclusive jet cross section using the midpoint algorithm in Run II at the Collider Detector at Fermilab (CDF)*. PhD thesis, University of Florida, 2006.

[104] T. Sjöstrand, S. Mrenna, and P. Skands, "A brief introduction to PYTHIA 8.1", *Computer Physics Communications*, vol. 178, no. 11, pp. 852–867, 2008, 0710.3820.

[105] G. Corcella, I. G. Knowles, G. Marchesini, S. Moretti, K. Odagiri, P. Richardson, M. H. Seymour, and B. R. Webber, "HERWIG 6: an event generator for hadron emission reactions with interfering gluons (including supersymmetric processes)", *Journal of High Energy Physics*, vol. 2001, no. 01, 2001, hep-ph/0011363.

[106] L. Lönnblad, "Ariadne version 4 — A program for simulation of QDC cascades implementing the colour dipole model", *Computer Physics Communications*, vol. 71, no. 1-2, pp. 15–31, 1992.

[107] F. Krauss, "Matrix Elements and Parton Showers in Hadronic Interactions", *Journal of High Energy Physics*, vol. 2002, no. 08, pp. 015–015, 2002.

[108] S. Catani, F. Krauss, B. R. Webber, and R. Kuhn, "QCD Matrix Elements + Parton Showers", *Journal of High Energy Physics*, vol. 2001, no. 11, pp. 063–063, 2001, hep-ph/0109231.

[109] J. Alwall, S. Höche, F. Krauss, N. Lavesson, L. Lönnblad, F. Maltoni, M. Mangano, M. Moretti, C. Papadopoulos, F. Piccinini, S. Schumann, M. Treccani, J. Winter, and M. Worek, "Comparative study of various algorithms for the merging of parton showers and matrix elements in hadronic collisions", *The European Physical Journal C*, vol. 53, no. 3, pp. 473–500, 2007, 0706.2569.

[110] F. Caravaglios, "A new approach to multi-jet calculations in hadron collisions", *Nuclear Physics B*, vol. 539, no. 1-2, pp. 215–232, 1999, hep-ph/9807570.

[111] S. Hoeche, F. Krauss, N. Lavesson, L. Lonnblad, M. Mangano, A. Schaelicke, and S. Schumann, "Matching Parton Showers and Matrix Elements", 2006, [hep-ph/0602031].

[112] X. Calmet and P. de Aquino, "Quantum gravity at the LHC", *The European Physical Journal C*, vol. 68, no. 1-2, pp. 305–311, 2010.

[113] X. Calmet, P. de Aquino, and T. G. Rizzo, "Massless versus Kaluza–Klein gravitons at the LHC", *Physics Letters B*, vol. 682, no. 4-5, pp. 446–449, 2010.

[114] P. de Aquino, K. Hagiwara, Q. Li, and F. Maltoni, "Simulating graviton production at hadron colliders", *Journal of High Energy Physics*, vol. 2011, no. 6, 2011.

[115] L. Vacavant and I. Hinchliffe, "Signals of models with large extra dimensions in ATLAS", *Journal of Physics G: Nuclear and Particle Physics*, vol. 27, no. 8, pp. 1839–1850, 2001.

[116] CDF Collaboration and T. Aaltonen, "Search for large extra dimensions in final states containing one photon or jet and large missing transverse energy produced in p-pbar collisions at sqrt(s) = 1.96 TeV", *Physical Review Letters*, vol. 101, no. 18, pp. 1–7, 2008, 0807.3132.

[117] CDF Collaboration and A. Abulencia, "Search for Large Extra Dimensions in the Production of Jets and Missing Transverse Energy in p-pbar Collisions at sqrt(s)=1.96 TeV", *Physical Review Letters*, vol. 97, no. 17, p. 7, 2006, hep-ex/0605101.

[118] X. Calmet and M. Feliciangeli, "Bound on four-dimensional Planck mass", *Physical Review D*, vol. 78, no. 6, pp. 1–3, 2008.

[119] T. G. Rizzo, "Unique signatures of unparticle resonances at the LHC", *Journal of High Energy Physics*, vol. 2008, no. 11, pp. 039–039, 2008, 0809.4659.

[120] P. Nadolsky, H.-L. Lai, Q.-H. Cao, J. Huston, J. Pumplin, D. Stump, W.-K. Tung, and C.-P. Yuan, "Implications of CTEQ global analysis for collider observables", *Physical Review D*, vol. 78, no. 1, p. 32, 2008, 0802.0007.

[121] J. M. Butterworth and Others, "The tools and Monte Carlo working group: Summary Report from the Les Houches 2009 Workshop on TeV Colliders", p. 144, 2010, 1003.1643.

[122] S. Karg and M. Krämer, "Next-to-leading-order QCD corrections to graviton production at hadron colliders", *Physical Review D*, vol. 81, no. 9, p. 19, 2010, 0911.5095.

[123] K. Hagiwara, P. Konar, Q. Li, K. Mawatari, and D. Zeppenfeld, "Graviton production with 2 jets at the LHC in large extra dimensions", *Journal of High Energy Physics*, vol. 2008, no. 04, pp. 019–019, 2008, 0801.1794.

[124] P. Mathews, V. Ravindran, K. Sridhar, and W. L. van Neerven, "Next-to-Leading Order QCD Corrections to the Drell-Yan Cross Section in Models of TeV-Scale Gravity", *Nuclear Physics B*, vol. 713, no. 1-3, p. 65, 2004, hep-ph/0411018.

[125] P. Mathews, V. Ravindran, and K. Sridhar, "NLO-QCD corrections to dilepton production in the Randall-Sundrum model", *Journal of High Energy Physics*, vol. 2005, no. 10, pp. 031–031, 2005, hep-ph/0506158.

[126] Q. Li, C. Li, and L. Yang, "Soft gluon resummation effects in single graviton production at the CERN Large Hadron Collider in the Randall-Sundrum model", *Physical Review D*, vol. 74, no. 5, p. 26, 2006, hep-ph/0606045.

[127] D0 Collaboration and V. M. Abazov, "Search for Large Extra Dimensions via Single Photon plus Missing Energy Final States at sqrt(s)=1.96 TeV", *Physical Review Letters*, vol. 101, no. 1, p. 011601, 2008.

[128] H. Davoudiasl, "Echoes from a Warped Dimension", *Nuclear Physics B - Proceedings Supplements*, vol. 200-202, pp. 149–158, 2010, 0909.1587.

[129] CDF Collaboration and T. Aaltonen, "A search for high-mass resonances decaying to dimuons at CDF", *Physical review letters*, vol. 102, no. 9, p. 091805, 2008, 0811.0053.

[130] D0 Collaboration and V. M. Abazov, "Search for Randall-Sundrum gravitons with 1 fb^{-1} of data from p-pbar collisions at sqrt(s)=1.96 TeV.", *Physical review letters*, vol. 100, no. 9, p. 091802, 2008.

[131] M. Rubin, G. P. Salam, and S. Sapeta, "Giant QCD K-factors beyond NLO", *Journal of High Energy Physics*, vol. 2010, no. 9, p. 38, 2010, 1006.2144.

[132] A. Djouadi, "The Anatomy of Electro-Weak Symmetry Breaking. II: The Higgs bosons in the Minimal Supersymmetric Model", *Physics Reports*, vol. 459, no. 1-6, p. 340, 2005, hep-ph/0503173.

[133] M. Drees, "An Introduction to Supersymmetry", no. November, p. 42, 1996, hep-ph/9611409.

[134] A. Djouadi, "The Higgs particles in the MSSM", *Lectures given at "Ecole de GIF 2001"*, 2001.

[135] S. P. Martin, "A Supersymmetry Primer", no. December, p. 128, 1997, hep-ph/9709356.

[136] E. Witten, "Dynamical breaking of supersymmetry", *Nuclear Physics B*, vol. 185, pp. 513–554, 1981.

[137] P. Fayet, "Mixing between gravitational and weak interactions through the massive gravitino", *Physics Letters B*, vol. 70, no. 4, pp. 461–464, 1977.

[138] P. Fayet, "Scattering cross sections of the photino and the goldstino (gravitino) on matter", *Physics Letters B*, vol. 86, no. 3-4, pp. 272–278, 1979.

[139] D. Freedman, P. van Nieuwenhuizen, and S. Ferrara, "Progress toward a theory of supergravity", *Physical Review D*, vol. 13, no. 12, pp. 3214–3218, 1976.

[140] D. Freedman and P. van Nieuwenhuizen, "Properties of supergravity theory", *Physical Review D*, vol. 14, no. 4, pp. 912–916, 1976.

[141] E. Cremmer, S. Ferrara, L. Girardello, and A. Van Proeyen, "Yang-Mills theories with local supersymmetry: Lagrangian, transformation laws and super-Higgs effect", *Nuclear Physics B*, vol. 212, no. 3, pp. 413–442, 1983.

[142] J. Wess and J. Bagger, *Supersymmetry and Supergravity*. Princeton University Press, 1992.

[143] D. G. Cerdeno and C. Munoz, "An Introduction to Supergravity", *JHEP Proceedings, 6th Corfu Hellenic School and Workshop on Elementary Particle Physics*, no. 3, pp. 1–27, 1998.

[144] T. Moroi, *Effects of the Gravitino on the Inflationary Universe*. PhD thesis, Tohoku University, hep-ph/9503210.

[145] T. Lee and G.-H. Wu, "Interactions of a Single Goldstino", *Physics Letters B*, vol. 447, no. 1-2, p. 10, 1998, hep-ph/9805512.

[146] J. Pradler, "Electroweak Contributions to Thermal Gravitino Production", p. 101, 2007, 0708.2786.

[147] M. Bolz, A. Brandenburg, and W. Buchmuller, "Thermal Production of Gravitinos", *Nuclear Physics B*, vol. 606, no. 1-2, p. 32, 2000, hep-ph/0012052.

[148] S. Weinberg, *The Quantum Theory of Fields: Volume 3, Supersymmetry: Supersymmetry v. 3*. Cambridge University Press, 2005.

[149] P. Fayet, "Weak interactions of a light gravitino: A lower limit on the gravitino mass from the decay $\psi \rightarrow$ gravitino + antiphotino", *Physics Letters B*, vol. 84, no. 4, pp. 421–426, 1979.

[150] T. E. Clark and S. T. Love, "Goldstino couplings to matter", *Physical Review D*, vol. 54, no. 9, pp. 5723–5727, 1996.

[151] J. Lopez, D. Nanopoulos, and A. Zichichi, "The Simplest, String-Derivable, Supergravity Model and its Experimental Predictions", *Physical Review D*, vol. 49, no. 1, p. 29, 1992, hep-ph/9210280.

[152] J. Lopez, D. Nanopoulos, and A. Zichichi, "Experimental consequences of one-parameter no-scale supergravity models", *International Journal Of Modern Physics*, vol. A 10, no. August 1994, pp. 4241 – 4264, 1995, hep-ph/9408345.

[153] M. Klasen and G. Pignol, "New results for light gravitinos at hadron colliders: Fermilab Tevatron limits and CERN LHC perspectives", *Physical Review D*, vol. 75, no. 11, p. 30, 2007, hep-ph/0610160.

[154] Y. Kats, P. Meade, M. Reece, and D. Shih, "The Status of GMSB After 1/fb at the LHC Introduction", 2011, arXiv:1110.6444v2.

[155] N. D. Christensen and C. Duhr, "FeynRules - Feynman rules made easy", *Computer Physics Communications*, vol. 180, no. 9, p. 63, 2008, 0806.4194.

[156] K. Mawatari, The simplified SUSY model that includes goldstino interactions implemented in MadGraph/MadEvent via FeynRules is available in the FeynRules website. [https://feynrules.irmp.ucl.ac.be].

[157] C. Degrande, C. Duhr, B. Fuks, D. Grellscheid, O. Mattelaer, and T. Reiter, "UFO The Universal FeynRules Output", *Computer Physics Communications*, vol. 183, no. 6, pp. 1201–1214, 2012, 1108.2040.

[158] CMS Collaboration, "CMS Physics Analysis Summary: Search for supersymmetry in all-hadronic events with missing energy", 2011.

[159] S. Frixione and B. R. Webber, "Matching NLO QCD computations and parton shower simulations", *Journal of High Energy Physics*, vol. 2002, no. 06, pp. 029–029, 2002, hep-ph/0204244.

[160] P. Nason, "A New Method for Combining NLO QCD with Shower Monte Carlo Algorithms", *Journal of High Energy Physics*, vol. 2004, no. 11, pp. 040–040, 2004, hep-ph/0409146.

[161] S. Alioli, P. Nason, C. Oleari, and E. Re, "A general framework for implementing NLO calculations in shower Monte Carlo programs: the POWHEG BOX", p. 57, 2010, 1002.2581.

[162] S. Frixione, F. Stoeckli, P. Torrielli, B. R. Webber, and C. D. White, "The MC@NLO 4.0 Event Generator", p. 36, 2010, 1010.0819.

[163] P. Torrielli and S. Frixione, "Matching NLO QCD computations with PYTHIA using MC@NLO", *Journal of High Energy Physics*, vol. 2010, no. 4, p. 16, 2010, 1002.4293.

[164] S. Frixione, F. Stoeckli, P. Torrielli, and B. R. Webber, "NLO QCD corrections in Herwig++ with MC@NLO", *Journal of High Energy Physics*, vol. 2011, no. 1, 2011, 1010.0568.

[165] F. A. Berends, R. Kleiss, P. De Causmaecker, R. Gastmans, and T. T. Wu, "Single Bremsstrahlung Processes in Gauge Theories", *Physics Letters B*, vol. 103, p. 124, 1981.

[166] P. De Causmaecker, R. Gastmans, W. Troost, and T. T. Wu, "Multiple Bremsstrahlung in Gauge Theories at High-Energies. 1. General Formalism for Quantum Electrodynamics", *Nuclear Physics B*, vol. 206, p. 53, 1982.

[167] R. Kleiss and W. Stirling, "Spinor Techniques for Calculating p anti-p $W^{\pm}/Z^{0}$ + Jets", *Nuclear Physics B*, vol. 262, pp. 235–262, 1985.

[168] R. Gastmans and T. T. Wu, "The Ubiquitous photon: Helicity method for QED and QCD", 1990.

[169] Z. Xu, D.-H. Zhang, and L. Chang, "Helicity Amplitudes for Multiple Bremsstrahlung in Massless Nonabelian Gauge Theories", *Nuclear Physics B*, vol. 291, p. 392, 1987.

[170] J. F. Gunion and Z. Kunszt, "Improved Analytic Techniques for Tree Graph Calculations and the G g q anti-q Lepton anti-Lepton Subprocess", *Physics Letters B*, vol. 161, p. 333, 1985.

[171] K. Hagiwara and D. Zeppenfeld, "Helicity Amplitudes for Heavy Lepton Production in e+ e- Annihilation", *Nuclear Physics B*, vol. 274, p. 1, 1986.

[172] A. Denner, H. Eck, O. Hahn, and J. Kublbeck, "Feynman rules for fermion number violating interactions", *Nuclear Physics B*, vol. 387, pp. 467–484, 1992.

[173] P. de Aquino, The simplified RS model implemented in MadGraph/MadEvent via FeynRules is available in the FeynRules website. [https://feynrules.irmp.ucl.ac.be].

List of acronyms

ADD	Arkani-Hamed-Dimopoulos-Dvali theory (large extra dimensions)
ALICE	A Large Ion Collider Experiment
ALOHA	Automatic Libraries Of Helicity Amplitudes for Feynman diagram computations
ATLAS	A Toroidal LHC Apparatus
BEH	Brout-Englert-Higgs
BSM	Beyond Standard Model
CERN	European Organization for Nuclear Research
CKM	Cabibbo–Kobayashi–Maskawa matrix
CMB	Cosmic Microwave Background
CMS	Compact Muon Solenoid experiment
CP	Charge-Parity
GMSB	Gauge Mediated Supersymmetry Breaking
IPHC	Institut Pluridisciplinaire Hubert Curien
KK	Kaluza-Klein
KU Leuven	Katholieke Universiteit Leuven
LEP	Large Electron–Positron Collider
LHC	Large Hadron Collider
LHCb	Large Hadron Collider beauty experiment
LINAC	LINear ACcelerator
LO	Leading Order
NASA	National Aeronautics and Space Administration
NLO	Next-to-Leading Order
NNLO	Next-to-Next-to-Leading Order

MACHO	MAssive Compact Halo Object
MGM	Massless Graviton Model
MSSM	Minimal Supersymmetric Standard Model
PDF	Parton Distribution Function
PS	Proton Synchrotron
QCD	Quantum Chromodynamics
QED	Quantum Electrodynamics
RS	Randall-Sundrum theory (warped extra dimensions)
SM	Standard Model
SPS	Super Proton Synchrotron
SUSY	Supersymmetry
UCL	Université Catholique de Louvain
UFO	Universal FeynRules Output
USP	Universidade de São Paulo
VUB	Vrije Universiteit Brussel
WIMP	Weakly Interacting Massive Particles
WMAP	Wilkinson Microwave Anisotropy Probe

Curriculum vitae

December 26, 1982
Born in São Paulo, Brazil.

Jan 2001 - Dec 2004
Student at Universidade Estadual de Campinas (Campinas State University), Faculty of Physics. Received the Bachelor degree in Physics.

Jan 2001 - Dec 2006
Student at Universidade Estadual de Campinas (Campinas State University), Faculty of Physics. Received the Teaching degree in Physics.

Jan 2005 - Apr 2007
Student at Universidade de São Paulo (University of São Paulo), Faculty of Physics. Received the M.Sc. degree in Physics. Thesis subject: "Beyond Standard Model Physics in theories with Extra Dimensions".

Apr 2007 - Set 2008
Ph.D. research at Universidade de São Paulo (University of São Paulo), Faculty of Physics. Thesis subject: "Beyond Standard Model Physics at the TeV scale: theory and phenomenology at the LHC".

Oct 2008 - May 2012
Joint Ph.D. research between the Katholieke Universiteit Leuven at the Institute for Theoretical Physics and the Université Catholique de Louvain at the Center for Cosmology, Particle Physics and Phenomenology.

May 2012
Ph.D. Defense: "Beyond Standard Model Phenomenology at the LHC".

Publication list

1. P. de Aquino, F. Maltoni, K. Mawatari, B. Oexl
   Jets plus missing energy in light gravitino production at the LHC.
   in preparation (2012).

2. P. de Aquino, W. Link, F. Maltoni, O. Mattelaer and T. Stelzer
   ALOHA: Automatic Libraries Of Helicity Amplitudes for Feynman diagram computations.
   accepted for publication in Comp. Phys. Comm. (2011)
   [arXiv:1108.2041]

3. P. de Aquino, K. Hagiwara, Q. Li and F. Maltoni,
   Simulating graviton production at hadron colliders,
   JHEP 1106 132 (2011) [arXiv:1101.5499]

4. N. D. Christensen, P. de Aquino, C. Degrande, C. Duhr, B. Fuks, M. Herquet, F. Maltoni and S. Schumann,
   A comprehensive approach to new physics simulations,
   Eur. Phys. J. C 71, 1541 (2011) [arXiv:0906.2474]

5. X. Calmet, P. de Aquino and T. G. Rizzo,
   Massless versus Kaluza-Klein Gravitons at the LHC,
   Phys. Lett. B 682, 446-449 (2010) [arXiv:0910.1535]

6. X. Calmet and P. de Aquino,
   Quantum Gravity at the LHC,
   Eur. Phys. J. C 68, 305-311 (2010) [arXiv:0906.0363]

7. P. de Aquino, G. Burdman and O. J. P. Eboli,
   Signal for an Extra-dimensional model of flavor at the LHC,
   Phys. Rev. Lett. 98, 131601 (2007) [hep-ph/0612055]